Molecular design of branched and binary molecules at ordered interfaces

by

Kirsten Larson Genson

A dissertation submitted to the graduate faculty

in partial fulfillment of the requirements for the degree of

DOCTOR OF PHILOSOPHY

Major: Materials Science and Engineering

Program of Study Committee:
Vladimir V. Tsukruk, Co-major Professor
David Vaknin, Co-major Professor
Kristen Constant
Monica Lamm
Zhiqun Lin

Iowa State University

Ames, Iowa

2005

Graduate College
Iowa State University

This is to certify that the doctoral dissertation of

Kirsten Larson Genson

has met the dissertation requirements of Iowa State University

_____
Co-major Professor

_____
Co-major Professor

_____
For the Major Department

TABLE OF CONTENTS

ACKNOWLEDGEMENTS

This project is the culmination of the past eight and a half years of my life and a multitude of people have contributed to it. First, I would like to thank past and present members of the SEMA lab for technical assistance and discussions. Thank you to the summer girls for sample fabrications and molecular modeling of the carbosilane dendrimers. Thanks to Josh Huffman, Jason Holzmueller, Ray Gundawidjaja, Kyle Anderson, and Yen-Hsi Lin for technical assistance. I gratefully acknowledge Beth Rybak, Maryna Ornatska, and Sergiy Peleshanko for technical assistance at Advanced Photon Source, especially the long nights and days collecting data. Special thanks to Melbs Lemieux for being a friend and colleague who listened to the good and the bad news and always helped me find my English.

Thank you to my POS committee members, Prof. Kristen Constant, Prof. Monica Lamm, and Prof. Zhiqun Lin for the time and guidance they have granted me over the years. Thanks to my co-Major Professor, Dr. David Vaknin, who moved beyond showing me a technique. I am especially grateful for the guidance from my major professor, Prof. Vladimir V. Tsukruk, over my entire academic career.

I need to recognize the groups who synthesized the samples for me to research. Dr. Dominic McGrath at University of Arizona for the photochromic monodendron samples, Dr. Eugene Zubarev at Rice University for the 12-arm star polymer and the gold nanoparticle samples, Dr. Myongsoo Lee's group at Yonsei University, Seoul, South Korea for the rod-coil molecules, Dr. Valery Shibaev's group at Moscow State University, Moscow, Russia for the carbosilane dendrimers, and Dr. Tsisilantsis at Patras University, Greece for the Greek star polymer samples.

Lastly, I thank my family for all the support they have provided me throughout this journey. Thanks to my parents, Jeff and Kathy Larson, who pushed me to take every possible opportunity, even when it was thousands of miles away. Kyle, Kerri and Anlin, I appreciate your ability to humble me as your sister even when I "overachieve." To Cindy, Dennis and Sarah, thanks for always believing in me even when you don't know what I'm talking about. To my husband, thanks for supporting me, pushing me, loving me, and taking me out to dinner after a long day. I couldn't have done this without you next to me.

ABSTRACT

This study examined five different branched molecular architectures to discern the effect of design on the ability of molecules to form ordered structures at interfaces. Photochromic monodendrons formed kinked packing structures at the air-water interface due to the cross-sectional area mismatch created by varying number of alkyl tails and the hydrophilic polar head group. The lower generations formed orthorhombic unit cell with long range ordering despite the alkyl tails tilted to a large degree. Favorable interactions between liquid crystalline terminal groups and the underlying substrate were observed to compel a flexible carbosilane dendrimer core to form a compressed elliptical conformation which packed stagger within lamellae domains with limited short range ordering. A twelve arm binary star polymer was observed to form two dimensional micelles at the air-water interface attributed to the higher polystyrene block composition. Linear rod-coil molecules formed a multitude of packing structures at the air-water interface due to the varying composition. Tree-like rod-coil molecules demonstrated the ability to form one-dimensional structures at the air-water interface and at the air-solvent interface caused by the preferential ordering of the rigid rod cores. The role of molecular architecture and composition was examined and the influence chemically competing fragments was shown to exert on the packing structure. The amphiphilic balance of the different molecular series exhibited control on the ordering behavior at the air-water interface and within bulk structures. The shell nature and tail type was determined to dictate the preferential ordering structure and molecular reorganization at interfaces with the core nature effect secondary.

CHAPTER 1. INTRODUCTION

1.1 Literature Review

1.1.1 Current Challenges in Nanotechnology

Coatings have been used for centuries as barriers between materials and a hostile environment. Depositing a protective coating on a surface to inhibit deterioration of the bulk materials greatly extends the service life of parts. Lacquer finishes applied to furniture and outdoor structures offers aesthetic appeal in addition to moisture protection. Similarly, the primary functions of the application of marine paints to ship hulls are to reduce the drag created by the adhesion of barnacles and other sea life and to inhibit the deterioration of the wood or steel hull. Today barrier films are used to improve outer apparel moisture resistance, food storage life, and wound healing. In addition to prohibiting the absorption or adsorption of detrimental molecules, the function of the barrier film incorporates attracting desirable gas or vapors. Understanding the behavior of the protective coating within the specific environment drives the study of thin films response under a multitude of conditions.

Coatings have been used to improve specific properties limited by the bulk material choice for the overall part function. Laminate layers of reinforced plastics used in alpine skis were chosen for high impact strength and flexibility but have less than desirable stiction. Thin layers of wax periodically used to coat the ski surface improve the ski motion on the snow surface. Similarly, the thin lubricant coating on the surface of hard disk drives enabled the efficient function and longer service life by reducing the friction coefficient and debris generated by contact of the read/write head with the disk. The application of an ultra thin surface film (few nanometers thick) can alter the behavior and properties of parts at interfaces, masking the bulk properties of the underlying material. Therefore, examining the surface structure and ordering behavior of thin films and the effect of molecular structure on the resulting properties would improve the film quality.

The biomedical and biotechnology fields have recently yielded the inspiration and model for nanotechnology, specifically the preferential organization of molecules at interfaces with precise environmental conditions.[1] Manipulation of surface structure for

pharmaceutical and biomedical applications can drastically affect the properties within several molecular layers.[2] Surface fouling of mechanical implants impedes the function of the implant and can ultimately disrupt the body more than the failed original (Figure 1).[3] Understanding the biological environment of the implant site and the function of the absorbed molecules leads to improved longevity of biological implants such as intraocular lenses and joint replacements. Targeted delivery and controlled release of drugs for biomedical applications, such as chemotherapy, benefit from the selective absorption of molecules on infected surfaces.[4] Side effects from the toxic drugs are reduced from target delivery of treatment to the infected site. Improved controlled release diminishes dosing errors due to missed or delayed pills. For these applications the surface structure and properties dictate the function success by controlling the material's response to the environment.

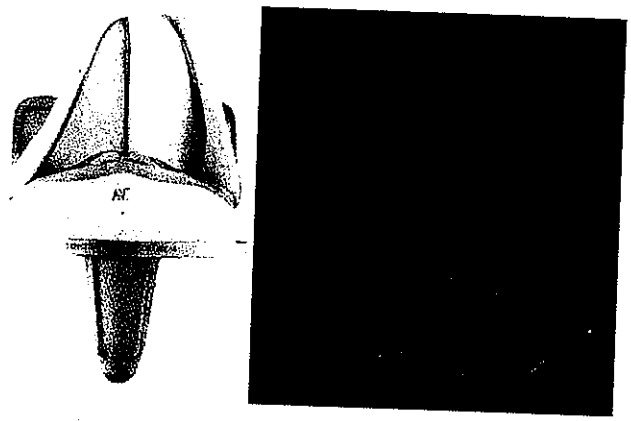

Figure 1. Surface fouling of biological implants such as a knee joint (left) or an intraocular lens (right).

Current challenges in drug delivery and medical implants are the selective adsorption of cells, proteins or drugs on surfaces or the prevention of adsorption of molecules at an interface. Targeted surface-molecule interactions are required to impede biofouling or promote drug delivery. Weber et al. demonstrate small changes in the polymer backbone chemistry significantly impacted the adsorption of fibrinogen on medical implants.[5] Understanding the protein/surface interactions relies on discerning the physicochemical aspects of natural and engineered systems.[6]

Development of targeted delivery of drugs, vaccines, and gene-treatments to the source of need has multiple benefits. Direct delivery to selective areas reduces the amount of medicine and increases the effectiveness of the treatment. The use of branched molecules offers several possible delivery options. Dendritic and branched molecules can be tailored through chemical composition and functional groups. The use of dendrimers in gene/drug delivery focuses in several micelle encapsulation[7], molecular encapsulation[8], and terminal group functionalized[9,10] (Figure 2).

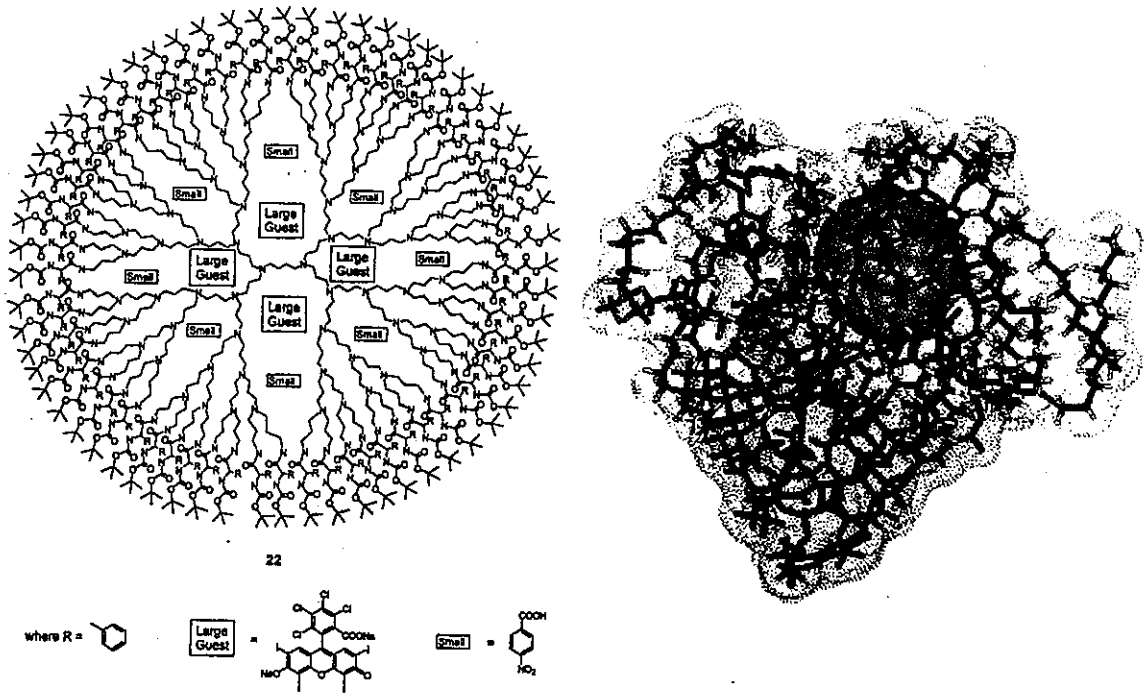

Figure 2. Target delivery and controlled release of drugs would utilize the large cavities develop between the branching arms of dendrimers (left), leaving room for large and small guest molecules and atoms or physical encapsulation in binary molecules (right). (Left image taken from Dykes[33], right image from Zhang et al.[11])

The recent advances in the development of complex nanomachines have driven the investigation "adaptive surfaces" for integrated mechanical, optical, microfluidic, and biological applications.[12,13,14] The devices require sophisticated sensing functions with spatial constraints for the film thickness. Complete on-demand changes in physical

properties of surface films require rapid response to stimuli and uniform surface coverage. Tuning the surface response to subtle differences in the surrounding environment, such as pH[15], temperature[16], and solvent quality,[17] necessitates the inclusion of two chemically competing polymers within the surface film. Uniform coverage of binary polymer brushes is crucial for uniform response across the surface.

The driving force for molecular design in nanotechnology is controlling the interactions of a surface with its surrounding environment. Manipulating the function of the surface by depositing a thin film with the desired structure or properties would resolve design issue of conflicting bulk and surface property requirements.

1.1.2 Branched Macromolecules

The beneficial properties of the branched architecture in the biomedical fields are centered on the organizational behavior. Biomedical fields concentrate on the supramolecular organizational of branched molecules and the variance in the density of the molecules.[18] Beyond the variable density of the branched structure is the property enhancing effects of the numerous end groups. The organic electro-optical research focuses on the photoharvesting and fluorescence properties of highly branched molecular structures. Organic alternatives to traditional conductive and fluorescence materials offer the ability to tailor the materials to the desired properties.

Current applications for branched molecules capitalize on the supramolecular organization, the chemical composition and architecture, and the transition of density.[19,20,21] Tailoring the synthetic route increases the favorable characteristics while reducing the unfavorable properties. Considerable numbers of studies have focused on the use of branched polymers in the biomedical field, mainly focusing on the selective targeting of treatment areas.[22] Branched polymeric materials can be used in optical and optoelectronic materials as replacements for traditional metal and ceramic based products. Use of branched molecules in large-scale industrial applications is limited due to the prohibitive cost of production.[23] Therefore, the proposed applications for branched molecules are often highly specialized to offset the astronomical cost.

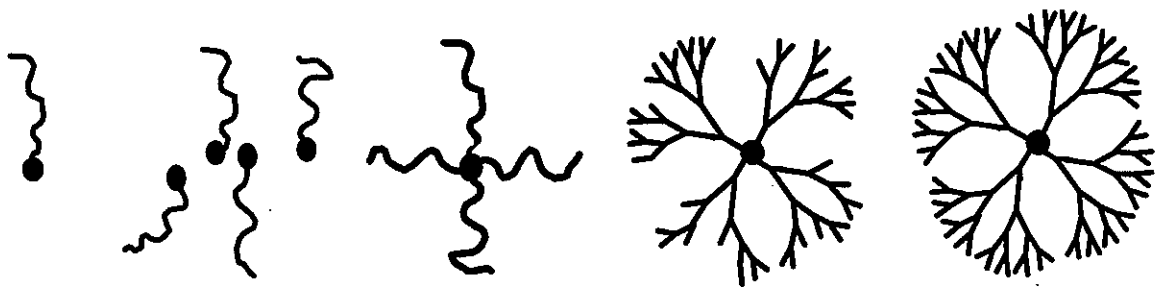

Figure 3. Dendrimers and Star polymer architectures

The tree-like architecture of dendritic and star polymers offers numerous advantages over traditional linear polymers as well as requiring more costly and time-intensive synthetic routes and purification steps. Although the limiting synthetic costs are offset by the improvement in properties, highly specialized compositional tailoring is confined to restricted uses. Branched macromolecules can be divided into three classes: dendrimers, hyperbranched polymers, and star polymers. Dendrimers are well-ordered, monodispersed, branched molecules with a direct relationship between the generation number and the number of terminal groups (Figure 3).[24] Hyperbranched polymers have similar but imperfect architecture of dendrimers due to the "one-pot" synthesis (Figure 3).[25] Combining the advantages of block copolymers and branched architectures initiates the motivation of star polymers (Figure 3).[26]

Unlike traditional polymers with large polydispersity of molecular weights, dendrimers are distinguished by their monodispersity. With every additional generation the product yield reduces due to the frequently incomplete reaction of the numerous terminal groups.[27,28] The purification step becomes essential to the monodispersity of the dendritic polymers with every exponential increase in the terminal branches. The incomplete reaction of the terminal groups for the higher generation is caused by a combination of several factors. One factor is the limited diffusion of the monomers to the reaction sites. Ideally the dendritic molecule forms a global conformation with the terminal groups located at the periphery. However, the terminal groups most likely are clustered near the periphery with most exposed for the reaction while a few are located behind another terminal group or an adjacent branch. Additionally, the available surface space at the periphery for the additional reaction eventually becomes less than the amount required by the total number of terminal groups.

The steric constraint on the possibility for complete reaction causes only partial reaction of the terminal groups.[29]

Unlike dendrimers, star polymers are less impacted by the chemistry and structure of the core architecture. The long polymeric arms are attached to a small defined core that contributes little to the overall ordering behavior and properties of the material. The attraction of star polymers is the ability to balance the polymeric nature of the attached arms with the highly branched core to develop a copolymer molecule that would blend the desirable properties of block copolymers and dendrimers. Star polymers are attractive for the possibility of incorporating chemically disparate polymers as individual arms or as blocks within the long arms. Unlike block copolymers with limited molecular reorganization due to the linear architecture, the attachment of multiple arms to a single point facilitates finer detail structures.[30] The effect of the end group functionality on the molecular ordering behavior is more dominant for star polymers than for linear polymers, but the polymeric nature of the arms is not sacrificed as for dendrimers.

1.1.3 Amphiphilic materials and interfacial behavior

The dimensions of applications in biomedical and advanced warfare fields have continued to shrink, thus driving the need for highly developed thin film technologies. At the nanometer scale materials maintain few bulk properties, thus the two-dimensional properties of materials become more influential than the three-dimensional properties. Design of ordered surfaces at the molecular level necessitates chemically competing fragments within a finite regime. The multitude of nanoscale applications drive the need for the fabrication of ordered molecular films at surfaces.[31] Tailoring the molecular architecture and functionality of fragments facilitate preferential ordering of molecules.

Langmuir and Langmuir-Blodgett (LB) monolayers form ideal thin films to understand the two-dimensional properties of branched molecular structure.[32] The use of amphiphilic thin films provides several improvements over other thin film fabrication techniques. Spin coating thin cast films offer little improvement over bulk materials due to the disorganized packing structure. Cast films are not conducive to intralayer organization due to the quick evaporation of the solvent impeding the molecular organization. Self-

assembled monolayers (SAMs) are limited to organized grafted monolayers of bulky polymeric molecules. The molecular organization limits the formation of uniform structures to reduce the unfavored molecular-molecular and molecular-subphase interactions.

Dendrimers have been used at interfaces to increase the interaction between the two surfaces because they introduce numerous interaction sites. The functionality of the end groups offers exciting possibilities to tailor the properties of the molecules. Most end groups are simple methyl, carboxylic, amine or alcohol groups. To change the end groups or tailor them to a specific use the synthesis can be terminated using different chemistry. Resin beads have had dendrimers grown on their surfaces to increase the attachment points between the solid substrate and the resin beads during solid phase synthesis.[33] Dendrimers have been used as catalyst with catalytic sites being introduced at the periphery, core or throughout the molecule.[34] Molecular organization in Langmuir monolayers is reliant an amphiphilic balance of the molecular fragments and the supramolecular architecture organization. Amphiphilic balance widely ranges from simple polar head groups and alkyl chains to complex branched molecules are composed of a simple hydrophilic head group and a hydrophobic alkyl tail.

1.2 Goals

The goal of this study is to understand the principles of molecular design of branched and binary molecules at ordered interfaces. An aspiration of this study was to discern the appropriate hydrophobic and hydrophilic balance in nontraditional amphiphilic molecules in two-dimensional films at interfaces. The affect of surface chemistry of the substrate, phase separation of polymer fragments, generational behavior of the dendritic core, functionality of the terminal groups, and contrasting polarity of the molecular segments will be analyzed to discern the balance of molecular fragments to induce favorable ordering. Another broad aim was to embed inorganic nanoparticles in organic molecular structures to utilize the high degree of ordering of branched molecules. This study examined the ordering behavior of branched molecules in surface films to resolve the affect of the functionality of molecular fragments on the selective response performance at interfaces.

1.3 Objectives

This project examined the molecular design of branched macromolecules at ordered interfaces and the effect of molecular architecture and chemistry on physical properties. Broad theme objectives are as following:

1. Examine the ordering of chemically competing molecular fragments within monolayers at the air-water and air-solid interfaces to resolve the influence of core architecture and chemistry on the packing structure within surface films
2. Fabricate and characterize Langmuir and (LB) films to understand the effect of end group functionality on the ordering behavior of branched macromolecules at interfaces
3. Discern the effect of the volume fraction of polymeric chains and functional fragments on the molecular ordering of thin films on hydrophobic and hydrophilic substrates
4. Analyze the impact of generation number on the ordering behavior and physical properties of dendritic molecules at the air-water and air-solid interface
5. Elucidate the packing structure of conflicting molecular fragments and phase separation of the polymeric chains induced by the surface chemistry of the substrate and subphase
6. Determine the molecular organization of binary molecules at air-water, air-solid, and liquid-solid interfaces and the ability of binary molecules to reorganize under favorable conditions.

1.4 Approaches

Comparison of linear polymers, star polymers, radial dendrimers, and monodendrons at surfaces revealed the influence of the structure, flexibility and chemistry of the molecular core on the packing structure at interfaces. The effect of shell functionality on molecular ordering was examined by comparing the attachment of liquid crystalline (LC) terminal groups and alkyl tails to dendritic cores versus long polymeric arms to defined cores of star polymers. The generational effect exhibited as an overall increase in molecular size versus

an exponential rise in the terminal groups was explored. Additionally the length and composition of the polymeric arms was varied as well as the ratio of the functional terminal groups. The influence of molecular composition was probed by studying the behavior of amphiphilic compounds with hydrophilic and hydrophobic tails.

The two-dimensional properties of Langmuir monolayers were analyzed to discern the effect of the branched molecular structure on the packing behavior nontraditional amphiphiles. The contributions of the degree of branching were investigated for dendritic amphiphiles. The cross-sectional area mismatch between the polar head group, the spacer group, and the hydrophobic alkyl tails were examined to ascertain the effect of the mismatch on the molecular organization. The intralayer packing structure were examined to determine the role of the core versus functional groups on the molecular interactions. By expanding the dendritic molecular structure to encapsulate the rod-coil design, the behavioral influence of both molecular design elements was discerned. Tree-like rod-coil molecules were examined to comprehend the influence of molecular fragment composition versus molecular architecture. The ratio of the functional terminal groups was varied to understand the effect of functional groups on the amphiphilic balance. Star polymers were varied in the chemical composition, length, composition ratio, and number of the polymeric arms. The influence of the chemical composition was investigated in conjunction with the length and number of the arms. Further studies examined the influence of the core and branching of the polymeric arms from the core on the molecular organization at the interfaces as well as bulk properties.

Molecular interaction are capable of overcoming the preferential radial ordering of flexible dendritic cores to form stagger layered packing structure in confined surface films. A mismatch of cross-sectional areas occupied by competing molecular fragments induces a kinked packing structure, compelling the smaller molecular fragments to reorganize to maintain a densely packed monolayer. The packing structure of monomolecular thin films depends upon the force the ordering behavior of the dominant molecular fragment exerts on the preferential ordering of the weaker fragment.

Ordering behavior of branched molecules can be driven by interactions with the surface. Ultra thin surface films were fabricated using several thin film techniques including LB, spin casting and physical absorption. The competing hydrophilic and hydrophobic

molecular fragments composed an appropriate balance favorable for highly c. monomolecular layers at the air-water interface. Physical absorption of molecules onto bare and functionalized substrates was used to determine the dominating molecular interactions at interfaces. Variation in fabrication techniques explored possible technique induced preferential ordering (LB) versus ordering facilitated by attractive forces (physical absorption). Substrate selection was demonstrated to play a role in the ordering of molecules in surface films, therefore quartz, mica, and silicon were used.

Interfacial studies of branched macromolecules at liquid and solid surfaces were carried out using a multitude of characterization techniques. A combination of X-ray reflectivity and grazing incident X-ray diffraction (GIXD) reveals internal ordering of the confined surface layers and insight into the organization of molecular fragments. Surface properties such as morphology, adhesion, elastic moduli, and friction behavior were obtained using a combination of contact and noncontact modes of AFM. Raman spectroscopy were employed to evaluate molecular conformation and deformation in surface films in addition to the morphology of surface. Photochromic behavior of dilute solutions and grafted thin films was analyzed using ultraviolet-visible light spectroscopy (UV-vis). Scanning electron microscopy (SEM) and transition electron microscopy (TEM) were used to image the topography and characterize the surface chemistry of surface films. The surface energy of polymer films was estimated by water contact angle measurements, and trends in effective thickness were estimated using ellipsometry.

CHAPTER 2. EXPERIMENTAL

The branched macromolecules presented in this study exhibit a variety of molecular architecture as well as an array of chemical compositions. The proposed molecular systems compose a diverse study on the influence of chemical composition versus molecular shape and architecture. The six primary systems are briefly presented below. Additionally, surface film fabrication techniques and various bulk and surface characterization techniques utilized in this study are described.

2.1 Scheme of Compounds

Molecular architecture affects the physical and chemical properties of materials at interfaces due to the confined space. The ability to tailor specific properties for surface applications drives molecular design. The properties of polymeric materials are determined by the architecture, chemical composition, and molecular size and shape. The interactions between the various individual fragments influence the overall balance and behavior of the molecules. Molecular interactions between functional terminal groups and favorable surface chemistry were examined to determine the reorganization. The degree of branching and symmetry of the branches dictate the packing behavior. The materials studied in this project present a diverse view of branched molecular structure. This project demonstrates dominant functional groups controlled the organization of chemically competing molecular fragments within monomolecular films at the interfaces.

The materials presented in this study provide a diverse view of dendritic and branched molecules (Figure 4). The core nature was analyzed by varying the molecular core rigidity from flexible discotic cores to rigid, aromatic rod and discotic core, and the effect of the core nature on molecular ordering at interfaces. In contrast the shell nature was varied from a single hydrophobic or hydrophilic tail to highly branched tails to multiple functional terminal groups to discern the influence of the dendritic shell on the molecular packing structure.

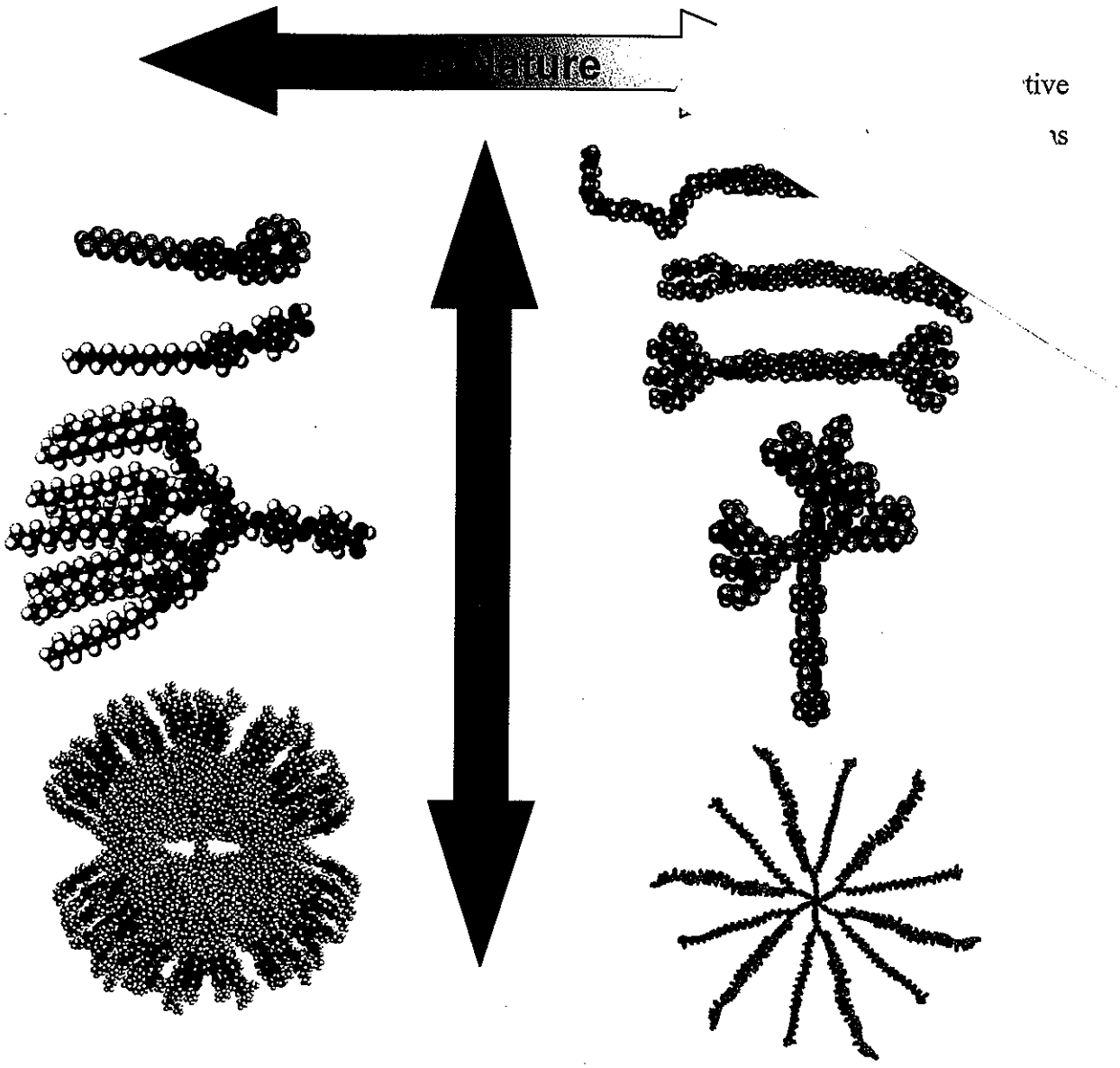

Figure 4. Scheme of materials presented in this study. The core nature varied from flexible, branched hydrophilic structures to rigid, defined, hydrophobic structures. The shell nature diverged from single hydrophobic tail to symmetric hydrophilic coils to multiple tails attached asymmetrically to numerous polar groups or long polymeric arms attached radially.

2.1.1 Functionalized Photochromic Monodendrons

The one of the challenges in the field of nanotechnology is controlling the selective response of thin films, especially the organized surface monolayers.[35] Recent investigations in this area have concentrated on tailoring the response of a thin film to environmental stimuli at the nanometer scale.[36] In this regard, molecules with azobenzene fragments have been considered as potential components of films with selective light-triggered response. Indeed, a multitude of studies focused on various molecules with azobenzene fragments such as holographic media,[37] for optical storage,[38] as reversible optical waveguides,[39] for photoalignment of liquid crystal systems,[40] and for drug delivery[41]. The azobenzene group is attractive due to the two stable isomers it assumes upon selective wavelength stimuli. The main complication of the inclusion of photoresponsive molecules in selective response monolayers is the preservation of the full and fast isomerization response.[42] Deposition of thin surface films onto solid supports often restricts the mobility of the photochromic fragments within the molecular architecture and thin films, thereby reducing the overall response and the reversibility. The tilted orientation of azobenzene containing molecules in self assembled monolayers reduced the surface coverage (50-60%) and lowered the monolayer thickness thereby resulting in a slight increase in thickness during photoisomerization.[43]

The focus was to understand the molecular packing of the dendrimers and its effect on the kinetics of the *cis-trans* conformation switching. Molecules containing an azobenzene spacer group have two stable isomers, the *trans* isomer when the angle between two benzene rings attached by a nitrogen double bond is 180° and the *cis* isomer when the angle decreased to approximately 120°. The *cis-trans* isomer conformation is stimulated by narrow wavelength bans. Proof of this isomer transition can be seen in the UV-vis spectra of dilute solutions of the azobenzene compounds. Selective appearance and disappearance of peaks before and after illumination with a UV lamp denotes the isomer transitions.[44,45]

Two series of photochromic monodendrons (**AD12-N** and **AA-N**, N representing the number of alkyl tails attached) have been synthesized by Dr. Dominic McGrath at the University of Arizona.[46,47] The monodendron series compared the effect of various polar head groups (crown ether, carboxyl, and epoxy) versus increasing number of alkyl tails on

the photochromic behavior of monodendrons and the influence of the cross-sectional mismatch on the lateral packing structure of the molecules at the air-water and air-solid interfaces.

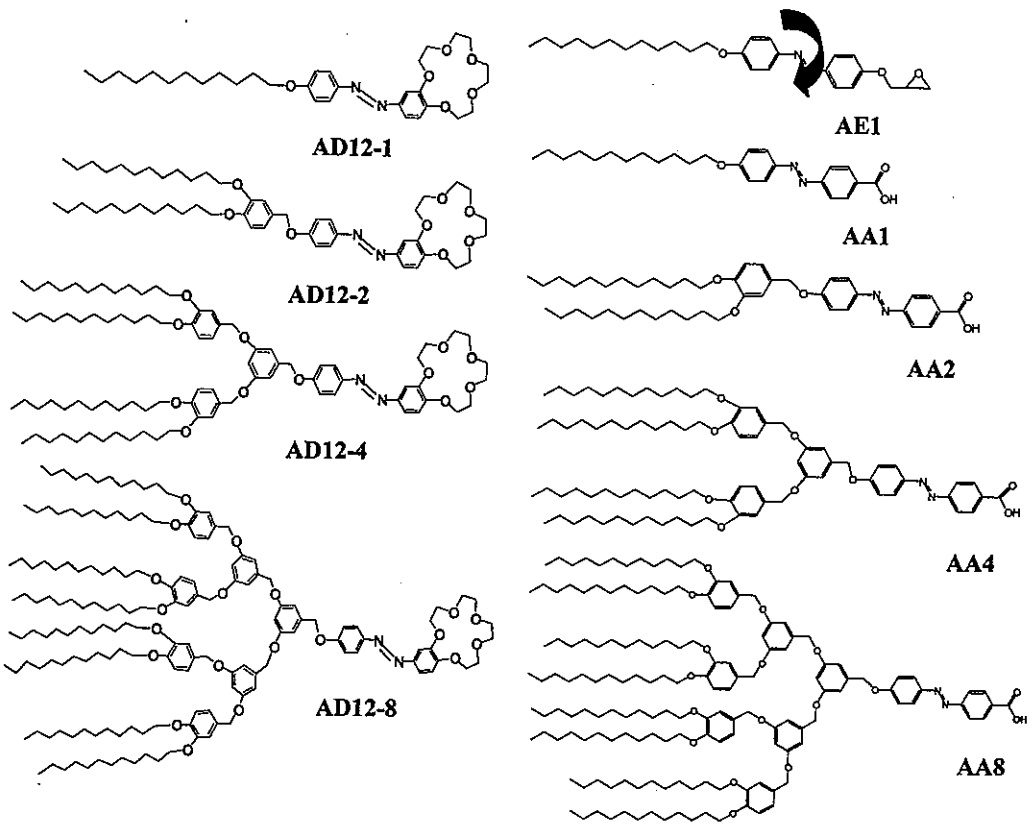

Figure 5. Chemical formulas for photochromic monodendrons **AD12-N** (left), **AA-N** (right), and epoxy terminated reference molecule **AE-1** (top right).

2.1.1.1 Molecules based on Bulky Discotic Core

The **AD12-N** molecules pair a bulky crown ether head with a varying number of C_{12} alkyl tails separated by an azobenzene group (Figure 5). The photochromic response of the molecules was examined in dilute solutions, at the air-water interface and on solid supported samples.[48] Previously published comparative studies have evaluated the behavior of these molecules on solid surfaces and a similar series with C_{10} tails at the air-water interface and deposited self-assembled layers.[49,50]

2.1.1.2 Molecules based on Traditional Polar Head Core

The **AA-N** molecules consisted of a carboxylic acid head group, an azobenzene spacer group and multiple dodecyl alkyl tails. The number of tails increased from one for (4-dodecyloxyphenylazo)benzoic acid (**AA-1**), to two, four, and eight for the second, third, and fourth generations of a dendritic series (Figure 5). The ability to maintain efficient photochromic within grafted surface films was analyzed by comparison of **AA-N** with a single tail reference molecule functionalized with an epoxy polar group (**AE-1**).

2.1.2 Liquid Crystal Terminated Carbosilane Dendrimers

The exploration of heteroatom dendrimer architecture offers greater possibilities in catalysis and organic-inorganic hybrid material applications, especially for the stable dispersion of metal nanoparticles. Additionally, the inclusion of silicon in the inner repeat units of the dendritic core offers favorable synthetic routes for ideal dendrimers as well as thermodynamically and kinetically stable molecules.[51,52,53] Carbosilane dendrimers are favorable for further functionalization because the low polarity and high energy of the Si-C bonds creates a chemically stable core. The exceptional flexibility of the carbosilane dendrimers also makes them an easily adaptable with overall shape dictated by interactions among terminal groups and terminal groups with supporting surfaces in cases of their adsorption on solid substrates.[54]

The incorporation of LC fragments in dendritic architecture is an intriguing design approach which can result in fabrication of hybrid structures combining LC properties and dendritic functionalities and shapes.[55] Competing trends of mesogenic fragments to arrange in highly ordered structures and dendritic cores to form symmetrical shapes can fuse into multitude of amalgam structures. The ellipsoidal shape of the dendritic core has been shown to adversely affect the order of the mesogenic fragments attached to higher generation dendrimers.[56] The functionality of the terminal groups might exert ultimate control on the molecular packing of dendrimer cores.[57,58,48] The combination of flexible dendritic cores and mesogenic groups creates novel LC behavior.[59] The inclusion of mesogenic groups at the periphery forced a transition to a disc shape facilitating a columnar ordering.[60] A fifth generation carbosilane dendrimer with 128 cyanobiphenyl groups was shown to have

significant pecularities in the LC behavior upon heating, unlike the lower generations dendrimers of the same type.[61] Surface studies of the fifth generation dendrimer showed that the film thickness and the substrate controlled the molecular packing.[62]

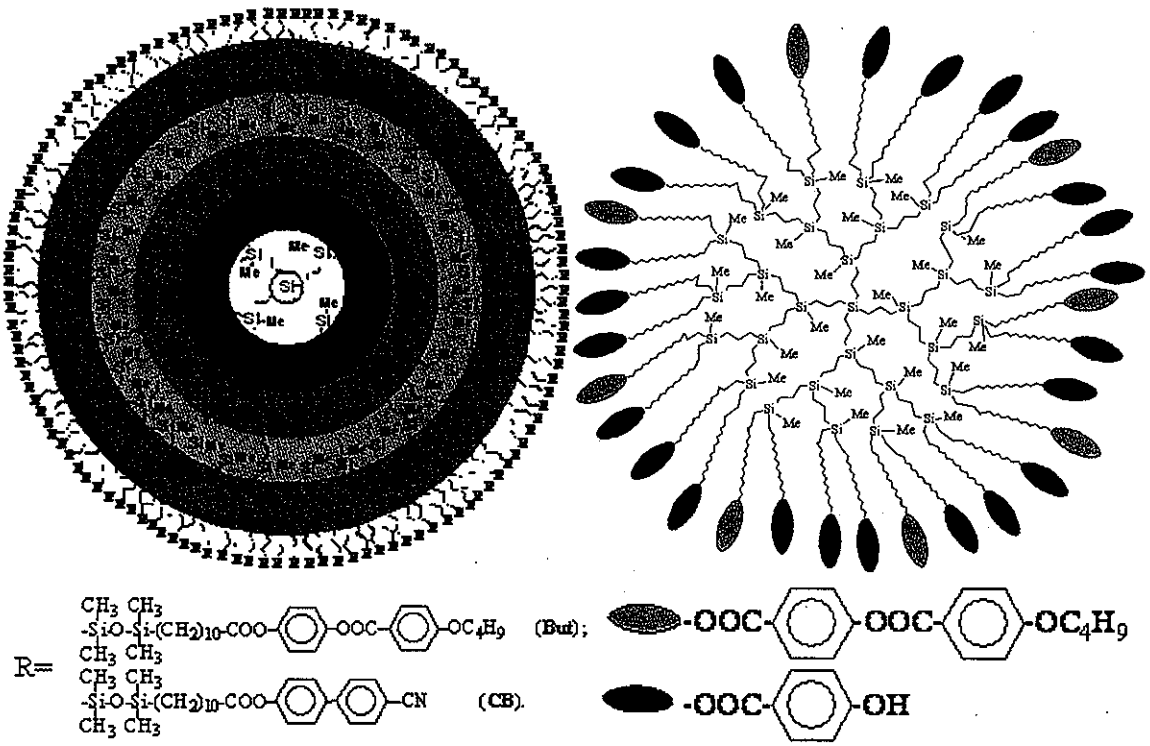

Figure 6. Chemical formulas of G-3(Und–PH-But-70%), G-5(Und-But)$_{128}$, and G-5(Und-CB)$_{128}$ LC carbosilane dendrimers.

Two generations of carbosilane generation functionalized with LC terminal groups were synthesized by Dr. Valery Shibaev at Moscow University, Russia.[63,64,65] The fifth generations of the carbosilane LC dendrimers were functionalized with a complete shell (100% substitution of terminal groups) of cyanbiphenyl (G-5(Und-CB)$_{128}$) and butoxyphenylbenzoate (G-5(Und-But)$_{128}$) groups while the terminal shell of the third generation of LC co-dendrimer (G-3(Und–PH-But-70%)) combined a blend of butoxyphenylbenzoate and phenolic terminal groups (Figure 6). Competing molecular interactions were observed to affect the packing structure within thin surface films.

2.1.3 Star Polymers

Star block copolymers possess an unusual molecular architecture which often generates properties not observed in linear analogues.[66,67] The self-assembling behavior of amphiphilic star polymers in selective solvents is particularly interesting. To this end, spherical,[68] cylindrical,[69] and vesicular[70] micelles have recently been documented by several research groups. By way of contrast, little is known about their behavior at the air-water interface and how it compares to linear diblock systems which were studied for several systems. Examples of the interfacial structures of homopolymers[71] and amphiphilic block copolymers were previously described.[72] Eisenberg and coworkers[72] reported on the discovery of surface micelles of polystyrene (PS)-poly(4-vinylpyridine) which formed spontaneously at the air-water interface. Such structures were fairly uniform and consisted of ~100 individual molecules. Another example of an amphiphile studied directly at the air-water interface was PS-poly(ethylene oxide) (PEO) as described by Silva et al[73] and Lennox et al.[74] It was shown that this copolymer forms highly ordered 2D arrays of spherical micelles at moderate surface pressure, although the actual mechanism of their formation remains highly debatable. Interestingly, several non-amphiphilic block copolymers such as PS/poly(*t*-butyl methacrylate), PS/poly(*t*-butyl acrylate), PS/poly(*n*-butyl methacrylate) and PS/poly(dimethyl siloxane) behave at the air-water interface in a manner similar to that of amphiphiles, which appears to be a universal behavior of di-block copolymers mainly defined by the volume ratio of the incompatible blocks.[75] A number of linear PS-poly(acrylic acid) (PAA) block copolymers have been studied in selective solvents, solid surfaces, and air-water interfaces and a variety of micellar structures and aggregates have been observed with shape, size, and symmetry depending upon their chemical composition and molecular weight.[76,77]

Unique morphologies were found in branched and star copolymers block copolymers that were not observed for linear block copolymers.[78] At the air-water interface, the behavior of star-shape copolymer is qualitatively identical to linear systems; the hydrophilic chain collapses into globules while hydrophilic chain spreads out to form pancake structure.[79] At high surface pressure, nonetheless, recent studies showed that crowding of hydrophobic PS chains at a single junction point in asymmetric heteroarm PEO-b-PS_m star polymer increased circular micellar stability.[80] Attachment of multiple chemically disparate polymeric chains to

a central core affected the packing structure of copolymers at interfaces. Star polymers incorporate long polymeric arms attached to a branched low molar weight core. Asymmetric star polymers, also termed hetreoarm star polymers, form unique nanostructures due to different polymer arms attached to a single core. Pairing chemically competing polymers creates the possibility for molecular adaptation to the surrounding environment.

Two series of star polymer were examined at the air-water and air-solid interfaces to discern the influence of branching and number of polymeric arms on the molecular packing structure. The influence of symmetry and volume fraction on the molecular ordering was examined for 12-arm binary star polymers. The number and volume fraction of the polymeric arms of block star copolymers was varied to elucidate the molecular organization of the star polymers within surface films.

2.1.3.1 Twelve-arm Star Polymers.

Binary star polymers $(PS_m)_6$-*star*-$(PAA_n)_6$ were synthesized by Dr. Eugene Zubarev at Iowa State University.[69] Twelve alternating hydrophobic/hydrophilic arms of polystyrene and poly(acrylic acid) were attached to a well-defined rigid aromatic core (Figure 7). The binary polymer arms length was varied from 25 PS and PAA mers for the small, symmetric star to 40 PS and 30 PAA mers for the larger, asymmetric star. The impact of symmetry and volume fraction on the molecular ordering of binary star polymers at interfaces was examined.

2.1.3.2 Block Star Copolymers.

Six block star copolymers (S*n* – *wt*, *wt* the molecular weight fraction of the PEO block) with an equal number of PEO and PS arms (*n*) were synthesized by Dr. Constantinos Tsiliantsis at Patras University, Greece. The molecular weight fraction of the polymeric blocks was varied as the molecular weight of the blocks was symmetrically distributed between *n* arms (Table 1). The symmetry of the number of PEO and PS arms was offset by the asymmetric molecular weight of the polymeric blocks thus comparing the role of molecular weight fraction versus number of polymeric arms (Figure 8). A linear block

copolymer with similar molecular weight fraction as the star polymer with the highest PEO block was included to discern the effect of branching on the interfacial behavior.

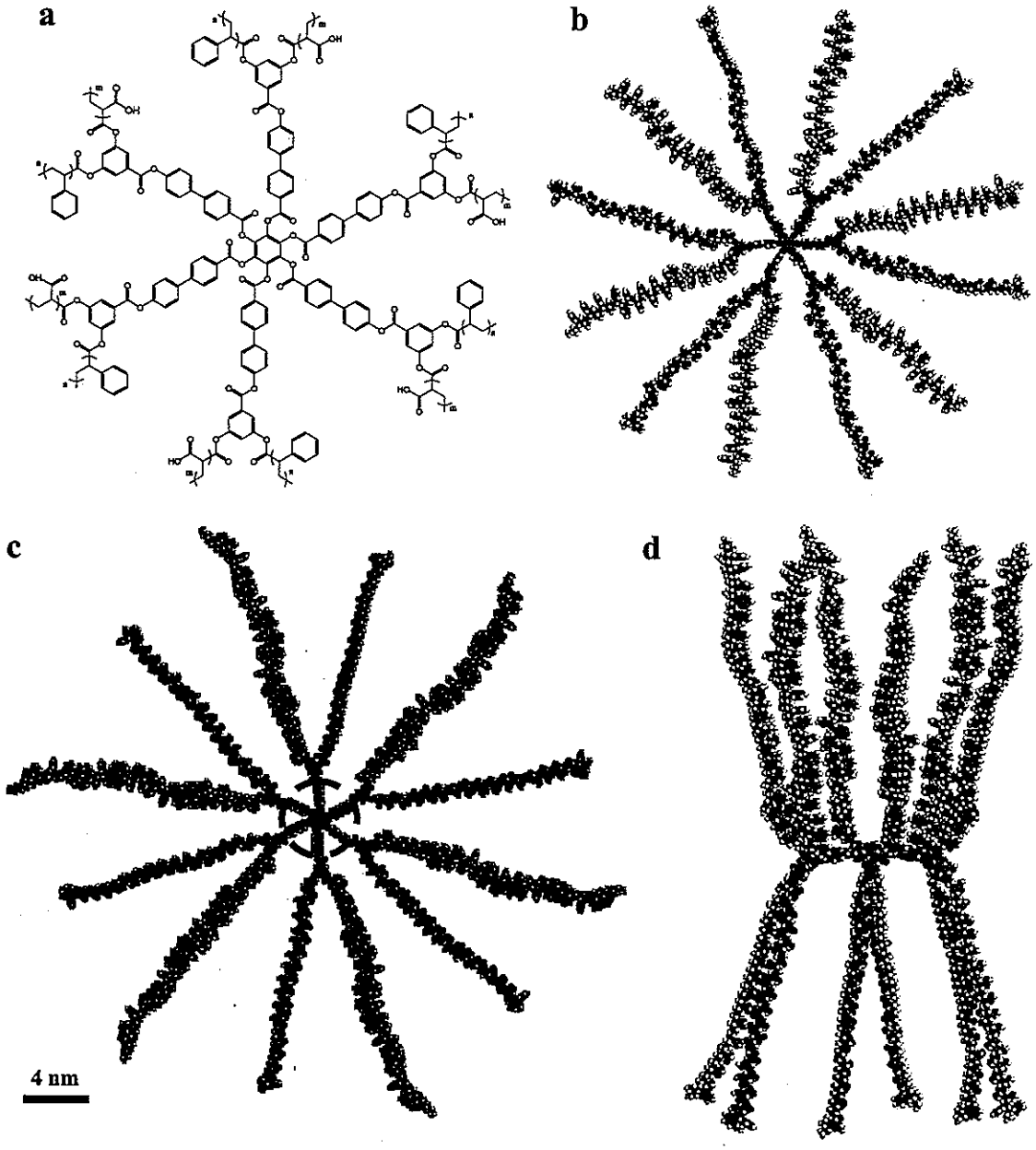

Figure 7. a) Chemical formula of $(PAA_m)_6$-s-$(PS_n)_6$ b) molecular model of $(PAA_{25})_6$-s-$(PS_{25})_6$ c) molecular model of $(PAA_{30})_6$-s-$(PS_{40})_6$ d) side view of $(PAA_{30})_6$-s-$(PS_{40})_6$ with a spatial separation of hydrophobic PS and hydrophilic PAA arms placed above and below the aromatic core, respectively. Dashed circle represents the calculated core area.

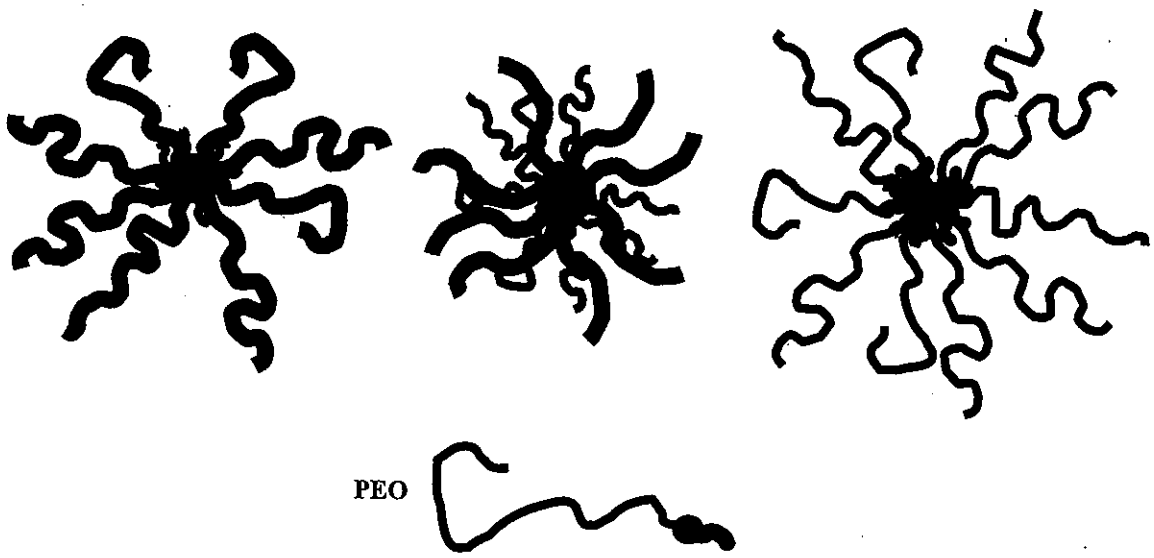

Figure 8. Schematics of star block copolymers with low (left) and moderate PEO content (center), (group **I**), and high PEO content (right) (group **II**). Schematic of linear block copolymer molecule shown in lower right corner.

Table 1. Molecular characteristics of PS_n-PEO_n star polymers

Sample	Composition	Number of Arms, *n*	M_n (PS)	M_n (PEO)	wt_{peo}	M_n total
S8-19	PEO_8-PS_8	8	27,000	5,600	0.19	241,000
S9-23	PEO_9-PS_9	9	22,000	6,500	0.23	245,000
S8-39	PEO_8-PS_8	8	15,000	9,100	0.39	185,500
S19-78	PEO_{19}-PS_{19}	19	3,000	14,200	0.78	339,000
S15-86	PEO_{15}-PS_{15}	15	3,000	22,500	0.86	393,000
S10-88	PEO_{10}-PS_{10}	10	3,100	25,000	0.88	284,000
L-88	PEO-PS	1	3,100	25,000	0.88	???

2.1.4 Branched Gold Nanoparticle and Polymer Brush Molecule

Ordered structures of nanoparticles are attractive for numerous nanotechonoly applications because of their novel magnetic, optical, electronic, and optoelectronic properties.[81,82,83] Controlled ordering of inorganic nanoparticles at interfaces is an important challenge in nanotechnology, requiring the prohibition of nanoparticle aggregation and facilitating organization within a defined pattern. Binary molecules incorporate the attractive

properties of the metal nanoparticle core with the controlled long range ordering of the polymeric shell. The "polymer nanotemplating" approach creates defined nanoscale architectures by nucleating inorganic crystals within a polymer matrix.[84,85,86,87] Hybrid building block composed of 3.2 nm diameter gold nanoparticles encapsulated in an eight generation full PAMAM dendrimers have been observed to self-organize on amphiphilic patterned surfaces.[88,89] A similar approach of encapsulating Cu, Pd and Pt nanoparticles in PAMAM dendrimers was demonstrated by Zhao and Crooks.[90,91,92] Functionalizing small inorganic nanoparticles with long polymeric brushes would isolated the core from the environment and develop binary materials with novel properties. Amphiphilic copolymers in the functional shell drive ordering at the air-water interface and in selective solvents.[93,94,95,96,97] Gold nanoparticles have been physically encapsulated in cross-linked diblock copolymer micelles eliminating the need for linking moities.[98] Mixed Langmuir monolayers of surfacants and ligand stabilized metal-core nanoclusters formed highly ordered nanostructured films.[99,100,101]

Accurate assessment of the molecular structure and composition of binary molecules is difficult using traditional techniques. NMR and GPC greatly underestimate branched structures and are ineffective for binary molecules. Traditional techniques such as FTIR lack the sensitivity to characterize monolayers. Molecular composition of binary molecules in monolayers is possible using surface enhanced Raman spectroscopy (SERS).[102103104105106]

The gold nanoparticle with y-shaped polymer brush corona (AuNP-PB-PEO) was synthesized by Prof. Eugene Zubarev at Iowa State University.[107] A hydrophilic PEO_{44} chain and hydrophobic PB_{20} chain attached to a y-shaped aromatic core were covalently bonded to the 1.5 nm diameter gold nanoparticle (Figure 9). Theoretical estimates of 15-25 y-shaped brushes per gold nanoparticle core were calculated from spacial estimates in addition to molecular models. The extended brush diameter for AuNP-PB-PEO was calculated to 28.5 nm with each y-shaped brush 13.5 nm fully extended. GPC estimated 7.4 brushes attached to the core although the technique typically underestimates the molecular weight of nonlinear particles.

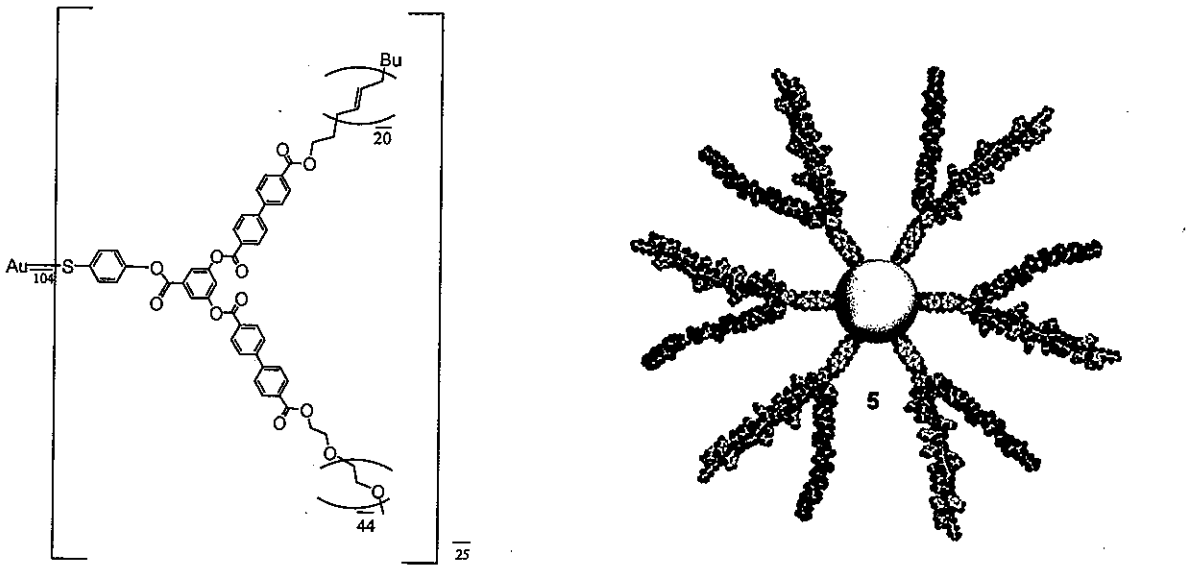

Figure 9. Gold Nanoparticle branched molecules

2.1.5 Rod-Coil Molecules

A current challenge to nanotechnology is the fabrication of one-dimensional structures with tunable physical and optical properties desirable for sensor and nano-array applications. The ability to dictate the three-dimensional shape and ordering of large, functional, supramolecular structures by controlling the molecular building block has been demonstrated.[108,109,110,111] Spontaneous assembly of molecules into one-dimensional structures such as ribbons and fibers, particularly with lengths beyond several microns, requires competing molecular behavior as seen in amphiphilic molecules. Shape persistence structure of regular, symmetric polyphenylene dendrimers and intermolecular π-π interactions drive the molecules to assemble into micron long nanofibers while preserving the fluorescent behavior of the molecules.[112,113] Oligoarylenes exhibit the ability to self-assemble into nanowires due to the preferential π-π stacking induced planarity thus displaying fluorescent behavior.[114] Recently, it has been demonstrated the assembly of one-dimensional crystalline structures does not require defined molecular architectures, but competing molecular fragments.[115]

Rod-coil molecules offer unique molecular architecture that form organized structures in bulk and two-dimensional thin films. The attraction between the rigid rod cores creates

the highly ordered nanostructures desired for nanoscale arrays of inorganic particles. Highly ordered arrays are the basis of microscale electric, mechanical, and optical machines. Current limitations in applications are caused by the lack of self-assembly and ordering of inorganic particles on the submicron scale. Imbedding inorganic particles in organic molecules and molecular structures with highly oriented formation would create organized nanoarrays of desirable inorganic particles.

Various rod-coil molecular architectures were synthesized by Dr. Myongsoo Lee at Yonsei University, Seoul, Korea. The volume fraction of flexible, linear coil segments symmetrically attached to a rigid core was varied to understand the effect of volume fraction ratio on molecular ordering. A similar rigid rod core was functionalized with symmetric coil blocks with varied degrees of branching to discern the influence of branching as the molecular weight remained constant. Finally, three tetra-branched coils were attached asymmetrically to a phenyolic rod core to determine the consequence of tree-like architecture on the packing structure at interfaces.

2.1.5.1 Linear Rod-Coil Molecules

Linear rod-coil molecules **CRC-N** (N corresponds to the number of monomeric units in the symmetric tails equaling 3, 6, 17, 22) were synthesized by Dr. Lee's group (Figure 10).[116] Flexible poly(propylene oxide) chains of varying lengths were symmetrically attached to a rigid rod core to discern the effect of varying the volume fraction ratio on molecular ordering at interfaces.

2.1.5.2 Dumbbell-shaped Rod-Dendron Molecules

The dumbbell shaped rod-dendron **RDM-N** (N represents the generation number indicating the degree of branching) series were provided by Dr. Lee's group.[117,118] Flexible branched coils of poly(ethylene oxide) were symmetrically attached to a rigid block of phenyl rings (Figure 11). The molecular weight remained constant as the degree of branching of the symmetric coil blocks was increased per generation.

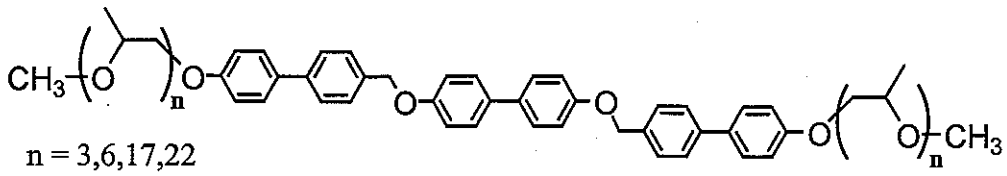

Figure 10. Chemical formula for the linear rod-coil molecules (**CRC-N**)

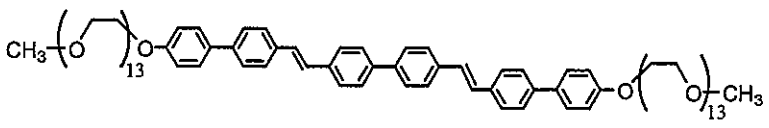

RDM1

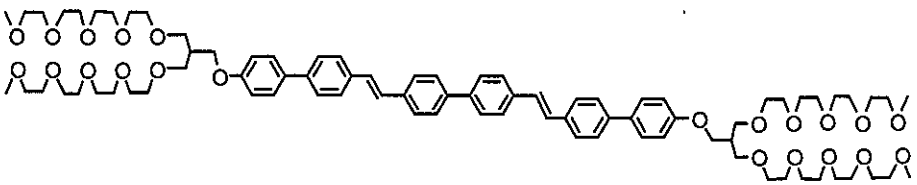

RDM2

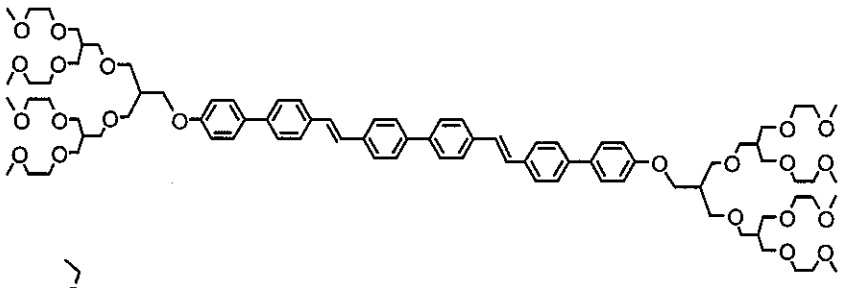

RDM3

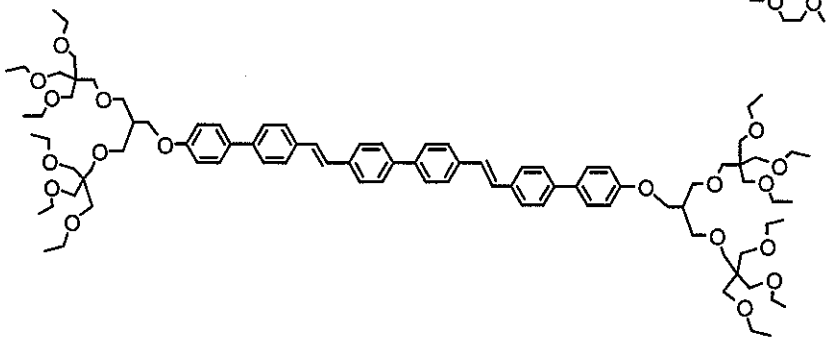

RDM4

Figure 11. Chemical formula for dumbbell shaped rod-coil molecules (**RDM-N**).

2.1.5.3 Tree-shaped Rod-Coil Dendron

Tree-shaped rod-dendron molecules (**MT-1** and **MT-2**) were supplied by Dr. Lee's groups.[119,120] Three tetra-branched poly(ethylene oxide) chains were attached asymmetrically to a rigid octa-p-phenylene core at the first and second phenyl rings (Figure 12). The end functionality of the flexible PEO chains was varied from methyl groups (**MT-1**) to hydroxyl groups (**MT-2**).

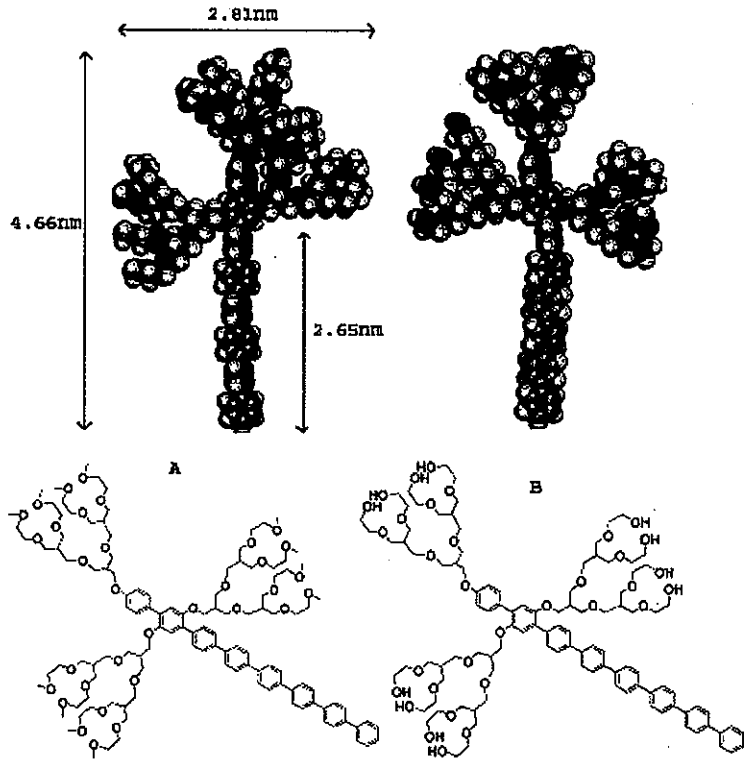

Figure 12. Chemical formula of tree-shaped rod-dendron molecules a) **MT-1**, methyl terminated branches and b) **MT-2**, hydroxyl terminated branches.

2.2 Surface Films Fabrication Techniques

Surface films can be differentiated by the type of interactions between the molecules and underlying substrate. Multiple coating techniques such as spin coating, dip coating, and spray coating are dependent on physical interactions to form surface coatings.[121] The ease of reproducibility and uniform homogeneity make the physical interaction fabrication processes more attractive. These techniques rely on the evaporation of solvent from a spread solution

on the substrate to form the film, thereby controlling film thickness by deposition conditions for dip and spin coating. More sophisticated fabrication techniques, such as LB and Layer-by-Layer improve control of the internal film structure and film thickness. The stability and functionality of the surface films based on physical interactions is highly susceptible to damage in under unfavorable conditions. Attaching the coating molecules to the surface through chemical bonds improves the stability under harsh environmental conditions. SAMs utilize small organic molecules with a reactive focal group that develops a covalent bond with the substrate surface. The precise control of the surface film fabrication creates well ordered structures with self-limiting capabilities but requires more complicated fabrication process.

The substrates for thin films layers were polished silicon wafers (Semiconductor Processing Co.) of the {100} orientation. Wafers were cleaned to remove any organic and inorganic contaminants from the surface following an established procedure.[122,123] The wafer was cut into appropriate sized pieces using a diamond cutter and rinsed thoroughly with NanoPure water. The sample wafers were then placed in a Teflon holder and sonicated for five minutes to remove any silicon dust. The sample wafers were then submerged in the holder in a 1:3 mixture of 30% hydrogen peroxide and concentrated sulfuric acid for one hour. The samples were rinsed three times with NanoPure water and dried under a stream of dry nitrogen. The samples were placed in individual bottles and stored in a desiccator. The silicon substrates were used bare or modified with a SAM of octadecyltrichlorosilane (OTS, Aldrich).[124]

2.2.1 Langmuir-Blodgett Films

A common technique used to create monomolecular films of amphiphilic molecules is depositing small amounts of molecules on the surface of a trough with a known surface area. An π~A isotherm is created by recording the pressure versus the area per molecule. The molecules self-organize into preferred orientations at the air-water interface, and can be studied on the liquid subphase or on a solid substrate after deposition.

Figure 13 illustrates the general procedures for molecular reorganizations of the amphiphilic compounds at the air-water interface and their transfer to solid surfaces.[32] The molecules remain at the air-water interface due to the balance of hydrophobic and hydrophilic segments in the molecular structure. The initial monolayer is disordered with molecule-molecule interactions minimal because of the large cross-sectional area per molecule (Figure 13a). Upon reduction of the surface area of the trough the molecule-molecule interactions become more visible in the surface pressure behavior of the film. In the low pressure regimes the molecules tilt slightly away from the surface normal to form an ordered structure (Figure 13b). Further reduction of the cross-sectional area per molecule induces the molecules to move closer to the surface normal and form close packed structures (Figure 13c). To deposit the monolayer onto a solid substrate the monolayer is compressed after a substrate is submerged into the liquid subphase. Upon reaching the desired surface pressure the barriers decrease in speed and the substrate is lifted from the liquid subphase (Figure

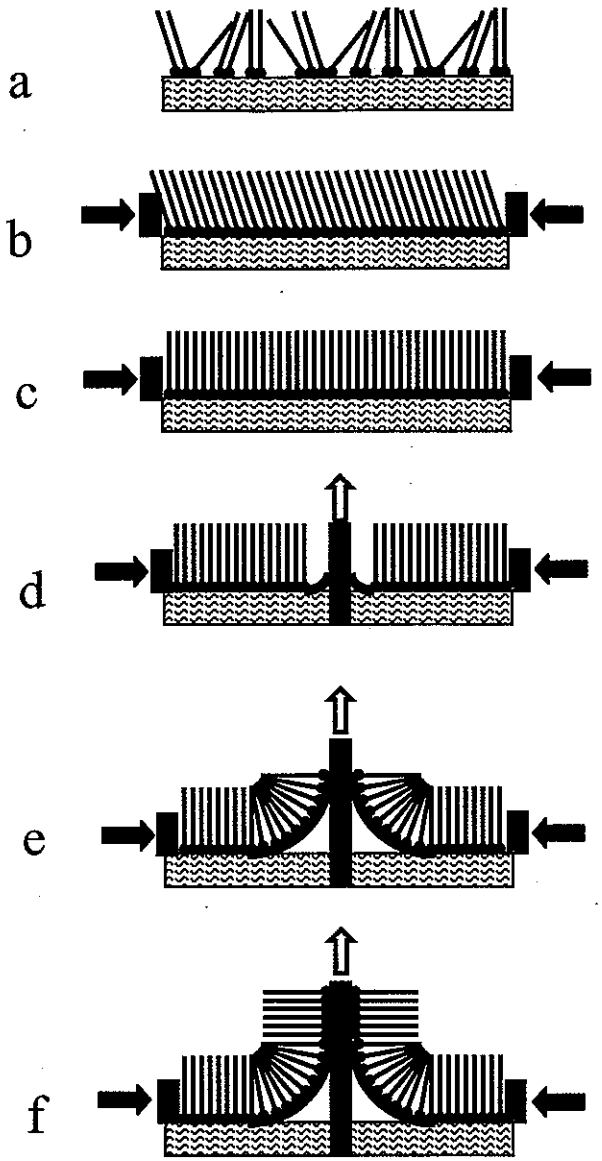

Figure 13. Schematic of fabrication of monomolecular films by the Langmuir and LB technique. a) Spreading of molecules on water surface b) Initial compression of monolayer results in low pressure regime c) High pressure regime d) Formation of meniscus of water to substrate e) Transfer of molecules to substrate f) Deposition of molecules on substrate.

13d-f).

Monolayers are prepared from dilute chloroform solutions by the Langmuir technique on an R&K-1 trough (Riegel & Kirstein, GmbH).[125] Dilute solutions of the molecules are prepared in chloroform and deposited on the water subphase (NanoPure, >18MΩ×cm) in small droplets and permitted to dry for 30 to 60 minutes allowing the chloroform to completely evaporate. The π~A isotherms are recorded as the monolayer is slowly compressed by two barriers at the opposite ends of the Langmuir trough. The monolayer is deposited at surface pressures chosen to represent the phase transitions seen in the π~A isotherm. The established procedure of LB films deposition starts with the compression of the monolayer at a constant rate to the desired pressure.[126,127,128] The surface pressure is held constant as the submerged silicon substrate is lifted from the trough.

2.2.2 Spin Cast Surface Films

Spin cast film are less organized surface films reliant on physical interactions between the molecules and the underlying substrate. The spin cast fabrication technique is desirable to create monolayers of molecules with weak amphiphilic nature. Film thickness is controlled by the solution concentration and the spin rate, allowing for thin surface films to be fabricated. The molecular organization within the surface film is limited by the rapid fabrication time but favorable interaction between the molecules and substrate surface chemistry facilitate ordering structures.

Toluene (Fisher) solutions of 0.03-0.08 wt% were spin cast at 3000 rpm and rinsed with toluene. The sample rinsing and the volume of solution deposited were varied to optimize the surface film formation. The thickness of the films was varied by the rinsing or adding additional droplets.

2.2.3 Self-assembled Monolayers

Surface films formed by physical interactions such as LB monolayers and spin cast films have limited stability in harsh environments. The attachment of the molecules by chemical bonds to the substrate surface enhances the film stability. The surface chemistry of the substrate is modified, controlling the interactions between the substrate and physically

deposited monolayers. Traditional SAM fabrication pair the reactive group on low molar weight molecules with a favorable chemical moiety on the substrate surface, thereby limiting the molecules and surfaces available for the fabrication technique.

Silicon substrates have been modified in this study to design specific interactions between the deposited molecules and the underlying substrate. The hydrophobicity of the silicon substrate was controlled by modifying the surface with a SAM of octadecyltrichlorosilane (OTS, Aldrich) by a documented experimental procedure.[129]

Cast films of the **AA-2** and **AE-1** molecules were deposited on clean quartz slides from dilute chloroform solutions. The films were annealed at 120°C for sixty minutes under vacuum, then rinsed three times in chloroform and dried under dry nitrogen. The samples were placed in a dark room and illuminated with 365 nm light for different periods of time.

2.3 Characterization Techniques

A combination of interfacial and bulk characterization techniques were utilized to determine the molecular ordering within surface films. Grazing incident X-ray diffraction (GIXD) and X-ray reflectivity examined the molecular fragment organization within Langmuir monolayers. Surface morphology and phase composition were analyzed Atomic Force Microscopy (AFM).

2.3.1 Interfacial X-ray Studies

Langmuir and LB monolayers offer the possibility to study molecular interaction in a two-dimensional setting in contrast with many structural characterization techniques that provide bulk properties. The molecular structure of the monolayers can vary from bulk structures of similar molecules because the lateral packing is limited in one direction. Traditional X-ray scattering techniques have several limitations. The first is the brilliance of the primary beam is too low to produce a high enough output signal. Secondly the techniques are limited to solid supported films. A solution to both of these problems is to perform X-ray reflectivity and grazing incident X-ray diffraction on liquid supported Langmuir films at surface pressures similar to the pressure films were deposited onto solid

substrates. Use of a high brilliance X-ray source is necessary for the high intensity of the primary beam.

X-ray reflectivity gathers data about the monolayer at the air-water interface and averages the data over the entire footprint of the beam on the surface. The data is then used to calculate a box model to describe the electron densities across the interface and relate them to the arrangement of the molecular fragments.[130] The box model consists of slabs of differing thickness and electron density stacked above the water subphase with known electron density (0.33×10^3 e/nm^3). Thermal vibrations and surface roughness are accounted for by smearing the interfaces. The calculated box model is compared with molecular models to determine arrangement of the molecular fragments. The reflectivity used to fit the experimental data is calculated from:

$$R(Q_z) = R_0(Q_z)\exp(-(Q_z\sigma)^2) \qquad (1)$$

where the $R_0(Q_z)$ is the reflectivity from step-like functions and the σ is the surface roughness. The reflectivity calculated for various trial electronic density profiles is compared with experimental results during the fitting procedure.

The data is presented in reciprocal space (Q) with Q_{xy} representing the vector in the H and K direction and Q_z representing vector in the L direction. During the X-ray reflectivity experiments the H and K vector remains zero and the incident and reflected angles are increased equivalent degrees to scan along the L direction. During the GIXD experiments the incident angle is fixed below the critical angle to ensure total reflectance as the H and K components (Q_{xy}) are studied to determine the diffraction pattern of the sample. The L component (Q_z) of the diffracted vector is fixed at different azimutal angles to discern the tilted behavior of the diffracting molecular fragments. Inversely, the H and K components are fixed and the L component increased at reflex points to further characterize the tilt behavior and ordering of the diffracting molecules.

Diffraction of the two-dimensional film at a grazing angle indicates the lateral packing structure on the Langmuir monolayers. Ideally, alkyl tails can be modeled as cylinders packing in hexagonal structures with the tails normal to the air-water interface.[131]

This phase is known as the "rotator phase" named for the rotating tails. Upon increasing the pressure, thereby increasing the density of the monolayer, the tails assume their true elliptical shape. The tails assume a "herring bone" packing structure, eventually transforming from hexagonal to orthorhombic structures. Kaganer and Loginov describe the multitude of packing structures in the framework of the Landau theory.[132] Additional information about the monolayer can be discerned from the width of the peaks. The narrower the peaks appear the larger the correlation lengths in the direction of the peak.

Cross-sectional mismatched between the polar focal group and the alkyl tail leads to tilt of the tails away from the surface normal. Traditional carboxyl focal groups have a slightly larger cross-sectional area than the alkyl tail therefore in the low-pressure regime the alkyl tails can tilt approximately 15-30° from the surface normal. Larger polar groups cause larger tilt angles between the alkyl tails and the surface normal. The direction of the tilt has been discovered to be in one of two usual directions: toward nearest neighbor (NN) and toward next nearest neighbor (NNN).[133]

The form factor of the diffracting object can be determined by measuring the rod scans along the surface normal at the 2D Bragg's reflections. Quantitative analysis of the intensity of the 2D Bragg reflection rod is preformed using the framework of the distorted wave Born approximation (DWBA)[134]

$$I \propto |t(k_{z,f})|^2 |F(Q_z)|^2 \qquad (2)$$

where $t(k_{z,f})$ is the Fresnel transmission function which gives rise to the enhancement around the critical angle of the scattered beam. Using a model of a cylinder of a length l and a fixed radius equal to the cross-sectional radius of alkyl chain to describe the alkyl tails, the tilt of the tail was varied to determine the orientation of the tails. In the model the intensity was adjusted for two tilt directions: one toward nearest neighbor (NN) and the second toward next NN (NNN).[133] The form factor of the tails is given by

$$F(Q_Z') = \sin(Q_Z'l/2)/(Q_Z'l/2) \qquad (3)$$

where Q_z' is defined along the long axis of the tails.

2.3.1.1 Synchrotron Studies.

X-ray reflectivity and a combination of X-ray grazing incident diffraction measurements are preformed on Langmuir layers using the Ames Laboratory liquid-surface diffractometer at the 6ID beamline at the Advanced Photon Source synchrotron at Argonne National Laboratory.[48,135,136,137] The monolayer is deposited on the surface of a Langmuir trough contained in a helium-filled chamber to decrease the oxidation of the molecules over the duration of the experiment. An insertion device is used to draw the primary beam from the storage ring. The beam is diffracted by a monochromator to remove all nondesirable high- and low-energy photons, allowing a narrow ban of photons before passing through a series of two movable slits to reduce the beam to the desired size. A downstream Si double crystal monochromator is used to select the x-ray beam at the desired energy (λ=0.0772 nm). The beam finally passes through collimating slits before entering the helium filled chamber. In depth descriptions of the experimental setup are found elsewhere.[138]

2.3.1.2 Home-Built XR Apparatus

X-ray reflectivity measurements of spread monolayers directly under UV illumination were carried out on a home built liquid-surface reflectometer (D. Vaknin, Ames Laboratory). The incident beam (CuK_α; λ = 1.5404 Å) is selected from the white beam of a Cu-rotating-anode generator (UltraX1-18; Rigaku, Japan) by Bragg reflection from the (111) planes of a Ge single-crystal monochromator. The monochromator was situated on an arch segment that rotates the monochromator about an axis parallel to its (111) planes and the liquid-surface. Rotating this arch to an angle t tilts the incident beam with respect to the surface to angle α, given by $\sin\alpha = (d_{111}/\lambda)\sin t$., where d_{111} is the Ge(111) d-spacing. The motorized θ–2θ stages of the monochromator crystal are corrected for each tilt angle to practically track the Debye-Scherrer-cone, maintaining a fixed-energy incident-beam. Elevators are used to adjust the height of the sample and the beam-paths (with the slits) of the incident and scattered beams. The vertical divergence of the incident beam is controlled by two sets of slits (approximately 50 cm apart) placed between the sample and the monochromator. The

divergence of the beam is varied during the experiment to roughly maintain a constant beam-footprint on the surface; beam-divergence near the critical angle is ~0.01 degrees and at the largest angle 0.09 degrees. A typical reflectivity curve takes 8-12 hours at 15kW power of the X-ray generator.

2.3.2 Bulk X-ray Diffraction

Wide angle X-ray scattering (WAXS) and small angle X-ray scattering (SAXS) of bulk polymer samples provided information on the molecular ordering in a three dimensional sample.[139] Bulk diffraction at low angles provided data for structural analysis of the bulk material. Using the d-spacings and peak shape from the diffraction patterns the degree of crystallinity, the unit cell size and the crystallite size can be calculated. Using the WAXS technique, often ranges above seven degrees, reveals molecule-molecule interactions. Peaks associated with the multiple orders of molecules can be observed in the low-angle range. The combination of small and wide angle X-ray scattering provides data of both molecule-molecule interactions and the ordering of layers of molecules in crystalline planes. WAXS and SAXS diffraction patterns were collected using a Scintage-2000 XDS diffractometer and Rigaku Miniflex diffractometer using copper radiation. The angular range for the samples was between 1 and 35°. The bulk powder samples were compressed into stainless steel holders.

2.3.3 Optical Microscopy

Optical microscopy provides higher resolution imaging of fine details of surfaces and interfaces.[140] The magnification and higher resolution capabilities of optical microscopy detect features invisible to the naked eye. The lack of contrast between multiple phases in polymer specimens limits the visualization. The use of cross polarizing light for transmission optical microscopy reveals the presence of polymer crystallites due to the polarizing effect of the crystalline structure. The development of digital cameras with time-lapse options facilitate the calculation of growth kinetics of crystallites and one-dimensional structures from polymer solutions.

Ribbon nucleation and growth of rod-coil molecules from solution was observed using optical microscopy. Visual analysis of the fiber structure facilitated the calculation of the growth kinetics and average ribbon dimensions. Optical microscopy images were obtained using a Vanguard 1282ECM microscope equipped with light transmission stage and digital camera. Movies of ribbon crystallization were created using timed auto capture feature.

2.3.4 Scanning Electron Microscopy

Visualization of polymer surfaces with optical microscopy is limited by the resolution, depth of focus, lack of phase contrast, and fixed angle between the sample and camera. Scanning electron microscopy (SEM) provides improved resolution and depth of focus capabilities. Additionally the angle between the sample and detector can be manipulated to obtain three dimensional aspects of the surface texture. The details of chemical composition can be discerned by employing an Energy Dispersive Spectrometry (EDS) detector, thus revealing the elements present at the surface. A clear disadvantage of SEM is the need of surface conductivity thus requiring the application of a thin film of gold to polymer specimens.

SEM images were obtained with a JEOL JLS-606LV at 10kV at Iowa State University and JEOL at Massachusetts Institute of Technology. Graphite substrate was used, and sample was sputter coated with gold prior to imaging.

2.3.5 Transmission Electron Microscopy

The spatial resolution and surface conductivity limits the use of SEM for thin polymer films. The higher resolution and thin film sample preparation features of transmission electron microscopy (TEM) are desirable for resolving fine detail and dimensions of particles and phases in the nanometer range. The lack of phase contrast between polymers requires labeling or dyeing to discern the phase composition of the thin films, although the contrast between inorganic particles and polymer matrix requires no special handling.

A Phillips CM30 electron microscope with a LaB6 filament and used to perform TEM studies of the monolayers deposited on covered TEM grids purchased from Ted Pella.

2.3.6 Atomic Force Microscopy

A powerful surface characterization technique known as AFM provides a topographic map of the surface of a sample in a two-dimensional image.[141] This is accomplished by scanning the surface with a nanometer scale probe at the end of a V shaped cantilever across the surface in a X-Y raster pattern on a micron scale (Figure 14). A laser beam is focused on the back of probe and reflected onto a segmented photodiode detector. The computer program monitors the constant feedback loop that maintains a constant force on the cantilever probe. The difference in height seen is then converted into topographical features on the three-dimensional image shown on the monitor. A schematic of the typical design for Tapping Mode in AFM is shown in Figure 14.

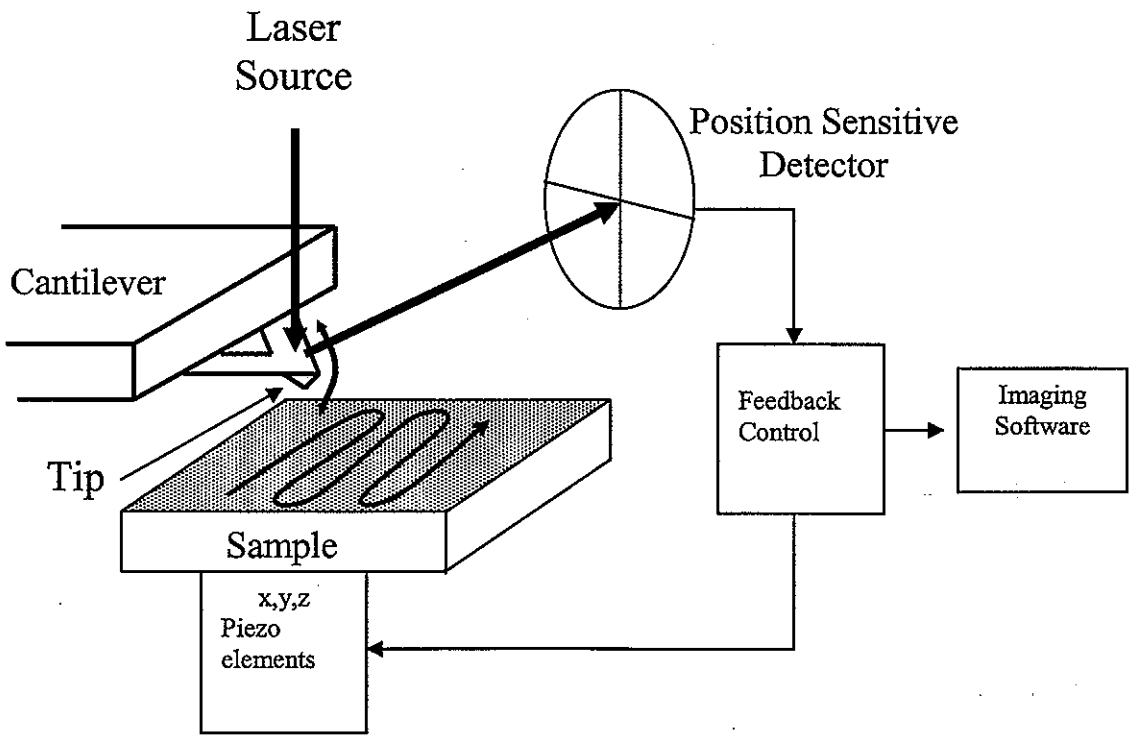

Figure 14. Schematic of a typical AFM in Tapping Mode. The figure is not drawn to scale.

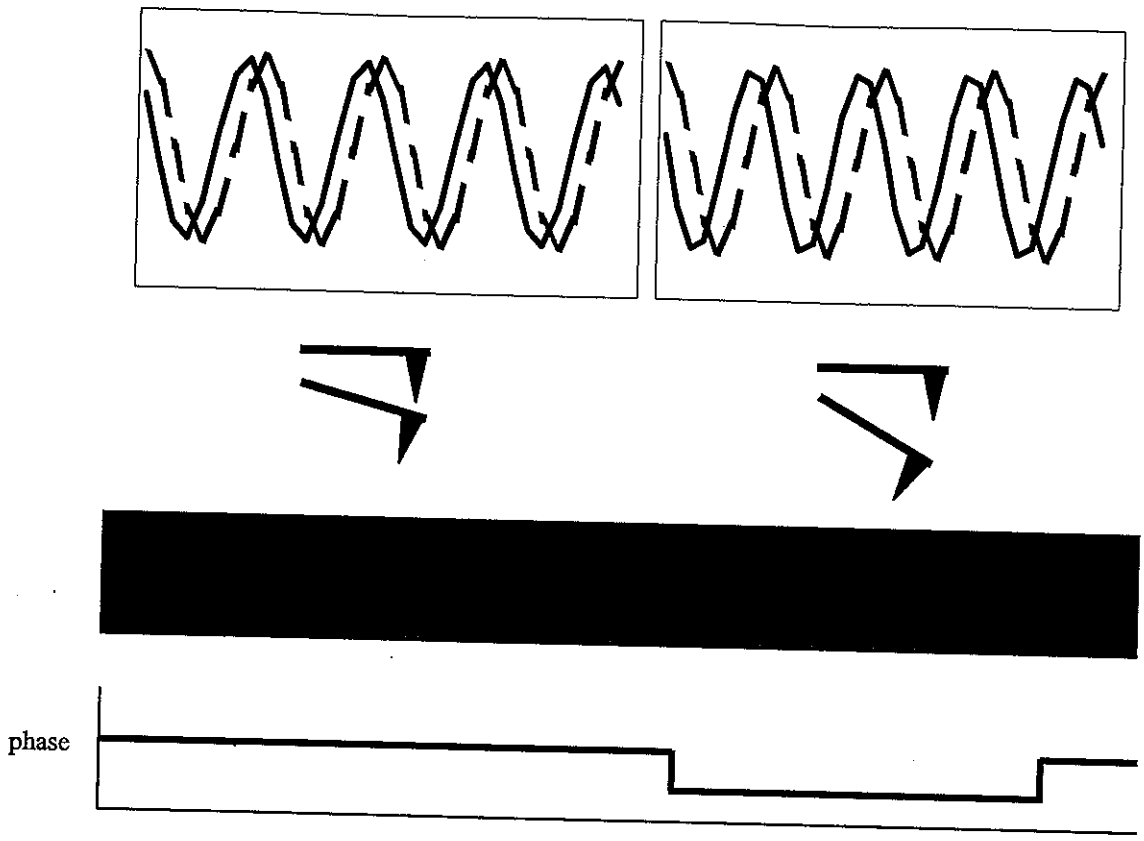

Figure 15. The phase shift in the oscillating frequency of the AFM tip indicates a change in the chemical structure of the monolayer.

For the molecular systems presented here, Tapping Mode imaging is performed on Dimension-3000 and Multimode microscopes (Digital Instruments).[142,143] Tapping Mode imaging is performed on samples too soft or unstable to scan in conventional contact mode, where the tip is dragged across the surface. In Tapping mode the tip is oscillated near the cantilever's resonant frequency using the piezoelectronic crystal to eliminate the damaged caused when the tip is dragged across the sample. When the oscillating cantilever comes in contact with the surface intermittently, the cantilever's oscillations are reduced due to the energy loss caused by the contact between the tip and the surface. The cantilever tip is deflected by changes in the vertical height of the samples, thereby reflecting the laser beam to a different spot on the photodiode detector. The detector perceives the changes in vertical height as differences in laser spot orientation and records them as contrast differences on the

two-dimensional image. In effect, the tip taps the sample and the image recorded is the relationship of the tip's interactions with the sample, and not directly a map of the topography of the surface.

In addition to morphology and height measurements Tapping Mode also offers information on the changes in the chemical structure on the polymer surfaces. Changes in phases might occur on plateaus or uniform films without affecting the height of the film. The interactions between the tip and the films will change however. The feedback system monitors the phase shift in the tip oscillations as well as the difference in the tips oscillating amiplitude. The phase shifts in the oscillations of the tip indicates a change in the film structure (Figure 15). Often the changes in morphology of the film can be seen with better resolution in the phase images.

Care is taken not to cause damage to the films by the AFM tip by employing a "light" tapping technique. Using low normal forces in scanning the sample controls the damage. The tip radius range is 10 to 30 nm and the spring constants are 40 to 60 N/m.[144]

2.3.7 Raman Microscopy

The specimen preparation restricts the characterization of surface composition by SEM and EDS. Additionally, the technique is limited to identifying elements present within the sampling, thus revealing little of the molecular composition at the interface. The use of Raman spectroscopy evaluates the molecular conformation and deformation at interfaces. While sample thickness limits conventional Raman spectroscopy, the inclusion of inorganic nanoparticles enhances the signal from thin surface films such as LB films. Traditional chemical analysis techniques were limited in analysis of the binary molecules composition.

The chemical composition of surface films was determined using Raman spectroscopy of LB films. The observation of characteristic peaks for known polymers confirmed the presence of molecular fragments. Confocal Raman spectroscopy was conducted with a custom designed set-up based on Aurora-III NSOM microscope (Digital Instruments). A Nd:YAG laser (532 nm) was used as the light source with intensity of 1 mW on the sample. The spectra were recorded by a cooled CCD camera with resolution of 0.32 cm^{-1}.[145]

2.3.8 Fluoroscence Spectroscopy

Fluoroscence spectroscopy reveals information about the molecular composition and physical organization of polymeric samples by confirming the presence of fluorescent emitting fragments and preferential ordering of the fragments.[146] Fluorescence occurs when a photon is emitted between states with the same multiplicity, creating one type of luminescence. The small time scale of the experiment agrees well with the time scale of conformation changes in polymers. Another advantage to fluorescence is the small sample size required to observe an effect in solutions or thin films. Therefore, fluorescence spectroscopy provides useful conformation and compositional information for polymers with aromatic fragments.

Fluorescence microscopy images were obtained from Olympus BX51 Fluorescence brightfield microscope and fluorescence spectra was obtained using Craic QDI 202 Microspectrophotometer.

2.3.9 Ellipsometry

Film thickness was determined by ellipsometry (a COMPEL Automatic Ellipsometer from InOmTech, Inc.) with an incident angle of 70°. Ellipsometry offers a nondestructive optical technique to measure the thickness of a film by measuring and interpreting the changes in polarized light that undergoes oblique reflection. The measured ellipsometric angles, Ψ and Δ which are related to the complex ratio of the Fresnel reflection coefficients R_p and R_s for light polarized parallel (p) and perpendicular (s) to the plane of incidence such as

$$\rho = R_p/R_s = \tan \Psi \exp(i\Delta) \qquad (4)$$

the complex reflectance ratio ρ is completely determined by an amplitude ($\tan \Psi$) and a phase (Δ) and characterizes the differential changes in amplitude and phase. These changes are related to a transformation of a shape and orientation of the ellipse of polarization, respectively.[147]

Initial estimates of the unknown parameters (sample thickness and refractive index) are used to construct a model of the sample structure. A set of experimentally calculated Ψ and Δ are then generated by varying the given parameters, and result in the true thickness and refractive index of the film.

After each wafer is cleaned with piranha solution and prior to film deposition the silicon oxide layer is measured. The average thickness is found to be between 0.9 and 1.3 nm for different wafers. The indices of refraction, estimated from similar molecules with known indices, used for the polymer layers are 1.49 for photochromic monodendrons, 1.55 for rod-coil molecules, and 1.45 for 12-arm star polymers. An average over six measurements from different location on the substrate was used and reported here.

2.3.10 Ultraviolet-visible Light Spectroscopy

The photochromic behavior of molecules can be studied using multiple techniques but the most common is observing the absoption versus wavelength spectra. The light is selectively refracted to expose the sample to single wavelengths at a time. The absorption is recorded by the detector and shown in wavelength versus absorption spectra.

The UV-vis spectra of chloroform solutions and monolayers are obtained with a Shimadzu-1601 spectrometer. Illumination of solutions and monolayers is done with a Blak-Ray ultraviolet lamp (UVP, Model B-100 AP, 100W) equipped with both a 365 nm bandpass filter and a 310 nm longpass filter from a distance of 0.4 m.

2.3.11 Contact Angle

Examining the contact angle of a droplet on a flat surface gives insight into the molecular composition of the surface and in turn the surface energy.[148] Analysis of water droplets on thin polymer films confirms the hydrophobic or hydrophilic nature of the surface, thereby predicting the molecular composition at the interface. Contact angle measurements were performed with sessile droplet method on a home-built apparatus. An average of three measurements was taken.

2.3.12 Molecular Modeling

To calculate the behavior of molecules at the interfaces is not a simple matter of drawing the molecules. The molecules are created using Cerius^2 3.8 package on a SGI workstation and Materials Studio 3.0 that allows 360° rotation around all three axes and minimization of the energy by correcting the bond lengths, angles, and orientation.[149] To simulate a filled space environment and to correct the influence created by the free space environment a force field is loaded before all calculations are preformed. The models presented here are all created using the Dreiding 2.21 force field library on the Cerius^2 program and the PCFF on the Materials Studio 3.0 program.[150] The combination of molecular dynamics and energy minimization was used to generate molecular models.[151] Using these models geographical parameters of the molecules are measured as well as models of the packing structures are developed using information from the characterization techniques.

CHAPTER 3. RESULTS – FUNCTIONALIZED PHOTOCHROMIC MONODENDRONS

The interfacial behavior of two series of photochromic monodendrons, their molecular ordering, and its contribution to reversible photoisomerization at interfaces were examined. Studying the effect of the cross-sectional mismatch on the molecular ordering compared the influence of the polar head group and the varying number of alkyl tails. The polar head group was altered from a bulky crown ether to a smaller carboxylic acid group to analyze the effect of the head group on the molecular ordering at interfaces. The cross-sectional mismatch was additionally manipulated by varying the number of dodecyl alkyl tails per generation. An epoxy terminated reference molecule was examined to understand the photoisomerization behavior in grafted films.

3.1 Molecules based on Bulky Discotic Cores

Organized surface layers with microstructure and properties depending upon external stimuli are of special interest for many prospective applications.[152] Among them, photoresponsive amphiphiles possess the possibility of forming ordered, two-dimensional monolayers with switchable microstructure. Azobenzene molecular fragments have two stable isomers under different wavelength stimulation making molecules with azobenzene fragments attractive for possible molecular switch and nonlinear optics uses.[153] The unique *trans-cis* photoisomerization of the azobenzene molecular fragments is promising for a diverse array of applications. Lack of complete control of the molecular orientation and packing structure of the azobenzene fragments within the monolayer hinders their functioning in the desired fashion. Progress in the control of orientation and structure of molecules in thin films focuses on both fabrication control and gaining a complete understanding of the interactions between molecular fragments.

3.1.1 Molecular Ordering at the Air-Water Interface

The properties of the **AD12-N** series have been studied at the air-water interface to develop a molecular model for all four molecules (Figure 4). All four molecules display

classic amphiphilic behavior with a sharp increase in surface pressure as the area per molecule reaches near monolayer collapse (Figure 16). The π~A isotherms show the lower two generations have a cross-sectional area deviant from the expected 0.2 nm^2 per molecular tails. The cross-sectional area for the crown ether head in flat-on orientation at the interface is determined to be 0.45 nm^2. The molecular area determined from π~A isotherms for the one, two, four, and eight tail compounds is 0.43, 0.48, 0.77 and 1.55 nm^2 respectively (Figure 16). From these results it appears the bulky crown ether head is dictating the molecular packing for the lowest two generations. However, for monodendrons with four and eight tails, cross-sectional area per tail decreases to about the expected value.

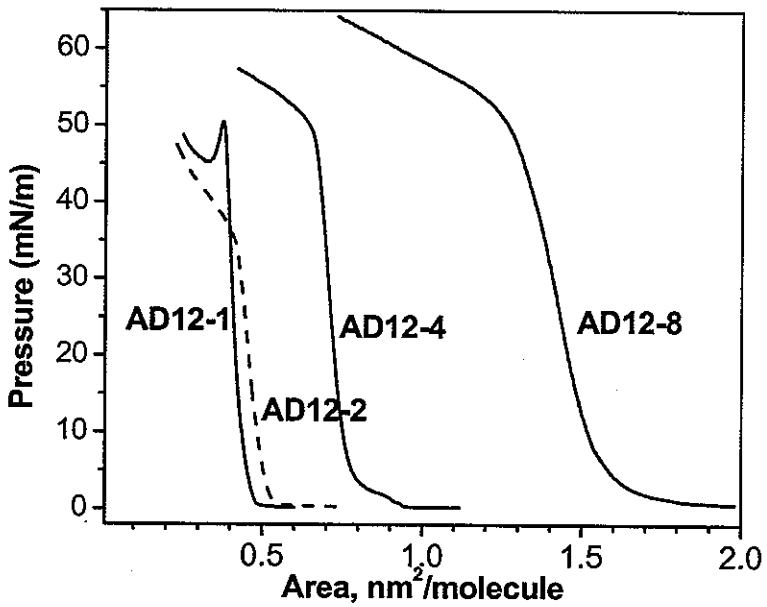

Figure 16. π~A isotherms for the **AD12-N** series

The **AD12-1** monolayer at lower pressures showed little ordering as indicated by the presence of only a wide diffuse halo, originated from the water subphase. Two-dimensional Bragg reflections do not appear in the diffraction patterns at pressures of 3 and 10 mN/m. XGID scans reveal three peaks only at the highest surface pressures tested here of about 20 mN/m. The peak profiles obtained with high resolution at the highest surface pressure (Figure 17) were fitted to Lorentzian type functions that provided peak positions at 10.0,

14.3, and 15.9 nm^{-1}, which correspond to 0.626, 0.440, and 0.394 nm d-spacings, respectively (Table 2). The shape, spacing and location of the two intense peaks with higher Q_{xy} values (14.3 and 15.9 nm^{-1}) correspond closely with literature values for (1,1) and (2,0) planes in an orthorhombic unit cell of alkyl chains.[131] Calculations with this indexation resulted in a unit cell size of 0.788 nm by 0.529 nm. This unit cell corresponds to a cross-sectional area of 0.208 nm^2 per alkyl chain of the molecule. This value is within the known area for densely packed and tilted alkyl tails (from 0.182 to 0.210 nm^2).[Error! Bookmark not defined.32,131,154] However, the 0.626 nm peak with lower intensity detected at this pressure does not fit a simple orthorhombic unit cell common for the alkyl tails. Selective disappearance of peaks indicates the alkyl tails are tilted in a preferred orientation. The (1,1) peak disappears in the high resolution XGID patterns of**AD12-1** at highest surface pressures while the two other peaks remain (Figure 17).

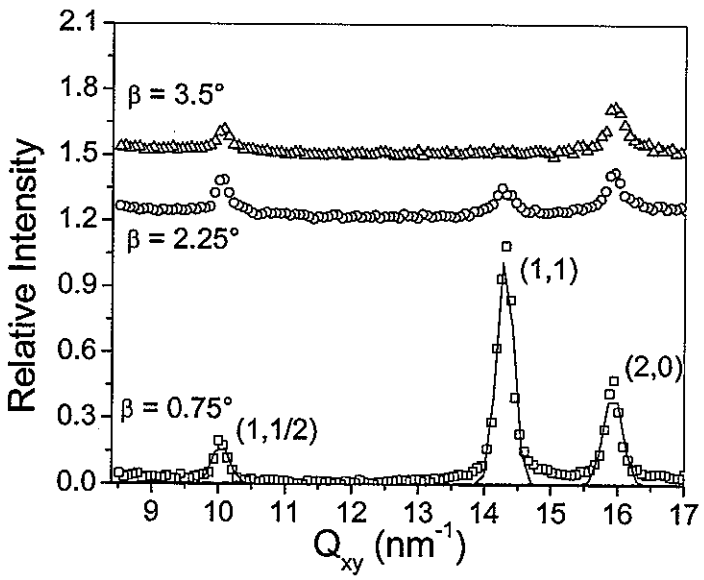

Figure 17. High resolution XGID of **AD12-1** monolayer at highest pressure as the detector is moved away from the surface horizon. The original intensities are offset for clarity.

After careful analysis of possible structural models, it is suggested that this peak corresponds to the formation of supercell packing. This proposition is based on the fact that the d-spacing for this peak has a simple fractional relationship that corresponds to the (1,1/2) index within the orthorhombic unit cell. The position of the (1,1/2) peak calculated using the

orthorhombic unit cell parameters ($a^* = 2\pi/a = 7.973\ nm^{-1}$ and $b^* = 2\pi/a = 11.877\ nm^{-1}$) is found to be $9.9nm^{-1}$, which is within the experimental uncertainty of the observed value $10.0nm^{-1}$. The appearance of the (1,1/2) peak suggests that b-direction includes two of the "primary" unit cells. In addition, comparison of the unit cell for **AD12-1** compound studied here with the common unit cell for alkyl chains, namely, heneicosanioc acid found in literature, demonstrates that **AD12-1** compound possess expanded dimension in the b-direction.[131] The necessity to pack bulky polar groups beneath the alkyl sublayer may result in structural non-equivalency on the neighboring tails causing the effect observed. Simple fatty acids like stearic acid have been used as comparisons for more complex systems because their chemical structure allows for simple models to describe their packing structures (Table 2).[131,155]

Table 2. Structural parameters of the Langmuir monolayers from different dendrimer compounds. The values for stearic acid were taken from Peterson et al.[155]

	Stearic Acid	**AD12-1**	**AD12-2**	**AD12-4**	**AD12-8**
d-spacings, (nm)					
Peak 1	--	0.626	0.862	--	--
Peak 2	0.424	0.440	0.471	0.418	0.417
Peak 3	0.418	0.394	0.422	- -	- -
Unit Cell Parameters					
a (nm)	0.836*	0.788	0.487	0.483	0.482
b (nm)	0.483*	0.529	--	--	--
Area per chaing (nm^2)	0.197	0.208	0.206	0.201	0.201
Chain Tilt (°)	16.5	~58	4	3	4
Correlation Length (nm)					
Peak 1	--	19.2	--	--	--
Peak 2	5.7	16.5	--	--	--
Peak 3	7.1	17.1	3.5	2.8	3.7

Increasing the number of alkyl tails from one to two changes the molecular area determined from the π~A isotherm slightly, but greatly changes the diffraction pattern (Figure 18). Two well-defined peaks appear for the **AD12-2** monolayer at both low and high-pressures. At higher surface pressure, these peaks become more intense and an additional intermediate peak appears. The higher Q region appears to have a weak peak that

can be refined to as a third peak. The d-spacings of the three peaks were 0.862, 0.471, and 0.422 nm (Table 2). The intensity of first two peaks is too low to be used in the calculation of the unit parameters and could be originated from mixed intramonolayer structure. Therefore, only the most intensive peak was indexed as the (1,0) reflection of hexagonal lattice with the lattice parameter a= 0.487 nm (Figure 18, Table 2). This unit cell gives the surface area of 0.206 nm^2 per alkyl tail, which is close to that for the first generation. The width of the diffraction peak indicates disordering of the unit cell. The hexagonal structure appears to be an intermediate stage between the previous supercell orthorhombic unit cell of the lower generation and an ordered hexagonal unit cell for higher generation molecules (see below). All diffraction peaks disappear upon the slight increase of reflection angle leading to the conclusion that the tails are in standing off orientation for this molecule unlike the molecule with one tail, **AD12-1**.

The diffraction pattern for the four and eight tails, **AD12-4** and **AD12-8**, unlike the two previous compounds, displays only one intensive peak even at the lowest surfacepressure (Figure 18). One sharp peak at Q=15.0 nm^{-1} for both higher generation molecules present in the diffraction pattern for all three surface pressures (Figure 18). A hexagonal unit cell was calculated for **AD12-4** and **Ad12-8** with a length of 0.482 nm and the surface area of 0.201 nm^2 per alkyl tail (Table 2). The broadness and asymmetry of the peak for **AD12-4** was refined into two overlapping peaks. The unit cell for **AD12-8** was nearly identical to the **AD12-4** unit cell but appeared to indicate a more regular hexagonal packing structure with limited short range ordering rather than hexagonal structure of the previous two generation. As with the **AD12-2** monolayer, the diffraction peaks disappear as the β angle was increased indicating upright orientation of the alkyl tails similarly to **AD12-2** and in contrast with **AD12-1**.

The small cross-sectional mismatch between a carboxyl head group and a hydrocarbon chain, generally, causes a slight tilt in the NN direction.[131] At lower and intermediate surface pressures, the tilt angle is in the range of 15-30°. Peterson et al calculated the area per tail for stearic acid to be between 0.195 and 0.200 nm^2 for higher pressures, smaller than the cross-sectional areas calculated for **AD12-1** and **AD12-2** but close to that observed for **AD12-4** and **AD12-8** (Table 2).[155]

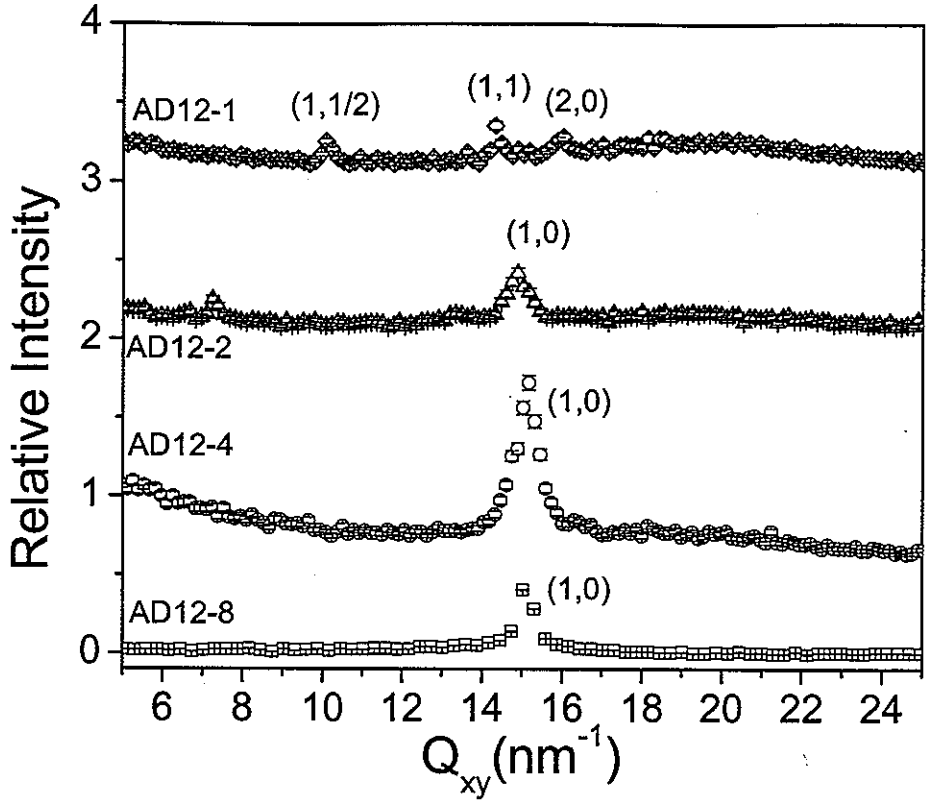

Figure 18. The observed diffraction patterns of the **AD12-N** series with peaks labeled with the corresponding Miller indices. The diamonds represent **AD12-1**, the triangles **AD12-2**, the circles **AD12-4**, and the squares **AD12-8**. The original intensities are offset for clarity.

The effective cross-sectional area per tail drops when four or more tails are attached to the polar fragment (Table 2). For molecules with multiple chains, the alkyl tails are oriented along the surface normal unlike the molecule with a single chain with a large tilt of the alkyl tails. For these compounds, the total cross-sectional area of the alkyl tails is much higher than the molecular area of the polar head. Thus, the loosely packed polar heads do not distort the dense packing of the alkyl chain although the intralayer correlations diminish significantly (Table 2).

Independent confirmation of a highly tilted alkyl chains for **AD12-1** within the monolayer at the highest surface pressure came from out-of-plane diffraction studies. As observed for diffraction data collected at an angle $\beta = 3.5°$, the (1,1) peak disappears while

the other two peaks remain visible, although with weaker intensity. This qualitatively confirms tilting of the alkyl chains for **AD12-1** in (1,1) direction. Rod scans (scanning out-of-plane (β angle) while fixing the Q_{xy} at a peak position) were used to determine the tilt angle of the molecular fragments with better accuracy.[138] For all three diffraction peaks rod scans displayed angular behavior with a sharp spike in intensity at an exceedingly low angle followed by gradually decreasing intensity (Figure 19). Modeling of these data for the lowest generation confirmed the molecular tilting of alkyl chains in a preferred direction. The fitting suggests the alkyl tails are tilted toward their next nearest neighbor at an angle in the range from 54 to 58° (Table 2). The tilting angle obtained from rod scans was virtually identical to one obtained from the reflectivity data (58°) within the uncertainties of both measurements (±2°).

To characterize the extension of alkyl chain ordering within the monolayer, correlation lengths are calculated within the Lorentzian approximation. The correlation length (ξ) is determined for all three peaks seen in the diffraction pattern using equation (5) [156,157]

$$\xi = 2/\Delta \tag{5}$$

where Δ is the full width at half maximum of the Lorentzian peak in units of nm^{-1}. The molecule with the most ordered (highest correlation length) intralayer packing is **AD12-1**, though the calculated lengths are close to the resolution limit. For all three diffraction peaks of the lowest generation, the correlation lengths determined to be in the range from 16.5 nm to 19.2 nm are close to the resolution limit of the instrument (about 20.0 nm) (Table 2). Thus, these values represent the estimation of the lowest limit propagation of order. These high values indicate that ordering on the air-water interface at the highest surface pressure far exceeds short-range order common for liquid-like packing of molecules in fluid or partially disordered states. [157] The tails are much more ordered and do form ordered regions which include at least 40 unit cells that corresponds to long-range positional ordering. The correlation length is reduced dramatically for the two-tail compound and is further reduced for the four and eight-tail compounds (Table 2). This decrease is obviously caused by the

steric conflicts within the branched tails. Multiple tails attached to a single core must stagger in their packing in order for them to fit in the single monolayer. A possible reason for this is by branching the alkyl tails off the same phenyl ring and the presence of the irregular phenyl rings within the monolayers are limiting factors on the propagation of the positional ordering of the peripheral alkyl tails.

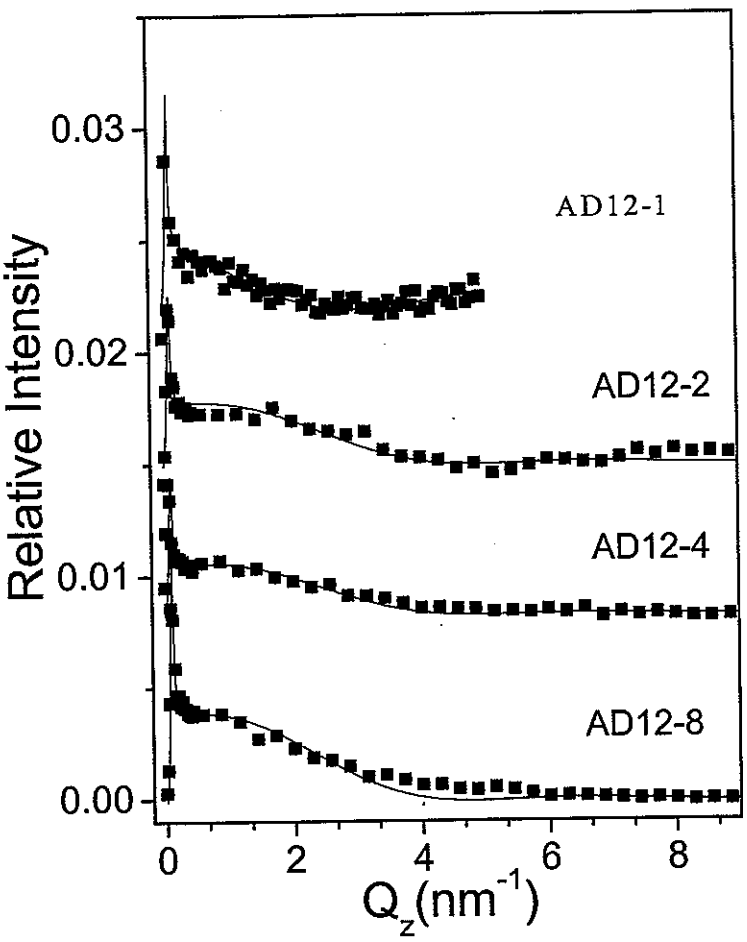

Figure 19. Representative rod scans for the main diffraction peaks at the highest pressure labeled with a sample name. Solid lines are the best fits. The intensities were offset for clarity.

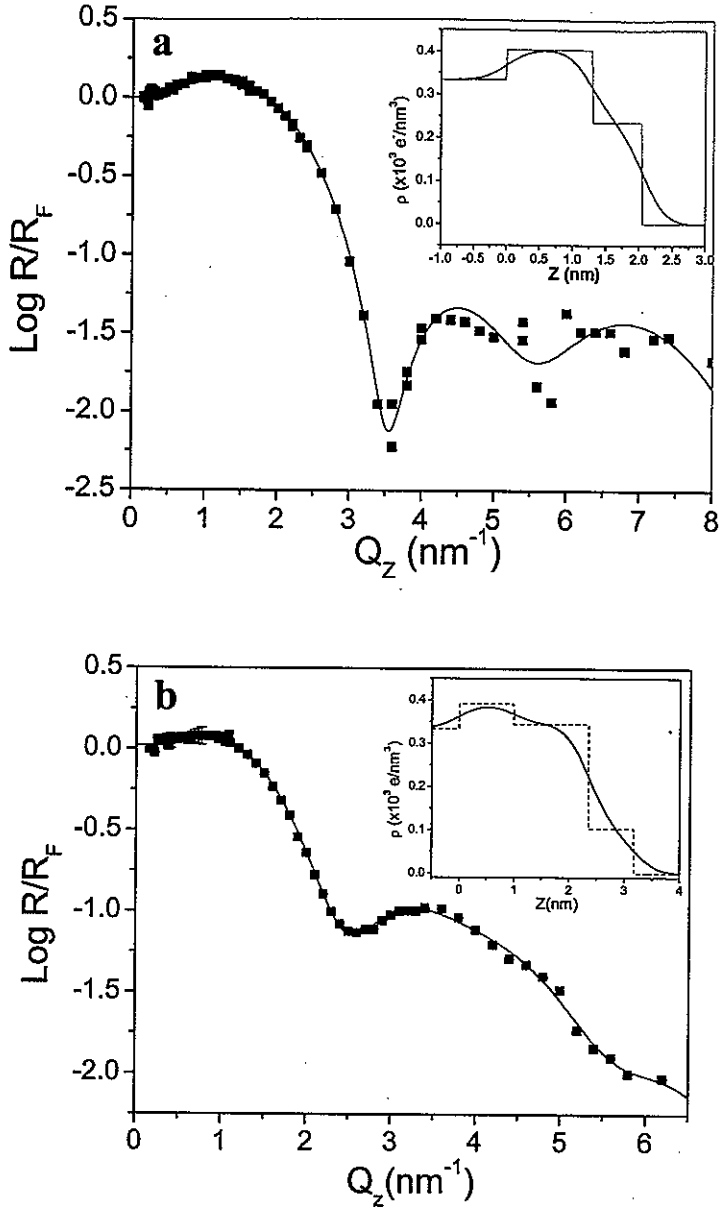

Figure 20. Reflectivity and corresponding models from a) **AD12-1** and b) **AD12-8**. The data are represented by symbols and the model by a solid line. The box models and smeared electron density for the fits are shown in the insets. The box models are used along with diffraction data to construct a molecular model of **AD12-1** and **AD12-8**.

Rod scans of selected diffraction maxima confirm conclusion about different orientations of the alkyl tails for highest three generations. The (1,0) peak for the two-tail

compound indicates the tails are tilted four degrees in the NN direction. The two lower Q value peaks for **AD12-2** were excluded from the rod scan analysis since they could not be indexed properly and the lower intensity of the peaks limited accuracy of the rod-scans. The results for the (1,0) peaks for higher generations show the tails tilted insignificantly, only three to four degrees from the surface normal. Representative data for rod scans and the corresponding fits for each sample are shown in Figure 19 and the tilting angles obtained from these fits are presented in Table 1. The results show that tails are in virtually standing off position for all compounds with multiple tails and the single tail compound has a tilt angle as high as 58°.

Reflectivity data provides complementary information on the packing of molecules at the air-water interface by revealing electron density distribution along the surface normal. Figure 20 shows the reflectivity data and the corresponding fits for **AD12-1** and **AD12-8** at the highest pressures, which is representative of all **AD12-N** compounds. The lower three generations can be fit using two box models at all pressures (Table 3). The eight-tail molecule was fit better using a three-box model. It is worth to note that the distinction between the crown ether and azobenzene fragment could not be resolved within current resolution and, thus, one box is assigned to the alkyl tail and a second one to the azobenzene-crown fragment.

At the lowest surface pressure, diffuse reflectivity with a poorly visible first minimum is observed for **AD12-1** (not shown). Increasing the surface pressure to 20 mN/m (compressed solid state of the monolayer) resulted in a much sharper first minimum and a weak second minimum. This indicates more ordered packing of the molecular fragments at higher pressures. Very low electron density of the alkyl tails at the lower surface pressures of 3 and 10 mN/m clearly indicates that they are loosely packed and disordered at these surface pressures as is confirmed by the diffraction data. Density of the alkyl layer increases significantly at the highest surface pressure indicating significant improvement of chain packing. However, even at the highest pressure studied here, the density of the alkyl tails extracted from the model ($0.24 \times 10^3 \pm 0.05$ e/nm^3) is lower than the expected electron density of densely packed alkyl tails ($0.3\text{-}0.33 \times 10^3$ e/nm^3) even considering the uncertainties of the

fitting procedure. This difference indicates the presence of additional defects in monolayer structure such as interdomain boundaries or partial conformational disorder.

Table 3. Fitting parameters from the box models used to fit the reflectivity data for all four compounds at the highest pressure. *Roughness is the same for all transitions between the elements of the fitting model.

	AD12-1	AD12-2	AD12-4	AD12-8	Uncertainties
Head Length (nm)	1.29	1.6	2.11	0.99	± 0.3
Head Density (x 10^{-3} e/nm^3)	0.41	0.40	0.38	0.39	± 0.02
First Tail Box Length (nm)	--	--	--	1.36	± 0.35
First Tail Box Density (x 10^{-3} e/nm^3)	--	--	--	0.34	± 0.03
Second Tail Box Length (nm)	0.75	1.15	1.13	0.82	± 0.2
Second Tail Box Density (x 10^{-3} e/nm^3)	0.24	0.28	0.28	0.10	± 0.04
Total Length (nm)	2.04	2.75	3.24	3.17	
Fully Extended Length (nm)	3.5	3.7	4.3	4.8	
Roughness* (nm)	0.27	0.47	0.38	0.34	± 0.03

* taken as an identical parameter for all interfaces

At the highest surface pressure the length of the topmost box for **AD12-1**, assigned to the terminal alkyl tails (l_{ref}) is much smaller than the calculated extended length of the tails (l_{max} = 1.52nm) (Table 2). This difference indicates that the alkyl tails are significantly tilted toward the surface. A measure for the tilt, θ, estimated from relation $\cos\theta = l_{ref} / l_{max}$ yielding a tilt angle of about 60°. Apparent reason for such highly tilted, almost flat arrangement of the alkyl tails in the compound studied is the availability of a large surface area for a single tail (0.43 nm^2) caused by the bulky crown ether group beneath the alkyl layer. This large tilt is unusual for alkyl chains within Langmuir monolayers. Typical tilting angle for amphiphilic

organic compounds with alkyl tails is close to 10-30° in condensed solid state. [158,159] This tilt is related to a modest mismatch of cross-sectional areas of non-bulky polar heads (usually, carboxyl groups) and hydrocarbon chains.

All **AD12-N** compounds have total lengths for the molecules at the air-water interface lower than estimated from extended conformation in standing orientation that is consistent with molecule tilting and conformational disorder of the molecular fragments. The monolayers show lower densities as compared to electron density for densely packed tails is $0.33x10^3$ e/nm^3 that indicates defective monolayer structure in the form, e.g., of clustering within the monolayer.

The cause of the supercell packing structure for **AD12-1** can be attributed to the influence of the large polar head, which can be misaligned in the b-direction so that the actual repeating unit is seen in every other unit cell. Indeed, as molecular modeling showed, for tilted and densely packed alkyl tails it was impossible to densely pack all polar fragments with the same orientation. Space constraints required a minor misalignment of alkyl tails to provide the appropriate packing density. It can be concluded that space constraints imposed by chemical attachment of the alkyl chains to the bulky polar heads appears to be the origin of the supercell of the alkyl tails. Indeed, an alkyl tail with the cross-sectional area of 0.21 nm^2 cover nearly 0.42 nm^2 of underlying surface area when tilted 58° from the surface normal.

Similarly, no flat-on orientation of the polar crown heads was observed for monodendrons studied recently by Pao et al.[160] The authors varied the number of branches (up to 9 peripheral tails) and the distance of the tails from the branching point and analyzed the density distribution along the surface normal. The smallest cross-sectional mismatch studied in this work was close to 2:1. The model presented in Ref. 48b showed the alkyl tails extended from the water surface with rod-like behavior while the branching and polar groups extend into the water at an angle away from the surface normal. The presence of large voids between the domains of the tails on a single molecule was also suggested. The area per peripheral alkyl tail determined from π-A isotherms was significantly larger than the expected for a single alkyl chain (0.26-0.36 nm^2) and was attributed to the presence of the bulky phenyl rings. This is in contrast with these studies with cross-sectional area per tails

reaching 0.20nm^2 despite the phenyl rings presence and indicates truly ordered state of the peripheral tails despite their branching.

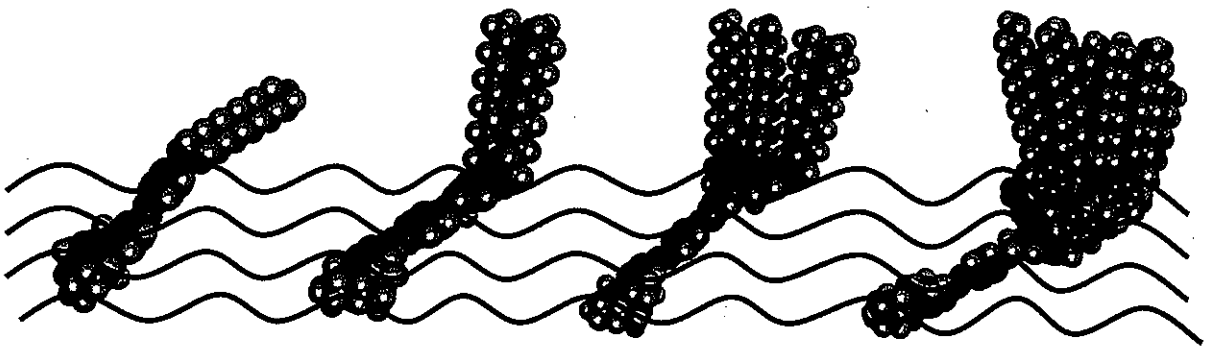

Figure 21. Molecular models of **AD12-1**, **AD12-2**, **AD12-4**, and **AD12-8** molecules (from left to right) at the air-water interface illustrating the molecular conformation and orientation of different fragments suggested.

All generations show a trend of the polar head and azobenzene spacer group adapting a tilted behavior beneath the water surface. For the first three compounds, the tilt angle is close to 50° from the surface normal but increases to 63° for **AD12-8**. The lower than expected thickness of the box model cannot be completely explained by the tilted structure of the molecular fragments or the calculated errors in the model. The effective thickness measured by X-ray reflectivity is averaged over the entire sample area and is not an absolute measurement of the monomolecular film. Therefore, a heterogeneous film structure with domains is suggested with a lower effective thickness than a complete film. Indeed, domain surface morphology has been observed for monolayers transferred on a solid substrate.[49,50]

In contrast, for molecules with multiple tails, the rod scans show minuscule tilts from the surface normal and thereby substantiates the conclusion made from the X-ray diffraction data on the standing tails. The rod scans and the diffraction patterns agree that the tails for the higher generations are orientated along the surface normal but the box model gives a smaller tail length due to, probably, the fact that the first several carbon atoms of the tails are submersed in the water subphase (Figure 21).

It is suggested that the origin of the second tail box in the three-box model for molecule **AD12-8** arises from the staggering of the peripheral tails. Rod scans and diffraction data indicate the tails are oriented along the surface normal but each tail is tethered to a phenyl ring that has another alkyl tail attached (Figure 19). The nature of the branching structure hinders the close packing of the tails without reorganization in the molecular structure as was tested on molecular models. The larger phenyl rings at different branching points have to adjust to the space constraints as the tails try to organize in the unit cell. The first and second carbon atoms of the alkyl tails are closely associated with the phenyl ring branching structure. The tilt angle originates at this site thereby forcing the carbon atoms to be partially associated with the head group. The standing off tails probably begins around the third carbon of the alkyl tail thereby explaining the short box that correlates with the tails. For all molecules, the head and azobenzene box was considerably shorter than expected leading to the suggestion that the group is tilted significantly away from the surface normal forming "kink" configuration (Figure 21). Taking the arccosine of the measured length divided by the molecular model length of the group an angle of 48 to 51° for the first three generations was calculated while the angle was increased for the highest generation to 63°. All models show the head groups fully submerged in the subphase but exact arrangement of the polar crown heads could not be deduced from the data collected.

3.1.2 Photoisomerization Studies

UV-vis spectrometry of dilute solution of the **AD12-N** molecules show the distinctive 365 nm peak that denotes the presence of the π-π^* transition of the *trans*-isomer of azobenzene fragment (Figure 22a). The 238 nm peak is characteristic of the phenyl rings present in the dendritic tails. After 1 minute illumination the 365 nm peak is near completely diminished while two new peaks appear at 455 nm and 318 nm, the first peak characteristic to the n-π^* transition (Figure 22b). The transformation can be reversed by storing the solutions in complete darkness for an extended period of time or can be accelerated by illumination with a 450 nm light.

Conformation of the effect of isomer transitions in deposited films is seen in high-resolution AFM studies of **AD12-4** films. The high-resolution images suggest **AD12-4**

organizes in orientated monolayers on solid surfaces. The phase image of the monolayer before illumination denotes 100-150 nm long, straight strips that form a continuous pattern (Figure 23a). After UV irradiation the pattern is broken and the strips appear to organize in fragments with the length limited to 10-20 nm (Figure 23b). The regular ordering is replaced with short-range ordered irregular domains. The thickness is not affected by this *trans-cis* isomerization thereby indicating in-plane intralayer reorganization.

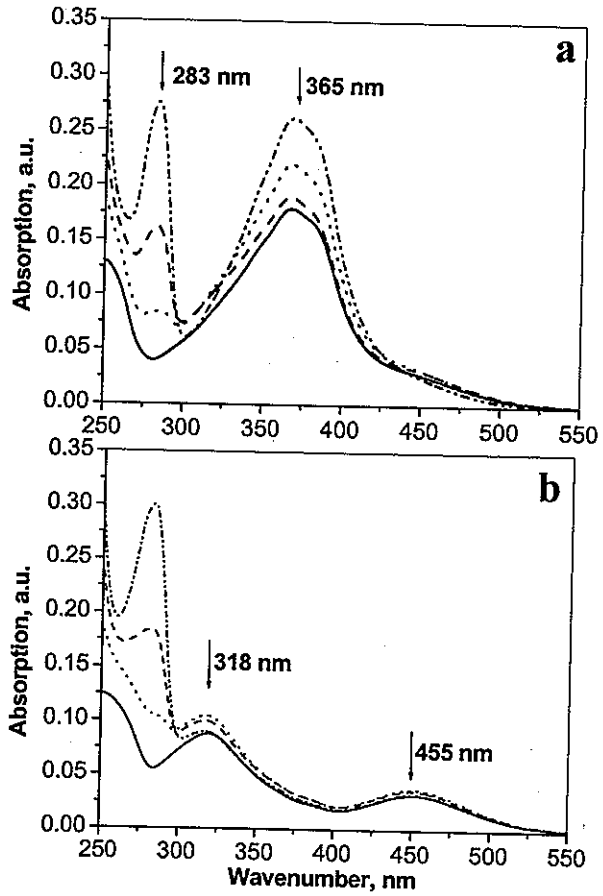

Figure 22. UV-vis spectrum for the **AD12-N** series in dilute solutions a) before irradiation and b) one minute after irradiation with 365 nm light.

3.2 Molecules Based on Traditional Polar Head Core

Replacement of the bulky polar group in previously studied monodendrons with a smaller functional group, i.e. a traditional polar group, was expected to promote chemically

grafting to solid surfaces while preserving the cross-sectional area necessary for complete and reversible photoisomerization within the surface monolayers. The attachment of a traditional carboxylic polar head to photochromic monodendrons generated a cross-sectional mismatch favorable for the azobenzene spacer group. In addition to the first direct observation of the *trans-cis* photoisomerization in Langmuir monolayers, photoisomerization studies demonstrated that lower generation monodendrons maintained the photochromic behavior after chemical grafting to the silicon substrates although with reduced reorganization time.

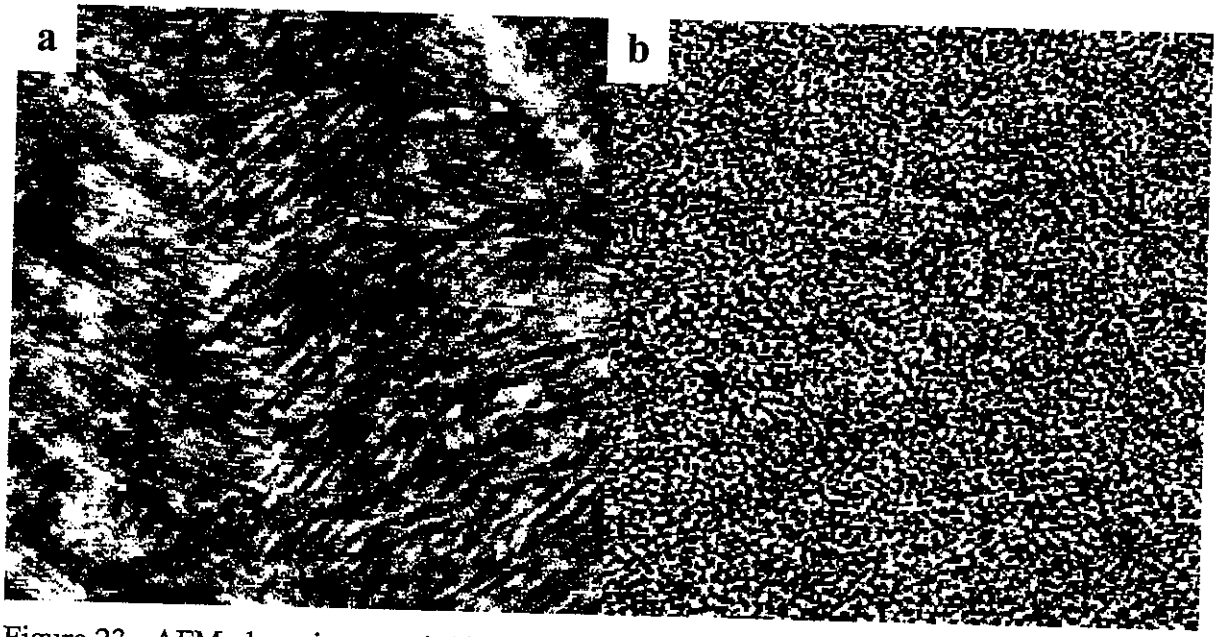

Figure 23. AFM phase images a) 100 x 100 nm of the initial oriented monolayer of **AD12-4** and b) 200 x 200 nm of the UV-illuminated monolayer. The Z-scale for both is 10°.

3.2.1 Molecular Ordering at the Air-water Interface

All four molecules displayed classic amphiphilic behavior at the air-water interface with a sharp increase in surface pressure as the molecular area was reduced (Figure 24). **AA-1** had a higher than expected alkyl-chain limiting cross-sectional area of 0.24 nm^2 per molecule while the three highest generations were observed to roughly follow the expected value of 0.20 nm^2 per alkyl tail with 0.36, 0.98, and 1.50 nm^2 for **AA-2**, **AA-4**, and **AA-8** respectively. The deviation of the one tail molecule from the expected molecular area

indicated that a single alkyl tail does not control the limiting cross-sectional area which is increased due to the presence of the bulky photochromic group and the polar head. The surface area per molecule increased with the increasing number of akyl tail in dendritic shells virtually doubling for each generation (Figure 24). In the end, the polar head and photochromic spacer had little influence on the cross-sectional area for the molecule with multiple (>2) alkyl tails in the dendritic shell.

The behavior of the azobenzene amphiphiles with different polar heads was first deduced by comparison of the pressure versus area (π~A) isotherms. The π~A isotherms for **AA-1** and **AE-1** indicated cross-sectional areas corresponding to the polar head size (Figure 24). The limiting cross-sectional area was calculated from the isotherms as 0.24 nm^2 for **AA-1** and 0.28 nm^2 for **AE-1**, which was slightly larger than the molecular area for traditional aliphatic chain amphiphiles.[161,162] Traditional amphiphiles composed of an alkyl tail and carboxylic acid polar head have been estimated to occupy approximately 0.18-0.20 nm^2 per molecule in condensed state.[163] The inclusion of the azobenzene fragment has been observed to increase the cross-sectional area of the single alkyl tail amphiphile to 0.30-0.35 nm^2 per molecule.[164] The smaller than expected molecular areas obtained for both molecules studied here suggested that this combination of the azobenzene group and polar heads dictate different intramonolayer packing as will be discussed in this communication. The collapse of the **AA-1** monolayer at moderate surface pressures was observed as a sharp change of slope at 25 mN/m. The larger surface area per molecule in **AE-1** (by ~15%) can be directly associated with the presence of the bulkier epoxy groups at the interface. The epoxy head group was suggested to be stable at the air-water interface for the limited time scale of the experiments. Epoxy rings were determined to be relatively stable in gels with high water content with only 10% of the rings opening after 24 hours in the absence of a catalyst and at room temperature.[165] Therefore, it is presumed a minimum number of epoxy rings open during the 1-10 hours per each experiment in oxygen-free environment. In fact, the result reported here for **AE-1** show unchanged monolayer packing in the course of repeated measurements.

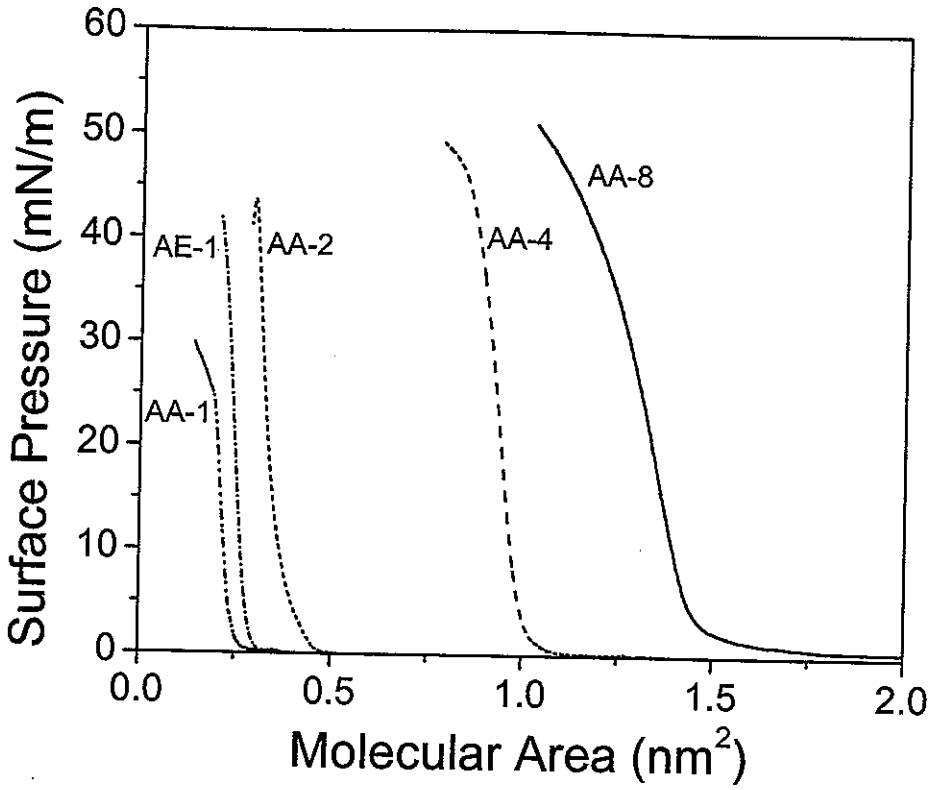

Figure 24. The π-A isotherms for all molecules demonstrated a classic amphiphilic behavior with lower generations deviating from expected molecular area trend.

Diffraction experiments provided insight into the effect of the azobenzene group and polar head on the intralayer structure of the alkyl tails. Observational GIXD patterns for both molecules at all surface pressures indicated an orthorhombic unit cell for the **AA-1** and **AE-1** molecules (Figure 25a, 26a). Four intense peaks appeared at low surface pressures and sharpened as the surface pressure increased. At lower Q_z a single sharp, intense peak was observed while at higher Q_z three additional intense peaks were observed for both **AA-1** and **AE-1** molecules. Unlike the previously studied molecule with a bulky crown ether polar head **AD12-1**,[48a] the current molecules lacked lower Q_{xy} peaks, indicating an absence of supercell packing structure.

The d-spacings for the two lower Q_{xy} peaks observed for **AA-1** were calculated as 0.467 and 0.371 nm corresponding to an orthorhombic unit cell with a = 0.742 nm and b = 0.601 nm at all surface pressures. The area per alkyl chain calculated from this unit cell was

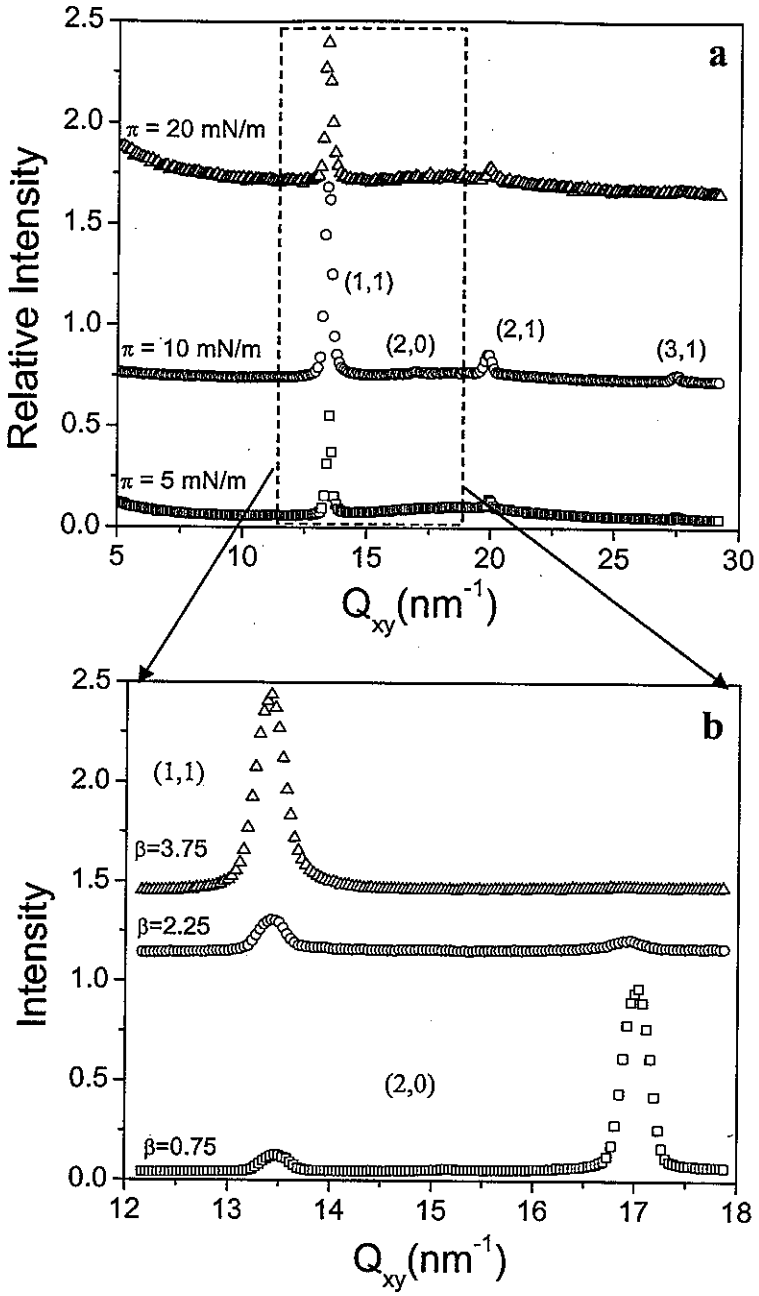

Figure 25. Intensity versus in-plane momentum transfer Q_{xy} GIXD (at β=3.75° to show all visible peaks) for **AA-1** a) at all observed surface pressures and b) the highest pressure at increased resolution. The dashed box indicates the area shown at higher resolution for different β to reveal the selective appearance of the (1,1) and (2,0) peaks. The intensities were offset to allow comparison.

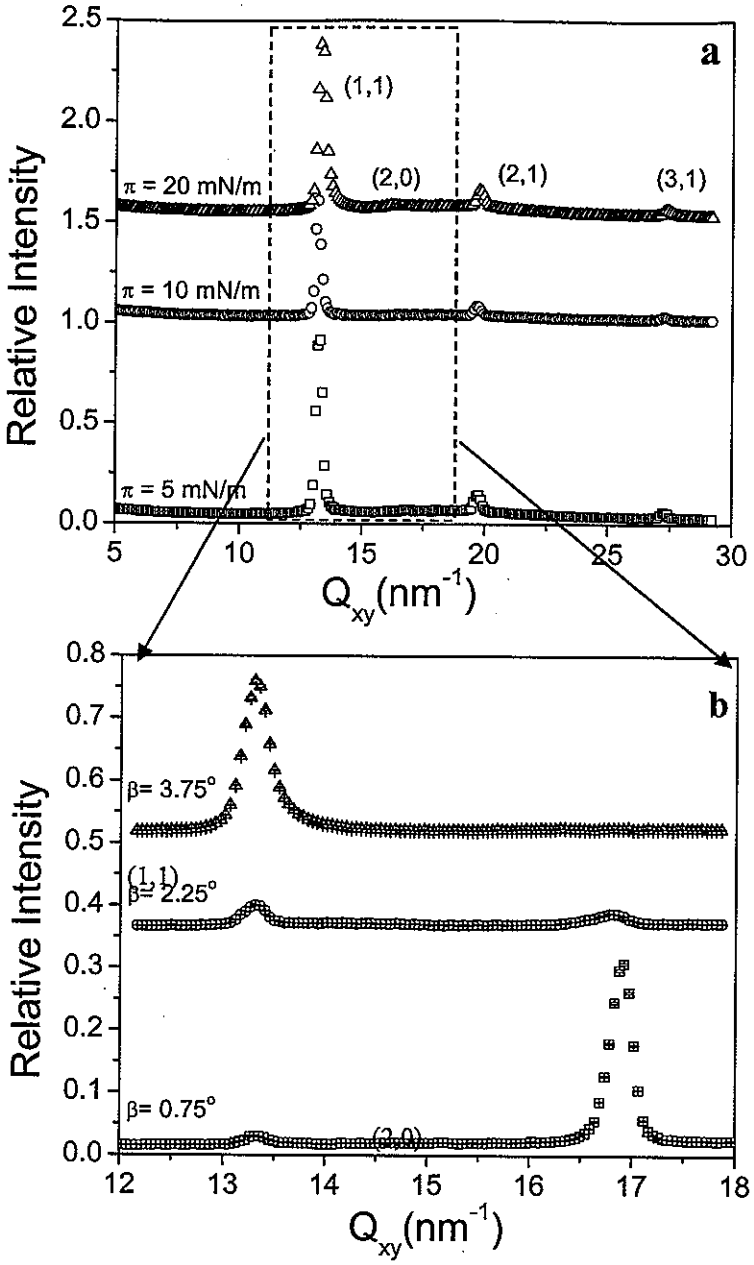

Figure 26. Intensity versus in-plane momentum transfer Q_{xy} GIXD (at β=3.75° to show all visible peaks) for **AE-1** a) at all observed surface pressures and b) the highest pressure at higher resolution. The dashed box indicates the area shown at higher resolution for different β to reveal the selective appearance of the (1,1) and (2,0) peaks. The intensities were offset to allow comparison.

0.223 nm^2 which is close to that directly obtained from Langmuir isotherms (Table 4). The large spacing between the two characteristic peaks for the orthorhombic unit cell indicated a transition to a unit cell of lower symmetry than the hexagonal unit cell (Figure 25b). Indeed, the area per alkyl chain was much larger than previously seen for single alkyl chains.[166] The additional peaks observed in the GIXD pattern were found to have a higher order of diffraction relationship with the orthorhombic unit cell.

Table 4. Comparison of lattice parameters of AA-N calculated from GIXD.

	AA-1	**AA-2**	**AA-4**	**AA-8**	**AE-1**
a (nm)	0.742	0.742	0.484	0.482	0.744
b (nm)	0.601	0.495	-	-	0.611
Area per tail (nm^2)	0.223	0.184	0.203	0.201	0.227
Tilt (°)	26	0	0	0	42

The d-spacings of the higher Q_z peaks were calculated to be 0.316 and 0.229 nm and indexed as the second order (2,1) and (3,1) peaks respectively (Figure 25a). The appearance of these additional peaks for higher azimuthal angles indicated the diffraction from higher orders of symmetry than traditionally seen for simple amphiphiles such as a herringbone structure. The appearance of the (2,1) peak is typically forbidden for a non-primitive orthorhombic lattice along with the (0,1) peak unless the two interpenetrating rectangular lattices were laterally shifted from one another or the two molecules per unit cell were not symmetrically equivalent.[167] However, the absence of the (0,1) peak suggested the alkyl tails of **AA-1** molecules formed a herringbone structure at the air-water interface. The (1,1), (2,1) and (3,1) peaks were weak but observable at lower Q_z and sharply increased in intensity at higher Q_z while the (2,0) peak was absent at higher Q_z GIXD patterns. This selective appearance of the peaks elucidated the alkyl tails were tilted towards the nearest neighbor (NN) direction.[132,167]

The increase in the cross-sectional area of the polar head from a carboxyl group to an epoxy group led increased surface molecular areas as was mentioned above (Figure 24). Correspondingly, a slight shift in the diffraction peaks toward lower Q was observed for **AE-1** at all surface pressures (Figure 26a). The four peaks were observed at 0.472, 0.372, 0.319, and 0.231 nm and indexed as the (1,1), (2,0), (2,1) and (3,1) peaks respectively at 20 mN/m.

The characteristic peaks were spaced further apart than the **AA-1** peaks, thus, resulting in unit cell parameters to be a = 0.744 nm and b = 0.611 nm. The area per alkyl tail was determined to be 0.227 nm^2, a value larger than expected for traditional orthorhombic unit cells. Similar to the **AA-1** molecule, the presence of high orders of reflections signified a high ordering of the alkyl tails. Therefore, the tails were concluded to be aligned in a moderately tilted packing structure due to the selective appearance of the peaks. As in the GIXD patterns for the **AA-1** molecules, the (1,1), (2,1), and (3,1) peaks appeared as weak peaks at lower Q_z and became sharper and more intense at higher Q_z. Dissimilarly however, the (2,0) peak appeared sharp and intense at lower Q_z and disappeared at higher Q_z. From the selective appearance of the indexed peaks it was determined the alkyl chains were tilted in the NN direction similarly to the **AA-1** molecules.

The higher resolution GIXD pattern at 20 mN/m for **AA-1** and **AE-1** shown in Figure 25b, 26b indicated the highly selective appearance of the (1,1) and (2,0) peaks as the detector was moved further away from the horizon. The data for both molecules at higher Q_z showed the (2,0) peak became much less intense while the (1,1) peak increased in intensity, indicating the alkyl tails were tilted in the (1,1) direction. The increase in spacing between the two characteristic peaks observed for the **AE-1** molecule corroborated the increase in the cross-sectional area per alkyl tail. The **AA-1** and **AE-1** molecules were found to have moderate long-range order. The correlation lengths calculated for the (1,1) peaks were 9.3 and 7.2 nm for **AA-1** and **AE-1** respectively. The molecules had increased correlation lengths in the (2,0) direction, seen in the sharpening of the peaks in Figure 25b, 26b.

The orthorhombic unit cells suggested for the **AA-1** and **AE-1** molecules from GIXD data are considerable larger than the unit cell calculated for stearic acid molecules with comparable alkyl tails (Table 4). Both molecules show a decrease in the a dimension and an increase in the b dimension of the unit cells. The area per alkyl chain increase from 0.197 nm^2, for the stearic acid molecule, to 0.223 nm^2 and 0.227 nm^2 for the molecules with carboxyl and epoxy head groups, respectively (Table 4). The larger unit cells suggest the azobenzene group interfered with the intralayer packing of the alkyl tails since the polar head itself cannot generate a larger cross-sectional area. The most noticeable is that the alkyl tails for **AA-1** and **AE-1** are packed in a herringbone manner (Figure 27). It is suggested that the

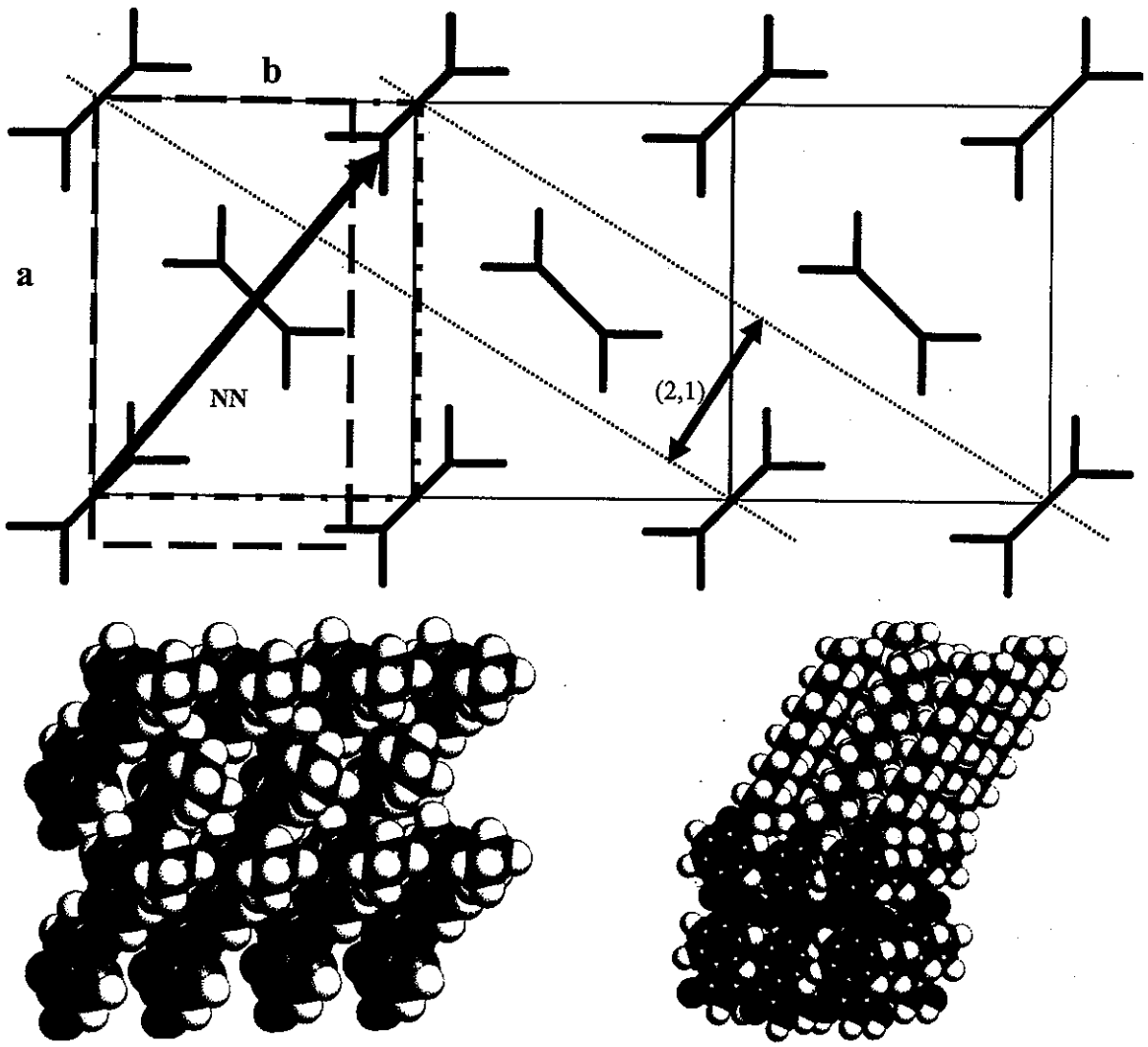

Figure 27. Unit cell comparison of **AA-1** (solid line, clear herringbone packing), **AE-1** (dashed line), and stearic acid (dashed dotted line) from literature[168] (top, left cell). The **AA-1** is expanded in the *b* direction to demonstrate the (2,1) plane (diagonal lines). Molecular model of **AA-1** organized in three unit cells viewed along the alkyl tails (bottom left) and side-view (bottom right).

presence of the azobenzene group created two symmetrically inequivalent sites and enlarged the orthorhombic unit cell along the *b*-axes by initiating their larger tilt towards the NN direction (Figure 27). The cross-sectional areas determined by the π~A isotherm for **AA-1** and **AE-1** were calculated to be 0.25 nm^2 and 0.29 nm^2 in the beginning of the formation of

the condensed monolayer and decreasing to 0.20 nm^2 and 0.23 nm^2 closer to the monolayer collapse, respectively. The known cross-sectional area for azobenzene groups was between 0.30-0.35 nm^2, which was slightly larger than the cross-sectional area for carboxyl group (0.24 nm^2) but fairly comparable for that for the epoxy polar group (0.30 nm^2).[163] The effect was not seen for the larger AD12-1 molecule (Table 2), indicating the larger polar head decreased the interference from the azobenzene group.

The inclusion of two dodecyl alkyl tails in the dendritic shell bought a reduction in the unit cell with an increase in long range ordering. At all surface pressures six sharp, intense peaks were observed in the diffraction patterns for **AA-2** (Figure 28a). The d-spacing for the two sharpest peaks were calculated at 0.412 and 0.371 nm and were indexed as the (1,1) and (2,0) peaks respectively. The four additional higher Q_{xy} peaks were indexed as the (2,1), (0,2), (1,2), and (3,1) peaks at 0.299, 0.249, 0.236, and 0.222 nm respectively. All peaks diminished in intensity at higher Q_z (larger azimutal angle) GIXD patterns, revealing the alkyl tails are parallel to the surface normal. In

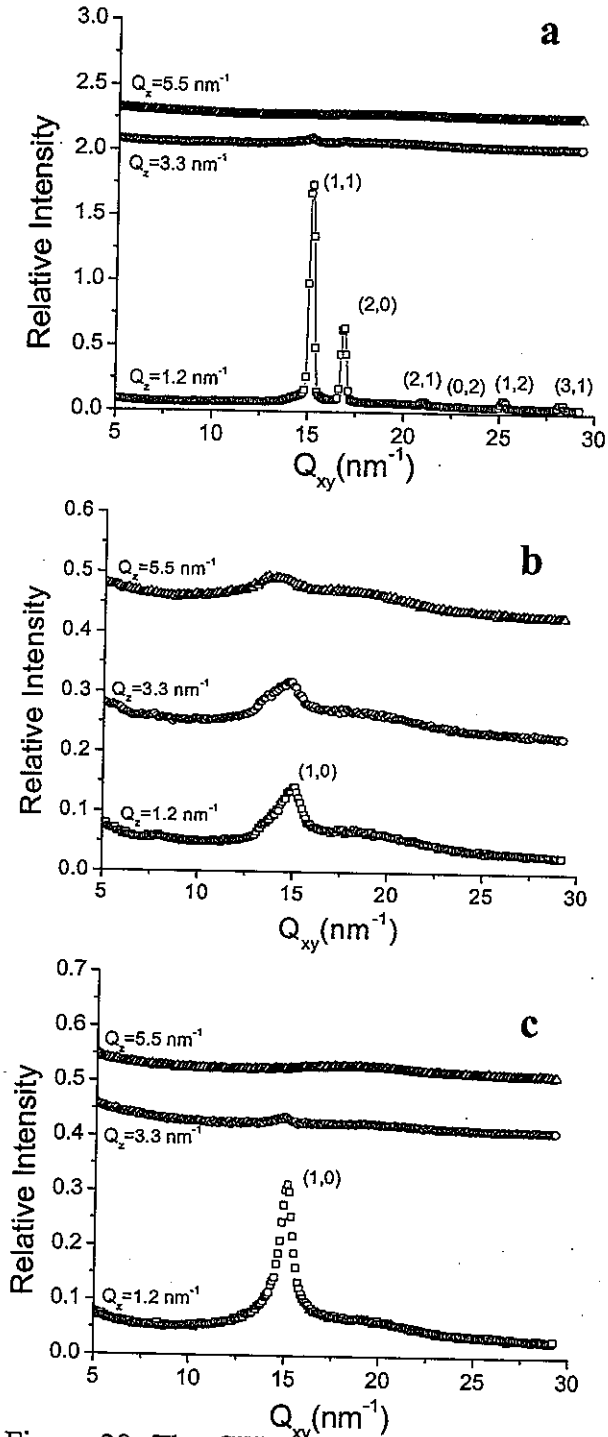

Figure 28. The GIXD patterns of the three highest generations observed for the Langmuir monolayers at 20 mN/m surface pressure.

contrast to the one tail molecule observed previously the **AA-2** molecules formed a regular orthorhombic unit cell with no indication of a herringbone structure. The lattice parameters were calculated as a= 0.742 nm and b= 0.495 nm with the area per tail equal to 0.184 nm^2 (Table 4). The a lattice parameter calculated for both **AA-1** and **AA-2** was equal to 0.742 nm while the b lattice parameter decreased approximately 0.1 nm from 0.601 nm for **AA-1** to 0.495 nm for **AA-2.**

A further increase in the number of alkyl tails disrupted the well-ordered orthorhombic lateral packing. A single broad peak was observed at all surface pressures for **AA-4** and indexed as the (1,0) peak with a d-spacing of 0.420 nm (Figure 28b). The four tail molecule formed a quasi-hexagonal unit cell with the lattice parameter a = 0.484 nm and the area per tail 0.203 nm^2 (Table 4). Similarly, the eight tail molecule had a single broad peak at 0.418 nm, revealing the alkyl tails formed a regular hexagonal lateral packing (Figure 28c). The lattice parameter decreased slightly to a = 0.482 nm and the area per tail decreased to 0.201 nm^2 (Table 4). The reduction of the area per tail as the dendritic shell became bulkier (from four to eight tails) suggest the alkyl tails of the larger molecule more readily rearranged at the air-water interface in dense and vertical manner. As Q_z increased (larger azimutal angle), the observed peaks for **AA-4** and **AA-8** significantly decreased in intensity strongly suggesting the alkyl tails were parallel to the surface normal.

Comparisons of the correlation lengths for the most intense peaks of all four molecules indicate the lower generation molecules had the highest long-range ordering. The correlation lengths for the (1,1) and (2,0) peaks were 9.3 and 11.0 nm for **AA-1** and 10.0 and 10.4 nm for **AA-2.** In contract, the correlation lengths for the four and eight tail molecules decreased to 2.9 and 3.2 nm respectively determined from the (1,0) peak. The shift from the long range ordering seen for the lower generation molecules to the limited short range ordering for the two highest generations suggests the crowded junction compromises the attached tails ability to organize in crystal lattice within planar monolayer.

Independent confirmation of the larger tilt angle and information about the tilt direction of the alkyl tails was determined from rod scans of the two most intense diffraction peaks observed for each molecule. The rod scans for **AA-1** and **AE-1** molecules in the (2,0) direction displayed the angular behavior with a sharp peak prior to a gradual decrease in

intensity, while for the rod scans of the lower Q_{xy} peak, the tilt projection shown along the (1,1) direction confirmed the nearest neighbor tilt direction (Figure 29). Modeling of the rod-scan data for **AA-1** and **AE-1** confirmed the tails tilted approximately 35° and 42°, respectively (Table 4). The tilt behavior of **AA-1** and **AE-1** in NN direction differed from the corresponding behavior for photochromic amphiphiles with shorter alkyl tails and flexible spacer between azobenzene group and polar head. Durbin et al observed a transition in the tilt direction of the molecules from the NN direction to the next nearest neighbor (NNN) while the tilt angle remained constant.[169] The azobenzene fragment was found to influence the cross-sectional area of the molecules while the van der Waals attraction between the short alkyl chains determined the packing structure of the molecules. Comparison with the bulk structure of azobenzene groups found the amphiphilic molecules formed a lattice structure of the H-aggregates of the photochromic group. In contrast, the amphiphilic molecules observed in this study appeared to show no transition from the NN to the NNN direction; however, the tilt angle correlated with the angles observed for both the shorter chain amphiphiles at the air-water interface and literature values for the bulk structure of azobenzene groups.[169,170]

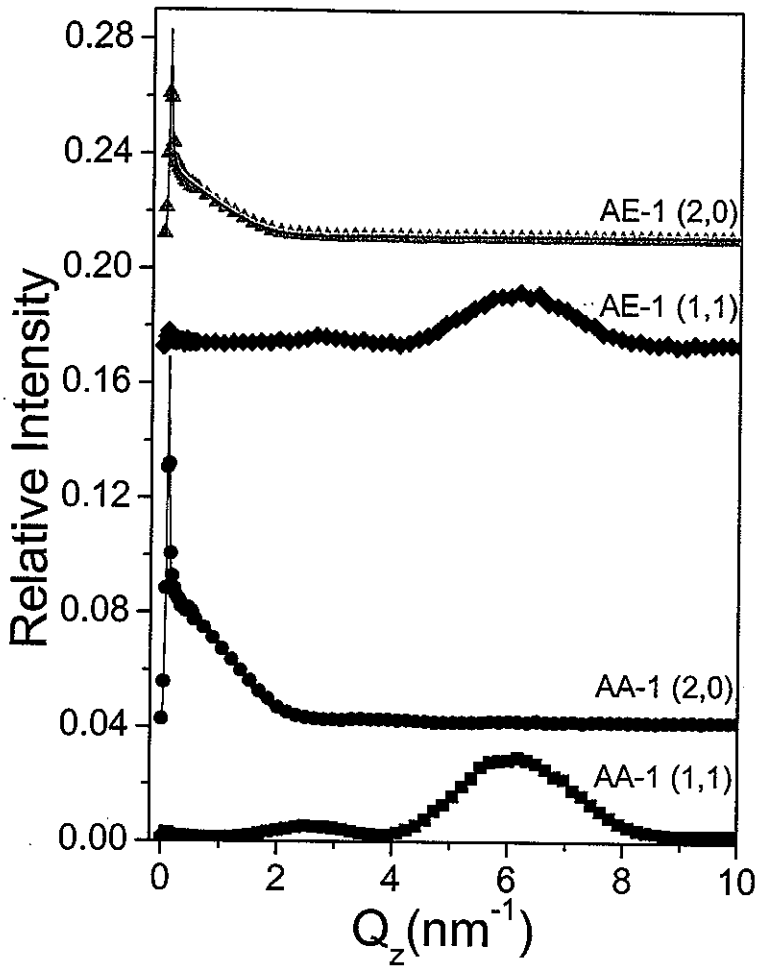

Figure 29. Rod scans of (1,1) and (2,0) peaks for **AA-1** and **AE-1** at 20 mN/m. The data represented by symbols and model fits are shown by lines.

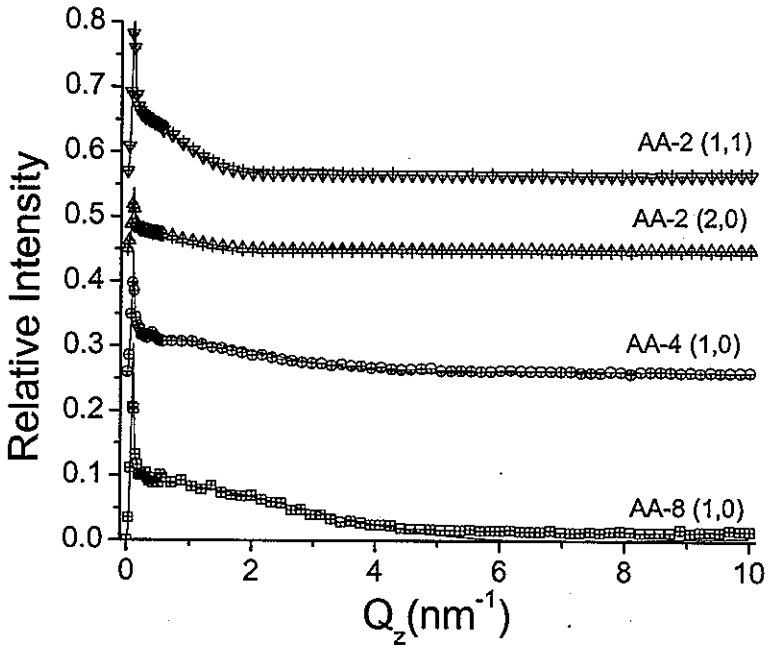

Figure 30. Rod scans for the reflexes (1,1) and (2,0) for AA-2 and the (1,0) for AA-4 and AA-8 with fits illustrate the perpendicular orientation of the alkyl tails. The intensities were multiplied by a factor of 10 and offset for clarity. The data are represented by symbols and the fit by lines.

Further confirmation of perpendicular arrangement of the alkyl tails of the higher generations was determined by analysis of rod scans of the most intense peaks of the three molecules (Figure 30). The rod scans for the **AA-2** molecule in the (1,1) and (2,0) directions displayed a sharp peak prior to a gradual decrease in intensity. The modeling suggested a 2.9 nm rod parallel to the surface normal. The length of the rod was nearly twice that of a dodecyl alkyl tail indicating the molecule is parallel to the surface normal up to the nitrogen double bond of the azobenzene spacer group. The rod scans for **AA-4** and **AA-8** in the (1,0) direction exhibited a similar trend (Figure 30). The model resulted in a rod length less than the expected length for a dodecyl tail indicating the lower portion of the tails being disordered. Apparently, the radial attachment of multiple tails to a single junction limited the ability of the alkyl tails to order beyond several molecules.

The arrangement of the molecular fragments within Langmuir monolayers was revealed by X-ray reflectivity studies (Figure 31 and 32). The data for both single tail

molecules showed a single well-defined minimum and an additional subtle minima observed at the highest surface pressures (Figure 31). The two- and eight-tail molecules (**AA-2** and **AA-8**) had a single, well-defined minima and an additional minima at higher Q_z for lower surface pressure (Figure 32a and 32c). The lower Q_z minima became less defined at higher surface pressure indicating no clear transition between the focal group and the alkyl tails. Dissimilarly, **AA-4** had two defined minima at low and high surface pressure with less definition of the minima observed for the intermediate pressure (Figure 32b).

A two box model was used to fit the data for both single tail molecules at all observed surface pressures where the first box was assigned to the hydrophilic polar head and azobenzene group and the second box was assigned to the hydrophobic alkyl tails (Figure 33). Ideally the molecule would be modeled using a three box model but the short length of the focal group and the lower resolution of the experimental setup led to the inclusion of the hydrophilic polar head and the azobenzene fragment in the first box.

The decrease in spacing for the defined minima for increasing surface pressure indicated an increase in the thickness of the head group box from 1.17 to 1.46 nm for **AA-1** (Table 5, Figure 33a). The change in thickness suggested the azobenzene group transitioned from 33.3° tilt from the surface normal to virtually vertical orientation (Table 5). The electron density for the first box was higher than calculated for densely packed azobenzene fragment and carboxylic acid polar heads, confirming the presence of water molecules. The attraction between the hydrophilic head group and the water subphase forced the head group to submerge into the subphase and pack partially below the air-water interface. Unlike the azobenzene group, the thickness of the second box remained virtually unchanged around 1.35 nm, suggesting the alkyl tails remained tilted at 25.7° from the surface normal at all surface pressures (Table 5). The difference in the tilt angle, determined from rod scans and reflectivity data, was within the uncertainities of both measurements.

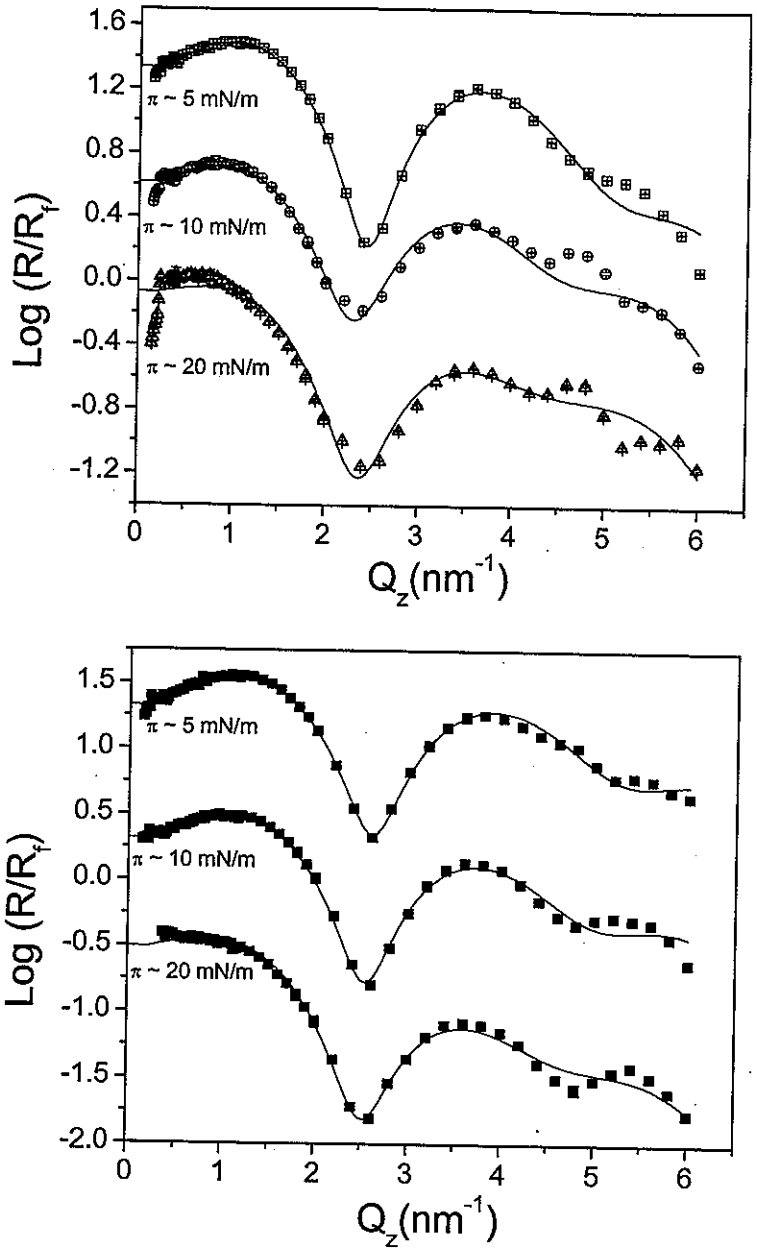

Figure 31. Normalized reflectivity data for a) **AA-1** and b) **AE-1** at different surface pressures observed. The experimental data were offset for clarity and were represented by symbols and fits are represented by lines.

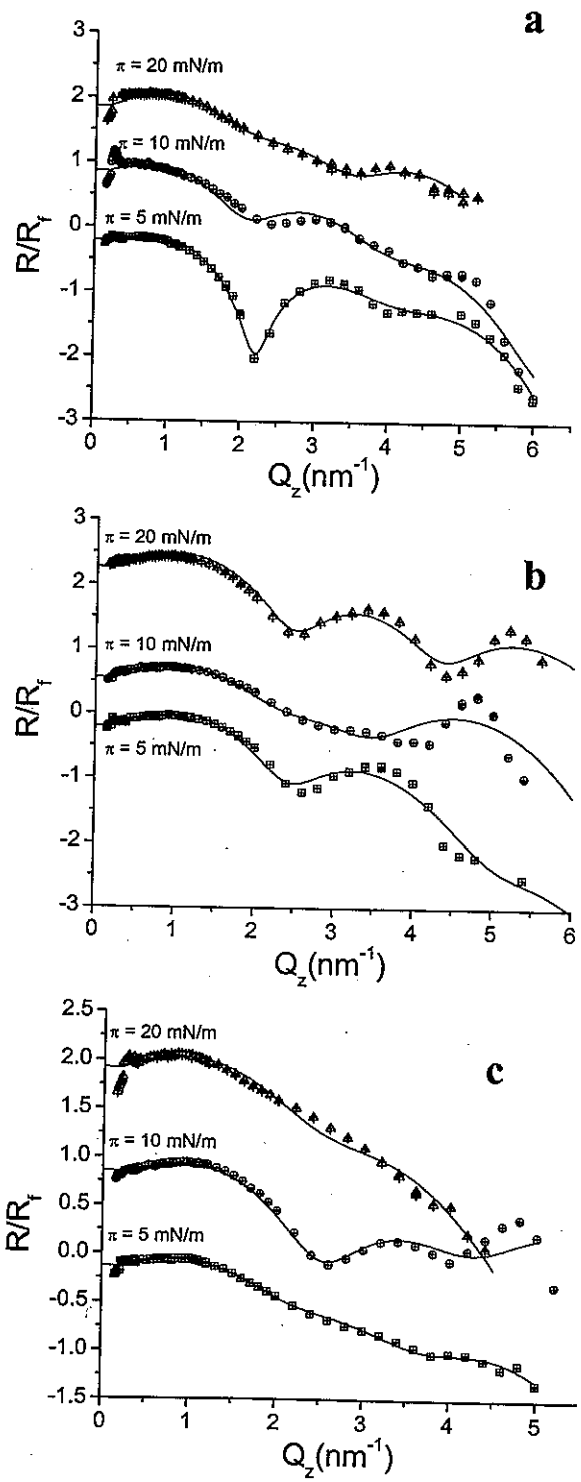

Figure 32. The X-ray reflectivity data of a) AA-2, b) AA-4 and c) AA-8 at all exploited surface pressures.

Table 5. Box model parameters for single tail molecules

Sample	AA-1			AE-1		
Surface Pressure (mN/m)	5	10	20	5	10	20
Head Box Length (±0.03 nm)	1.17	1.39	1.46	1.18	1.27	1.39
Head Box Electronic Density (±0.02 x10^3 e/nm^3)	0.42	0.39	0.40	0.47	0.45	0.41
Tail Box Length (±0.03nm)	1.36	1.37	1.32	1.22	1.24	1.24
Tail Box Electronic Density (±0.02 x10^3 e/nm^3)	0.31	0.30	0.18	0.24	0.23	0.19
Surface Roughness (±0.04 nm)	0.261	0.258	0.269	0.218	0.249	0.302
Total Thickness (±0.06 nm)	2.53	2.76	2.78	2.40	2.51	2.63
Azobenzene Tilt Angle (±3.0 deg)	33.3	17.8	0	37.2	30.9	20.1
Tail Tilt Angle (±3.0 deg)	25.7	25.7	25.7	35.3	35.3	35.3

The area per alkyl tail projected along the **AA-1** molecular axes was calculated by $A=A_o\cos(\theta)=0.25\cos(25.7)=0.225$ nm^2, comparable to the area per tail calculated by GIXD (0.223 nm^2) (Table 4). The electronic density for the alkyl tails' box was lower than that calculated for densely packed alkyl chains. However, the density calculated by the box model was equivalent to the density calculated from molecular models of the tilted molecules. Both boxes were observed to decrease in electronic density at 20 mN/m. The monolayer was previously discerned to undergo a collapse at 25 mN/m as was concluded from the π-A isotherm (Figure 24). The large decrease in the electronic density of the box model indicated the alkyl tails form cluster packing prior to the complete collapse of the monolayer.

Similar to the **AA-1** molecule, for the **AE-1** molecule at rising compression the X-ray reflectivity data showed a well-defined minimum, indicating an increase in the head group box thickness from 1.18 to 1.39 nm (Table 5, Figure 33b). Unlike the **AA-1** molecule, the orientation of the azobenzene group for **AE-1** was calculated to be changed from 37.2° at low surface pressure to 20.1° at 20 mN/m. This difference demonstrates the role of the larger epoxy polar head group which induced a larger tilt angle of the azobenzene group that could not easily be changed by the monolayer compression. Moreover, the head group box possessed higher electronic density confirming the presence of water molecules packed among the epoxy head groups and overall denser packing of these fragments (Table 5).

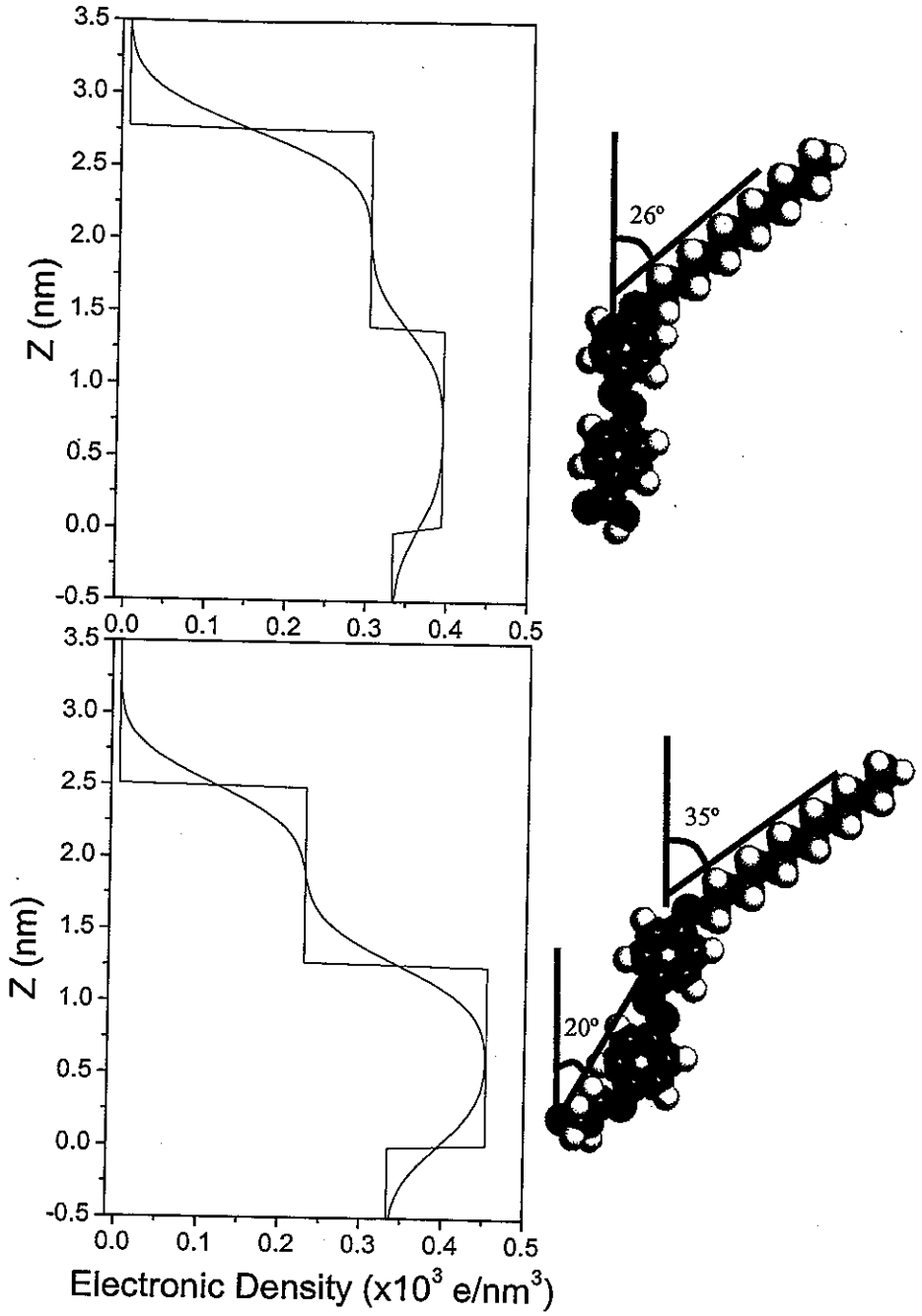

Figure 33. Box model for molecules a) **AA-1** and b) **AE-1** in condensed state at 10 mN/m (left) and corresponding molecular models at highest surface pressure (right).

Additionally, the box model showed the thickness of the second box was approximately 1.24 nm for all pressures, thereby indicating the alkyl tails to be tilted 35.3° from the surface

normal at all pressures, while forming a kinked structure. The overall thickness of the monolayer is substantially (0.1-0.2 nm) smaller for **AE-1** molecules (Table 5). The projected cross-sectional area per alkyl tail (0.228 nm^2) was comparable to the area per tail (0.227 nm^2) determined by GIXD. The larger azobenzene group and the epoxy polar head forced a larger cross-sectional area, as was concluded from the π-A isotherm (Figure 24). The larger cross-sectional area then forced the alkyl tails to tilt further to achieve the preferred densely packed structure. However the alkyl tail box had a lower electronic density than predicted for densely packed, tilted alkyl tails. This lower than expected electronic density suggested the tails formed a cluster structure at the air-water interface.

Comparison of the box models for the moderate surface pressure demonstrated the influence of polar head groups on the overall molecular conformation as presented in Figure 33 for individual molecules (see Figure 27 for densely packed monolayers). The thickness of the alkyl tail boxes for both molecules proved the tails remained tilted although the cross-sectional area decreased. Conversely, the carboxylic head group and azobenzene fragment of the **AA-1** shifted from a tilt angle similar to the alkyl tails to a virtually vertical orientation (Figure 33a). Dissimilarly, the epoxy head group and azobenzene fragment of the **AE-1** molecule still remained significantly tilted in the condensed state (Figure 33b). The tilt of the alkyl tail becomes much larger in **AE-1** molecule. This represents significant difference in the intramonolayer packing of the two molecules which can improve the ability of the azobenzene group attached to the bulkier epoxy heads for photoisomerization in condensed state.

The data for **AA-2** and **AA-4** was modeled using a two-box model for electron density distribution along the surface normal at all surface pressures as well as the two lower surface pressures of **AA-8** (Table 6, Figure 34). The polar head group and the azobenzene fragment composed the first box with higher electron density and the attached alkyl tails are located in the second box. The length of the focal group and proximity to the spacer group reduced the contrast between the fragments and thereby confining the fragments within one box. Previous studies of similar molecules in addition to lower generations demonstrated the relative size of the polar group to the bulky spacer group was near the surface roughness calculated for the box models thereby predicting a two box model more favorable than a

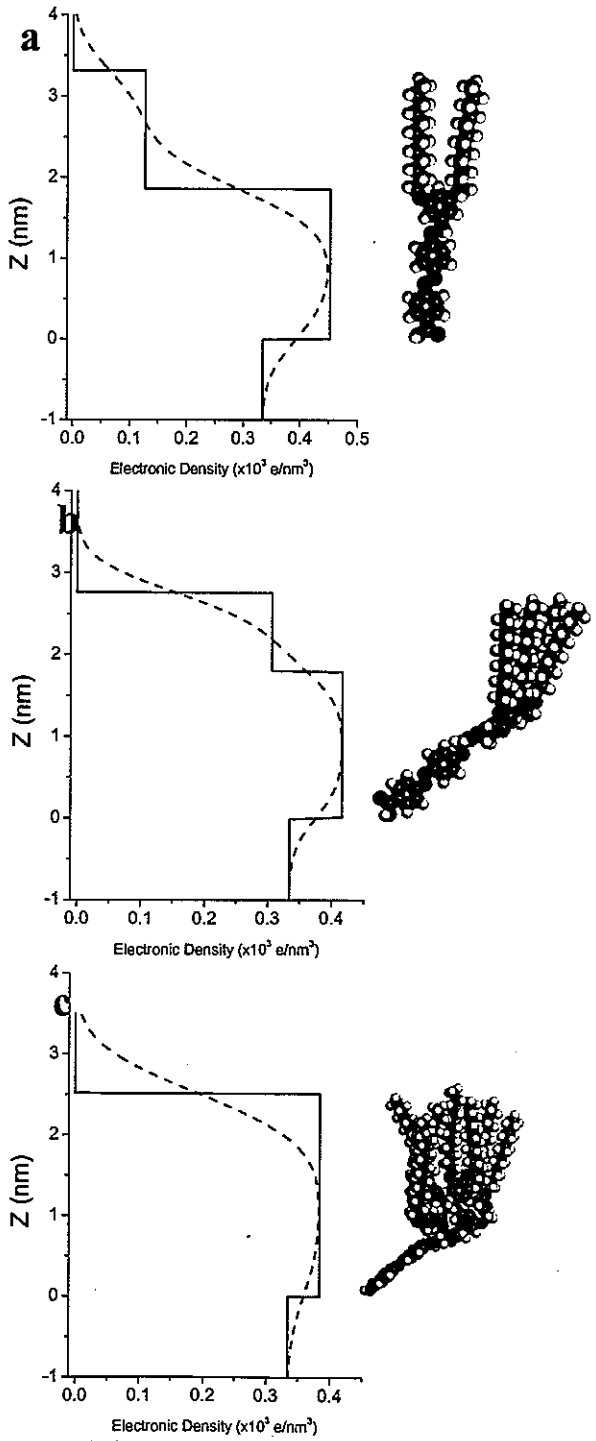

Figure 34. The box models calculated from X-ray reflectivity data shown in Figure 4 and molecular models with molecular dimensions matching density distribution for a) AA-2, b) AA-4 and c) AA-8 for the highest surface pressure (20mN/m).

three box model.[171] The highest surface pressure of **AA-8** was modeled using one box model, indicating the contrast between the focal group and the eight attached alkyl tails diminished.

Table 6. Parameters of the box models calculated X-ray reflectivity for AA-2, AA-4, and AA-8 under ambient light conditions.

		Head Box		Tail Box			
Sample	Pressure (mN/m)	Length (nm)	Density ($x10^3$ e/nm^3)	Length (nm)	Density ($x10^3$ e/nm^3)	Roughness (nm)	Thickness (nm)
Ambient Light Conditions							
AA-2	5	1.58	0.40	1.40	0.21	0.36	2.98
	10	1.70	0.39	1.42	0.32	0.43	3.12
	20	1.85	0.45	1.45	0.13	0.40	3.30
AA-4	5	1.15	0.43	1.42	0.37	0.44	2.57
	10	1.86	0.44	1.33	0.13	0.32	3.19
	20	1.79	0.42	0.97	0.31	0.34	2.76
AA-8	5	1.75	0.41	1.45	0.10	0.36	3.20
	10	1.71	0.38	1.05	0.27	0.25	2.76
	20	2.51	0.38	-	-	0.50	2.51

Comparison of the electron density distribution for all molecules as a function of surface pressure applied to the Langmuir monolayers suggests the alkyl tails and azobenzene groups undergo the most dramatic rearrangements under different conditions. The one tail molecules had lower electronic density calculated for the highest pressure indicative of an early monolayer collapse into a domain structure as was demonstrated before.[171] This molecule within monolayer was composed of vertically oriented azobenzene group and highly tilted alkyl tail (Figure 34a). This molecular ordering provided the appropriate balance between cross-sectional areas of the bulky azobenzene group and a single alkyl tail. Comparison of this model to the electron density distribution for the **AA-2** molecule with two alkyl tails showed significant structural reorganization (Figure 34). Two alkyl tails became oriented vertically in a register with the azobenzene group due to change in cross-sectional mismatch the azobenzene group. As the monolayer compressed the focal groups became more densely packed in addition to 15% lengthening in vertical direction caused by lateral compression (Table 6). The length of the alkyl tail box remained consistent with the

vertically oriented fully extended chains although the electronic density decreased for the highest surface pressure, suggesting the monolayer collapsed into a domain structure at 20mN/m. The electron density distribution calculated for the **AA-4** molecule was similar to the two tail molecule (Figure 34). At higher pressure, the second box for the four tail molecule reduced in length as the electronic density increased as expected for densely packed alkyl tails (Table 6). At the lowest surface pressure, the monolayer of **AA-8** displayed a similar trend to the **AA-4** molecule. At the highest surface pressure, the denser monolayer slightly decreased in overall thickness, suggesting the molecule adopted a tilted orientation to achieve a densely packed structure.

3.2.2 Monolayer Structure at the Air-solid Interface

Comparison of monolayer thickness at the air-water and air-solid interface to the estimated length from molecular model concluded the inclusion of multiple alkyl tails in the dendritic shell, particularly four and eight tails, force the molecules to adopt a tilted orientation (Table 7). Previous studies demonstrated **AA-1** oriented perpendicular to the surface as the **AE-1** molecules formed a kinked structure.[171] The good agreement observed between the estimated length of the **AA-2** from molecular models and the liquid and solid supported monolayers confirm a similar parallel orientation to the surface normal for the two tail molecule. The lower effective thickness of the solid supported monolayer of **AA-2** was attributed to the domain structure observed by AFM. The thickness of liquid and solid supported monolayers was significantly lower than the estimate length of the molecular models for **AA-4** and **AA-8**. Comparison of the length of the tail box from X-ray reflectivity and the length estimated from the rod scans suggested the lower third of the alkyl tails were disordered due to the close association to the phenyl rings in the dendritic shell. The larger cross-sectional mismatch of the higher generations resulted in a kinked structure similar to the **AD12-N** at interfaces with azobenzene groups lying virtually parallel to the solid surface.[48]

The deposition of the monolayer on solid supports provided further insight in the two-dimensional morphology of the monolayer (Figure 35). AFM imaging of the deposited **AA-1** monolayers showed the domain formation prior to the monolayer collapse with lateral

domain dimensions below 1 μm. The monolayers deposited at 5 mN/m appeared uniform with an effective thickness of 2.3 nm and a surface roughness of 0.35 nm which are fairly close to that determined from X-ray data at the air-water interface (Table 5). A moderate increase in surface pressure did not disrupt the uniform film and also showed negligible changes in monolayer thickness and surface roughness. At higher surface pressures, a second domain layer appeared to form on top of the monolayer (Figure 35a). Unlike the **AA-1** molecule, **AE-1** molecules formed a monolayer with a domain structure at all observed pressures. The surface coverage increased at the highest pressures as the overall size of the domains decreased, although the shape and structure of the semi-continuous domains with lateral dimensions below 1 μm remained unchanged (Figure 35b).

Table 7. Comparison of thickness (nm) of solid and liquid supported monolayers with theoretical lengths.

	AFM	Ellipsometry	XR	Model
AA-1	1.9	3.1	2.8	2.9
AA-2	4.1	2.8	3.3	3.5
AA-4	NA	2.7	2.8	4.1
AA-8	NA	3.1	2.5	4.6
AE-1	1.9	3.3	2.6	3.1

Evidence of the long range ordering of the two tail molecules was observed for solid supported monolayers (Figure 36). At the lowest surface pressure, **AA-2** formed large leaf-like domains with overall lengths of several microns (Figure 36a). The thin arms of the leaf-like domains measured several hundred nanometers across. Upon increasing the surface pressure to 30 mN/m the domains decreased in overall size and became more regularly shaped and densely packed (Figure 36b). The lateral dimension of the domains was approximately one micron. Higher resolution AFM of the solid supported monolayers deposited at higher surface pressure revealed the domains composed of a lamellae-like structure. Figure 36c illustrates the random orientation of the lamellae structure (more clearly observed in the phase image) with the shift in the directional organization inside of the domain. The d-spacing was calculated to be 5.7 nm indicating interdigitated bilayer packing similarly to that observed for crown-containing monodendrons.[49]

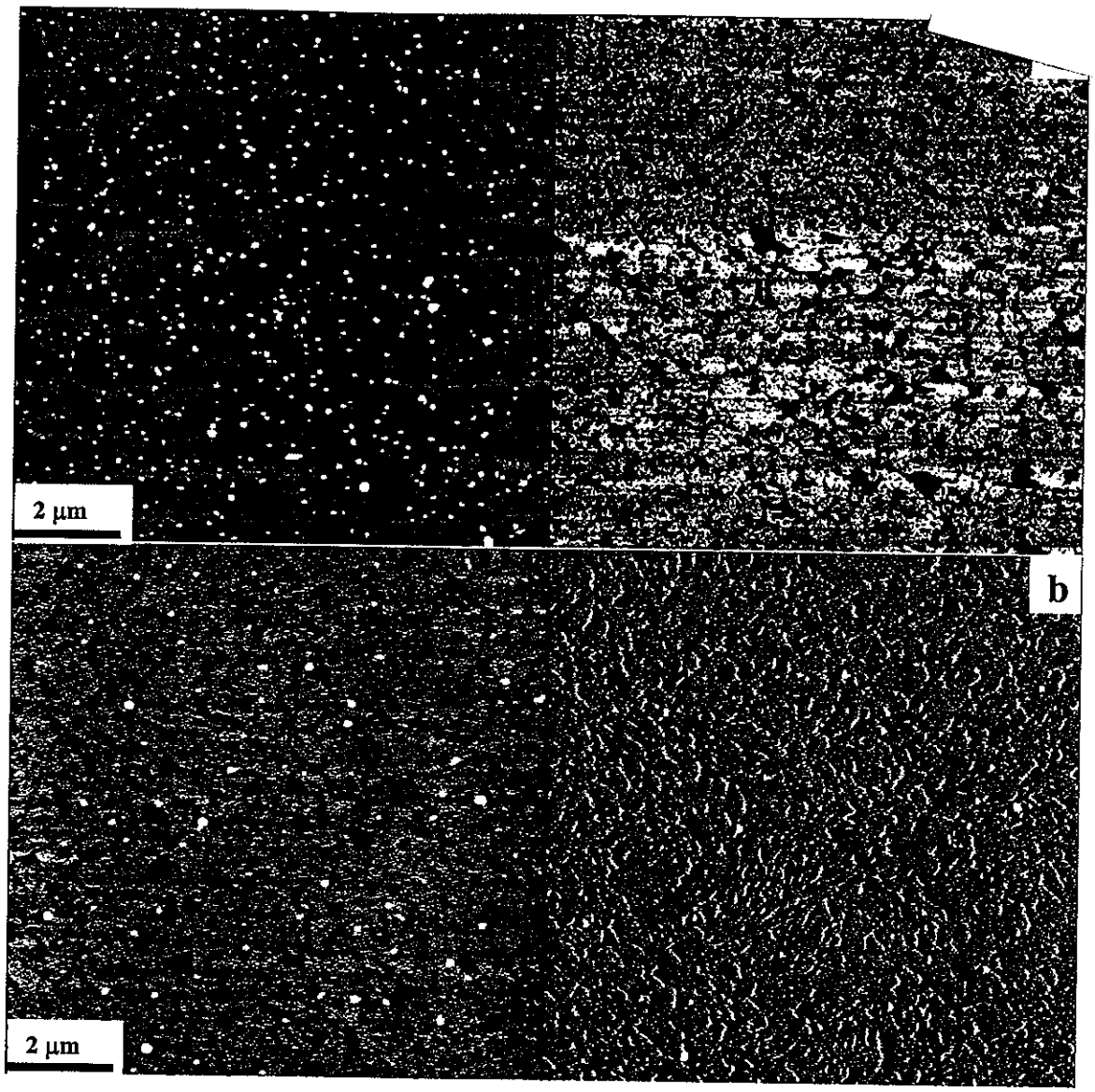

Figure 35. AFM images for LB monolayer formed from large domains for a) **AA-1** at 20 mN/m and b) **AE-1** at 30 mN/m. The z-range for topography (left images) was 5 nm and the z-range for phase (right images) was a) 30 degrees and b) 5 degrees.

The limited short range ordering of **AA-4** and **AA-8** was evident for monolayers deposited at all surface pressures. The four and eight tail molecules formed uniform monolayers with very limited areas of short lamellae-like structures (Figure 37). The lower

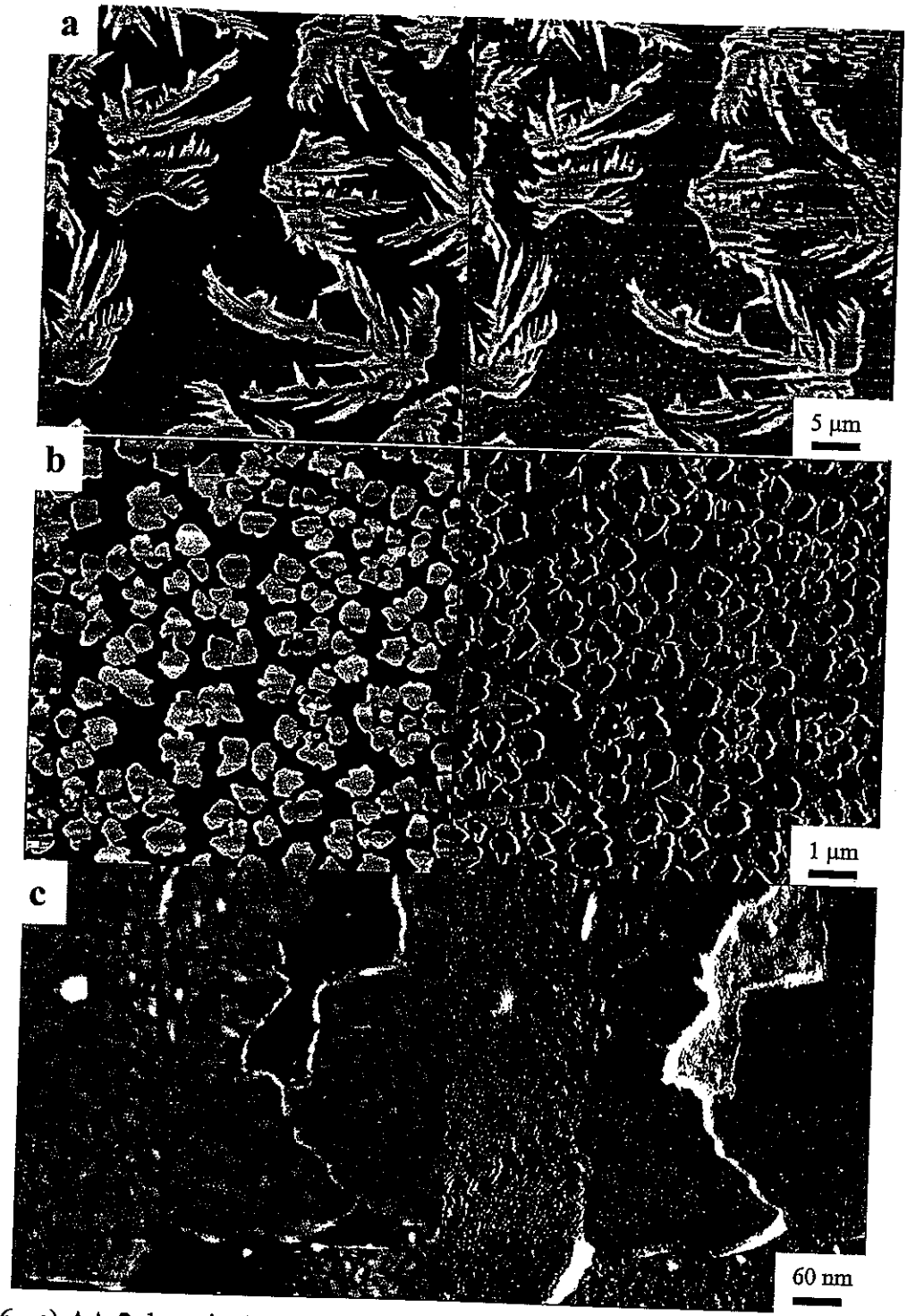

Figure 36. a) **AA-2** deposited at 3mN/m and b) at 20mN/m. c) High resolution AFM image demonstrating lamellar structure observed within the domains shown in b). Scale: topography (L) and phase(R) for a) & b) z=10nm and phase =40 degrees. For c) z=5nm and phase=10 degrees.

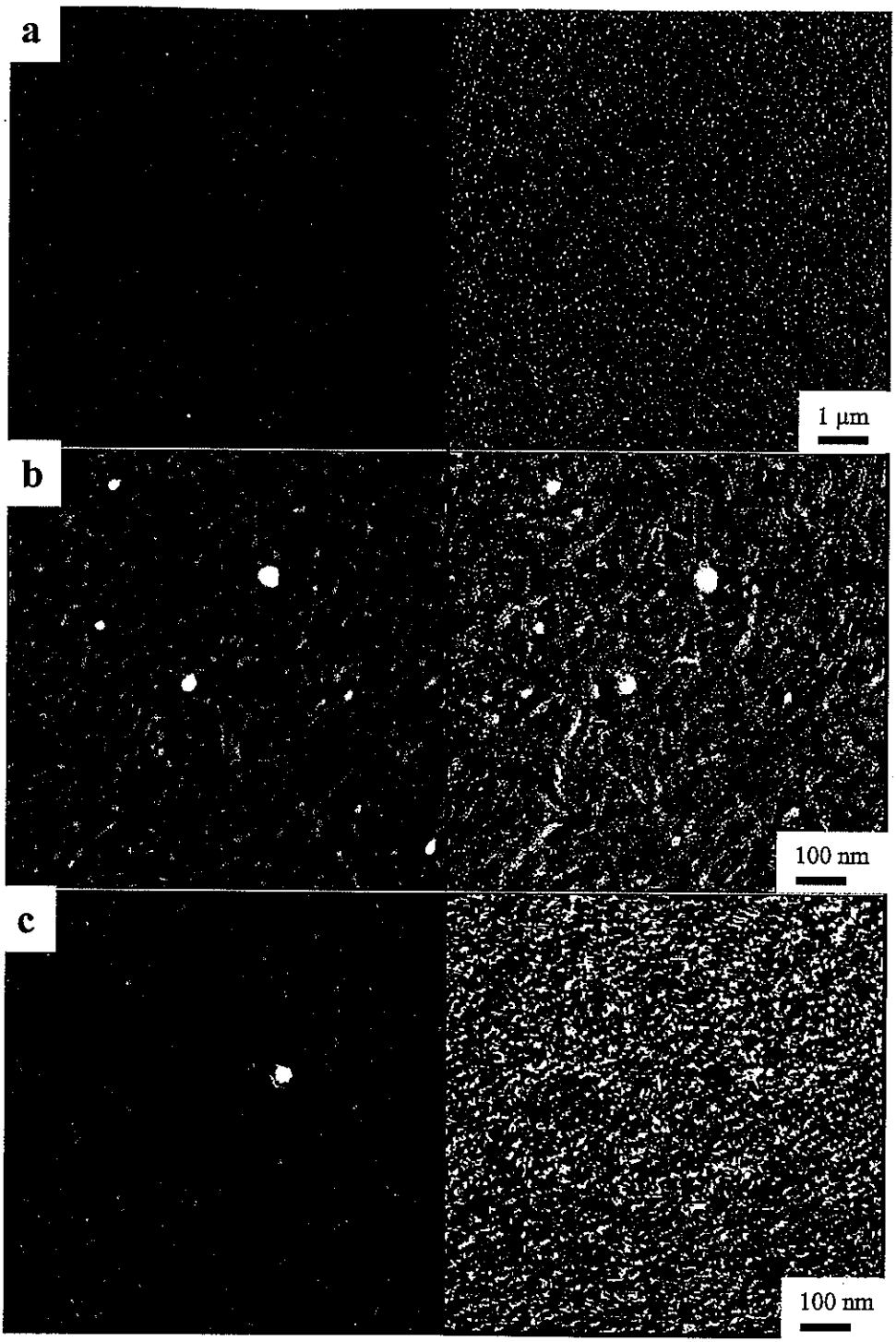

Figure 37. a) AA-4 deposited at 5mN/m pressure, b) AA-4 depostied at 20mN/m pressure and c) AA-8 deposited at 20 mN/m pressure. Scale for all images: topography (left) z-range of 5nm, phase (right) z-range of 10 degrees.

than expected effective thickness of the monolayers suggested the focal group of the higher generation molecules was significantly tilted from the surface normal (Table 4). The cross-sectional area of the dendritic shell for **AA-4** and **AA-8** was three to six times larger than the cross-sectional area of the acid head group thus creating a large mismatch. This allowed the focal group fragment to adopt large tilt angles thereby greatly reducing the monolayer thickness.

3.2.3 Photoisomerization Studies

The photochromic response of the monodendron molecules was examined in dilute solutions and at interfaces to determine the effect of confinement on the response time. Responsive thing film applications require rapid response time, similar to the timescale observed in dilute solutions. The preservation of the mobility of the photochromic groups in thin films is desirable for reduced response time.

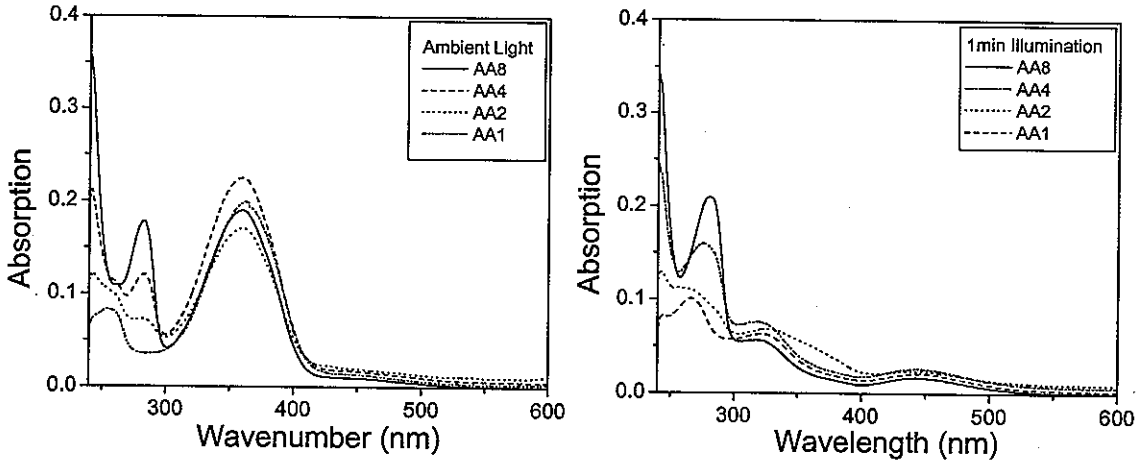

Figure 38. UV~vis spectra for AA-N in dilute solution in a) ambient conditions and b) after 1 min illumination with 365 nm UV wavelength.

3.2.3.1Photoisomerization in solution. The photochromic isomerization of all four generations was readily observed in dilute solutions. In ambient light conditions, the π-π^* absorbance band was observed at 365 nm, denoting the **AA-N** molecules are in the *trans* isomer, with an additional peak observed at 290 nm attributed to the phenyl rings in the

dendritic shell (Figure 38a). [49,50,172] After one minute illumination, the absorbance at 365 nm was replaced with two strong bands at 318 and 455 nm, indicating a predominant transformation to the *cis*-isomer (Figure 38b). Therefore, the presence of bulky epoxy terminal groups does not suppress the photoisomerization ability of the azobenzene groups in these novel compounds.

3.2.3.2 Photoisomerization within Langmuir monolayers. The question of the preservation of the reversible photoisomerization in the monolayer state is important for the fabrication of surface monolayers at the solid surfaces. The photoisomerization of the lower generation monodendrons was studied at the air-water interface to determine the mobility of the molecules in loosely packed two-dimensional monolayer films (Figure 39). The selected Langmuir monolayers were compressed to 10 mN/m and exposed to repeated cycles of 365 nm light and ambient light as the surface pressure was held constant. Kinetic studies of one and eight tail molecules at the air-water interface were not preformed to due stability concerns. The four tail molecule exhibited a very modest 3.5% increase in molecular area upon UV illumination. In contrast the **AA-2** molecule had a 8.8% molecular area increase for the monolayer UV

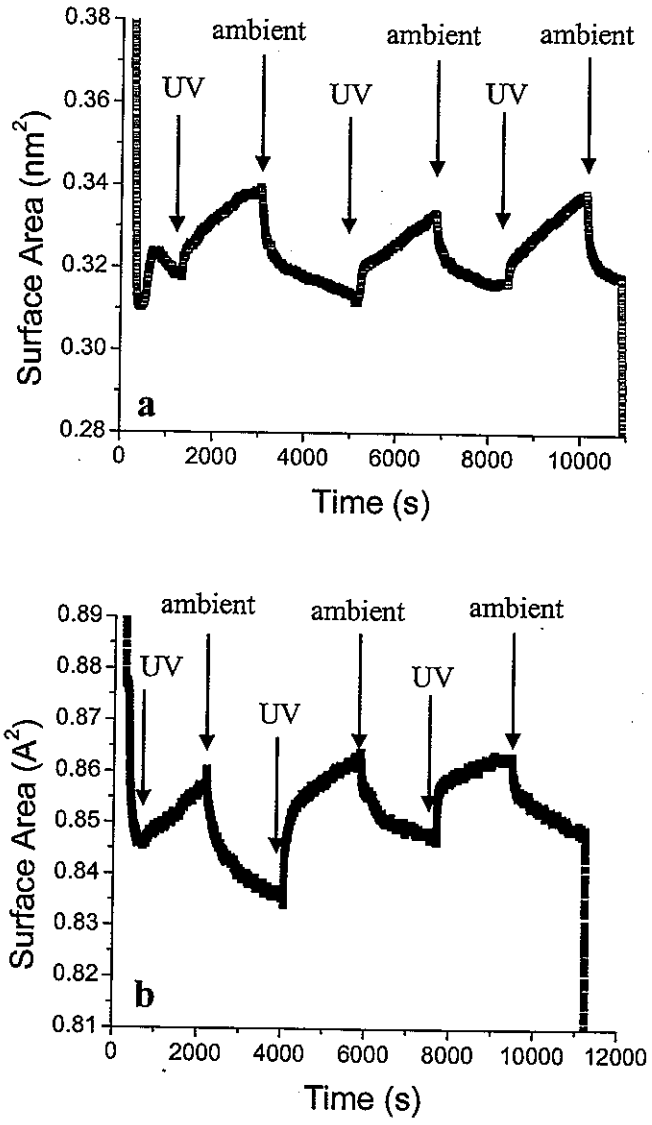

Figure 39. Variation of molecular area versus time for **AA-2** as the Langmuir monolayer was exposed to repeated cycles of 365 nm and ambient light..

illuminated for several minutes with gradual relaxation to the initial value (Figure 39). The smaller difference in cross-sectional area for the **AA-4** monolayer indicated the inability of the molecules to fully achieve complete photoisomerization transition due to the densely packed alkyl tails. The cross-sectional mismatch of the four alkyl tails attached to the azobenzene spacer group and the smaller carboxylic focal group allowed for significant rearrangement of the focal group fragment without considerably affecting the ordering of the alkyl tails. The large difference in the molecular area for the **AA-2** molecule observed for the *trans* and *cis* isomers denotes the two tail molecules possess the preferential cross-section mismatch to preserve the photoisomerization of the molecules within the densely packed monolayer at the air-water interface.

The two and four tail molecules were further analyzed by X-ray reflectivity under UV illumination to elucidate the ordering of the molecules in the *cis* isomer. Although the reference molecule **AE-1** demonstrate a similar trend in molecular area during the UV kinetics studies as **AA-4**, the molecules proved unstable under UV illumination at the air-water interface on the timescale of the X-ray reflectivity experiments. Surprisingly, the X-ray reflectivity data for monolayers of **AA-2** and **AA-4** exposed to UV illumination indicated more uniform films with a slight decrease in the overall film thickness as compared to *trans*-state of azobenzene groups (Table 6). The data for both molecules has one defined minimum at lower Q_z with additional less defined minima at higher Q_z (Figure 40). The defined minima shifted slightly to a lower Q_z value at moderate pressure in comparison to a higher Q_z position for lower and higher surface pressure for the two and four tail molecule.

A two-box model of electron density distribution was used for all pressures for both molecules with a similar assignment of the molecular fragments as used for the monolayers analyzed under ambient conditions (*trans*-state of azobenzene groups). The head group box with elevated electron density for the two tail molecule in *cis*-state was similar in length to that under the ambient light (Table 8, Figure 40). However, the electronic density decreased significantly, from 12.5% for the lowest surface pressure to 22% for the highest surface pressure due to larger molecular area observed for the UV illuminated monolayer. In contrast, the length of the tail box was 22% lower for the UV illuminated monolayers and the electronic density was slightly lower than expected for densely packed alkyl tails (Figure

40a, Table 8) suggesting the alkyl tails tilt during the molecular reorganization. Unlike monolayers observed under ambient conditions, the alkyl tail box of the UV illuminated monolayer remained relatively consistent indicating a more stable monolayer.

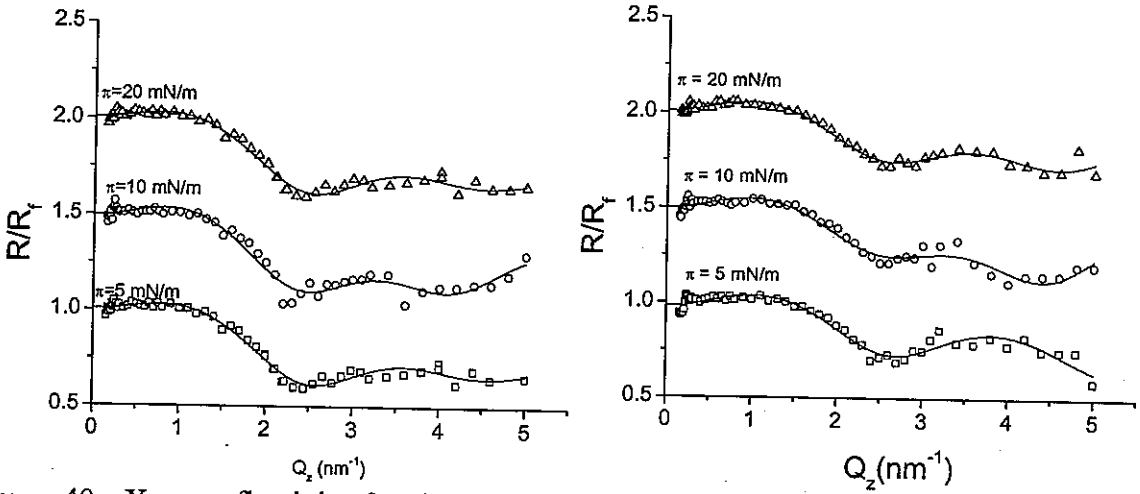

Figure 40. X-ray reflectivity for a) AA-2 and b) AA-4 monolayers at all surface pressures under 365 nm illumination. Data and model represented by symbols and lines respectively.

Table 8. Parameters of the box models calculated X-ray reflectivity AA-2 and AA-4 under 365 nm illumination at the air-water interface.

		Head Box		Tail Box			
Sample	Pressure (mN/m)	Length (nm)	Density ($x10^3$ e/nm^3)	Length (nm)	Density ($x10^3$ e/nm^3)	Roughness (nm)	Thickness (nm)
AA-2	5	1.58	0.35	1.13	0.30	0.18	2.71
	10	1.84	0.36	1.05	0.29	0.15	2.89
	20	1.57	0.35	1.13	0.30	0.18	2.70
AA-4	5	1.21	0.36	1.22	0.33	0.18	2.43
	10	1.93	0.35	0.82	0.30	0.08	2.75
	20	1.68	0.35	0.96	0.31	0.13	2.64

The attachment of four tails to the azobenzene group changed the surface behavior significantly. Comparison of the box models of **AA-4** for *trans* and *cis* states of the azobenzene groups showed similar trends in the molecular ordering (Figure 34c, Figure 41b, Table 6, and Table 8). Overall the electronic density of the focal group box was reduced 20% as the length increased slightly (<5%) for the *cis* isomer monolayer, correlating with the

larger molecular area observed for the stimulated monolayer. Compressing the monolayer to moderate surface pressure exhibited an approximate 38% elongation of the focal group box as the tail box length was reduced 6% for ambient conditions to 33% for the UV illuminated monolayer. Unlike the ambient condition monolayers, the alkyl tails attached to the *cis* isomer adopted a tilted behavior to recover the enlarged molecular area.

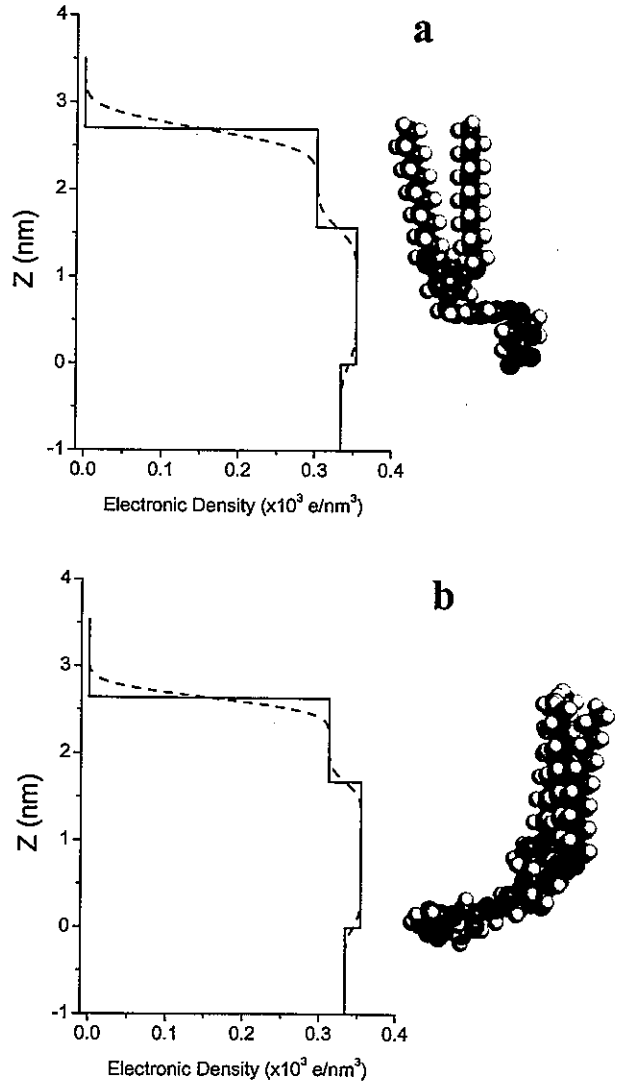

Figure 41. The electron density distribution models calculated from data shown in Figure 40 for a) AA-2 and b) AA-4 monolayers under 365 nm illumination at the highest surface pressure (left) and molecular models (right).

Photoisomerization within chemically grafted layers. Finally, the photoisomerization of the two tail molecule **AA-2** with the largest variation of cross-sectional area upon UV illumination was analyzed after chemical grafting of these molecules to the solid substrate. Direct comparison was done with epoxy-terminated single-chain molecule designed for direct chemical grafting, **AE-1**.[171] The substrate for the **AA-2** was first functionalized with a poly(ethylene imine) (PEI) monolayer using a previous reported experimental procedure to assist the grafting of the carboxyl terminated molecules.[173,174,175] The epoxy terminated reference sample formed an uniform layer with a few small hole defects (<100 nm diameter) and particle contaminants within a one micron square region. The 5.7 nm depth of the layer defects suggested a possible bilayer structure while the 2.8 nm height of the particle contaminants indicates additional molecules remained on the surface after rinsing. The **AA-2** molecule formed a similar uniform layer with significantly more, larger particle contaminants. The 3.9 nm thickness determined by AFM cross-sections indicate a grafted monolayer. As in previous studies of photoisomerization of solid support monolayers the grafted **AA-2** films exhibited a fine texture before photoisomerization that was disrupted after photoisomerization.[176]

A broad, asymmetric peak was observed at 365 nm for the grafted **AA-2** layer indicating the characteristic π-π^* absorption band in addition to a smaller peak observed at 250 nm previously attributed to the additional phenyl ring in the dendritic shell (Figure 42). The asymmetry of the peaks was attributed to constructive interference of the background peak of the PEI film. After four hours illumination of 365 nm UV light in a dark environment the absorption bands at 250 and 365 nm decreased with complete dissipation of the 365 nm peak after four days of illumination. The grafted film of the **AA-2** molecules showed weak indications of *cis* to *trans* isomerization. After two days relaxation in a dark environment the grafted films were exposed to ambient light for 24 hours to determine if relaxation would occur under dark conditions or only stimulated by favorable light. Comparison of the UV-vis spectra for the **AA-2** and **AE-1** molecules revealed the epoxy terminated reference sample had improved photoisomerization capabilities for grafted thin films.

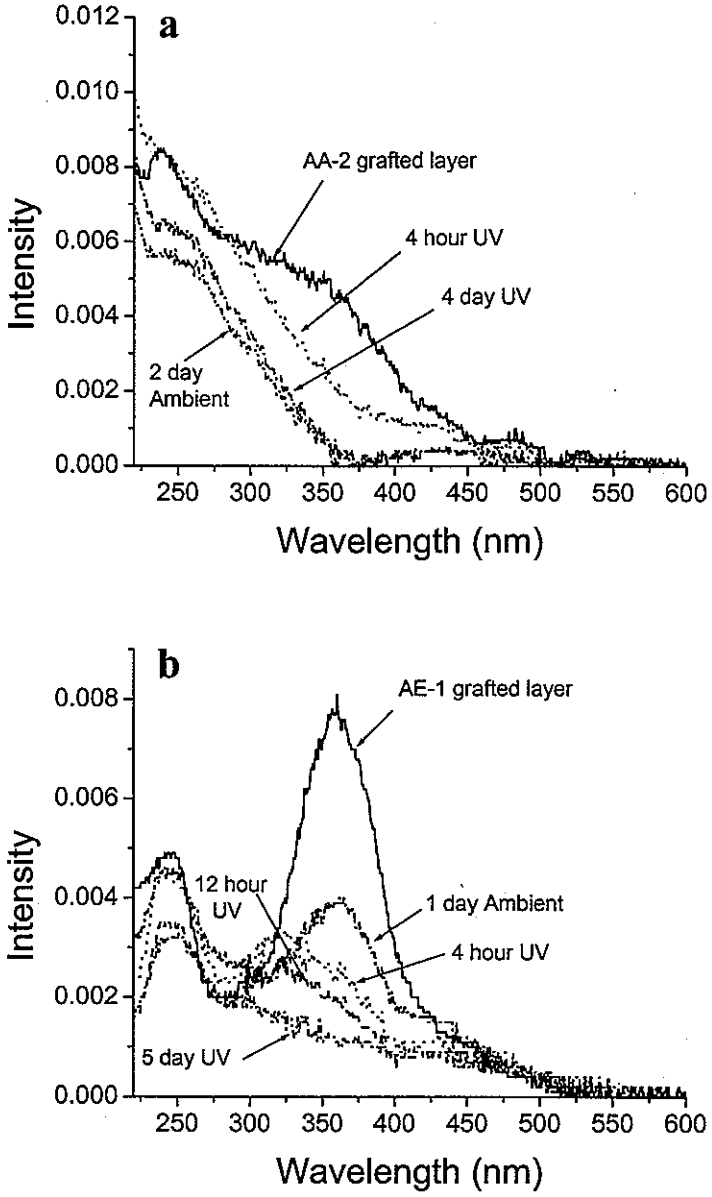

Figure 42. Kinetic studies of the photoisomerization of grafted films of a) **AA-2** and b) **AE-1**.

The grafted films of **AE-1** exhibited a broad absorption band at 365 nm corresponding to the π-π^* band and an additional band at 250 nm. After four hours illumination the peaks at 365 and 250 nm were significantly reduced and a less intense, broader peak appeared at 455 nm, signifying a nearly 80% photoisomerization of the grafted

layer (Figure 42). After five days of UV illumination the 365 nm absorption band was completely dissipate and low intensity peaks were observed at 250 and 455 nm indicating a complete transformation from *trans* to *cis* isomers. After two days relaxation the grafted film of **AE-1** underwent a partial transformation from *cis* to *trans* isomers (Figure 42). The grafted films of the epoxy terminated reference molecule achieved approximately 50% transformation after one day relaxation in ambient light.

3.3 Discussion and Conclusions of Photochromic Monodendrons

Comparison of all the photochromic monodendrons at the air-water and air-solid interfaces suggests the molecular architecture and the chemical nature of the molecular fragments controlled the ordering behavior, thereby dictating the degree of the photochromic response. The lowest generations of both molecular series exhibited the highest level of long range ordering while the intermediate generations (4 tail molecules) displayed the lowest level of ordering at interfaces. The role of the hydrophobic alkyl tails, hydrophilic polar groups and the photochromic spacer groups on the molecular ordering is examined below.

It should be noted that it has not been observed any indications of a phase transition from flat on to stand off arrangement of hydrophobic tails at different surface pressures. Rather, at low surface pressure ("gas phase") observed no indications of molecular ordering with ordered monolayer forming only at high surface pressure. This behavior is attributed to the chemical architectures of monodendron molecules with hydrophobic tails attached to the crown polar head at a single point. Indeed, this architecture does not provide for the driving forces, which can act in favor of flat-on orientation of crown heads as was suggested for several crown-containing amphiphilies.[177,178,179] Instead, the "kink" structure is formed with the polar head and azobenzene spacer being submerged in the water subphase in tilted conformation (Figure 21).

It is suggested that the presence of the long spacer (azobenzene group) between the polar head and the peripheral groups is instrumental in the ability of low-generation amphiphilic monodendrons to form ordered intramonolayer organization. A common structure for multi-tails molecules is hexagonal packing of standing-off alkyl chains and with correlation length close to 0.40 nm. To adopt this dense packing under constraints imposed

by the polar heads and chemical branching, a significant portion of the molecules is submerged in the water subphase forming a "kink" configuration while standing tails adapting staggered arrangement to fulfill constraints imposed by the chemical attachment to different branching points.

Previously it was demonstrated a large cross-sectional mismatch between a bulky polar head and varying number of alkyl tails in the dendritic shell force the molecules to adopt kinked structures to form densely packed ordered structures.[48] The single alkyl tail molecule formed a supercell orthorhombic packing structure due to the significant tilt of the alkyl tails caused the azobenzene spacer group and the bulky crown ether head alternately stack within the monolayer. As observed here, the previous molecules formed less ordered structures as the number of alkyl tails increased in the dendritic shell. It has been demonstrated the four tail molecule with a crown ether polar group reorganized in solid supported films by the disruption of oriented stripes after photoisomerization. A similar disruption in ordering was observed for grafted films of the two tail molecule with the carboxylic acid group here.[176] The homogeneous fine texture of the **AA-2** grafted films became disorganized and heterogeneous film after photoisomerization. Similar disruption in texture for crystalline phases during photoisomerization has been observed for carbosilane dendrimers in spin cast and annealed thin films.[180]

Functionalizing dendrimers with azobenzene terminal groups to improve the fragment spacing required to preserve the photoisomerization within monolayers was shown to have similar behavior as low molar weight surfactants, but had higher probability of interaction of the azobenzene groups of neighboring molecules.[181] Similar to the monodendrons shown here, the generation number of carbosilane dendrimers with azobenzene groups at the periphery had little effect on the photoisomerization of the mesogenic groups is solution.[182] The photochromic behavior of the terminal groups was affected by the crystalline structure induced by the film preparation. The amorphous structure of the spin cast films caused overlapping of the azobenzene groups of neighboring molecules forming h aggregates whereas the photoisomerization behavior in the crystalline films was similar to low molar mass compounds. Attraction between azobenzene terminal groups to interdigitate forced

highly polar cores of dendrimers to flatten and form multilaminar vesticles in solution, similar in behavior to low molar weight surfactants.[183]

The replacement of the traditional carboxylic polar head with the epoxy group increased the cross-sectional area of the molecule in addition to broadening the orthorhombic unit cell of the alkyl tails. Similar to the two lower generations of the **AA-N** molecules, the epoxy functionalized molecule formed a herringbone structure with reasonable long range ordering. Unlike the **AA-1** and **AA-2** molecules that ordered parallel to the surface normal, the **AE-1** reference molecule formed a kinked structure similar to the previously studied molecules with a larger polar group.[48a] Although the **AE-1** displayed limited molecular area differences during photoisomerization in Langmuir monolayers, the photoisomerization of the grafted layers of epoxy terminated reference molecule was more successful than for the **AA-2** molecule.

In addition to the variance of molecular area during photoisomerization, it was directly observed the *trans-cis* photoisomerization in a Langmuir film *in situ* using X-ray reflectivity. The 8% increase in molecular area observed for *cis* **AA-2** reduced the monolayer thickness as the molecule kinked, thereby disrupting the perpendicular orientation of the entire molecule. Unlike the two tail molecule, the **AA-4** molecules displayed less molecular rearrangement due to the cross-sectional area controlled by the four alkyl tails. The area available for the focal group is twice the required space, therefore the fragment reorientation had little effect on the monolayer structure. The packing density of the azobenzene fragment in Langmuir-Blodgett monolayers has been shown to affect the degree of photoisomerization of the surface films.[42] Although the larger dendritic shell preserved the cross-sectional area for the photoisomerization it limited the observed effect due to the cross-sectional mismatch greatly favoring the alkyl tails.

The influence of the dendritic shell containing multiple dodecyl tails has been discerned to assert a great effect on the higher generations versus the influence of bulky azobenzene spacer group which affect the lower generations. The influence of the azobenzene is directional determined by the decrease in the *b* lattice parameter upon the increase in the alkyl shell from one to two tails. The four and eight tail molecules formed uniform monolayers with limited short range ordering seen in liquid and solid supported

films. The highest generations adopted a kinked structure with the alkyl tails parallel to the surface normal while the focal group was tilted a large degree toward the surface as seen as an overall decrease in effective thickness of deposited films.

All molecules were capable of repeated photoisomerization in dilute solutions under preferential light conditions. At the air-water interface the two tail molecule possessed the ideal cross-sectional mismatch that facilitated the *trans* to *cis* isomerization and retained the mobility for the *cis* to *trans* isomerization for specific stimuli. The **AA-4** and **AE-1** molecules exhibited a limited photoisomerization response at the air-water interface. Conversely, kinetics studies of grafted thin films revealed that although both the **AA-2** and **AE-1** molecules showed complete *trans* to *cis* isomerization, only the epoxy terminated reference molecule was observed to partially transform from *cis* to *trans*. The importance of the range of mobility of the molecules was shown in the increased time scale of the kinetics experiments from dilute solutions to liquid supported monolayers to thin films grafted to solid substrates.

The flexible discotic core balances the increasing number of hydrophobic alkyl tails with little influence on the lateral packing structure of the tails past the second generation. The cross-sectional mismatch in the first generation creates the large tilted structure of the alkyl tails. The cross-sectional mismatch creates a dense packing structure for polar discotic cores with a lower than usual density of the tail box. The tails compensate by tilting toward the surface in order to form a close packed structure. The attraction between the alkyl tails forces them to tilt nearly 60° from the surface normal to retain the orthorhombic packing structure of the tails. Surprisingly the large tilt tails only slightly enlarges the orthorhombic unit cell. The correlation lengths indicate the molecules form domains tens of nanometers across. The reflectivity data however suggests the **AD12-1** molecules form domains with gaps between the domains.

The degree of branching severely effects the formation of an ordered monolayer. While the cross-sectional mismatch favors the alkyl tails in the higher generations, the lowest generations clearly maintains the ordered packing structure for far greater lengths. The tails for the lowest generation are tilted nearly 60° from the surface normal to achieve a densely packed unit cell. The large degree of tilt is eliminated for the higher generations due to the

reduction in cross-sectional mismatch. The additional of alkyl tails with the increase in the generation number reverses the cross-sectional mismatch between the discotic core and the alkyl tails to be in favor of the branched tails. Increasing the number of tails per molecule raises the density of the layer, eliminating the need for the tails to tilt toward the air-water interface. The correlation lengths decrease significantly with the generational increase in the number of tails. The second and third generation form quazi-hexagonal lateral structures. The highest generation forms a regular hexagonal packing structure with an increase in the correlation length of the peak over the third generation.

CHAPTER 4. RESULTS – LIQUID CRYSTAL TERMINATED CARBOSILANE DENDRIMERS

The molecular ordering of two generations of carbosilane dendrimers with LC terminal groups was examined to ascertain the influence of generation and core nature. Additionally, the LC terminal groups were varied from a mixed shell for the third generation molecule to a full shell of either CB or BPB groups to analyze the role of the shell nature on the packing structure. The competing core nature and shell nature was studied to resolve the stronger influence on the molecular ordering in surface films.

4.1 Surface Films on Hydrophilic Substrates

The measured effective thickness of the three monolayer samples for all three molecules was considerably lower than the diameter of the molecules determined by molecular models (around 12.9 nm for fifth generation molecules, see below) (Table 9). The effective thickness of the surface layer of G-5(Und-But)$_{128}$ varied from 2.1 nm to 6.1 nm depending upon deposition conditions with a similar trend in film thickness observed for G-3(Und–PH-But-70%) molecules (Table 9). Dissimilarly, G-5(Und-CB)$_{128}$ molecules formed the thinnest layers (1.7 nm to 3.0 nm), lacking a discernable trend in film thickness. The uniformity of these films and their internal microstructure were probed with AFM. The thickness of surface layers well below the unperturbed, symmetrical diameter of molecules indicated their pancake conformation after deposition on the hydrophilic silicon substrate.

The G-5(Und-But)$_{128}$ films had a peculiar microscopic surface texture with regularly spaced circular surface areas with elevated height (0.3nm above surrounding film) and an average diameter of 350 nm occupying 17% of the monolayer surface (Figure 43a). 2D Fourier transform indicated a very weak, short-range ordering of these circular elevations. The small height of the circular domains conflict with the idea of a thicker film expected with the molecular dimensions but signify more condensed packing of the molecules. Closer examination of the surface film surrounding these areas revealed an internal lamellae structure with weak but visible regular spacing (Figure 43b, right). The interlamellar spacings calculated from cross-sections of the AFM images were within 5.4 to 5.9 nm for

films prepared under different conditions (Table 9). These periodicities are well below the overall molecular diameter determined from the models (12.9 nm), but slightly larger than the diameter of the G5 carbosilane core itself (5.3 nm) (Figure 44).

Table 9. The effective thickness, *t*, of the surface films of LC carbosilane dendrimers and the corresponding d-spacings.

Sample #	Substrate	*t*, nm	d, nm
G-5(Und-But)$_{128}$			
1	Si	2.2±0.2	5.7±0.4
2	Si	3.5±0.1	5.4±0.1
3	Si	6.1±0.2	5.9±0.4
4	OTS	0.3±0.2	
G-3(Und–PH-But-70%)			
1	Si	2.5±0.2	6.2±0.4
2	Si	3.8±0.1	5.2±0.5
3	Si	5.5±0.4	NA
4	OTS	0.4±0.1	NA
G-5(Und-CB)$_{128}$			
1	Si	1.7±0.5	NA
2	Si	3.0±0.1	NA
3	Si	1.6±0.2	NA
4	OTS	0.2±0.1	NA

High resolution AFM imaging revealed that the surface areas of condensed packing had similar nanostructure with internal lamellae as the more loosely packed monolayer surrounding them for G-5(Und-But)$_{128}$ films (Figure 45). Although the layered ordering appears to be slightly denser than the layer outside the circular domains with increased height the interlamellar spacing remains within the margin of error (Table 9). The grain nanostructure are packed with stacks of 3 - 6 correlated lamellae with spacing of 5.4-5.9 nm. Abrupt change of orientation was observed for lamellar stacks with correlated defects propagating across multiple lamellae (Figure 454b,c). Cross-sectional analysis of the lamellae structure revealed an undulating height along the lamella with weakly defined modulation of 10 nm.

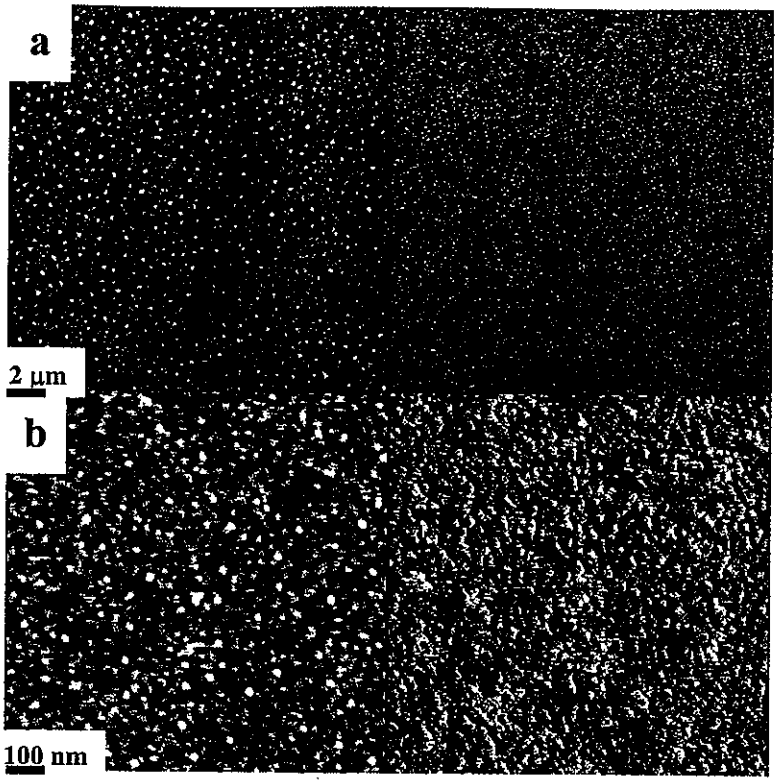

Figure 43. Irregular ordering of the condensed areas for the surface films of G-5(Und-But)$_{128}$ on hydrophilic silicon substrate. Topograpy image shown on left and phase image shown right. Z-range a) 5 nm (topography), 20 degrees (phase), and b) 5 nm (topography), 5 degrees (phase).

For the thicker surface films of the G-5(Und-But)$_{128}$ molecules on the hydrophilic silicon substrate the formation of smaller point-like domains of considerable height was observed (Figure 46a). The 4.4 nm thick domains with the average diameter of 100 nm were composed of several irregular regions with lamellar ordering which was better defined than for surrounding surface areas (Figure 46b). The inter-lamellar spacing for these surface areas was 5.1 – 5.7 nm, closely resembling that observed for thinner surface films (Table 9). The spacings observed here were comparable with the intermolecular spacings calculated from X-ray diffraction.[184]

Similarly, the surface films for the G-3(Und–PH-But-70%) molecules showed a microscopic surface texture with the circular surface areas of a similar height as seen for the larger molecule (Figures 47a). Upon further scrutiny a comparable nanostructure of small

grains composed of poorly ordered internal lamellae was observed (Figure 47b). The inter-lamellar spacings for the G-3(Und–PH-But-70%) monolayers were within 5.2 – 6.4 nm (Table 9). The comparison of the overall molecular diameter (10.7 nm) and the core diameter (3.4 nm) suggest deviation from simple symmetrical shape as will be discussed below. The fabrication of thicker surface films from G-3(Und–PH-But-70%) molecules made the film surface more uniform (not shown).

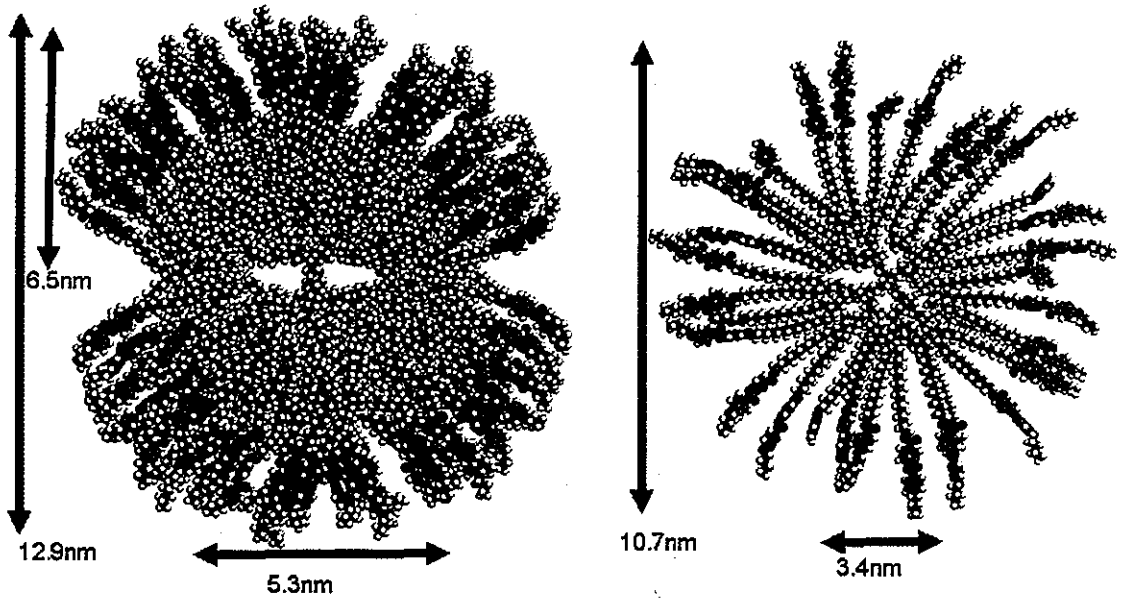

Figure 44. Molecular model of G-3(Und–PH-But-70%) and G-5(Und-But)$_{128}$ in symmetrical conformation.

Comparison of the molecular models with the film thickness and the d-spacings of the lamellae structure indicates that a simple spherical model with symmetrical extension of the branches does not fit to the experimental facts. The compression of the dendrimer molecules into a flattened oblate shape is required to agree with the experimental data. The in-plane lamellar structure observed with d-spacing equal to approximately half of the molecular diameter can be formed if the laterally compressed molecules are staggered in the alternating manner as demonstrated in Figure 48. Such molecular arrangement creates running ridges of the densely packed terminal groups separated by grooves with spacing between neighboring grooves formed by depleted densities of the central cores of about 6 nm wide. In addition, a

modulation along the ridges with periodicity about 10 nm is formed. The layered structure with these molecular dimensions suggests a highly compressed dendrimer core and layered packing of polar terminal groups in a close contact with the hydrophilic silicon surface. Very flat arrangement of dendrimer molecules makes them incommensurate with lamellar spacing observed in the bulk state, thus suggesting more complicated layered packing (Figure 48).

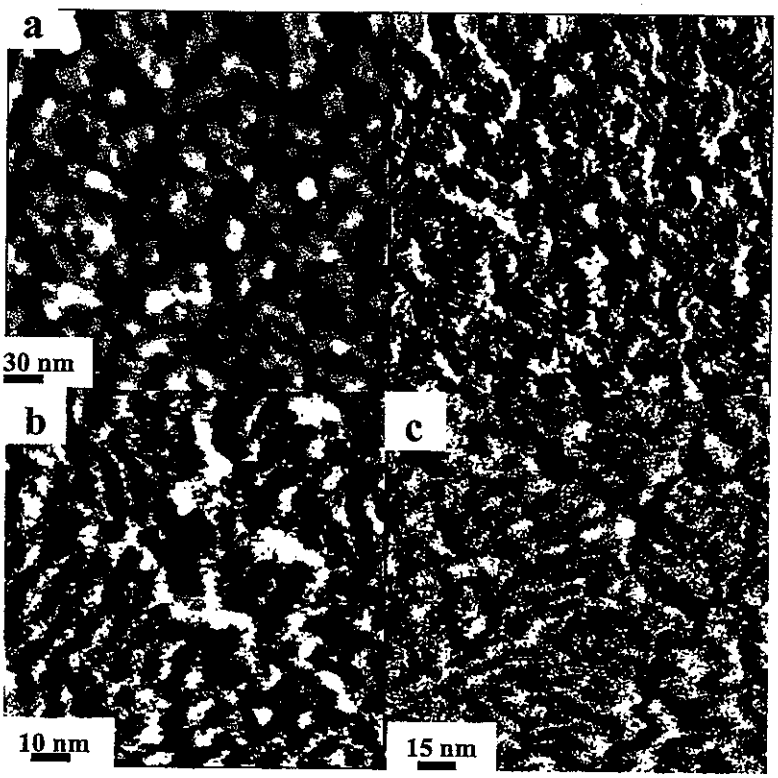

Figure 45. The grain nanostructure with internal lamellae of 2.2 nm surface films of the G-5(Und-But)$_{128}$ molecules is easily discerned from the high resolution AFM image a) within condensed area, b) and c) phase images demonstrating the short range ordering observed at highest resolution. Z-range for images: topography 5 nm (left), phase 10 degrees (right).

The molecular model should include lateral compression of the molecule in addition to the oblate conformation of the molecules. It is suggested that the terminal LC groups form dense layered structures that exerted constraints upon the core perpendicular to the ordering direction. The flexible core rearranged from a flattened radial shape to a compressed elliptical orientation with the terminal groups aligned in the major axis direction (Figure 48).

The dominant polar interactions between the terminal groups and the substrate reduced the influence of the dendrimer cores making them flat with the effective thickness of the molecules about 3 nm.

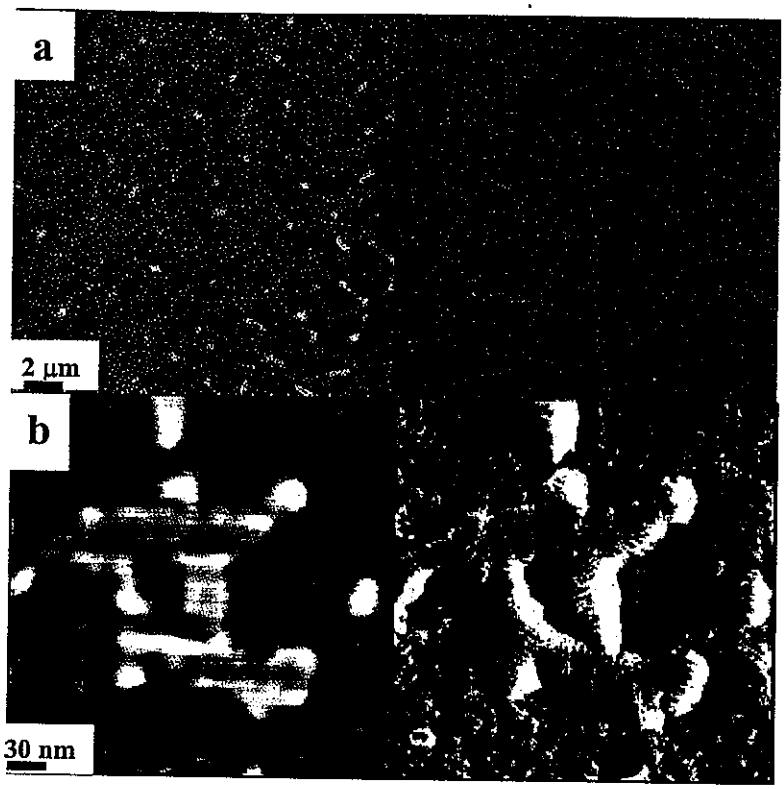

Figure 46. a) Bilayer formation of G-5(Und-But)$_{128}$ observed as small point like domains for 3.8 nm thick surface films. b) High resolution AFM revealed the internal structure of the domains to be similar to the underlying monolayer. Topography image (left) and phase image (right) with z-range of a) 20 nm (topography), 20 degrees (phase) and b) 20 nm (topography), 15 degrees (phase).

The divergence in chemical composition of the fifth generation molecules caused by replacing the butoxyphenylbenzoate terminal groups with more polar but shorter cyanbiphenylic terminal groups disrupted completely the lamellar ordering within the surface films. In contrast, the G-5(Und-CB)$_{128}$ molecules formed uniform surface films with no indication of internal ordering and much lower surface microroughness (not shown). The thickness varied within 1.6-3.0 nm (Table 9). Here, it is suggested that lower tendency to

form stable bilayer packing of cyanbiphenyl groups shifts the balance and prevents the layering of the terminal groups confined by the radialyl symmetrical dendritic cores. In fact, independent studies suggested although both mesogenic terminal groups have tendencies to form smectic structures the shorter cyanbiphenyl groups are more prone to form less ordered states such as nematics with lower thermal stability.[185,186] Cyanbiphenyl groups are known for their tendency to form nematic phases and weak layered phases due to strong dipole-dipole interactions but very short rod-like shape. Unlike, phenylbenzoate groups form very strong bilayer packing due to a steric effect (longer rod shape) and additional enthalphic contribution (phase separation between polar central fragments and hydrophobic alkyl tails).[187]

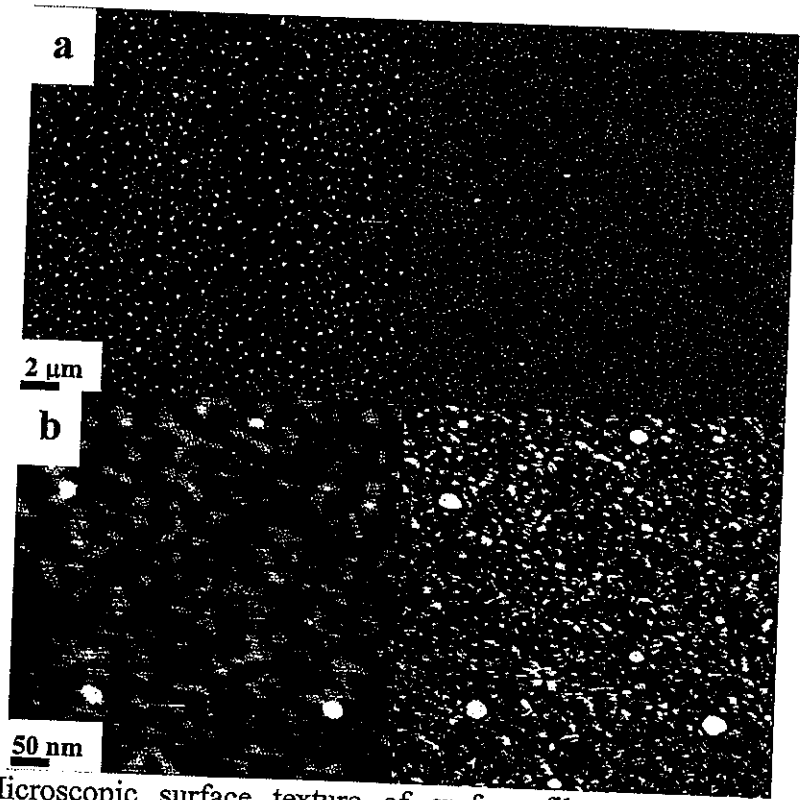

Figure 47. Microscopic surface texture of surface films of G-3(Und–PH-But-70%) molecules on hydrophilic silicon substrate with irregularly ordering areas of condensed packing. Topography image (left) and phase image (right) with z-range of a) 5 nm (topography), 20 degrees (phase) and b) 5 nm (topography), 5 degrees (phase).

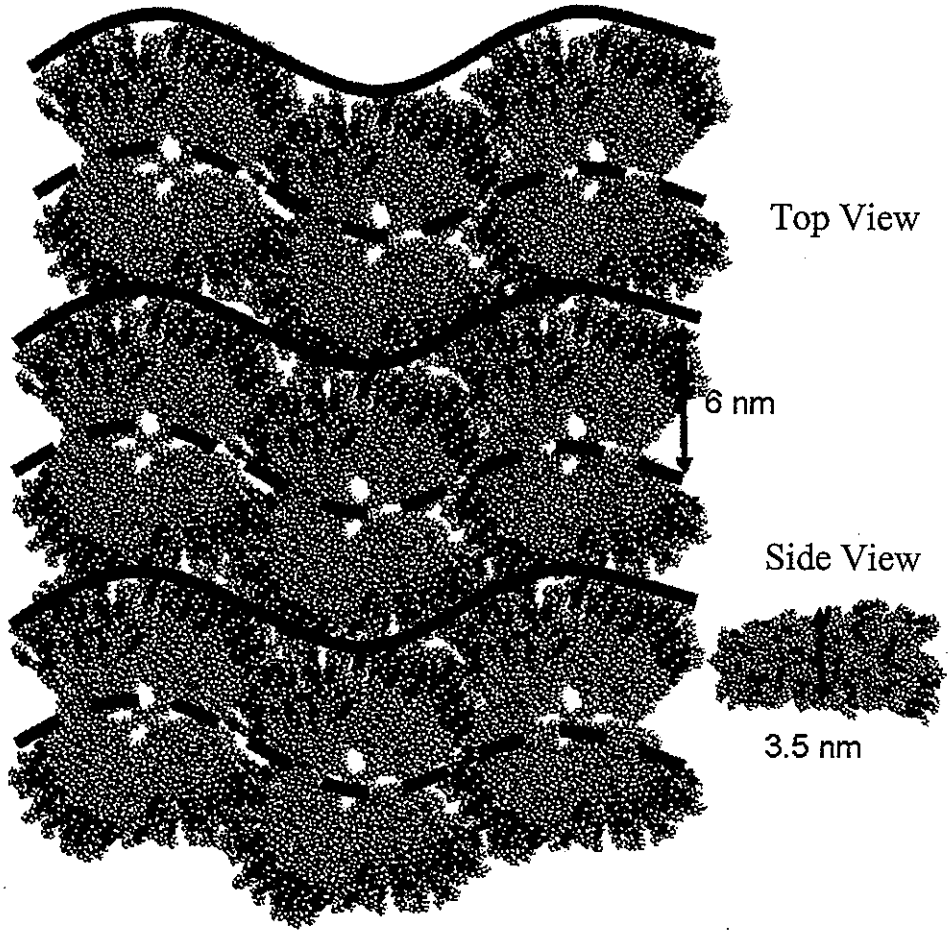

Figure 48. Molecular model of staggered layered ordering of flattened G-5(Und-But)$_{128}$ molecules (topview) and a side view of an individual molecule (right).

The molecular ordering of the G-5(Und-CB)$_{128}$ on hydrophilic silicon oxide (amorphous) and mica (crystalline) substrates was previously studied by Ponomarenko et al.[188] The film thickness in this study varied from very thin comparable to surface films studied here (3 nm) to very thick films with 100 nm thickness. The authors observed that the spin-cast films on silicon formed a network-like morphology that non-uniformly covered the surface as a result of intensive dewetting of hydrophobic material on the hydrophilic substrate. Individual molecules with a diameter of 5.5 nm were observed forming short-range rectangular and hexagonal ordering within the 3 nm thick domains. The molecular ordering was found to be much more pronounced on the mica substrate with 4.7 nm spacing between molecules inside the columns and 5.7 nm spacing between neighboring columns.

The ordering transitioned from rectangular to hexagonal ordering upon annealing of the macromolecular layers on the mica. Thus, similar dendrimer molecules deposited on highly crystalline mica substrates formed lamellae nanostructures with short range ordering similar to that observed for the G-5(Und-But)$_{128}$ molecules on the hydrophilic silicon substrates.[185,186] This difference in surface organization points out to a critical role of the crystalline and charged mica surface in the ordering of highly polar terminal groups of the LC dendrimers. Apparently, the replacement of this highly ordered substrate studied before with the amorphous silicon dioxide in this study shifts the interfacial balance toward a less organized surface structure of the CB-containing dendrimers. The G-5(Und-CB)$_{128}$ molecule lacked similar ordering in bulk structures at room temperature supporting suggestion that the layered ordering seen for the surface films was initiated by the crystalline ordering of the supporting substrate.[189]

4.2 Surface Films on Hydrophobic Substrates

Unlike the films discussed above, the surface films on the hydrophobic surfaces with very small effective thickness lacked indications of layered ordering (Table 9, Figure 49a). However, G-3(Und–PH-But-70%) molecules showed grainy texture and round doughnut nanoscale features were revealed at higher resolution images (Figure 49b). These round features possess diameter of 10 ± 2 nm which is fairly close to that expected for G-3(Und–PH-But-70%) molecules in flattened conformation indicating that individual dendrimer molecules were observed (Figure 44). The elevated rim is formed by the bulky terminal groups and the dendrimer core formed a thinner central area. Obviously the tendency of the terminal cyanbiphenyl groups to layering is overpowered by a core trend to induce their symmetrical arrangement favoring hydrophobic-hydrophobic interfacial interactions.

4.3 Discussion and Conclusions of Carbosilane Dendrimers

In conclusion, the different molecular packing was revealed for the LC carbosilane dendrimers with 128 strong polar cyanbiphenyl groups and polar butoxyphenylbenzoate groups within molecularly thin surface films. The dendrimers with 128 butoxyphenylbenzoate terminal groups was observed formed organized layered structures

caused by the phase separation of the flexible cores and mesogenic terminal groups and the strong trend of the latest to form bilayer packing. The dilution of the outer mesogenic shell with a non-mesogenic component partially disturbed the layered packing within monolayer.

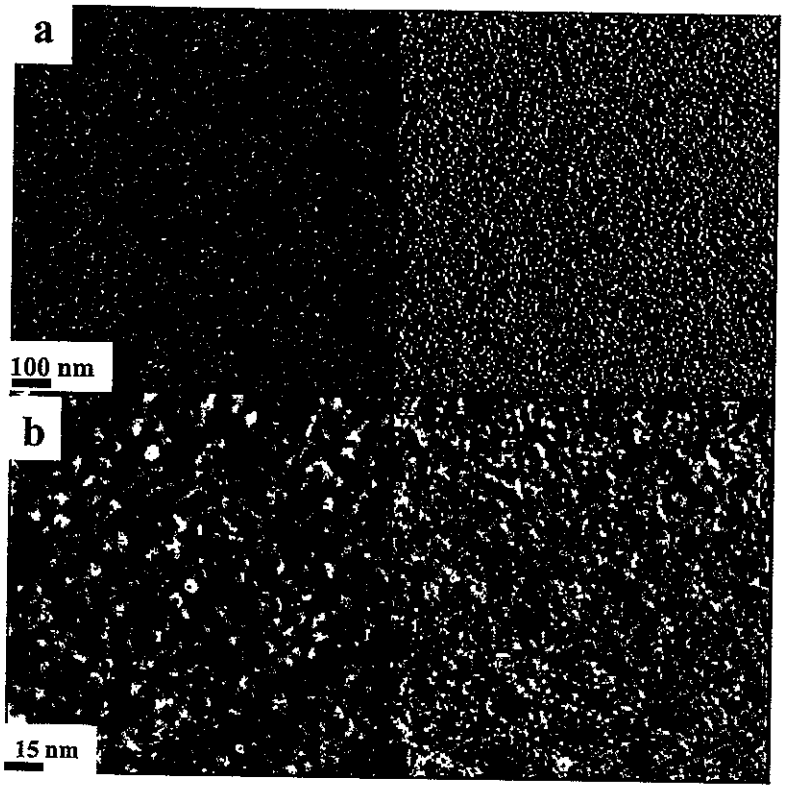

Figure 49. Surface films on a hydrophobic surface: a) Uniform microscopic texture of the G-5(Und-But)$_{128}$ molecules, b) finer grainy texture of the G-3(Und–PH-But-70%) surface films with circular molecular shapes. Topography image (left) and phase image (right) with z-range of a) 5 nm (topography), 5 degrees (phase), b) 2 nm (topography), 5 degrees (phase).

Complete disruption of the regular lamellar ordering was observed if butoxyphenylbenzoate terminal groups are replaced with shorter and more polar cyanbiphenyl groups with less stronger trend toward layered (smectic) ordering. The adsorption on the hydrophobic surface does not result in the formation of dense surface layers due to antagonistic interactions between highly polar terminal groups and a methyl-terminated surface. Moreover, a circular shape of the dendrimer molecules with

cyanbiphenyl terminal groups demonstrated that the dendritic core dominated molecular ordering making symmetrical round ordering preferable for dendrimer molecules with highly hydrophobic cores.

CHAPTER 5. RESULTS – STAR POLYMERS

Two series of star polymers were studied to elucidate the influence of volume fraction and core nature on the molecular ordering at interfaces. The first series contained twelve alternating hydrophobic and hydrophilic polymeric arms on aromatic core. The effect of the volume fraction was examined by comparison of a larger, asymmetric star polymer with a smaller, symmetric star polymer. The second series was composed of six block star copolymer samples and a linear block copolymer reference sample. Similar to the 12-arm star polymer series, the influence of volume fraction of competing polymeric blocks was examined to understand the molecular reorganization at interfaces. The role of the core nature was studied by comparing the interfacial behavior of the 12-arm star polymers and the block star copolymers.

5.1 Twelve-arm Star Polymers

Two 12-arm star polymers composed of six PS and six PAA arms alternately attached to a hexa-functionalized aromatic core were studied at interfaces (Figure 7). The length of the polymeric arms varied from 25 mers each to 40 mers per PS arm and 30 mers per PAA arm. The amphiphilic nature and molecular ordering of the 12-arm star polymers was studied at the air-water interface. The ordering behavior of the 12-arm star polymers was further examined at the air-solid interface. The role of the volume fraction of the polymer blocks, the alternating attachment of the 12 arms, and the symmetry of the polymeric blocks was analyzed.

5.1.1 Molecular Ordering Behavior at the Air-water Interface

Both heteroarm star block copolymers studied here possess well defined star shape with dissimilar arms attached to the rigid, shape persistent core as visualized by molecular models presented in Figure 7. In an extended conformation and face-on orientation, the molecules occupy very large surface areas with the diameter of 17 and 24 nm for $(PAA_{25})_6$-s-$(PS_{25})_6$ and $(PAA_{30})_6$-s-$(PS_{40})_6$ molecules, respectively (Table 10). In this conformation, the rigid core

occupies a small surface area as compared to polymer arms and significant free surface is available between adjacent arms.

These molecules formed stable Langmuir monolayers at the air-water interface and showed the classical pressure versus molecular area (π~A) behavior without any significant plateau at intermediate pressures (Figure 50). This shape of the isotherms indicated an absence of any significant structural rearrangements within compressed monolayer usually observed for amphiphilic block copolymers with comparable composition (content of hydrophilic block of about 30%, Table 10). Detectable increase in the surface pressure was observed for the surface area per molecule below 20 nm^2 that is much smaller than the surface area per molecule estimated for extended conformation and face-on orientation (Figure 7). This indicates significant overlap of the molecules upon compression or reorganization of their conformation under very low pressures.

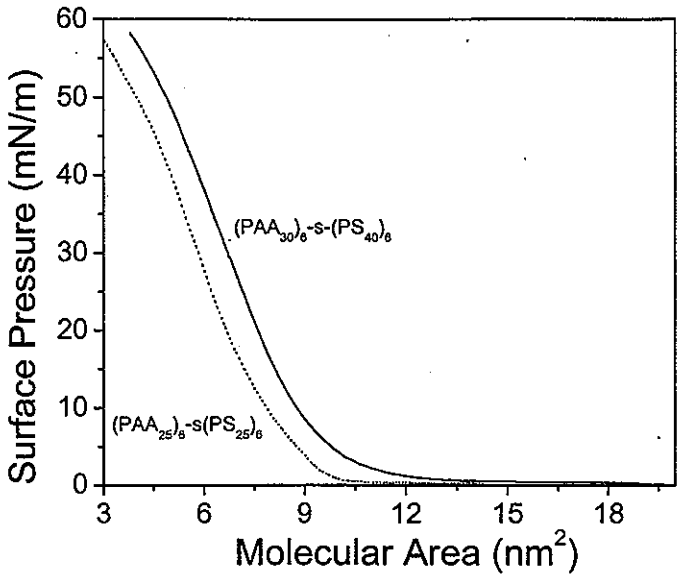

Figure 50. π~A isotherm of $(PAA_{30})_6$-s-$(PS_{40})_6$ (solid line) and $(PAA_{25})_6$-s-$(PS_{25})_6$ (dashed line).

The steady growth of pressure as the cross-sectional area decreased with the limiting value for $(PAA_{25})_6$-s-$(PS_{25})_6$ star slightly lower (9 nm^2) than that for $(PAA_{30})_6$-s-$(PS_{40})_6$ star (10 nm^2) (Figure 50). These values are close to the cross-sectional area of the rigid core region (shown in Figure 7 as dashed circle) calculated to be 9.6 nm^2 (excluding the space between adjacent arms) for either 12-arm star polymer. The very modest increase in cross-sectional area for the larger asymmetric star molecules and very similar shape of the isotherms indicated the molecular packing is only slightly affected by the bulkier PS chains. On the other hand, both values are close to the core area indicating that dense lateral packing of rigid cores is a defining factor in the formation of condensed monolayer with both types of arms playing a minor role at highest packing densities (Figure 7).

Table 10. Molecular dimensions of the 12-arm star polymers.

	$(PAA_{30})_6$-s-$(PS_{40})_6$	$(PAA_{25})_6$-s-$(PS_{25})_6$
Core Diameter (nm)	4.2	4.2
Total Diameter (nm)	23.9	17.4
PS extended length (nm)	10.0	6.6
PAA extended length (nm)	8.7	6.8
PS end-to-end distance (nm)	2.3	2.0
PAA end-to-end distance (nm)	1.9	1.8
Area of core (nm^2)	9.6	9.6
A_o (nm^2)	10.0	9.1
Area of coiled PS arm (nm^2)	2.2	1.6
Area of coiled PAA arm (nm^2)	1.6	1.3
Volume of PS arm (nm^3)	6.5	4.1
Volume of PAA arm (nm^3)	3.1	2.6
PAA volume fraction	0.29	0.35

This interfacial behavior under compression suggests that the PAA and PS arms are disassociated from the plane of the core upon compression to the condensed state (see a simple model with oppositely extended arms in Figure 7). It is clear that actual state of the arms is different from this simple molecular graphics representation and should include different levels of ordering. Considering this surface behavior and the architecture of the star molecule and literature data, it is reasonable to expect that hydrophilic PAA arms were submerged into the water subphase whereas the hydrophobic PS arms are packed above the air-water interface, effectively pinning the core plane. The calculated cross-sectional area on the larger PS arms in coiled state was 2.17 nm^2 per arm while the shorter PS arms should occupy 1.63 nm^2 (Table 10). Taking into account the six PS arms attached to each aromatic core, the cross-sectional area per molecule with coiled arms for $(PAA_{30})_6$-s-$(PS_{40})_6$ was estimated as 13.1 nm^2 and 9.8 nm^2 for $(PAA_{25})_6$-s-$(PS_{25})_6$, which is close but still below the onset of formation of the condensed monolayer.

The decrease in cross-sectional area below these values should force the flexible arms to elongate in the vertical direction thereby decreasing the effective cross-sectional area per molecule. However, it was suggested that the transformation to truly brush-like packing regime is not possible in this system due to the presence of rigid disk-like core limiting effective grafting density of flexible chains to 1.6 nm^2/chain. It is important to emphasize that

arms are not emanating from one and the same point as usually happens in conventional star polymers but rather from six equidistant peripheral points of a fairly large and rigid core (4.2 nm) that keeps the junction points of arms spatially separated. In addition, considering that the PS block at room temperature is well below the glass transition (even accounting for low molecular weight and possible presence of trapped residual solvent), the mobility and compressibility of the PS phase will be severely limited, it is safe to suggest that the state of PS blocks will stay virtually unchanged. As a result, even at high pressure the PS arms will stay in a collapsed state covering the aromatic core. The same limitation is imposed by the core on the hydrophilic PAA arms submerged in the water subphase but because of their dissolved state they remain mobile enough to change their state (to that allowed by the limiting grafting density) under compression. It was suggested that this key difference between the star-shaped molecules with sizeable rigid core and diblock amphiphiles that do not have the incompressible core and therefore can undergo the pancake-brush transformation at high surface pressures defines the shape of the Langmuir isotherms observed here. In order to corroborate this hypothesis and to obtain insights into the structure of the monolayers, X-ray reflectivity measurements and AFM imaging were used as discussed below.

Because the data for star molecule with shorter arms were not sufficient quality, the discussion below will concentrate on the $(PAA_{30})_6$-s-$(PS_{40})_6$ molecules. The X-ray reflectivity curves for this molecule displayed multiple minima at all surface pressures (Figure 51). X-ray reflectivity measurement for the larger 12-arm star polymer before compression showed three well-defined minima signifying an organized monolayer formation. At higher surface pressure, the minima became more defined and the spacing decreased indicating an increase in monolayer thickness and the chain elongation (Figure 51). The overall angular variation of intensity decreased much faster at higher pressures which suggested the sharpening of the monolayer interfaces. These results demonstrate that the $(PAA_{30})_6$-s-$(PS_{40})_6$ molecules formed dense uniform monolayers at all pressures with the overall thickness increasing as the surface pressure is raised.

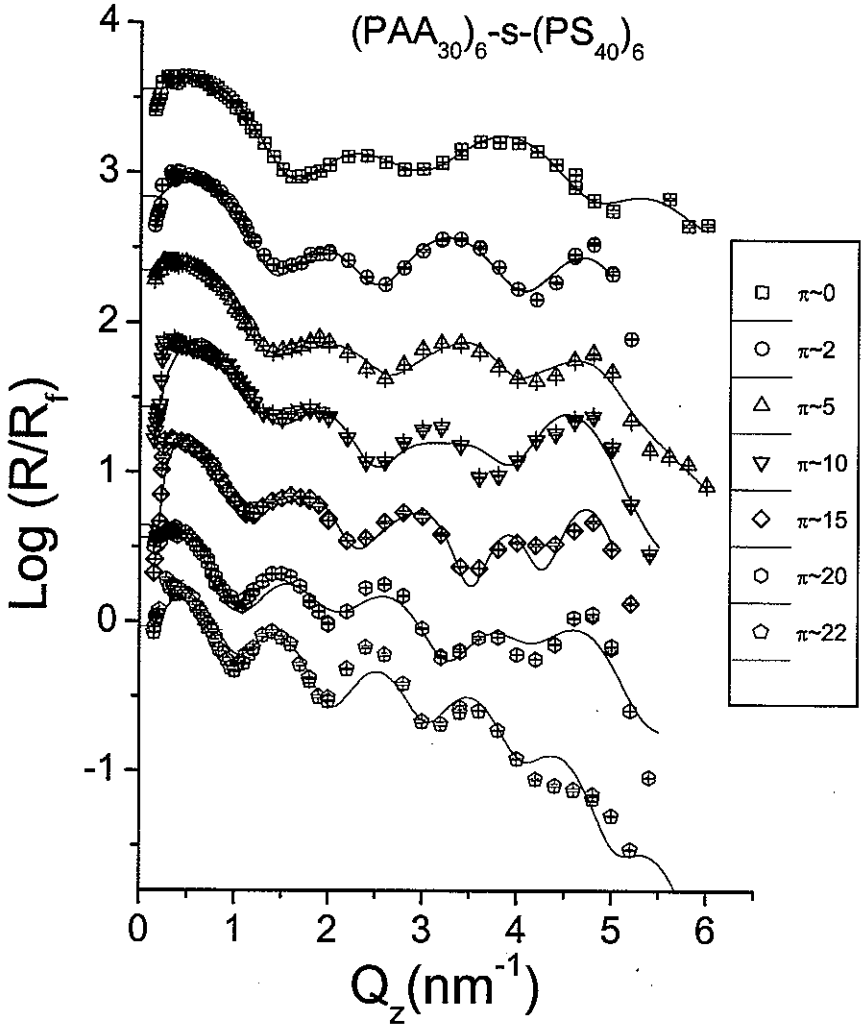

Figure 51. X-ray reflectivity data and model for $(PAA_{30})_6$-s-$(PS_{40})_6$ at different surface pressures. Data represented by symbols and model represented by line. Intensities offset for clarity.

The reflectivity data were modeled using a four box model as presented in Figure 52 along with examples of spread and compressed molecules built with consideration of most critical parameters (overall thickness, separate thicknesses of PS and PAA phases, and cross-sectional area per molecule) (Table 11). These boxes with constant electron density represented the submerged PAA chains, the core region, the mixed collapsed and the extended PS chains.[190] At low surface pressure and large cross-sectional area electron density

distribution confirmed a clearly organized monolayer with defined layered structure. The slight difference in electronic density at the water surface for the first two blocks ($0.365x10^3$ and $0.368x10^3$ e/nm^3 respectively) corresponding to PAA arms and the aromatic core indicated a slight shift in density of the polymeric chains. The confinement of the hydrophobic aromatic core within a plane created a densely packed layer above the hydrophilic PAA chains. Considering the thickness of the first box of 1.25 nm close to the PAA chain dimensions (Tables 10, 11), it can be suggested that the hydrated PAA chains are randomly coiled underneath the aromatic core (Figure 52a). The densest region of the film was located near the air-water interface associated with the aromatic cores (second box, Table 11). The PS chains (third box) formed a dense layer of 1.7 nm thick above the water surface which is close but slightly lower than the PS random coil size and indicates the collapsed state of the PS chains with density close but slightly below to that for the bulk PS. The presence of the fourth box with extremely low electron density ($0.048x10^3$ e/nm^3) indicated the extension of some PS chains beyond the collapsed PS layer (Figure 52a).

Table 11. Comparison of box model parameters of PAA_6-*b*-PS_6 star polymer

Box Model Parameters		Surface Pressure (mN/m)				
		0	2	10	20	22
First Box	Length (nm)	1.25	1.36	2.77	3.24	6.25
	Electronic Density ($x10^3$ e/nm^3)	0.365	0.377	0.376	0.362	0.386
Second Box	Length (nm)	1.05	1.60	1.77	--	--
	Electronic Density ($x10^3$ e/nm^3)	0.368	0.387	0.575	--	--
Third Box	Length (nm)	1.75	1.76	1.48	2.72	--
	Electronic Density ($x10^3$ e/nm^3)	0.315	0.327	0.331	0.317	--
Fourth Box	Length (nm)	1.11	0.934	1.65	1.37	1.55
	Electronic Density ($x10^3$ e/nm^3)	0.048	0.068	0.108	0.053	0.05
Surface Roughness (nm)		0.20	0.173	0.264	0.281	0.28
Total Thickness (nm)		5.16	5.65	7.67	7.33	7.8
PS Thickness (nm)		2.86	2.69	3.13	3.18	3.09

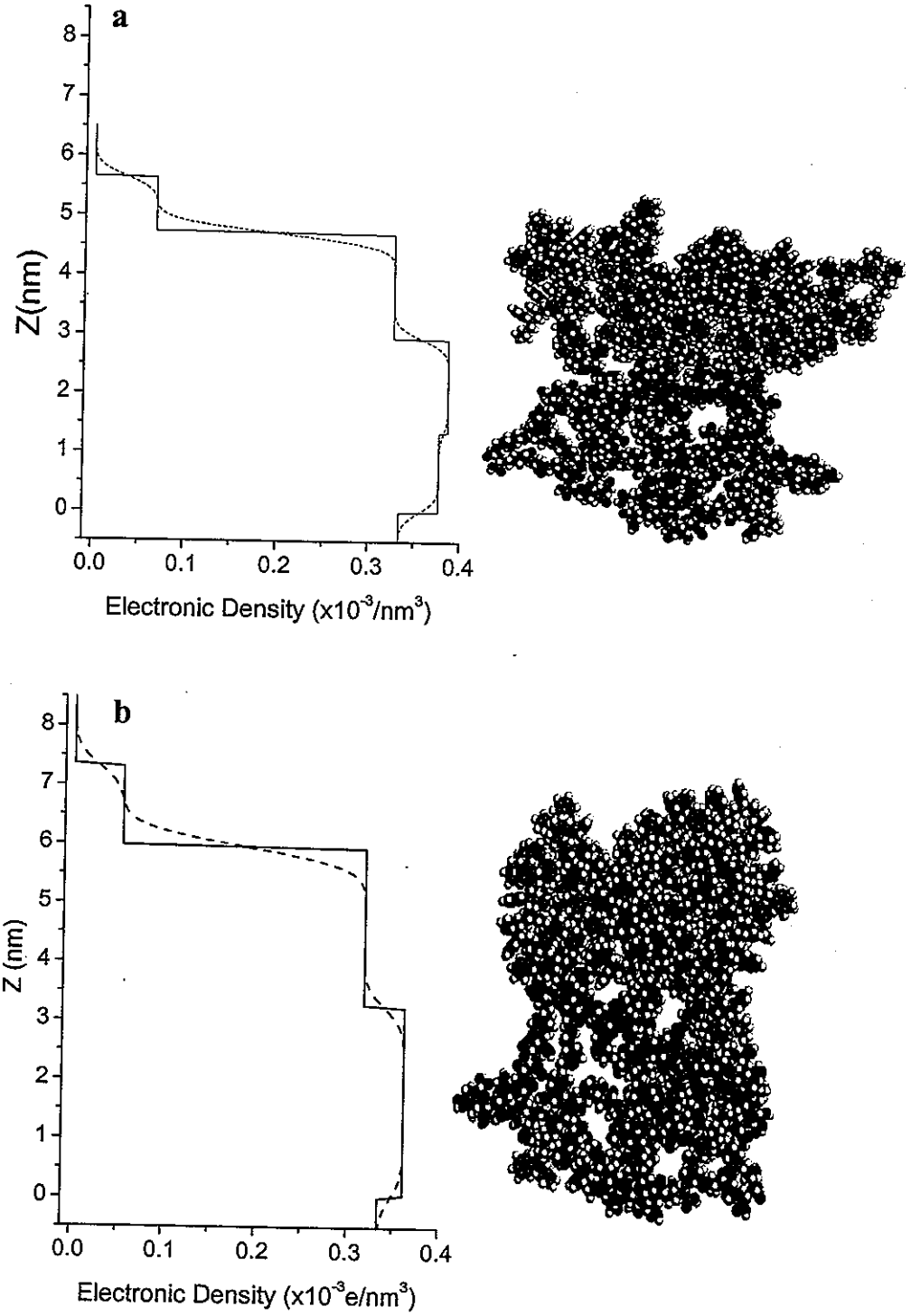

Figure 52. Box models of $(PAA_{30})_6$-s-$(PS_{40})_6$ at a) low pressure regime (2 mN/m) and b) high pressure regime (20 mN/m). Corresponding molecular models shown to the right.

Upon compressing the monolayer to the low pressure regime (from 0 to 2 mN/m) the four box model showed an overall increase in length and electronic density for all boxes indicating the monolayer became more densely packed as the chains elongated. The overall thickness increased from 5.2 nm for the monolayer before compression to 5.7 nm at 2 mN/m (Table 11). The cross-sectional area decrease forces the chains to elongate slightly in the vertical direction to compensate for the overall decrease in area. More significant, all four boxes increased in electronic density with a clearer distinction between the first two boxes. These two boxes containing the PAA chains became slightly denser although the boxes lengthened moderately (from 1.05 nm to 1.60 nm for the second box) while the third and fourth boxes containing the PS chains remained with similar thickness while increasing in density.

The overall thickness of the Langmuir monolayer as well as the density increased for all layers as the surface pressure increased from 2 mN/m to <20 mN/m as was indicated above (Figure 52, Table 11). At the intermediate pressures, the monolayer was modeled using four box models with the steadily increased thickness and electronic density for the first box from 1.3 to 2.8 nm indicating the significant *extension of PAA chains* submerged in the water subphase (Figure 52b). The thickness exceeds the PAA chain dimensions pointing out on initial elongation of the submerged PAA chains. The second box associated mainly with the aromatic cores remained the densest region of the layer. The third box associated with the PS chains very modestly increased in thickness.

For the highest surface pressures corresponding to the condensed state of the monolayer (≥20 mN/m), two and three box models were used to analyze the data. The first box was assigned to the submerged PAA chains and the second and third boxes were assigned to the collapsed and extended PS arms, respectively (Figure 52b). The lack of resolution and small difference in electronic densities at higher surface pressures did not allow the aromatic core region to be distinguished from the hydrated and densely packed PAA chains for the highest pressure studied here. The higher electronic density of the first box inferred the molecular core was located in the PAA box increasing the effective density (Table 11). Unlike the lower surface pressures where a dense region contained the aromatic core and parts of the PAA and PS chains, the model for the 20 mN/m monolayer demonstrated a clearly defined transition between the PAA and PS chains. The lower electronic density of the second box (0.317×10^3

e/nm^3) confirmed the presence of collapsed PS arms located above the air-water interface thereby pinning the aromatic core at the interface. Upon reaching the highest surface pressure the vertical electron density distribution can be described the best with a two box model with the insignificant difference in density between the PAA and PS phases except some very low density region on a top of the layer indicating, probably, initial stage of the monolayer collapse. The total thickness of the monolayer increased to 7.9 nm at the highest surface pressure (Table 11). Considering that the density of packing of PAA and PS became indistinguishable, separate PS and PAA layer thicknesses cannot estimate in this state.

5.1.2 Monolayer Organization at the Air-Solid Interface

AFM imaging of LB monolayers deposited on a hydrophilic silicon surface provided additional information about morphology of monolayers assuming that the monolayer morphology was not altered by the monolayer transfer that was usually suggested for organic monolayers.[32,191,192,193] As was observed, at very low compression (large surface area per molecule) the molecules already formed initial micellar morphology. The monolayer deposited at 20 nm^2 per molecule (twice the limiting cross-sectional area) showed large circular domains of various sizes packed loosely with limited contact between the domains (Figure 53a). The average diameter of the domains was close to 400 nm, with some structures as large as several microns across. The exclusion of the larger domains resulted in the calculated mean diameter of 300 nm accurately representing the overall size of the domains. This surface morphology suggested the spontaneous long range ordering of the molecules at the air-water interface. The circular domains appeared to be two-dimensional micelles with total thickness 2.5 to 3 nm as determined by AFM that was close to ellipsometry measurements which was indicative of pancake-like organization within the monolayer with PAA chains spreading thin beneath the PS domains.[194,195,196,197,198] The individual domains appeared very uniform with a low surface microroughness (below 0.15nm) indicating molecularly flat domains with no indication of ordered intra-monolayer structure (Figure 53b). The decrease in the thickness of the monolayer as they were transferred from the air-water interface to the air-solid interface was apparently caused by the dehydration and collapsing of the PAA chains in contact with solid substrate (see below).

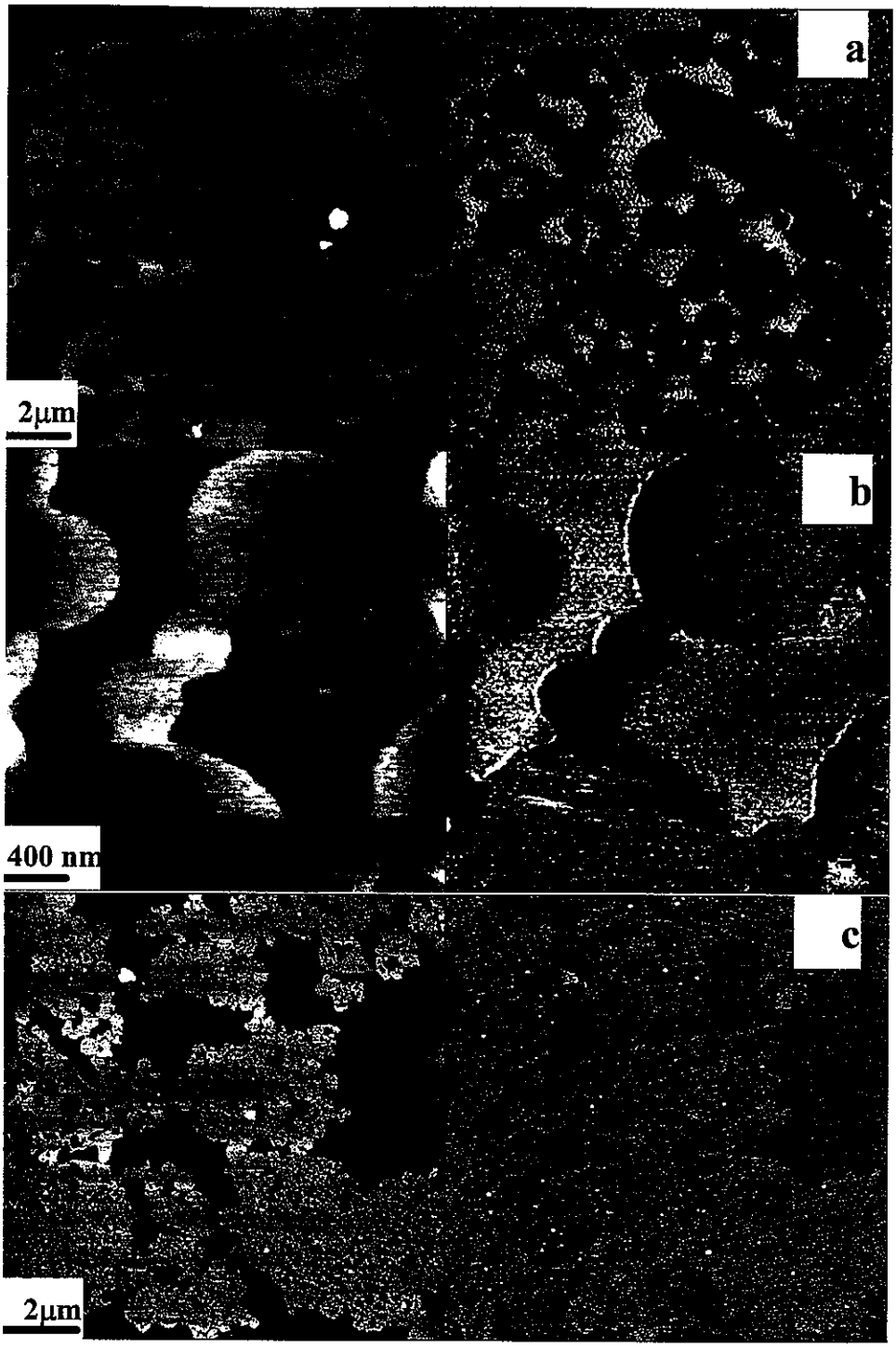

Figure 53. AFM images of two-dimensional micelles of $(PAA_{30})_6$-s-$(PS_{40})_6$ formed at a) and b) at 0 mN/m surface pressure (20 nm^2 per molecule) and c) at low surface pressure (5 mN/m). The z range for topography (left) was 15 nm and for phase (right) was 20 degrees.

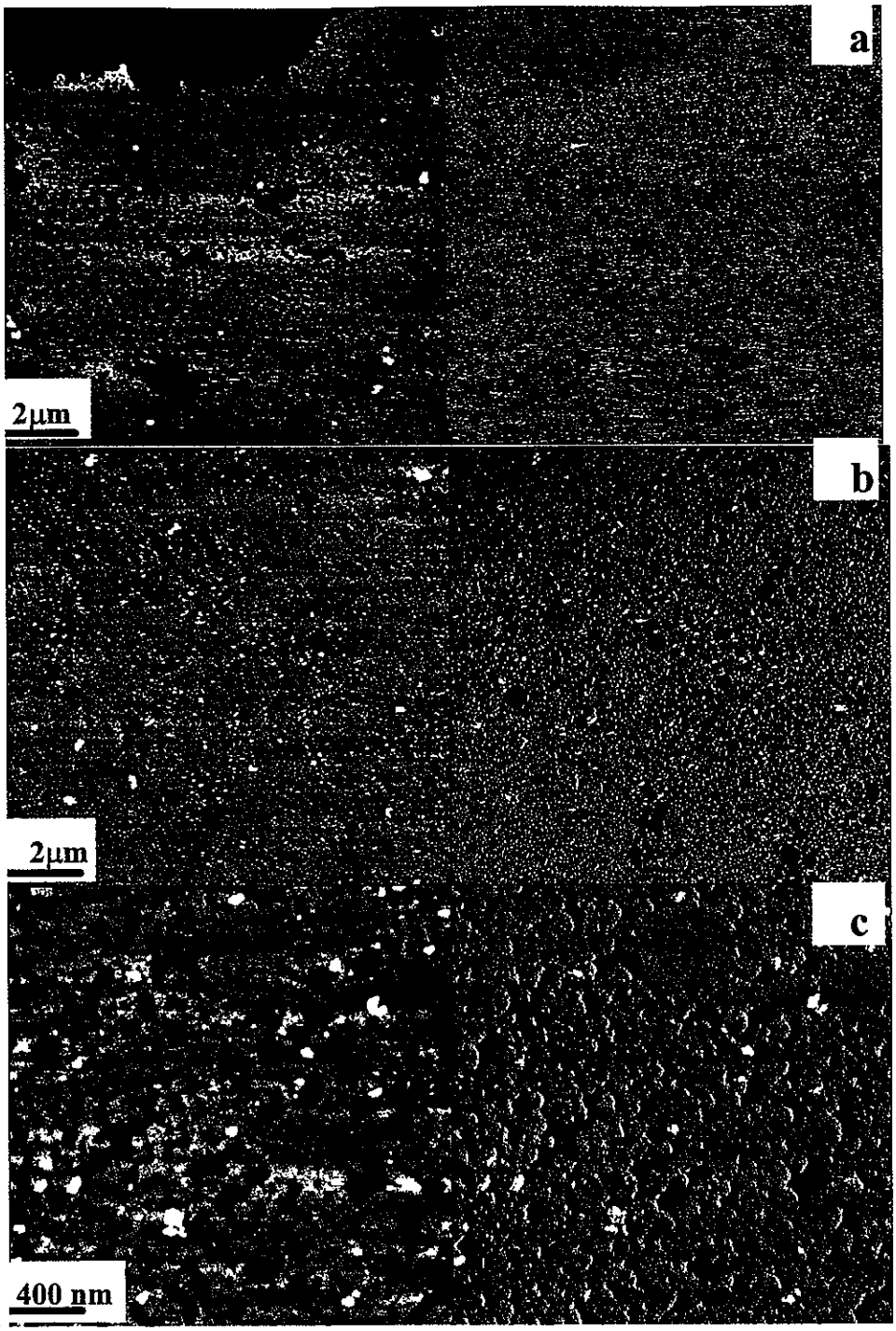

Figure 54. AFM images of two-dimensional micelles of $(PAA_{30})_6$-s-$(PS_{40})_6$ formed at a) moderate surface pressure (10mN/m), b) and c) high surface pressure (30 mN/m). The z range for topography (left) was 10 nm and phase (right) was 10 degrees.

Upon compressing the monolayer to 5 mN/m, the molecules maintained the two-dimensional circular micellar structure (Figure 53c). The number of circular domains increased as the average diameter decreased to 200 nm. The circular domains partially fused, forming larger aggregates while the surface coverage increased to nearly 50% of the total surface area that becomes close to the "jamming" limit of the random surface arrangement of circular domains.[199] The thickness of the PS domains remained nearly the same (2.7 nm). The further increase in the surface pressure to 10 mN/m showed additional densification of the monolayer (Figure 54a). The monolayer appeared almost uniform with small irregular defects present throughout the film indicating the circular domains merged into larger pancake-like monolayers with only a slightly higher thickness (3.1nm). This value was still several times smaller than the maximum possible length of PS and PAA arms in their fully extended conformations and indicates their collapsed and spread state.

Upon further increase in the surface pressure to 30 mN/m the circular domains merged into a virtually continuous monolayer (Figure 54b). The reduction in the average diameter of the circular structures was offset by increasing in their number. The two-dimensional micelles formed a web-like continuous morphology similar to the larger aggregates composed of partially fused circular domains seen in Figure 54c. The coverage area of the substrate was calculated to be higher than 80% in most locations that exceeded the limits for dense surface packing of circular domains and indicated their merging with the formation of uniform monolayer. The height of the domains determined from AFM cross-sections increased to 3.5-4.0 nm while the overall effective thickness obtained from ellipsometry increased to nearly 5 nm indicating a presence of a thin underlying layer below the two-dimensional micelles. An explanation for this appearance of an underlying layer was determined to be flattened molecules spread between and under the circular micelles. This structural feature may be responsible for the fact that the observed surface micelles possessed an exceedingly high two-dimensionality with diameter being nearly 100 times greater than their thickness. It was interesting to note that such circular micelles represent 2D microstructures with facial amphiphilicity (hydrophobic top and hydrophilic bottom). This was in contrast to much smaller surface micelles usually formed by linear diblocks.[200]

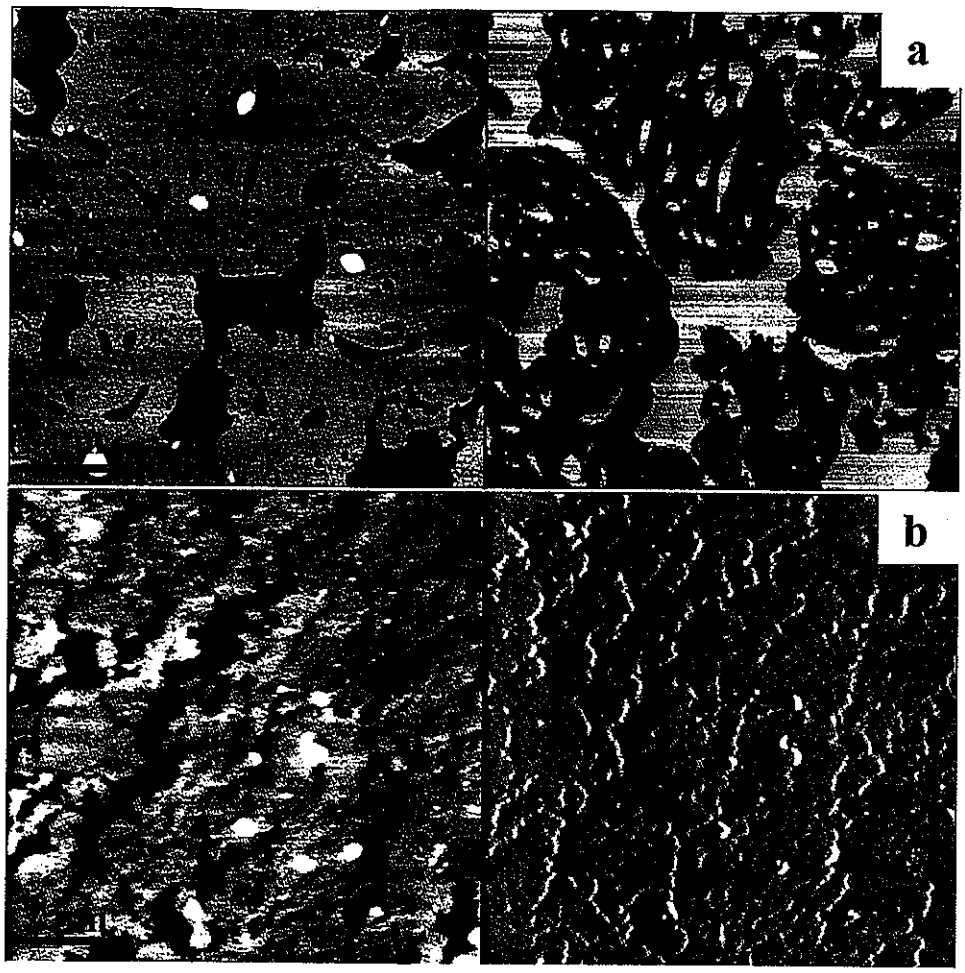

Figure 55. AFM images of two-dimensional micelles of $(PAA_{25})_6$-s-$(PS_{25})_6$ formed at a) moderate surface pressure (10 mN/m) and b) high surface pressure (30 mN/m)The z range for the topography image (left) was 10 nm and the phase (right) was 10 degrees.

Finally, the smaller symmetric star polymer $(PAA_{25})_6$-s-$(PS_{25})_6$ formed incomplete, defective domains with no indication of the circular two-dimensional micelles seen for the larger molecule (Figure 55a). At moderate pressure (10 mN/m) the molecules formed large domains up to several microns in diameter with small, rounded holes of varying size distributed throughout the surface (Figure 55a). The measured effective thickness of the monolayer was 2.6 nm and the domain height was 2.3 nm. As the surface pressure was increased to 30 mN/m, the surface coverage increased with the effective thickness increasing to 3.7 nm. The domains formed a dense morphology with a high concentration of crack-like defects running across micron sized surface areas (Figure 55b).

5.1.3 Discussion and Conclusions for the 12-arm Star Polymers

Here, discussion will mainly be focused on the results related to asymmetric, long chain $(PAA_{30})_6$-s-$(PS_{40})_6$ star polymer because of the insufficient quality of the data for star molecule with shorter chains. It seems that the decrease of the length of the PAA and PS arms in $(PAA_{25})_6$-s-$(PS_{25})_6$ greatly influenced the interfacial behavior of the star block copolymer making its monolayer structure much less defined. Significant decrease in the PS block content and the length of the both types of chains reduced segregation level, thereby disrupting the formation of the two-dimensional circular micelles.

Comparison of the monolayers parameters measured by ellipsometry, contact angle, AFM, and X-ray reflectivity allows for general conclusions to be made on structural reorganization of the monolayer in different physical states (Figure 56). In fact, this combination of experimental techniques brings to discussion very different but closely related parameters of the monolayer morphology: overall effective thickness of the monolayer at the air-water interface (X-ray reflectivity) and solid surface (ellipsometry), the separate thicknesses of top PS domains and bottom PAA phase at both water (X-ray reflectivity) and solid (AFM in combination with ellipsometry) surfaces, and the surface coverage with PS domains on the solid surface along with the presence of the hydrophobic PS chains (AFM and contact angle). The trends observed for all these parameters are very instructive and allow to make non-trivial conclusions about surface microstructure. The results discussed here are very consistent considering that they were obtained with four independent techniques on two independent sets of samples at different surfaces

The analysis of this trend shows a consistent and sharp increase in the effective monolayer thickness at both water and solid surfaces at very low surface pressure below 5 mN/m (Figure 56). For surface pressures higher than 5 mN/m virtually constant thickness is observed. Considering significant increase in surface coverage in this range, most of the increase observed was attributed to the formation of denser population of the domains with virtually unchanged thickness (except very low surface areas for pressures below 2 mN/m). This conclusion is also supported by isotherm data which shows that the surface area per molecule at surface pressures of 5 mN/m and higher is very close to A_o, which is mainly

defined by the rigid cores as discussed above (Figure 50). The contact angle initially increases sharply to 95° and stays constant in a whole range of pressures (Figure 56). This value is identical to that observed for grafted PS chains in solid state [201] and indicates uniform composition of the monolayer surface composed of PS chains.

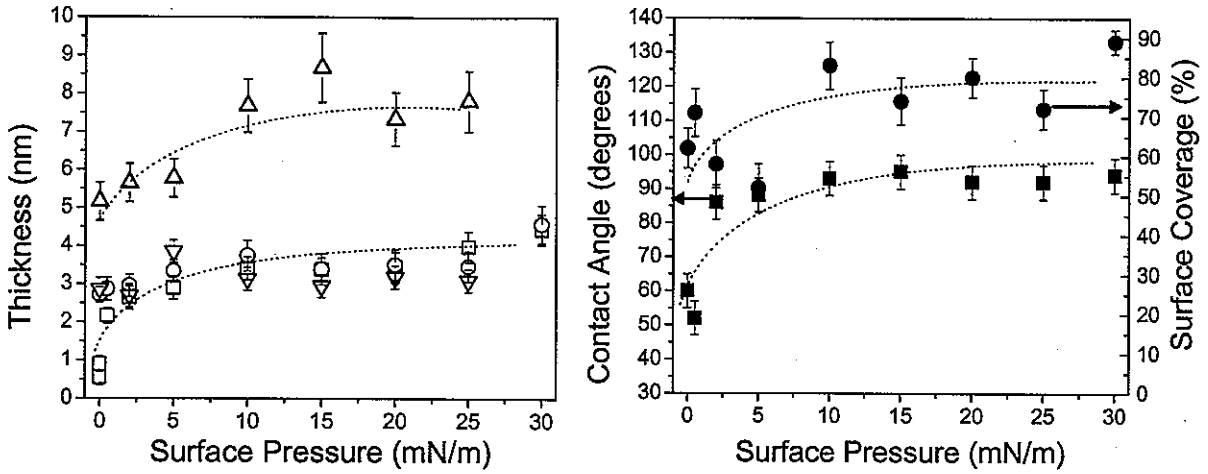

Figure 56. Monolayer parameters determined by X-ray reflectivity, ellipsometry, contact angle, and AFM, top: triangles - the total monolayer thickness at air water interface; squares – the total monolayer thickness at solid surface; circles – PS domain thickness at solid surface; inverse triangles – PS domain thickness at the air-water interface. Bottom: squares – contact angles; circles – surface coverage.

However, the thickness of the condensed monolayer at the water surface and on the solid substrate differs more than twice: 7.9 ± 0.5 nm versus 3.1 ± 0.5 nm (Figure 56). The much smaller total thickness for solid-supported LB monolayers as compared with the same monolayer at the air-water interface indicates significant difference in internal microstructure of the monolayers. Direct comparison of the total thickness of the monolayer and the thickness of the PS phase immediately allows concluding that the PAA chains submerged in water are extended to 4.8 ± 0.6 nm but are spread in the thin layer of around 0.3 nm at the solid surface. Constant extension of the PAA chains over almost a whole region of surface pressure tested (from 5 to 30 mN/m) can be attributed to the factor of limited grafting density imposed by the presence of the sizeable rigid cores which prevent the truly brush regime and full extension of

the PAA chains. This is in a sharp contrast with conventional block-copolymers with point-like junctions where the molecules undergo constant change under compression.[200, ,202]

The height of the PS domain determined by AFM was consistent with the thickness of the PS blocks determined by X-ray reflectivity as well as ellipsometry at all surface pressures (Figure 56). Unlike PAA chains which undergo tremendous spreading in the course of transfer to a solid surface, the thickness of PS domains remains almost unchanged, around 3 nm. This last value is fairly close to the dimensions of the collapsed PS chains (Table 10). Thus, despite the significant surface area available for random coiled PS chains provided by the large rigid core, even higher compression does not affect the state of the PS chains.

Finally, Figure 57 provides a schematic representation of the segregation behavior of the star molecules $(PAA_{30})_6$-s-$(PS_{40})_6$ as revealed by this study. At the air-water interface, the PAA arms submerge into the water subphase, creating a dense, hydrated PAA layer below the core plane with significantly extended PAA chains in the condensed monolayer state. To form a more stable micellar structure, the PS chains aggregate above the aromatic core, creating a collapsed PS layer. Upon transfer to the solid substrate, the PAA chains dehydrate and spread very thin between hydrophobic PS layer and hydrophilic silicon substrate (Figure 57). The moderate length of the PS and PAA chains allows the chains to form dense layers, occupying the space directly above and below the aromatic core. This is also responsible for the formation of stable circular micellar structures with diameter of 200-300 nm which include several thousands molecules and are distinguished two-dimensional structures with "two-faces": highly hydrophobic and highly hydrophilic. Remarkable stable molecular packing of the star molecules with virtually unchanged characteristics in a wide range of compressions is a signature of the amphiphilic star polymer with rigid core studied here. It is suggested that this is caused by limited grafting density of the PS and PAA chains attached to the sizeable rigid core which prevents the monolayer to undergo reorganization from "gaseous" to condensed state. These changes triggered by decreasing surface area per molecule usually result in a wide variety of dot, spaghetti-like, rectangular, or lamellar surface morphologies observed in linear or modestly branched amphiphilic di-block copolymers of different types.[194,202] Stability of these micellar structures at the water and solid surfaces over a wide range of surface pressures is a signature of these amphiphilic star polymers making them unique polymeric surfactants.

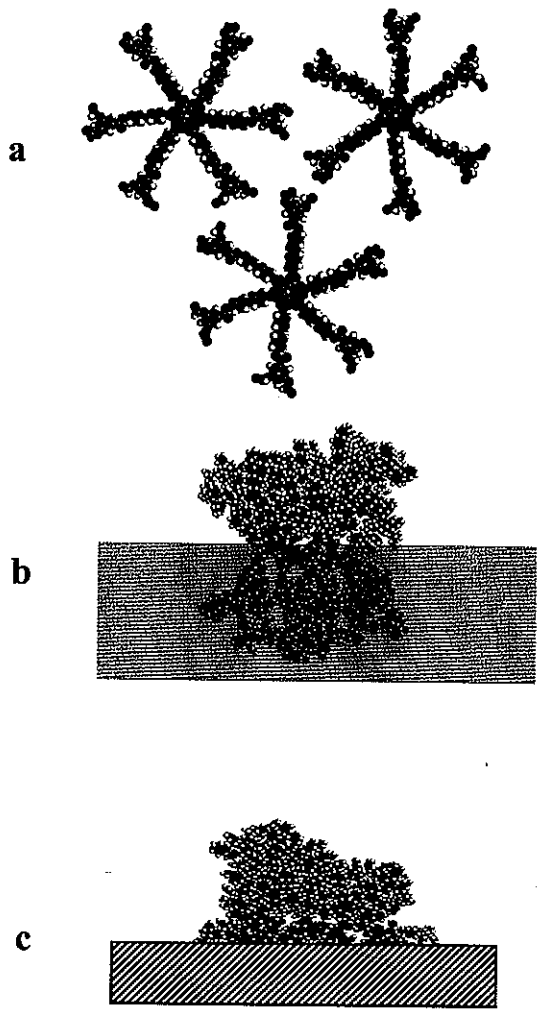

Figure 57. Schematic of $(PAA_{30})_6$-s-$(PS_{40})_6$ monolayer microstructure: a) top view of the core to core packing behavior (the polymeric arms are removed for clarity), side view of the molecule packing at the air-water interface (b) and the air-solid interface (c).

5.2 Block Star Copolymers

Six star block copolymers are composed of an equal number of PEO and PS arms attached to a central core. The weight content of the PEO block varied from 19% to 88% as the number of arms varied from eight arms of PEO and PS each for S16-19 to 19 arms of PEO and PS each for S38-78 (Table 1, Figure 58). All arms of the same nature have the same molecular weight. The effect of the volume fraction was analyzed for the block star copolymers at interfaces in addition to role of molecular architecture in the molecular

organization in surface films. An example of a linear diblock copolymer was included for one particular composition for comparative purposes (L-86, Table 1). For practical purposes, all compounds studied here are split into two groups: group **I** with lower PEO content (<50%) and group **II** with predominant PEO content (79-88%) (Figure 1). Within the first group the total number of arms was fairly constant and within the second group the number of arms increased for block copolymers with lower PEO content (Table 1).

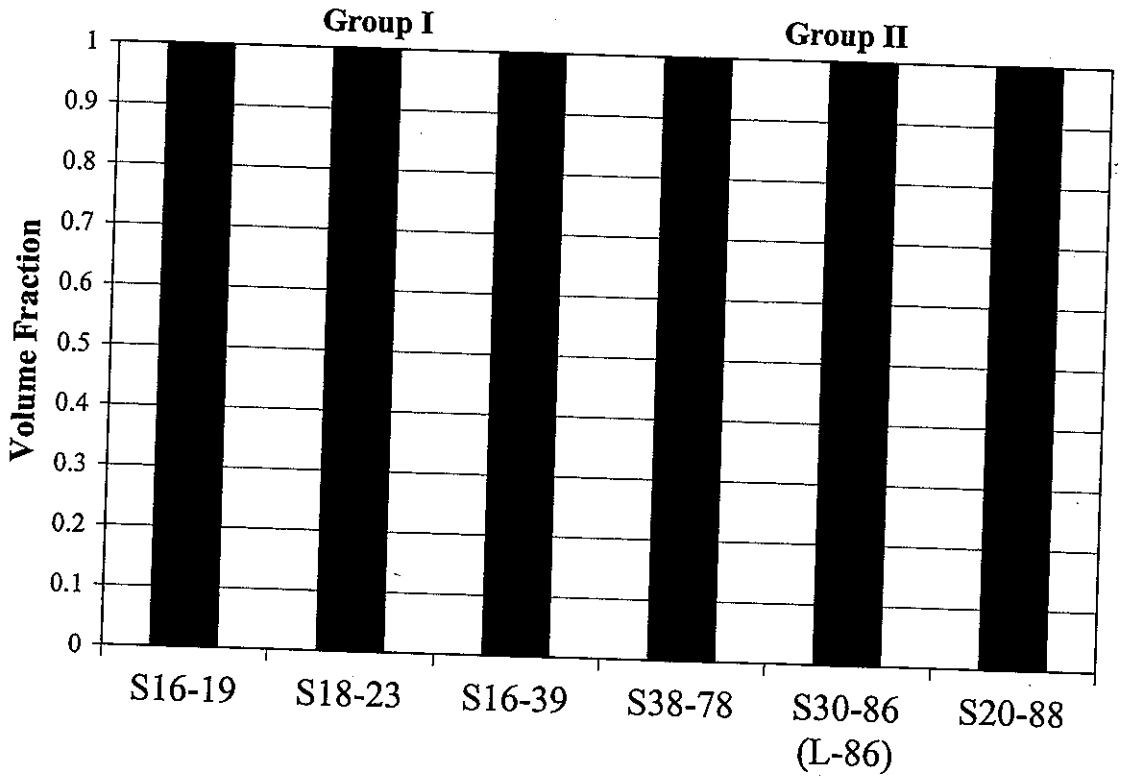

Figure 58. Graphic representation of the weight fraction of the PEO and PS blocks for the star block copolymers.

5.2.1 Ordering at the Air-Water Interface

All star block copolymers formed stable Langmuir monolayers at the air-water interface indicating appropriate amphiphilic balance (see π~A isotherms in Figure 59). The reversibility of the Langmuir monolayers from star polymers was examined by repeated cycles of compression and expansion to the low pressure regime. The reversible behavior for the star copolymers with a larger PEO content (group **II**) was improved over the molecules

with a larger PS content (group **I**). The star copolymers S38-78, S30-86, and S20-88 showed a very small hysteresis (5-10% surface area) even after a short relaxation time (10 minutes). A slightly larger hysteresis (10-15% surface area) observed for star polymers S16-19, S18-23, and S16-39 indicated partially irreversible behavior due to the presence of glassy PS phase. Apparently, a much longer relaxation would be required for the PS-dominant star block copolymers for complete reversibility of the surface behavior.

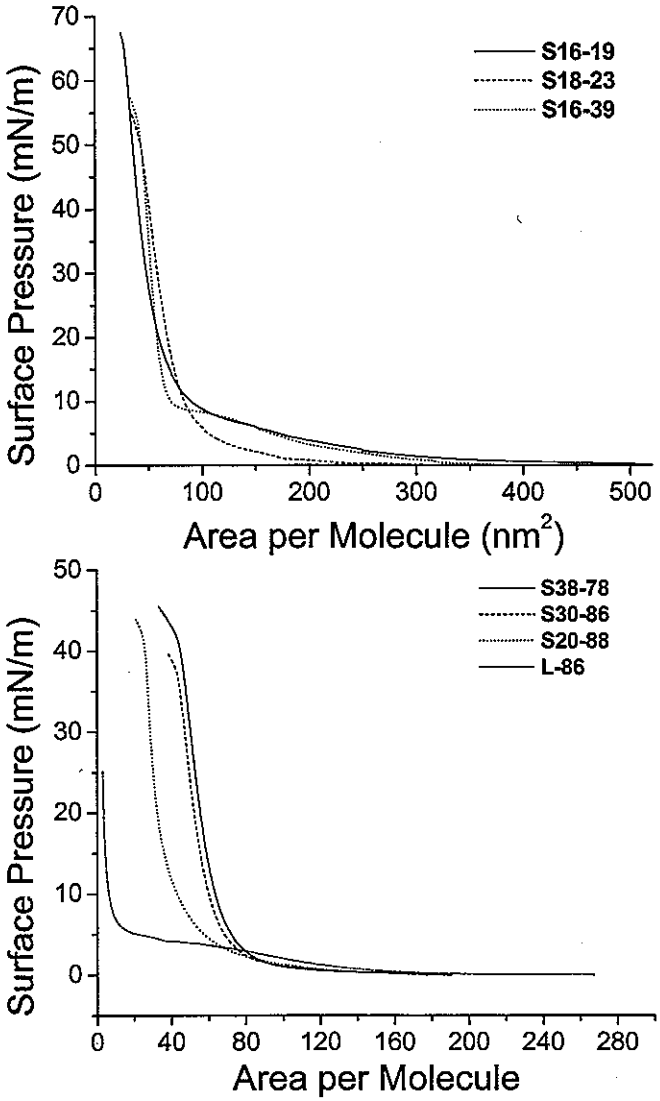

Figure 59. Langmuir isotherms of PS_n-PEO_n star block copolymers with a) low PEO content: S16-19, S18-23, and S16-39 and b) high PEO content: S38-78, S30-86, and S20-88.

The star copolymers from group **I** with larger PS content exhibited larger initial surface molecular areas and a low-pressure plateau (Figure 59a, Table 12). The star copolymers from group **II** displayed smaller initial cross-sectional areas and a more gradual transition in surface pressure with no plateau prior to the steep increase in surface pressure before monolayer collapse (Figure 59b, Table 12). The lower PS content (accompanying with shorter length of PS chains, Table 1) translated in reduced initial surface molecular area A_1 and limiting cross-sectional area A_o (Table 12).

From chemical composition, the limiting surface areas per molecule was estimated from known limiting surface areas for PEO monomeric unit (0.28 nm^2)[203] and for PS monomeric unit (0.06 nm^2)[204] reported for PEO-PS linear and star copolymers with a limited numbers of arms (Table 12). Theoretical surface area per molecule in condensed state A_o^t is calculated from the surface area per monomer, a_o, number of monomers in a single arm, N, and number of arms, n: $A_o^t = a_o$ N n and corresponds to situation when PS chains in coiled conformation are the limiting factor in monolayer compression. Direct comparison of the theoretical surface area per molecules estimated from chemical composition and actual surface area in condensed state shows consistent correlation between these parameters (Figure 60). However, for group **II** significant higher experimental area in comparison with theoretical area (dashed line in Figure 60) was observed indicating that the concurrent increase of the number of arms from 20 to 38 promotes much faster increase of surface area. This phenomenon can be due to effect of the crowding forcing multiple PS arms spread in lateral directions rather than stretching out of interface. Correspondingly, further increase in the PS content masked by the reduced number of arms led to modest increase in the surface area due to reduced crowding effect.

Table 12. Surface area per molecule of PEO_n-PS_n block star block copolymers determined from π-A isotherms.

	Experimental				**Calculated**	
Sample	A_o (nm^2/M)	A_1 (nm^2/M)	N_{PS}	N_{PEO}	$A_{PS,\,tot}$ (nm^2/M)	$A_{PEO,\,tot}$ (nm^2/M)
S16-19	70	500	259	127	128	288
S18-23	81	325	211	148	117	369
S16-39	68	400	144	207	72	464
S38-78	66	192	29	323	38	1,710
S30-86	62	180	29	511	30	2,145
S20-88	40	185	30	568	20	1,590
L-86	8	160	31	464	2	130

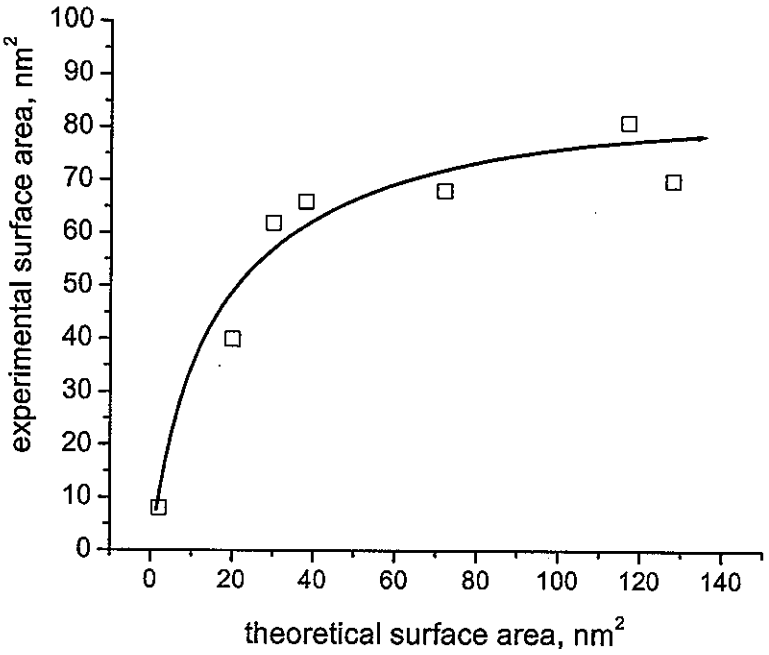

Figure 60. Variation of surface molecular area vs molecular area estimated from chemical composition.

5.2.2 LB monolayers at the solid surface: group I.

The influence of the number of branches and the weight fraction of the polymeric blocks was observed in deposited monolayers to discern the effect of the architecture. The two star copolymers with the lowest PEO content (group **I**) formed lamellae with random orientation and low degree of branching (Figure 61). The continuous lamellae of S16-19 had moderate height (6.8 $\pm$ 0.2 nm) and width (180 $\pm$ 40 nm) (Table 13). The lamellae snaked and randomly looped, covering approximately a quarter of the substrate surface at lower surface pressure. At higher surface pressure the surface coverage rose to 66% as the lamellae height grew to 9.0 nm but the lamellae width remained constant. The lamellae at the highest surface pressure become oriented in the dip direction suggesting that at the higher surface pressure the lamellae ordering is controlled by the capillary forces acting along the dipping direction. The S18-23 star copolymer with an additional PS and PEO arms and slightly longer PEO arms formed dense packed lamellae (Figure 61). The lamellae height and width

was lower than for previous compounds at all surface pressures (Table 13). Conversely, the effective thickness of the S18-23 star polymers films rose (2.1 ± 0.2 nm at low surface pressure, 3.6 ± 0.2 at higher surface pressure) due to the increase in the surface coverage (44% at lowest surface pressure, 77% at highest surface pressure). Higher resolution AFM imaging revealed fine circular substructures of the lamellae for both star copolymers (Figure 61c). This confirms that the predominant type of aggregation for star copolymer with lowest PS content is circular aggregation as expected for given chemical composition in bulk state and in monolayers from star block copolymers with few arms.[80,204,205] However, unlike these compounds, a large number of arms (32 and 36 arms) promoted further aggregation of circular domains into continuous and branched lamellae.

Table 13. Characteristics of LB monolayers from star block copolymers.

Sample	Thickness (nm)			Domain Height (nm)			Area coverage		
	P=1	P=5	P=25	P=1	P=5	P=25	P=1	P=5	P=25
S16-19	1.1	1.4	2.7	7.0	6.6	9.0	0.24	0.29	0.66
S18-23	2.1	2.2	3.6	5.5	5.4	6.7	0.44	0.64	0.77
S16-39	1.0	1.8	2.7	3.3	3.6	3.4	0.36	0.63	0.93
S38-78	0.8	2.4	3.4	1.5	2.5	1.1	0.57	0.74	0.97
S30-86	2.4	2.8	4.3	1.2	2.6	2.3	0.59	0.94	1.00
S20-88	2.6	4.7	7.3	8.1	9.5	9.6	0.29	0.49	0.97
L-86	0.5	0.4	6.1	N/A	N/A	N/A	N/A	N/A	N/A

The star polymer with a moderate PEO content (S16-39) stands alone in group **I** (Table 1, Figure 58). Unlike two other star copolymers S16-39 formed very uniform monolayer at low and high surface pressures (Figure 62a,c). Fine circular domains formed densely packed and partially ordered network visible at higher resolution (Figure 62b). The glassy PS blocks form 3.5 nm high spherical micelles with limited hexagonal ordering on the underlying soft PEO layer, typical preferential structure for circular micelles. The diameter of very uniform circular was calculated to be 60 ± 5 nm with heights about 3.5 nm (Table 13). The domain height remained relatively constant as the surface pressure increased, thereby causing a similar trend in the effective thickness of the monolayers (Table 13). The

density of the circular micelles rose and diameters decreased as the surface pressure increased.

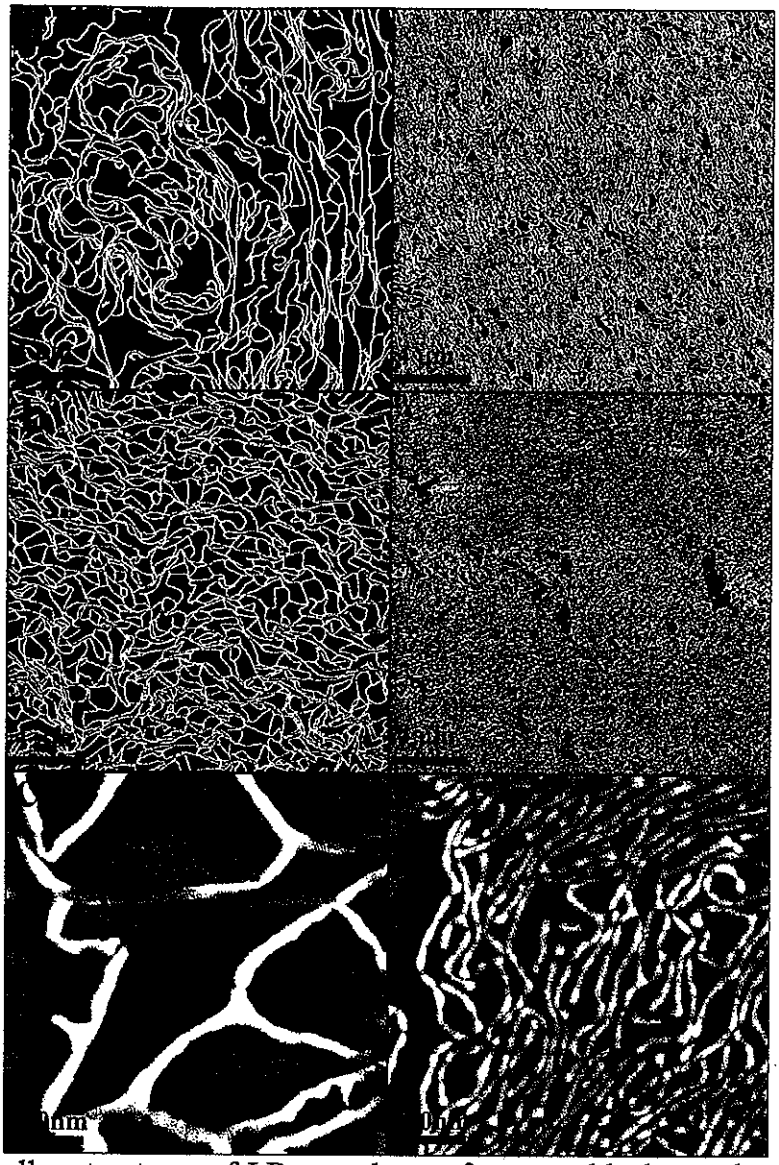

Figure 61. Lamellar structures of LB monolayers from star block copolymers with lowest PEO content S16-19 (right) and S18-23 (left) deposited at a) 1 mN/m and 5 mN/m (b and c).

5.2.3 LB monolayers at the solid surface: group II.

The star polymers with the highest number of arms, molecular weight and predominant content of PEO chains formed homogenous monolayers with bi-continuous

network of PEO and PS phases (Figure 63). The S38-78 star block copolymer with 38 arms formed very uniform monolayers with fine texture: bi-continuous network at low surface pressure and dense packing of nanoscale domains as the surface pressure rose. The S30-86 star polymer was observed to form a coarser network of PS domains at low surface pressure and a uniform monolayer at 25 mN/m (Figure 63c, d). The uniform surface morphology of these star block copolymers is similar to the morphology of the selected linear block copolymer L-86 with 86% of PEO phase (not shown). However, the overall thickness of linear block copolymer at low surface pressure was much smaller than that for star block copolymer indicating that removing crowded constraints of the multiple arms attached to a single core results in larger in-plane spreading (Table 13). The effective thickness of LB monolayers increased significantly for higher surface pressure indicating the PEO phase formed a thicker layer underneath the PS blocks, thereby allowing the smaller PS block to form an uniform topmost layer (Table 13).

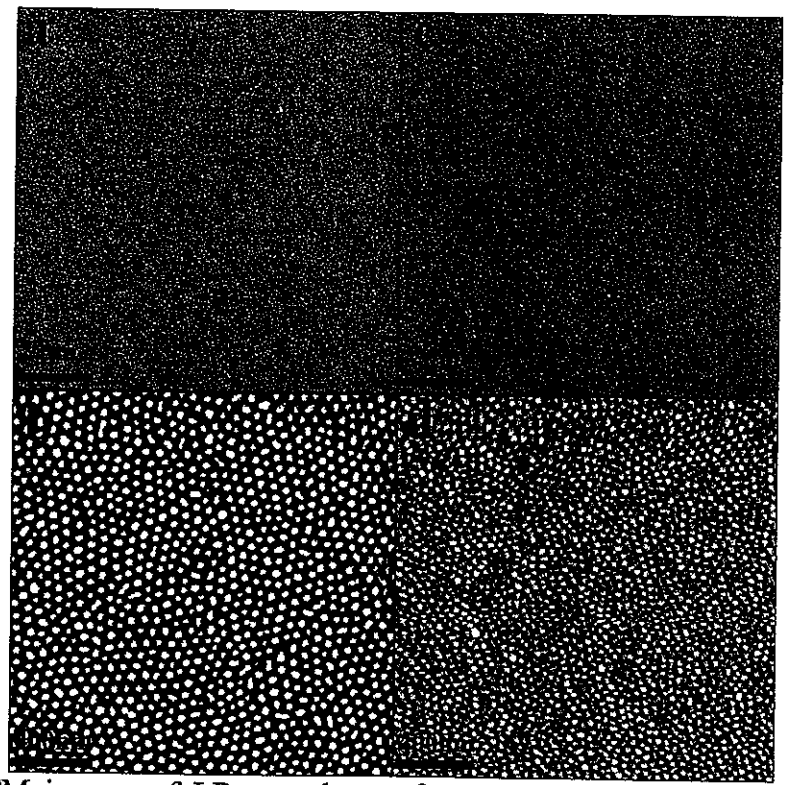

Figure 62. AFM images of LB monolayers from star block copolymers with moderate content of PEO (S16-39) at 1 mN/m (a and b) and 5 mN/m (c and d)

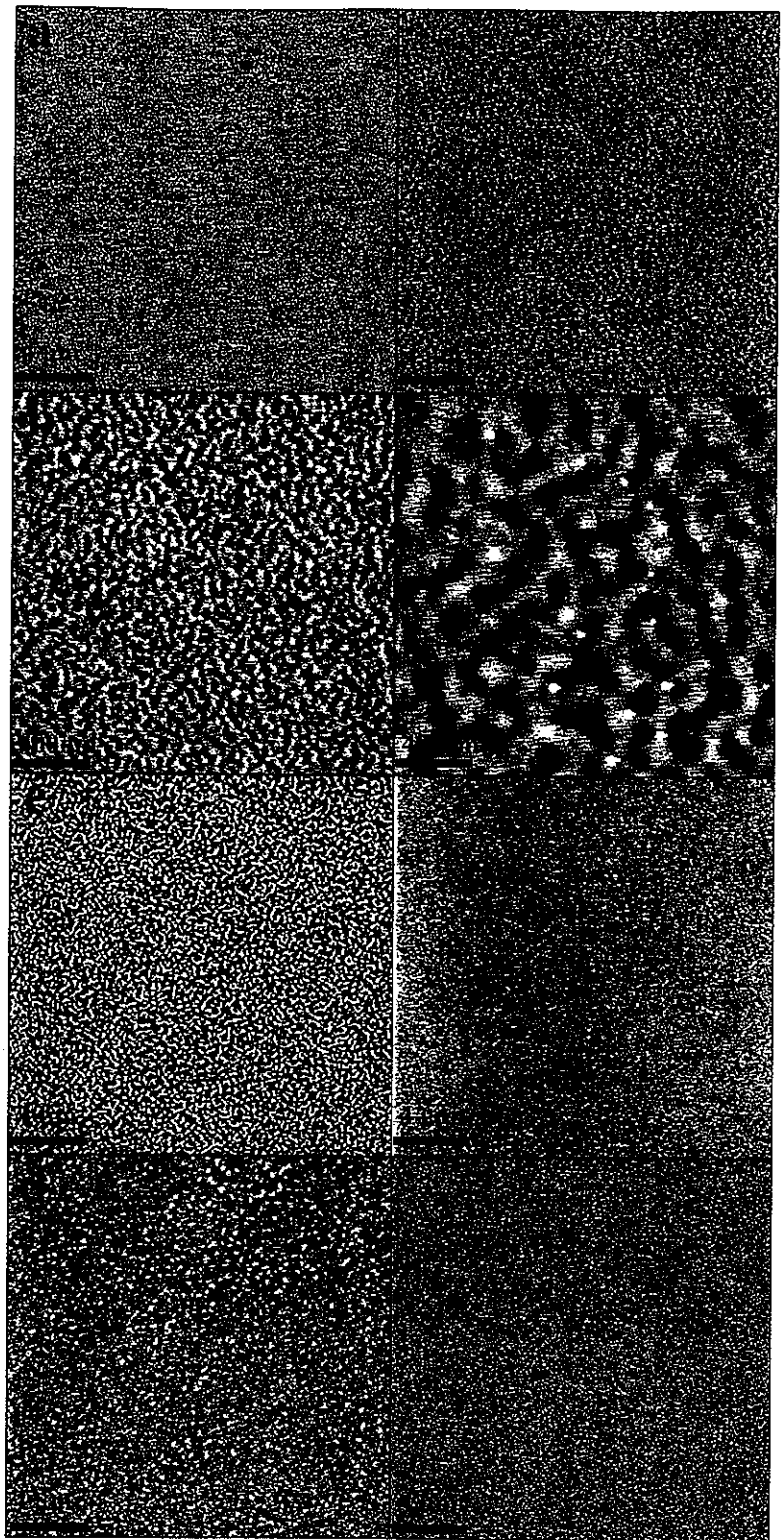

Figure 63. AFM images of LB monolayers from star block copolymers: S38-78 (right) and S30-86 (left) deposited at 1 mN/m (a,b), 5 mN/m (c), and 25 mN/m (d) surface pressures.

Very peculiar surface morphology was observed for the star block copolymer S20-88 with the highest PEO content but reduced number of arms (Table 1, Figure 58). This compound formed well-defined dendritic structures at all surface pressures (Figure 64). At low surface pressure, highly branched dendritic morphologies merged into long branched backbones oriented in the dipping direction (Figure 64a, b). The height and width of the dendritic structures were very similar suggesting a uniform growth. The higher resolution AFM images revealed a heterogeneous domain surface indicating the dendrites formed as aggregate structures of fine circular domains (Figure 64).

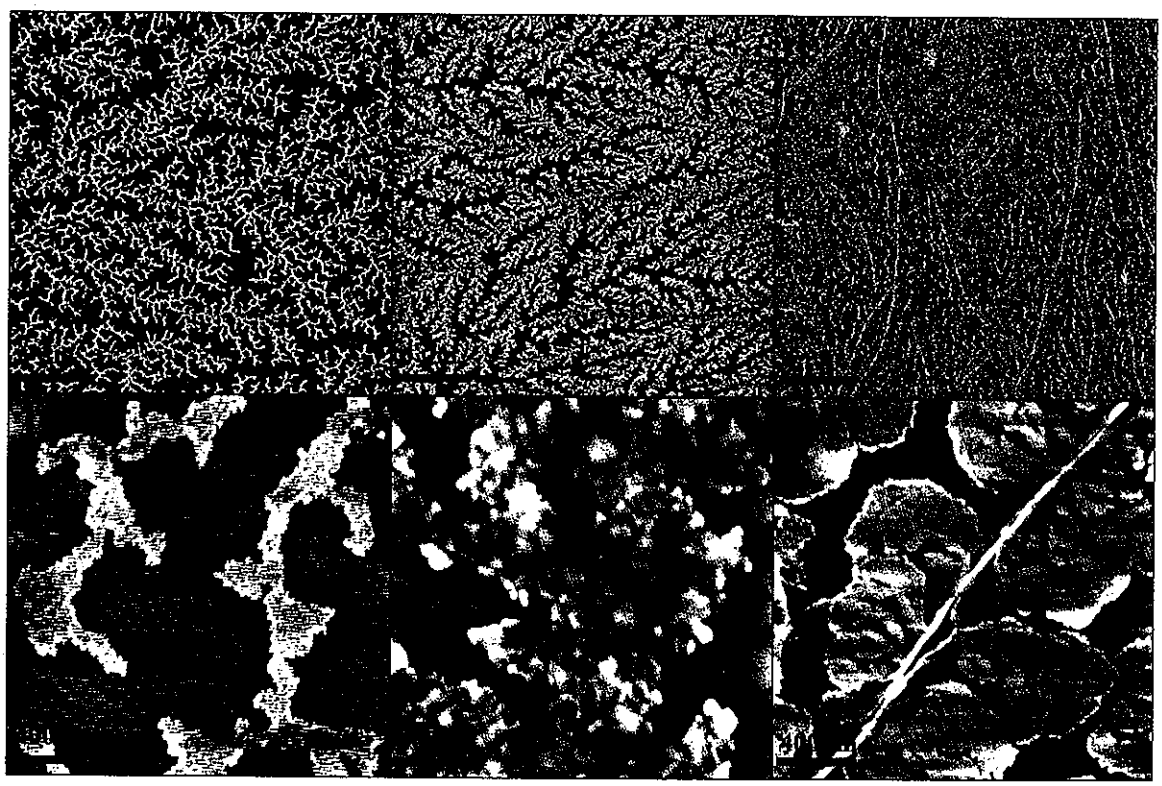

Figure 64. AFM images of LB monolayers from star block copolymers: S20-88 at 1 mN/m (a-b), 5 mN/m (c-d), 25 mN/m (e-f).

The rise in surface pressure to 5 mN/m increased the surface coverage from 29% to 49% in addition to domain height growth from 7.3 $\pm$ 0.2 nm to 8.1 $\pm$ 0.2 nm as observed in

denser and more regular dendritic structures (Figure 64c, d). The growth of the dendrites along backbone structures oriented in the dipping direction was more clearly observed in these monolayers. The length of the backbones reached tens of microns with the length of branches of 2-3 microns.

At the highest surface pressure the dense dendritic structure merged into a continuous domain structure with remnants of the growth structure still evident (Figure 64e). The effective thickness rose to 7.3 ± 0.2 nm as the surface coverage exceeding 90%. The surface roughness of the irregular domains decreased at the higher surface pressure. An interesting feature is the appearance of straight ridges along the dendrite backbones. The ridge were 1.5 nm higher than the surrounding domains, suggesting the dominating PEO phase thickened as the molecules were compressed along the denser backbone regions. The overall shape of the compressed structures reminiscent initial highly branched morphology with branches squashed in transversal direction.

Finally, it was concluded that the overall behavior of amphiphilic star block copolymers with a large number of arms follows general trends observed for PS-PEO star copolymers discussed before except some features as will be discussed below.[204,205] Following this trend, it is suggested different types of molecular organization for amphiphilic star block copolymers studied here depending upon chemical composition and architecture (Figure 8). Cartoons of corresponding structural reorganizations are presented in Figure 9. First, the molecular ordering of star block copolymers with the low PEO content is controlled by the predominant PS block thus forming circular domains aggregated into continuous lamellar morphology (Figure 65). The shorter PEO chains limit contact between PEO arms of neighboring molecules thus allowing the PS chains to form continuous one-dimensional structures. A twofold increase in molecular weight of the PEO arms and decreasing length of PS arms results in collapsed the lamellar structure and formation of individual, densely packed circular micelles. This type of molecular ordering is consistently observed for star block copolymers with the PEO content reaching 86% with compounds with highest content forming virtually uniform morphology with PEO underlying layer covered with PS phase (Figure 65). Concurrent increase in a number of dissimilar arms attached to a single core (up to 38 for S38-86) prevents microscopic phase separation of dissimilar chains and the

formation of individual circular domains expected for this chemical composition. Instead, the PEO chains are vertically separated forming underlying hydrophilic carpet.

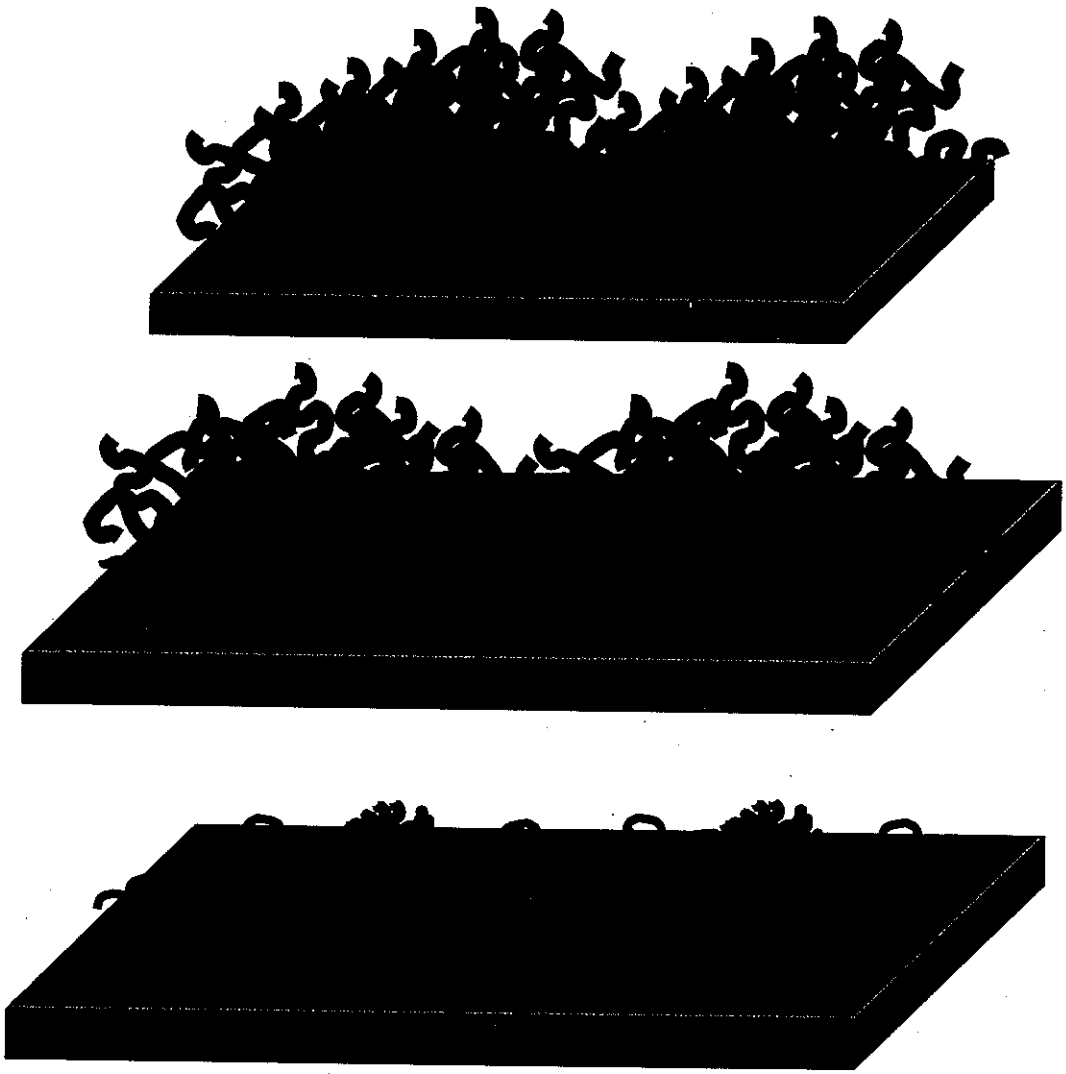

Figure 65. Schematic of molecular ordering in LB monolayers from star block copolymers with low (top), moderate (middle), and high (bottom) PEO content.

However, reducing the crowding of PS and PEO chains (number of arms from 38 to 20) for the S20-88 compound with the highest PEO content promotes in-plane phase separation with formation of peculiar dendritic surface morphology. This type of surface morphology is an indication the monolayer growth via diffusion-limited aggregation with

preferential directional addition of the components. This aggregation can be caused by the crystallization of the predominant PEO component triggered by reduced constraints because of lowered number of arms in the molecules. This growth combined with lateral compression eventually leads to directional growth of PEO monolayer with PS phase vertically segregated in the form of circular domains and one-dimensional features. Such a unique morphology has been never observed for PS-PEO star block copolymers with a low number of arms.

5.3 Discussion and Conclusions of Star Polymers

Both star polymer series demonstrated the effect of composition of the molecular shell on the ordering behavior at the air-water and air-solid interface. The 12 arm star polymer formed 2D circular micelles at the air-water interface. As the molecular area was reduced the large circular micelles aggregated and formed a continuous monolayer. The domains maintained the circular shape while the average diameter decreased as the number of domains rose at the lower molecular areas. Comparison of the monolayer dimensions with theoretical molecular dimensions confirmed the molecular area was controlled by the glassy PS blocks. The PAA blocks submerged in the water subphase and elongated as the cross-sectional area was reduced, thereby significantly contributing to the monolayer thickness at the air-water interface. Upon deposition the PAA dehydrate and collapse under the aromatic core and PS block, thus reducing the monolayer thickness at the air-solid interface.

The block star copolymers formed a variety of morphologies at the air-water interface. The morphology trend deviated from the morphology-composition relationship observed for linear block copolymers. The transition from cylindrical lamellae to spherical micelles was suppressed due to the attachment of multiple polymeric arms to a central core. The PS chains were determined to control the molecular organizations at interfaces when the PEO content was below 50%. The star polymers with the most number of arms and higher PEO content formed homogeneous monolayers at interfaces indicating the longer PEO arms control the molecular organization. A peculiar dendritic morphology was observed for the star block copolymer with the highest PEO content due to the crystallization of the predominant PEO block.

Comparison of the star polymer molecular series revealed the volume fraction of the glassy, hydrophobic block controls the molecular organization at interfaces. Variance in the volume fraction ratio easily disrupted long range organization of the star polymers at the air-water and air-solid interfaces. The attachment of multiple polymeric arms to a central core reduced the length of the individual chains and thus affected the monolayer packing. The influence of the branched central core was limited due to the large length of the polymeric chains and the small fraction (<10%) it contributed to the molecular weight.

CHAPTER 6. RESULTS – BRANCHED GOLD NANOPARTICLES AND POLYMER BRUSHES MOLECULES

Random layering and aggregation of inorganic nanoparticles prohibit the use of these desirable particles in highly structured applications. To induce long range ordering and to eliminate aggregation behavior, the inorganic nanoparticles are functionalized with organic shells. The inclusion of branched molecules with competing molecular fragments within the functional shell can drive organization at interfaces in addition to insulating the nanoparticles from neighboring molecules. The ordering of gold nanoparticle functionalized with binary polymer brushes was studied to elucidate the effect of phase separation on the organization of inorganic particles at interfaces.

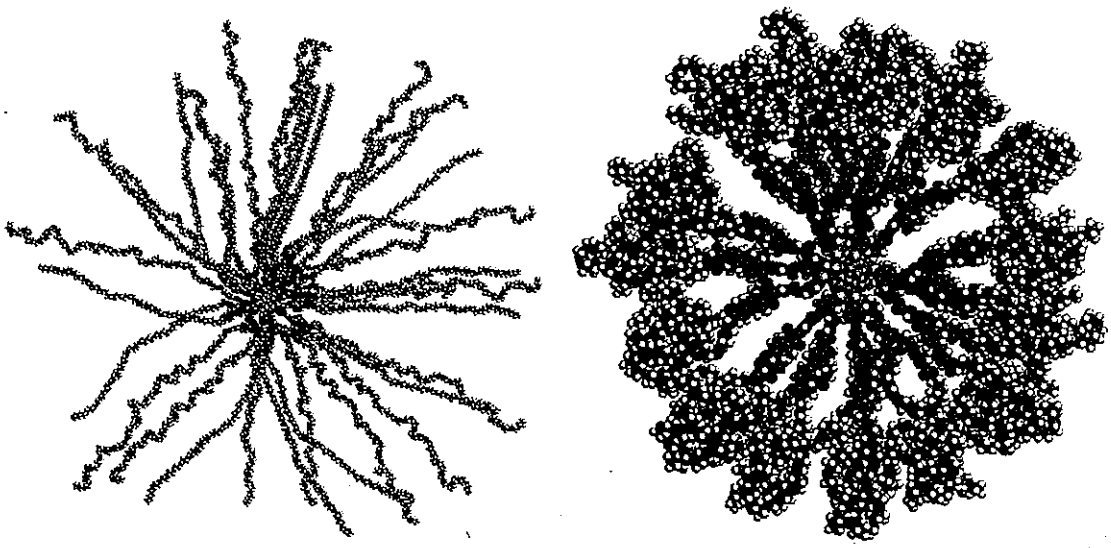

Figure 66. Molecular model of polymer brush functionalized gold nanoparticle with extended polymeric arms (above) and collapsed polymeric arms (below).

6.1 Surface Behavior

The polymer brushes paired a hydrophilic PEO_{44} chain and hydrophobic PB_{20} were attached to a Y-shaped aromatic core prior to the brushes were covalently bonded to the 2 nm diameter gold nanoparticle (Figure 66). Theoretical estimates of 15-25 Y-shaped brushes per gold nanoparticle core were calculated from spacial estimates in addition to molecular

models. GPC estimated 7.4 brushes attached to the core although the technique typically underestimates the molecular weight of nonlinear particles. The extended brush diameter for AuNP-PB-PEO was calculated to 28.5 nm with each Y-shaped brush 13.5 nm fully extended (Figure 66). The collapse of the Y-shaped polymer brushes to form a dense shell surrounding the gold nanoparticle core reduced the molecular diameter to 13 nm (Figure 66). The cross-sectional area of the molecule with the compressed polymer shell was 132.7 nm^2.

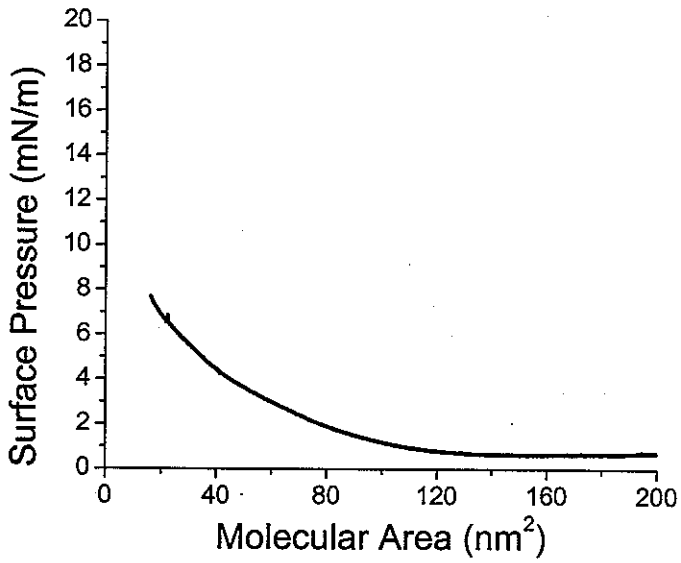

Figure 67. The π-A isotherm of AuNP-PB-PEO displayed the instability of the composite molecule at the air-water interface with a low pressure collapse of the molecule.

The AuNP-PB-PEO molecules formed stable monolayers at the air-water interface with reversible amphiphilic behavior (Figure 67). The large range of molecular areas observed prevented the complete surface pressure versus molecular area isotherms (π-A isotherm) to be observed in one experiment. The initial molecular area was calculated to be 120 nm^2 per molecule with the limiting cross-sectional area determined to be approximately 50 nm^2 from the transition in slope. The experimental molecular area was approximately 1/5 the theoretical cross-sectional area of the fully extended molecular confirming the polymer brush corona collapse to encapsulate the gold nanoparticle core. The cross-sectional

molecular area calculated from the π-A isotherm was in good agreement with the estimated molecular area of the collapsed polymer brushes. Below 50 nm^2 per molecule the slope of the π-A isotherm increased suggesting a shift in the monolayer ordering. Despite the change in slope, 18 mN/m was the highest observable surface pressure suggesting early monolayer collaspe. The large size of the composite molecule created instability in the monolayer as demonstrated by the low surface pressure for the monolayer collapse.

6.2 Monolayer Organization at Solid Surfaces

The instability displayed in the low pressure behavior of the molecules at the air-water interface was further confirmed for the deposited monolayers. The AuNP-PB-PEO molecules formed irregular, round domains (average diameter 4 μm) at all molecular areas studied. The number of domains rose for the monolayer deposited at the lowest cross-sectional area (30 nm^2) causing denser packing of the domains (Figure 68a and 68b). A thin underlying monolayer was observed to spread between the domains suggesting the molecules adopt two conformations. More condensed domains formed from laterally compressed molecules with slightly increased thickness above the underlying layer of spread molecules. Comparison of the domain height verse the gold nanoparticle core diameter further supported this conclusion. The height of domains modestly increased from 0.4 ± 0.1 nm for monolayers deposited at >80 nm^2 to 0.6 ± 0.1 nm for monolayers deposited at 30 nm^2 per molecule. The formation of domains as a partial bilayer was not supported by the height difference of the domains calculated from AFM cross-sections.

The collapse of the polymer brushes into a dense corona surrounding the gold nanoparticle core was further observed in high resolution AFM. The molecules formed a circular texture within the domain structures with a similar texture observed for the underlying monolayer at all surface areas (Figure 68c and 68d). The phase contrast of the dimpled structure concluded the binary molecule formed a disk-like structure with the gold core ringed by the less dense polymer corona. The ring diameter calculated by cross-sectional analysis was 11 ± 1.5 nm, close to diameter of molecular model when the polymer corona densely packed around the gold core.

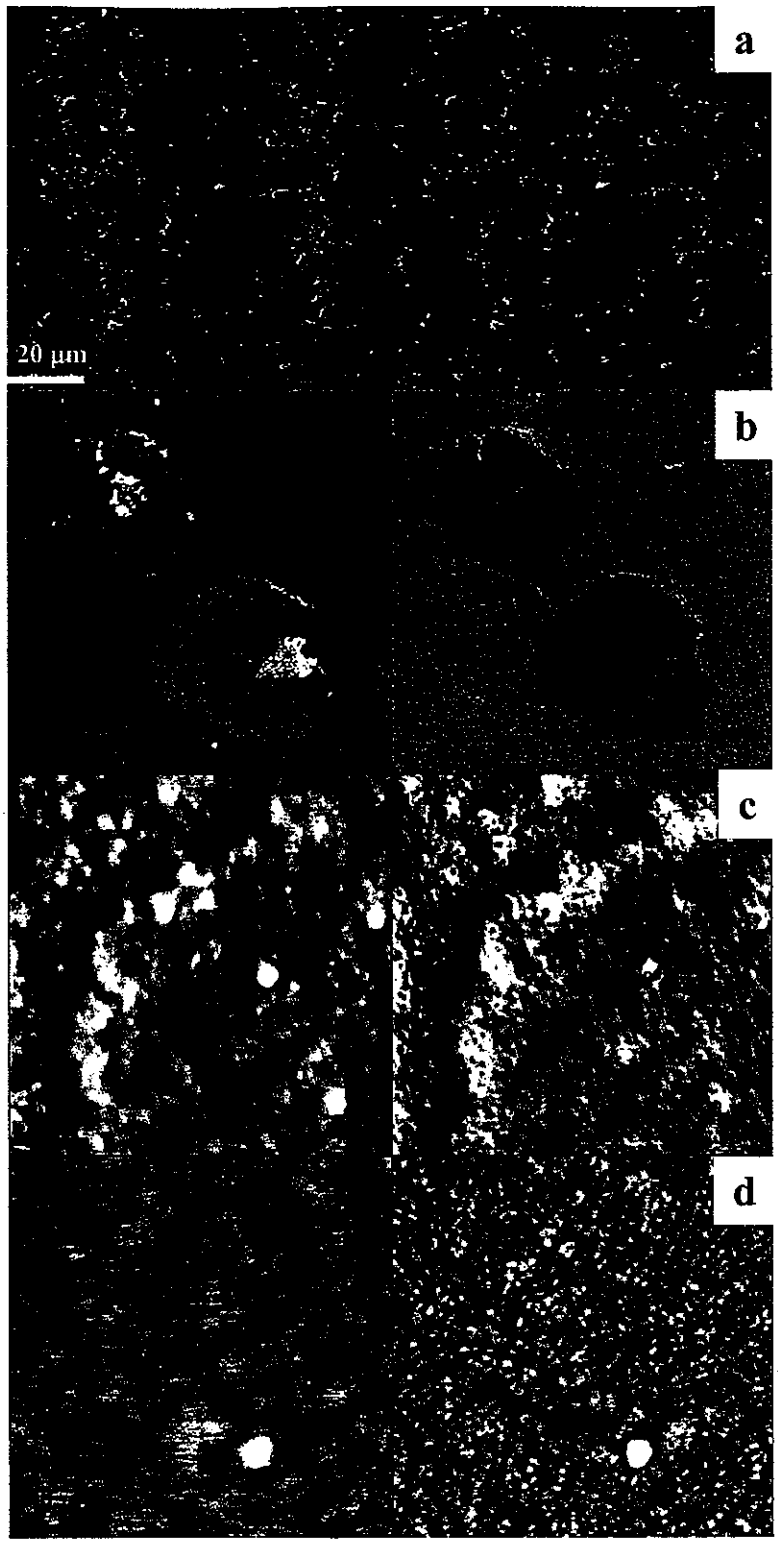

Figure 68. Observational AFM of the LB monolayer deposited at 30 nm^2 (a and b) and high resolution AFM of domain edge for the LB monolayer deposited at 30 nm^2 (c) and the underlying monolayer (d). Z-range for topography (left) was nm and phase (right) degrees.

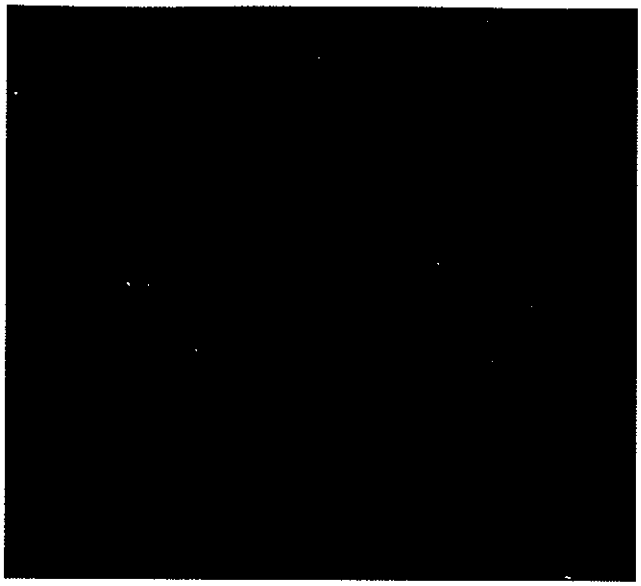

Figure 69. TEM image of the LB monolayer of the polymer brush functionalized gold nanoparticle molecule deposited at 60 nm^2.

Further evidence of the disk shaped molecular conformation was determined from TEM images of monolayers deposited at lower molecular areas (Figure 69). The molecules formed irregular circular structures with widely varying diameters. The gold nanoparticle core was indistinguishable from the polymer brush shell due to low contrast and resolution since the molecular dimensions were near the resolution limit. The average molecular diameter calculated was 12 ± 7 nm for a monolayer deposited at 60 nm^2 per molecule. The range of molecule diameters calculated from TEM was considerably larger than the range calculated from the high resolution AFM. The LB monolayers deposited on the silicon substrate appeared more densely packed than the monolayers deposited on the TEM grid, suggesting the densely packed monolayers exerted more control over the molecular dimensions and reduced the range of diameters observed.

The inclusion of gold nanoparticles assisted the observation of the presence of PEO and PB chains in Langmuir-Blodgett by Raman spectra due to surface enhancement. Three peaks attributed to the polymer brushes were observed in the Raman spectrum of the deposited monolayer with estimated thickness less than 2 nm (Figure 70). The peak at 1495

cm^{-1} was assigned to the PEO chains while the peaks at 2000 and 2279 cm^{-1} were assigned to the PB chains.[206]

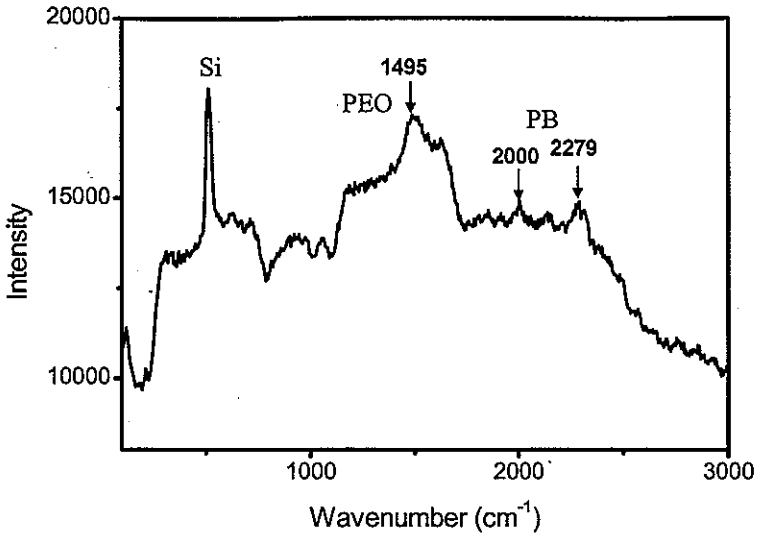

Figure 70. Raman spectrum of the polymer brush functionalized gold nanoparticle monolayer deposited at 60 nm^2.

6.3 Discussion and Conclusions of Gold Nanoparticle Molecules

A gold nanoparticle core functionalized with Y-shaped amphiphilic polymer brushes formed monolayers at the air-water and air-solid interface. The flexible PEO and PB arms segregate at the air-water interface as the hydrophilic PEO arms submerge in the water subphase. The long polymeric arms disassociated into blocks, insulating the gold nanoparticle core from the neighboring molecules and the underlying subphase. The cross-sectional area determined from π-A isotherms confirmed the collapse of the polymer brushes around the gold nanoparticle core, thereby forming a polymeric corona. Comparison of the monolayer thickness determined by AFM and the molecular dimension calculated from models indicates a flatten conformation of the binary molecules at interfaces. The minimal height difference between the domains and the underlying monolayer combined with similar texture observed for both suggests the molecules formed condensed areas with greater thickness within the less dense monolayer as the area per molecule was decreased. Direct observation of the PEO and PB polymer brushes by surface enhanced Raman spectroscopy was produced by the incorporation of the gold nanoparticles within the monolayer.

CHAPTER 7. RESULTS – ROD-COIL MOLECULES

Three series presented in this thesis are based on a rigid rod core with flexible branches radiating symmetrically or asymmetrically from the ends of the core. A rigid phenylene core is functionalized with flexible tails of differing lengths attached at opposite ends of the core. The second series holds the molecular weight of all four samples constant while the number of tail branches is increased (Figures 10, 11, and 12). To maintain the equal molecular weight the flexible tails are decreased in length. The effect of increasing the degree of branching in the flexible tails will be discussed as well as the effect of increasing the number of focal groups. Finally, tetra-branched flexible branches are attached asymmetrically to a rigid rod core to discern the effect of the tree-like architecture on the ordering behavior of rod-coil molecules. The results from all three studies are presented below.

7.1 Linear Rod-Coil Molecules

The length of the flexible coils is increased while the rigid core fragment remains consistent for the **CRC-N** series. Therefore the degree of branching is eliminated to study the effect of the influence of varying the molecular weight of the oligioether tails. To balance the hydrophobic behavior of the rigid rod core flexible poly(propylene oxide) tails are attached to the terminal ends of the core. By increasing the number of monomeric units in each tail the ratio of the volume fraction transition from favoring the rigid core block to favoring the flexible coil block. For **CRC-3**, **CRC-6**, **CRC-17**, and **CRC-22** the number of mers in the flexible tails is indicated by the number in the molecular name (Figure 10).

The π~A isotherms for all **CRC-N** have an initial increase in surface pressure upon decrease in molecular area and a plateau in pressure before the final steep increase in pressure and a final collapse (Figure 71). The increase in length of flexible tail translates into an increase in area per molecule. The initial area per molecule is determined by extrapolating a line along the rise in the π~A isotherm to zero pressure. By this technique the area per molecule for **CRC-3** is determined to be 0.5 nm^2 and **CRC-6** is 0.74 nm^2. The complete π~A isotherm for the molecule with the longest tails, **CRC-22** with technically

difficult to obtain within one run due to the high cross-sectional area and limited compression ratio of the LB trough. The area calculated for the rigid core is 1.5 nm^2 for face on orientation and 0.3 nm^2 for edge on orientation. The intermediate area indicates unstable amphiphilic behavior and likely the formation of a mixed structure or bilayer at the air-water interface.

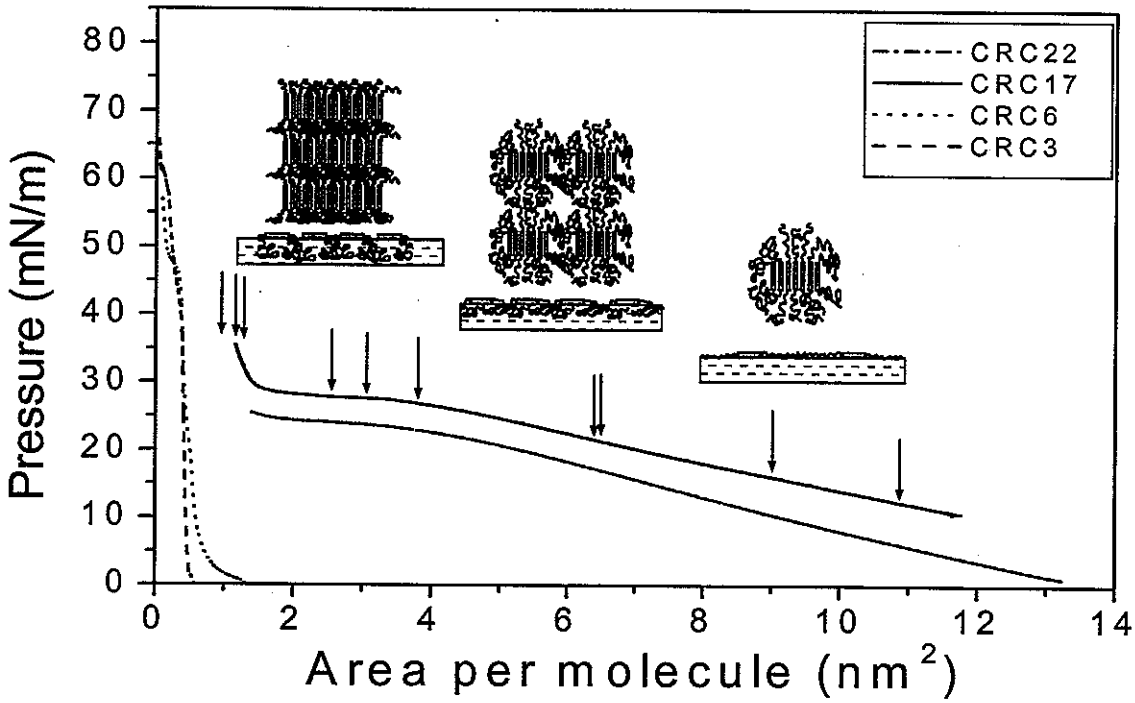

Figure 71. The π~A isotherms for the rod core based linear molecules. For **CRC-17** the arrows indicate the various samples studied in detail. Top and side views of molecular models of the reorganization of the **CRC-17** molecules at the air-water interface as the surface area is decreased are shown also. The transitions from circular micelles, rectangular lattice of circular micelles, and lamellar ordering of coalesced micelles.

CRC-3 and **CRC-6** prove not to form stable amiphiphilic monolayers. The monolayer collapse was evident in the incomplete monolayer structure of the lower generations. AFM studies of deposited monolayers for surface pressures near plateau and final sharp increase show domain structures and wrinkles in the morphology (Figure 72). The defects in the monolayer and the smaller than expected cross-sectional area for the two

compounds suggest the air-water interface is unfavorable for the formation of monolayers. The balance of volume fractions favoring the hydrophobic rod block appear to be unable form a stable monolayer.

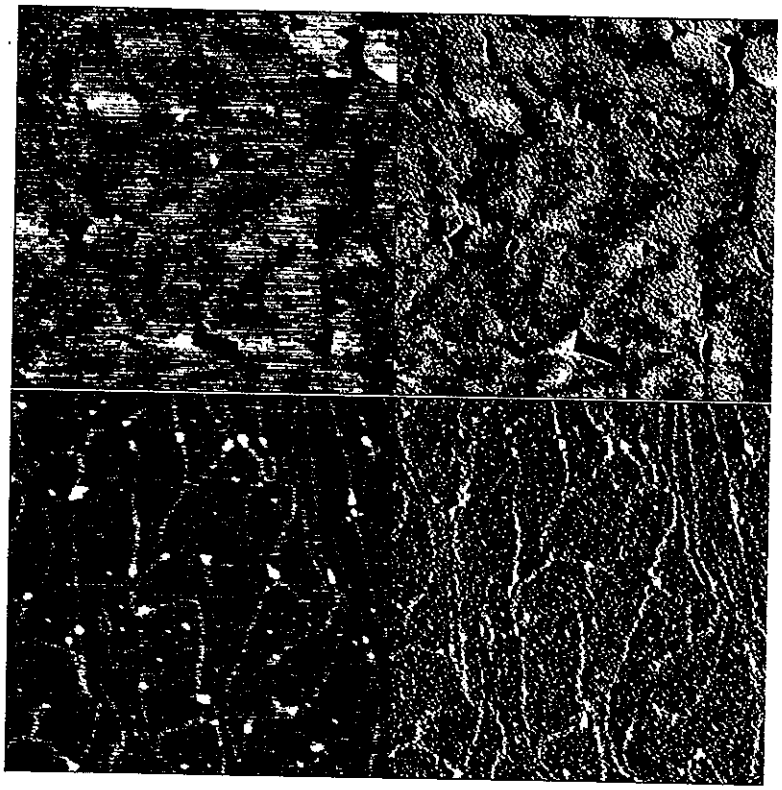

Figure 72. AFM topography and phase images of a) 2 x 2 μm image of **CRC-3** and b) 2 x 2 μm image of **CRC-6**. Z range is 10 nm for topography and 15 degrees for phase.

Unlike the shorter tailed molecules, the **CRC-17** molecules with longer flexible tails demonstrated classic amphiphilic behavior with steadily rising surface pressure for the surface area per molecule below 13 nm^2, constant pressure for the surface area within 3.3 – 1.5 nm^2, and final collapse for the surface area below 1 nm^2 (Figure 71). Reversibility of the monolayer behavior at the air-water interface was tested by repeating compression-expansion cycles for the monolayer several times. A very modest hysteresis was observed for each cycle for **CRC-17** indicating modest creep and a short recovery time for the long PPO chains to expand to original random coil conformation. The **CRC-17** monolayers were deposited on

the solid substrates at different surface pressures, from different solutions, and under variable "annealing" conditions (monolayer relaxation before the deposition) and showed consistent results. The **CRC-17** monolayer possess a variety of molecular organizations at various surface pressures resembling that predicted for the bulk rod-coil molecules.[207,208]

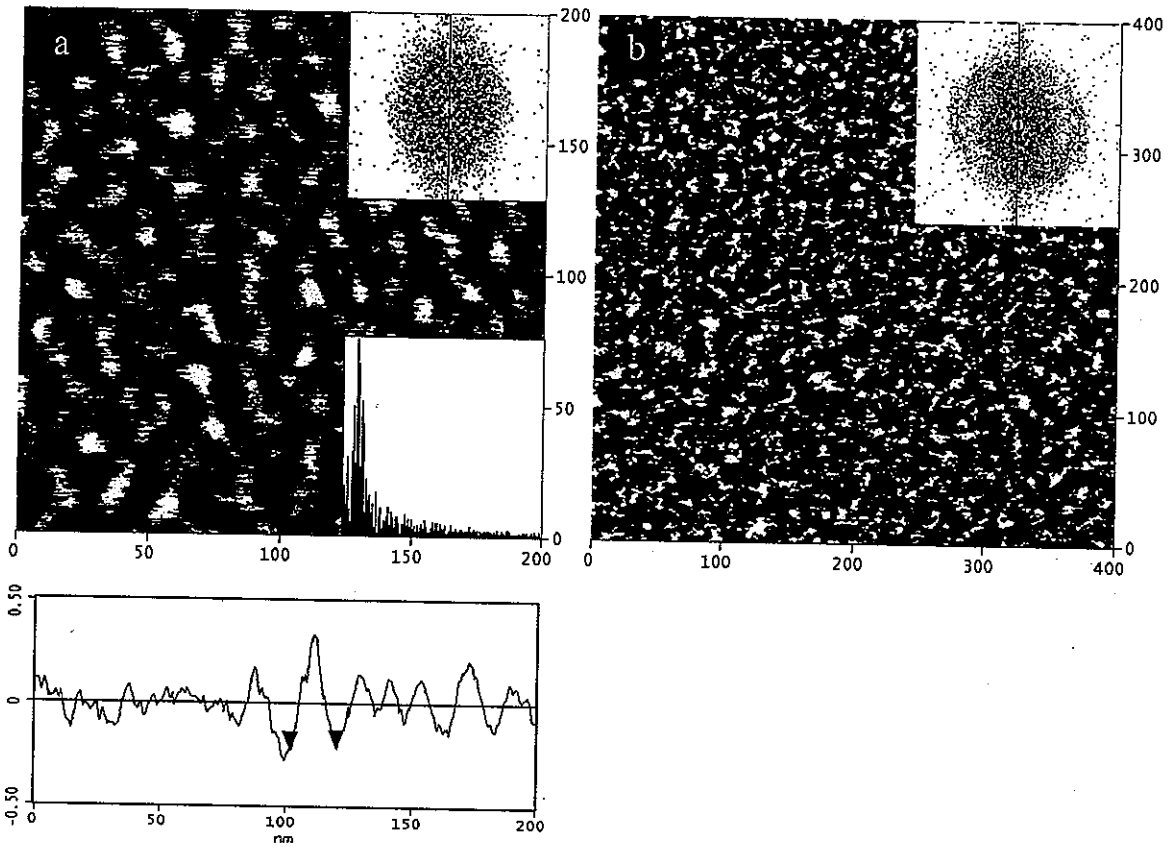

Figure 73. AFM topography images of **CRC-17** of monolayers deposited at a) 3.6 nm^2 per molecules, 400 x 400 nm, Z-range is 1 nm and b) 2.2 nm^2 per molecules, 200 x 200 nm, Z-range is 0.8 nm. 2D Fourier transforms for both monolayers are shown in inserts.

AFM observations for **CRC-17** showed that monolayer films were smooth and uniform on a microscopic scale (5-20μm across). Higher magnification revealed a variety of surface morphologies (Figures 73 and 74). At a high area per molecule of 7-12 nm^2 close to the cross-sectional area of **CRC-17** molecule lying flatly on a surface (about 8 nm^2), grainy surface morphology was visible with distance between the grains of 18±4nm and a lateral

dimension of the grains of 12±3 nm (evaluated taking into account tip radius of 20 nm) that is close to the length of the molecules in the near extended conformation (12-16 nm, depending upon the degree of PPO chain curling). Short-range ordering in the micellar packing was expanded over 5-7 grains as demonstrated by cross-sections (Figure 73). Heights of these grains were in the range of 0.3-0.4 nm that corresponded to the overall thickness of the monolayer of 0.34 nm obtained from ellipsometry. This confirmed a flat arrangement of **CRC-17** molecules under these conditions.

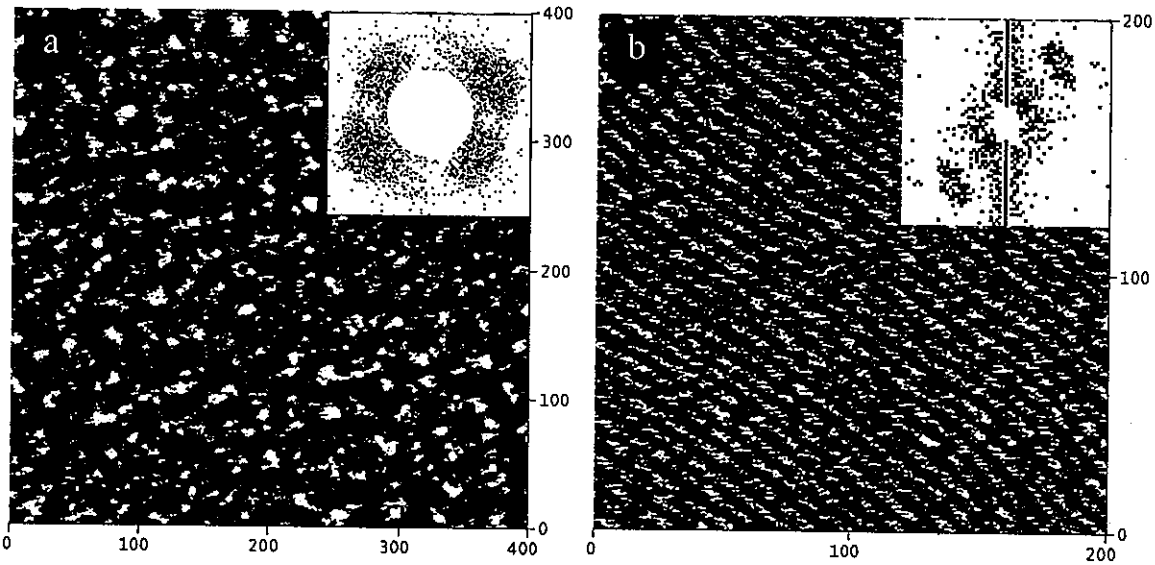

Figure 74. AFM images of the **CRC-17** monolayer at high surfaces pressures. a) Topographical image at the surface area of 3.6 nm^2 per molecule, 400x400 nm; the Z-range is 1nm; the inset shows the 2D Fourier transform. b) Topographical image at 2.2 nm^2 per molecule, 200x200 nm; the Z-range is 0.8nm; the insert shows the 2D Fourier transform.

Compression of the **CRC-17** monolayer to the surface area per molecule below 7 nm^2 lead to the first signs of aggregation of grainy structures and the formation of poor ordered clusters as confirmed by the appearance of a diffuse halo on 2D Fourier transforms. Further compression below 4 nm^2 (significantly smaller than the molecular area of a flat molecule, 8 nm^2) resulted in the formation of relatively well-ordered lattice of rectangular type as confirmed by the four-point Fourier transform (Figure 74a). The unit cell dimensions are 10.6 x 9.7 nm. The thickness of the monolayer in this state increased twofold to 0.6-0.75 nm.

Finally, at lower surface area per molecule (below 2.5 nm^2), on a verge of monolayer collapse (the molecular area of the rigid block is about 1.5 nm^2), a perfect lamellar lattice becomes visible with periodicity of 6.5 ± 0.6 nm (Figures 74b). The lamellae are very well ordered on a microscopic scale and possess high orientational ordering as can be seen from the 2D Fourier pattern (Figure 74b). Uniform height is observed within the lamellae. Across the lamellar structures, 4-5 nm long elevations are separated by 2 nm long grooves of 0.3 nm deep. On a larger scale, micrometer size domains possess sharp boundaries of abrupt change of lamellar orientation and minor bending of the lamellae within the domains (Figure 74b). The thickness of the monolayer increases to 1.5 nm in this range and rises to 4 nm for surface areas below 1.5 nm^2, within the collapse region.

Molecular reorganization of the rod-coil molecules within the Langmuir monolayer can be understood considering theoretical treatment of phase states of rod-coil molecules in the bulk state and known behavior of water-soluble flexible chains at the air-water interface.[207,208] First, for a given chemical composition of **CRC-17** molecules with a volume fraction of the rod block of about 20% (as calculated from volume fractions of different blocks), theory predicts the formation of cylindrical micelles and their aggregates with rod blocks tightly packed and surrounded by coil blocks. 2D analogous of a cylindrical micelle is a circular micelle. Ordered lattices of cylindrical structures are expected for rod volume content higher than 30%. Finally, for rod content higher than 50%, the formation of lamellar morphology is expected. Although the phase transition theories discussed consider a diblock rod-coil molecule, it is suggested that the same transitions and phases can be expected for a triblock rod-coil molecule. This is confirmed by numerous studies of bulk morphologies of block-copolymers. E.g., Molau[209] and Dawkins[210] suggested similar models for expected morphology AB and ABA block copolymers with varying volume fractions.

Indeed, it is observed that at a very low surface pressure where molecules lie flat and the molecular area is close to unperturbed molecular dimensions, the rod-coil molecule forms micellar structures with dimensions close to the length of the molecule with slightly coiled tails. Taking molecular area of about 8 nm^2 and packing coefficient of 70%, it can be estimated that a single aggregate contains 20-30 molecules packed in a manner similar to a "monolayer" puck proposed by Fredrickson for the bulk structure (Figure 71).[207]

Decreasing the surface area available for the rod-coil molecule results in both significant shrinkage of inter-micellar distance and increasing layer thickness. This kind of transition can be associated with molecular reorganization caused by partial desorption of water-soluble tails from the air-water interface into the aqueous phase.[211] At higher surface pressures, the enthalpy gain achieved by this reorganization exceeds the loss of entropy caused by folded and compressed flexible tails. This restructuring leads to the formation of an ordered lattice from micelles composed of the topmost rod-block and partially submerged flexible tails (Figure 71). The total layer thickness doubles and "effective" content of the rod-blocks in the topmost layer increases to 31% due to partial submerging of the flexible tails. This composition at the air-water interface should favor to cylindrical packing of micellar aggregates.[208] Indeed, this type of molecular reorganization is observed for the **CRC-17** monolayer at this surface pressure. A total number of molecules in one circular micelle estimated from the unit cell dimensions remains unchanged (20-30 molecules). The rectangular unit cell observed is different from the hexagonal structure predicted for the bulk state.[208] However, it is similar to the tetragonal lattice of micellar aggregates with unit cell parameters of 9.0 x 8.3 nm observed for this molecule in the bulk LC state.[212]

The compression of the monolayer to the surface area comparable with rod-block dimensions, initiates the second molecular reorganization. This reorganization can be related to the folding of the flexible tails and their dehydration due to expelling associated water molecules from densely packed areas beneath the air-water interface (Figure 71).[211] In this state, flexible tails can adopt brush-like conformation increasing a total thickness of the layer to about 1.5 nm. The thickness of grafted flexible molecules of comparable molecular weight is within 1-3 nm depending upon the grafting density.[213,214,215] As a result of chain desorption, effective content of the rod blocks at the air-water interface increases further to about 50%, thus, causing the formation of lamellar structures favorable for such content.[208] Micelles are coalesced to form uniform lamellae. Further compression leads to the monolayer collapse and the formation of the second layer.

CRC-22 molecules with a lower content of rod blocks (below 15%) do not show the richness of the phase behavior of the previous molecule despite a similar shape of the π~A isotherm (Figure 71). This was puzzling considering that even modest compression would

result in sufficient change of effective composition and, thus, similar molecular reorganizations. The very high fraction of water-soluble blocks disturbs a delicate amphiphilic balance of the rod-coil molecules at the air-water interface, preventing reorganization of rod blocks immersed with a sea of hydrophilic block beneath. Probably steric constraints imposed by a high volume of PPO blocks compressed in the water subphase on chemically attached rod blocks affect their ability to aggregate in ordered structures.

In fact, the monolayer displays poorly ordered micellar aggregates at all pressures. Only at the highest reachable pressure, in the collapse region (area per molecule of below 1.5 nm^2), weak tracks of lamellar structures within the collapsed monolayers increases from 0.6 nm at 10 nm^2 per molecule to 4.1 nm at 1.5 nm^2 per molecule at the highest pressure. The thickness of the monolayer at higher surface pressures indicate a rearrangement of the coil blocks, but the lamellar structure formed is incomplete. Unlike the **CRC-17** molecules, which partially submerged the PPO coils, the **CRC-22** molecules fully submerge under higher pressure creating a bilayer of compressed molecules. Instead of submerging the tails until the volume fractions is favorable to a phase change, the entire molecule is pushed out of the surface plane and supports the molecules that remain at the air-water interface, thereby increasing the monolayer thickness while having little noticeable effect on the surface morphology.

The linear rod-coil molecules show a modest trend between the molecular structure at the air-water interface and the total length of the molecule. The two lowest molecular weight generations form bilayer structures with defects and wrinkles seen in the morphology. The molecules with three and six PPO mers per tail appear to lack the ability to organize into stable monolayers. The weak attraction between coil blocks and the water subphase is outbalanced by the repulsion of the hydrophobic core. Greatly increasing the molar ratio between the rod and coil blocks allows for the molecules to form stable monolayers with interesting phase transitions. The decrease in area per molecules for the **CRC-17** results in a transition from micellar formation to organization of the micelles in an orthorhombic structure and finally lamellar structure. The flexible coils reorganize and submerge in the water subphase, thereby supporting the hydrophobic cores. The delicate balance in the amphiphilic behavior is disrupted when five additional PPO mers were added to each tail.

The **CRC-22** forms disorganized micelles at high area per molecule and limited lamellar structure at lower area per molecule. The longer coil tails prove unable to reorganize as well as the tails of the **CRC-17** molecules. The necessary balance in rod to coil blocks appears to be optimum for the **CRC-17** molecule.

7.2 Dumbbell Shaped Rod-Dendron Molecules

The structural organization properties of dendrimers can be influenced by introducing branching in the architecture of a dendrimer while molecular weight remains constant. This is seen in the **RDM-N** series of molecules with the degree of branching increasing as the generation increases. The first generation has one tail attached to each end of the rigid core. The number of branches increases to two, four and six tails per end for the second, third and fourth generations respectively. The length of the flexible oligioether tails decreases as the branching increases to maintain the constant molecular weight and chemical composition. Thereby all differences between generations can nearly be attributed to the degree of branching and the influence of molecular weight can be discounted.

The first differences between generations can be seen in the π~A isotherms for the **RDM-N** series. The π~A isotherms show the formation of stable monolayers for all four molecules with a consistent increase in the surface pressure until collapse (Figure 75). π~A isotherms for **RDM-1**, **RDM-2**, and **RDM-3** display a gradual increase in pressure for areas (1.1-1.6 nm^2) slightly below the expected molecular area (1.5 nm^2) for the rod block laying flat on the surface as estimated from molecular models. This behavior suggests the flexible tails submerge in the subphase and support the hydrophobic rigid core. Sharp increases in the surface pressure below the estimated cross-sectional area of the core indicate the collapse of the monolayer of **RDM-2** and **RDM-3**, and suggest the formation of bilayers. The first generation lacks this behavior suggesting the branched tails have a nondisturbing effect on the molecular packing of the rod segments. The **RDM-4** sample has a steady increase in surface pressure for areas below 2.5 nm^2. This area is near the cross-sectional area of the entire molecule laying flat on the surface thereby implying the high degree of branching and the short length of the tails prevent the tails from submerging as would be expected for the hydrophilic tails.

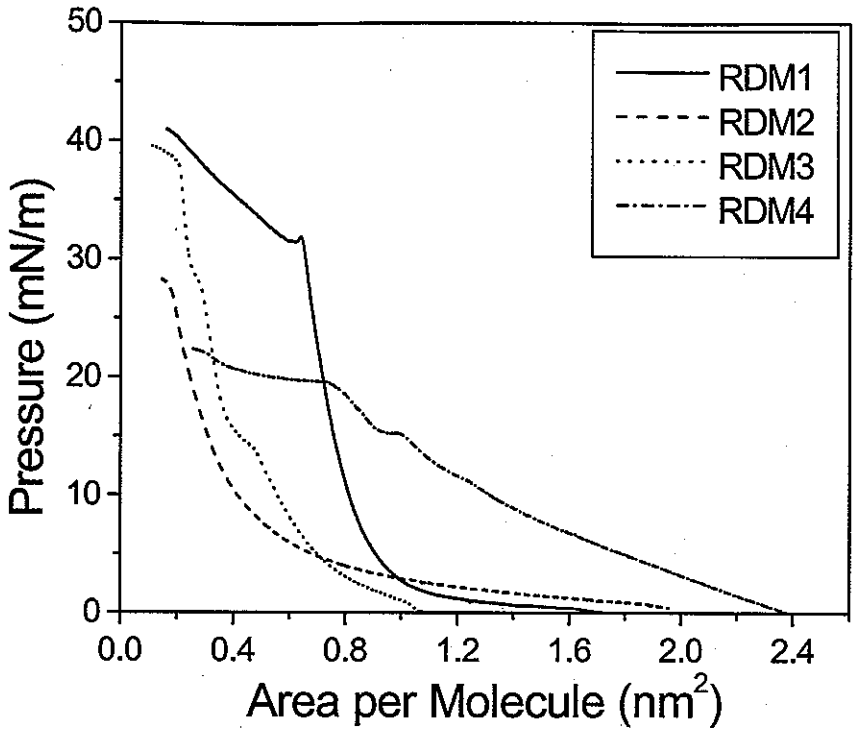

Figure 75. π~A isotherms for the **RDM-N** series.

The differences are more apparent in the AFM studies of the deposited monomolecular films. Topography images of **RDM-1** show a continuous, incomplete monolayer (Figure 76a). Although the monolayer does not cover the entire surface the segregation is incomplete. Rather than organize in domains the molecules spread over the entire surface area and create a continuous monolayer with large holes in the structure.

Unlike the first generation, **RDM-2** and **RDM-3** form circular aggregates that lack uniformity in the films (Figure 76b,c). The molecules form domain aggregates with no macromolecular organization within the individual domains. Although both generations lack uniform structure, they differ from one another as well. Topography images of **RDM-2** show domains several hundred nanometers across with varying shape and size (Figure 76b). **RDM-3** appears to form a grainy monolayer with small circular grains of additional height sparsely distributed. The thickness (1.4-2.3 nm) measured by ellipsometry is several times higher than the diameter of the rod-coil molecules (0.5 nm), confirming the monolayer collapse.

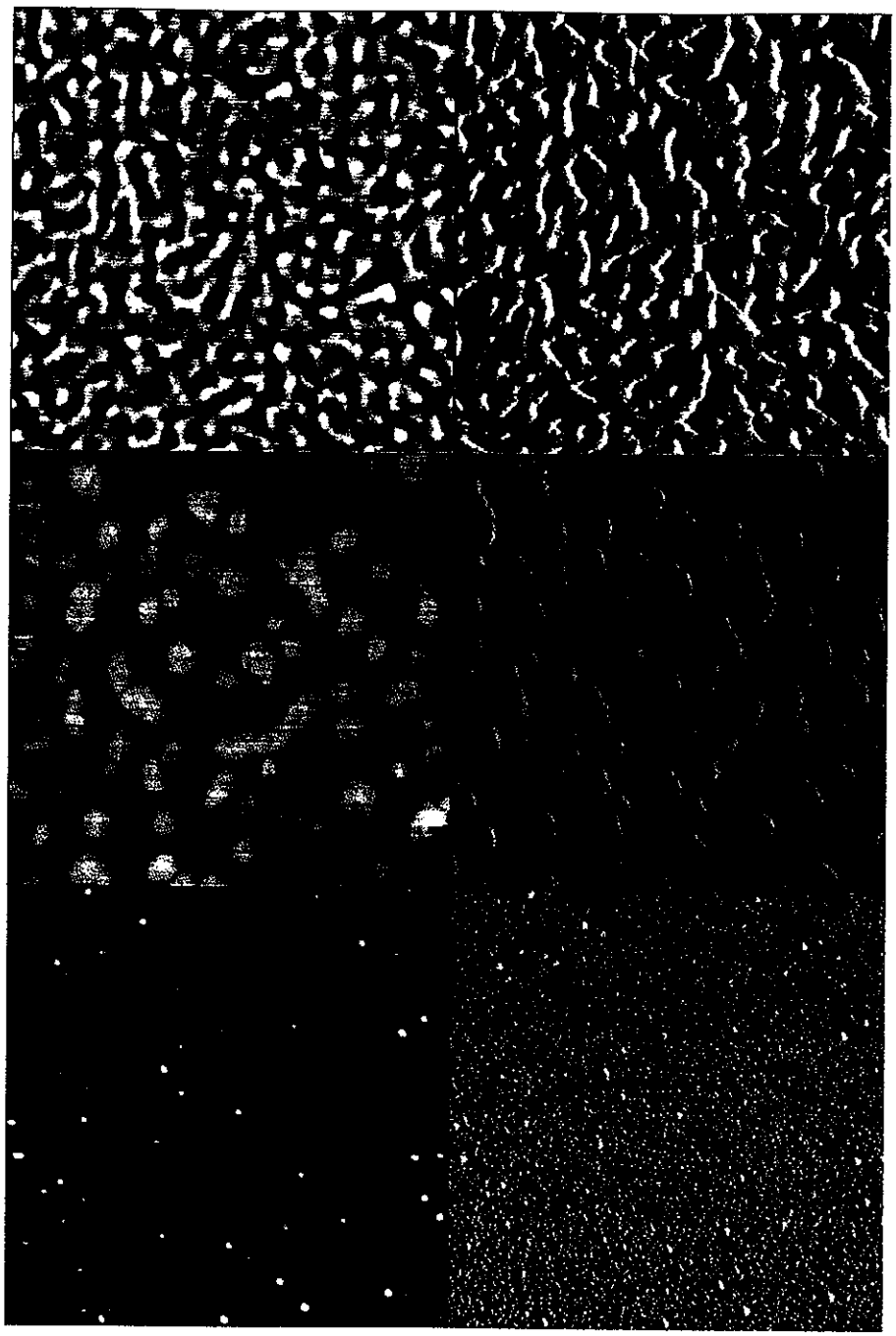

Figure 76. a) 1 x 1 μm image of **RDM-1** b) 1 x 1 μm image of **RDM-2** c) 2 x 2 μm image of **RDM-3**. Z range for all images is 10 nm for topography (left image) and 10 degrees for phase (right image).

The 1.7 nm thick deposited layer of **RDM-4** shows well-developed domain morphology with dimensions of several microns across and a texture of 50 nm grains (Figure 77a,b). The structure is on a larger scale than the other three molecules in the series. The lack of uniformity in monolayers of all samples suggested a lack of organization of the entire series of molecules.

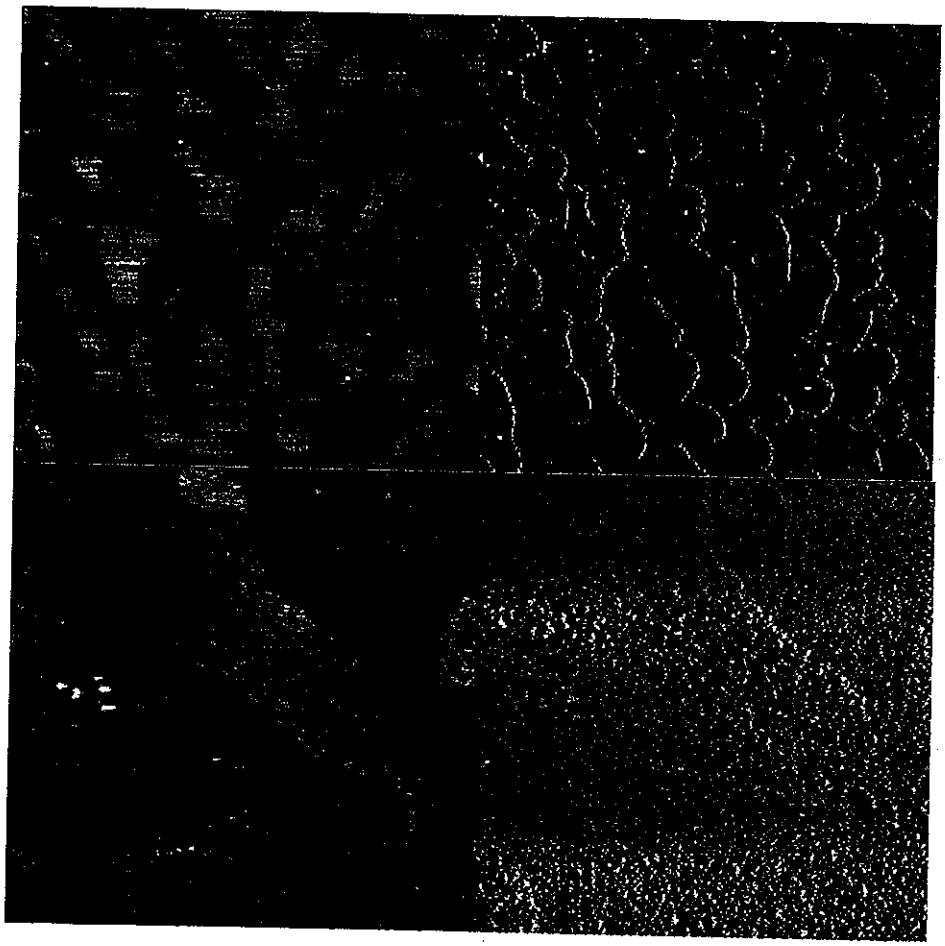

Figure 77. a) 10 x 10 μm image and b) 2 x 2 μm image of **RDM-4**. Z range is 10 nm for topography (left) and 10 degrees for phase (right).

Comparison of the π~A isotherms for all four compounds indicates a lack in stable amphiphilic behavior for all generations. The rigid hydrophobic rod cores are balanced with the flexible poly(ethylene oxide) tails attached to the opposite ends of the core. By branching the flexible tails the mobility of the tails becomes more limited. To maintain the balance in

the chemical composition of all four generations the length of the tails is decreased. The subsequent decrease in the length of the tail decreases the flexibility of the tails. The number of terminal focal groups and the volume they occupy is increased with the increase with the generation number. The limiting surface area per molecule for the first three generations is between the expected cross-sectional for face-on or upright orientation of the rod cores. These compounds likely form multilayer structures with the molecules preferring to pack molecule on molecule than interactions with the water subphase. The fourth generation appears to have a flat-orientation with the poly(ethylene oxide) tails remaining at the air-water interface. The shorter tails lack the mobility to partially submerge in the water. The compounds lack a uniform trend in molecular packing.

The AFM images for all generations show domain structures in the higher surface pressure regions. The aggregation of the molecules indicates the molecules prefer to associate in limited ordered layers. The formation of bilayer structures reveals the preference of the molecules to interact with other molecules rather than the water subphase subsequently the silicon substrate. The balance between the hydrophobic and hydrophilic fragments is incomplete of all compounds. The hydrophilic tails are too short to overcome the preference of the rigid core to avoid the water subphase. However the tails are balanced equally on opposite ends of the core therefore the molecule is incapable of packing edge-on to satisfy the rod core and the flexible tails. The formation of the bilayer structure allows for the molecules to partially satisfy both fragments. The thickness of the deposited layers suggests bilayer structures for the second and third generations.

These samples clearly demonstrate the role of balancing the amphiphilic nature of the molecules at the air-water interface. The balance between the hydrophilic tails and the hydrophobic cores is held constant for all four generations. The effect of branching causes the formation of different domain structures for all generations. The transitions from incomplete desegregation to small domains eventually to larger domains composed of smaller grains suggest the degree of branching dictates how easily the molecules can form stable domains. Varying the degree of branching of the dendrimers using a rigid rod core while the molecular weight remained constant proved to have no organizational consistencies.

7.3 Tree-like Rod-Dendron Molecules

The crystallization of the rod segment as well as the competing nature of the rod-coil molecules render the molecules more attractive for ordered self-assembly.[108,216] The tree-like rod-dendron molecules demonstrated a multitude of ordering structures under a variety of conditions in solution and at interfaces, thus suggesting possibly novel ordering phenomena at an evolving air-solvent interface. Previously, it was reported organized surface films of the rod-coil molecules ordered in short range lamellae and two-dimensional micelles.[217] Similar octa-p-phenylene rod-dendrons, which crystallize in a primitive orthorhombic lattice in bulk conditions, were revealed to assemble into capsule-like micelles (diameter of 46 nm) under dilute solution conditions.[218]

7.3.1 Molecular Organization in Monolayers

The competing nature of the rigid rod core and the branched coil tails was examined at the air-water and air-solid interface to elucidate the influence of the molecular architecture on the amphiphilic balance. The terminal group functionality of the tree-like rod-coil molecules was varied to analyze the effect of the shell nature on the molecular ordering behavior at the air-water interface.

7.3.1.1 Molecular Ordering at the Air-Water Interface

The rigid, hydrophobic rod core for both molecules was paired with three branched flexible, hydrophilic PEO chains possess excellent amphiphilic properties. When placed on water in dilute quantities, these molecules typically organize with the hydrophilic PEO branches spread under the water surface as demonstrated for a number of PEO-containing branched molecules.[215,219] Both molecules displayed stable amphiphilic behavior at the air-water interface with **MT-1** demonstrating a classic amphiphilic behavior (Figure 74).

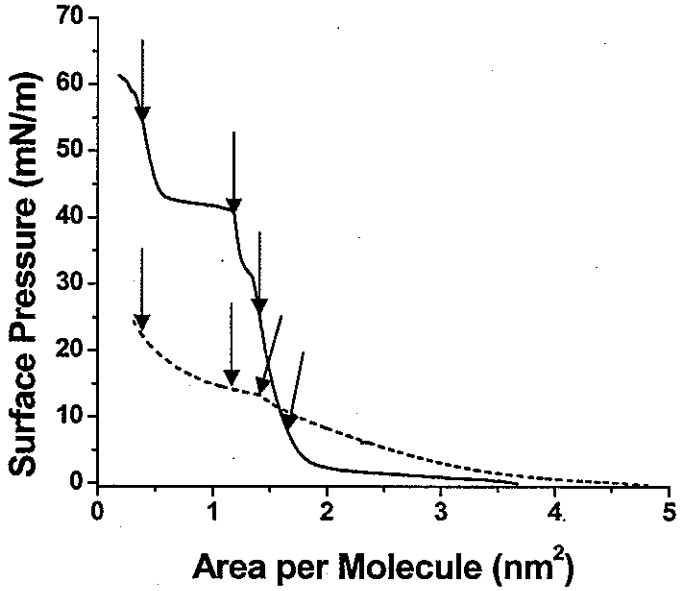

Figure 78. The asymmetric rod-coil molecules form stable monolayers at the air-water interface as shown for π-A isotherm for **MT-1** (solid line) and **MT-2** (dashed line), with deposition points indicated.

The monolayer compression resulted in steady and reversible increase in surface pressure followed by monolayer collapse at 60 mN/m for **MT-1** and 20 mN/m for **MT-2**. **MT-1** underwent several phase transitions observed as the multiple shoulders and plateau regions in the pressure versus molecular area (π-A) isotherms. By extrapolating the steepest slope of the isotherm prior to transition states back to a surface pressure of zero, the limiting cross-sectional molecular area in each particular phase can be determined.[32] The initial limiting cross-sectional of **MT-1** (1.68 nm^2) indicated the PEO chains partially submerged into the water subphase. The lower than expected cross-sectional area contradicted a face-on orientation of the rod core in favor of a tilted orientation. The observed shoulder at 1.44 nm^2 and the plateau at 1.15 nm^2 indicated the collapse of the initial monolayer due to the organized formation of a bilayer structure. The complete collapse of the monolayer of **MT-1** was observed for molecular areas below 0.5 nm^2. The hydroxyl terminated molecule lacked the dense packing structure of the first molecule suggested by the larger initial molecular area

(2.84 nm^2). A similar shoulder in the π-A isotherm near 1.25 nm^2 was observed for **MT-2** although the molecule lacked the sharp phase transitions and appeared to collapse at relatively low surface pressures. Both molecules were deposited at multiple cross-sectional areas of interest to elucidate the nature of intra-monolayer reorganization (see arrows in Figure 78).

7.3.1.2 Monolayer Structure at the Air-Solid Interface

The **MT-1** formed uniform monolayers for thin films deposited at the lowest surface area per molecule (1.60 nm^2) as shown in Figure 4. High resolution AFM exhibited a disordered, finger-like lamellae structure arranged in groups of two or more rows (Figure 79c). Cross-sectional analysis revealed the lamellae width was 4-8 nm, with 3-5 nm spacing, and were approximately 30 nm long with 0.5 nm height observed the surrounding monolayer. Similar surface morphology was observed for LB monolayers deposited at lower cross-sectional areas (1.41 nm^2) with the lamellar structures observed more pronounced. The slight reduction of molecular area resulted in a reduction of RMS roughness in addition to a small increase in effective thickness suggesting the monolayer experienced an increased in uniformity and thickness (Table 14).

At lower cross-sectional area of 1.21 nm^2 (above the first shoulder on the surface-pressure isotherm, Figure 78), significant changes of surface morphology accompanied by significant increase in thickness were observed (Table 14, Figure 80). At this molecular area, the formation of anizodiametric domains occurred. Long, thin domains were readily seen, with occasional cases of neighboring domains aggregating together and forming a doubly wide structure. The long thin domains can be seen to be aligned in the horizontal direction which is perpendicular to the dipping direction indicating an important role of the vertical lifting in domain orientation as well as high mobility. Occasionally, the domains terminated in much wider, irregular structures as seen in Figure 80b. These secondary surface structures are comprised of flat, irregular-shape domains of several hundred nanometers. These domains, with a thickness of 3 nm, represented secondary, topmost layers which started forming at high lateral compression of the underlying monolayer as an initial stage of the bilayer formation in the pre-collapsed state.[32] Cross sections of the AFM images revealed the

height of the thin, ribbon-like domains had an average height of 1.5 nm with a sharp contrast between domains and the underlying monolayer (Figure 76d). The true width of the thin domains ranges from 15 to 35 nm, accounting for tip dilation.

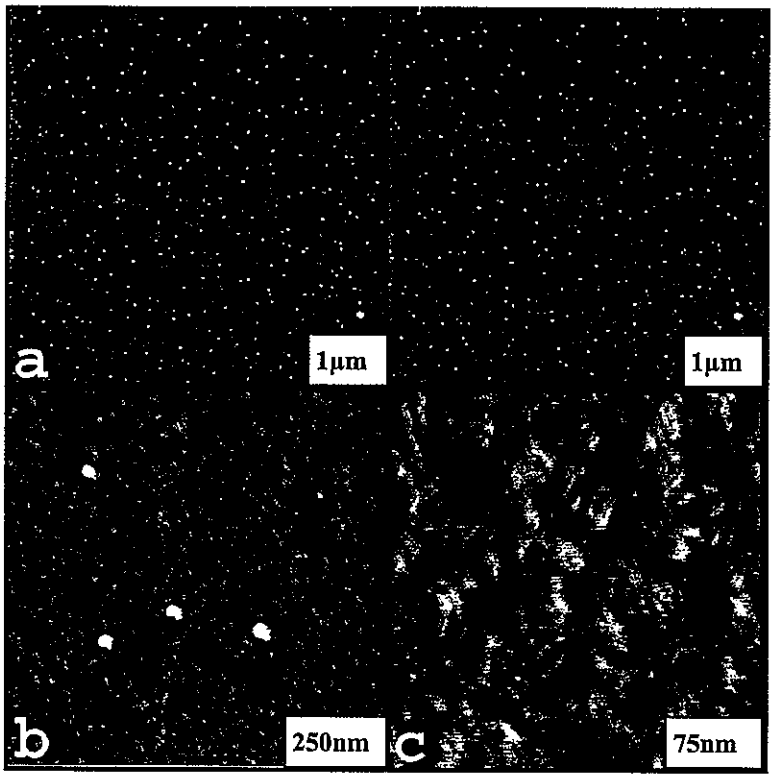

Figure 79. AFM images of LB monolayer from **MT-1** deposited at 1.60 nm^2. a) topography (left image) and phase (right image). Height z-range = 5nm, phase z-range = 20 degrees. b) AFM topography scan. Height z-range = 5nm. c) topography. Height z-range = 2nm.

High resolution AFM of larger, flat, and thicker bilayer domains of up to several hundred nanometers across revealed the presence of very fine, ring shaped surface nanostructures randomly packed within the topmost surface of the outer layer (Figure 81a). The ring diameter determined from the distance between their rims unaffected by the AFM tip dilation was very uniform for all rings observed (Figure 81b). These ring structures were analyzed by multiple cross section of multiple areas and found to have overall external

diameters of 9-12 nm with an interior opening of smaller than 8 nm (see cross-section in Figure 81).

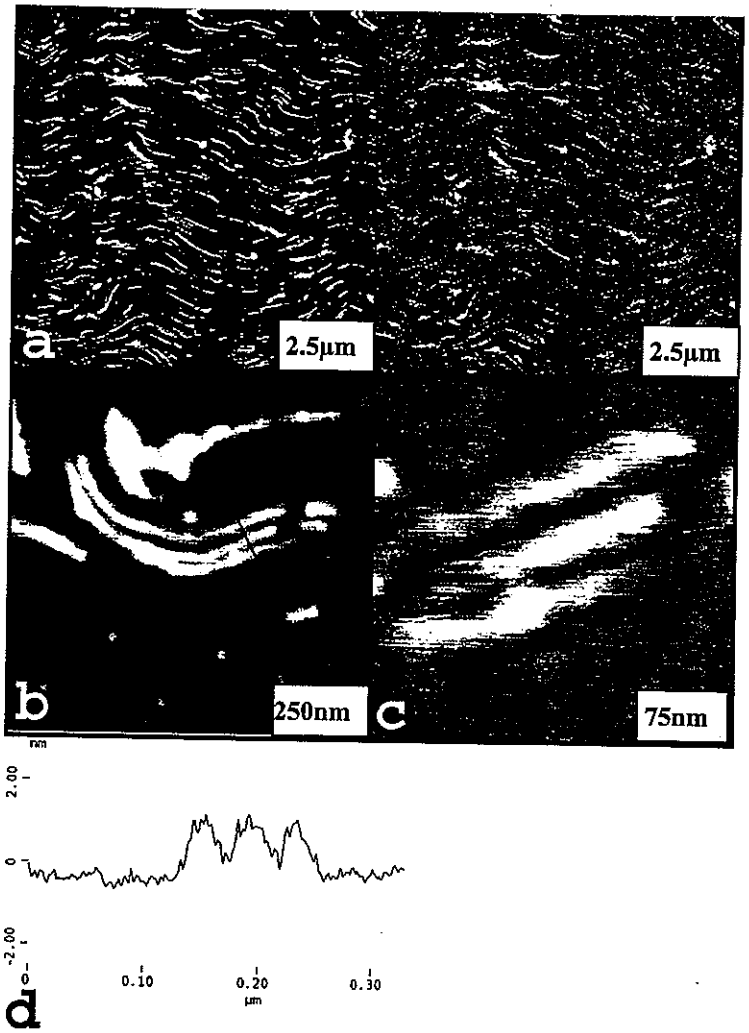

Figure 80. AFM images of LB monolayer from **MT-1** deposited at 1.21 nm^2. a) topography (left), z-range 10nm and phase (right), z-range 10 degrees. b) topography, z-range 5nm. c) topography, z-range 5nm. d) Line cross-section (line in (b)) shows domain height of 1.3-1.5 nm and average thickness of 33nm.

The effective thickness of monolayers deposited at cross-sectional areas above 1.0 nm^2 further suggested the rigid rod core packed loosely above the spread PEO chains (Table 14). The measured thickness (1.1-1.5 nm for **MT-1**, 1.2 nm for **MT-2**) for the less dense

monolayers supported the idea of the rigid cores supported by the spread PEO branches at the air-water interface. Both molecules followed the same general trend expected for PEO-containing branched molecules [220] with lower thickness indicating greater segregation of the hydroxyl-terminated PEO chains in **MT-2**. Reduction of the molecular area below the observed phase transitions (1.2 nm^2 for both molecules) compelled a twofold increase in monolayer thickness (Table 14). Further compression of **MT-1** below 0.5 nm^2 per molecule compelled the largest increase in effective thickness attributable to the multilayer formation upon complete monolayer collapse.

Table 14. LB monolayer properties.

Sample	Area/Mol (nm^2)	Roughness RMS (nm)	Monolayer thickness (nm)	Domain height (nm)	Contact Angle
MT-1	1.60	0.19±0.02	1.1±0.05	0.0	35±1°
	1.41	0.12±0.02	1.5±0.05	0.0	39±1°
	1.21	0.43±0.02	2.0±0.1	1.9±0.2	41±1°
	0.43	0.75±0.02	5.0±0.1	2.1±0.3	47±1°
MT-2	1.41	0.19±0.02	1.2±0.05	0.0	53±1°

The surface composition of the deposited monolayers was revealed by comparison of the water contact angle with the effective thickness. The deposited monolayers for both molecules exhibited low to moderate hydrophobic character (contact angle in the range of 35-62°), indicating a mixed surface composition (a contact angle of 80-120° is expected for surface composed of phenyl rings). Contact angle measurements revealed increasing hydrophobicity for denser monolayers associated with greater exposure of hydrophobic fragments (Table 14). The contact angle measurements for **MT-2** indicated a more hydrophobic surface that can be associated with larger submerging of hydroxyl terminated PEO chains resulting in less exposure at the air-solid interface. As a result, the interactions of the hydrophilic groups are better shielded, resulting in an increase of the effective contact angle.

Replacement of these hydrophobic terminal groups with hydroxyl groups in **MT-2** resulted in complete disappearance of the surface nanostructures observed for **MT-1**. The

comprehensive study of **MT-2** revealed only uniform surface topography without any signs of characteristic surface micellar structures. The additional 12 hydroxyl terminal groups shifted the amphiphilic balance toward the highly hydrophilic branched PEO. This resulted in a much less stable monolayer due to the tendency of the molecules to sink into the subphase at higher lateral compression without forming organized 2D structures.

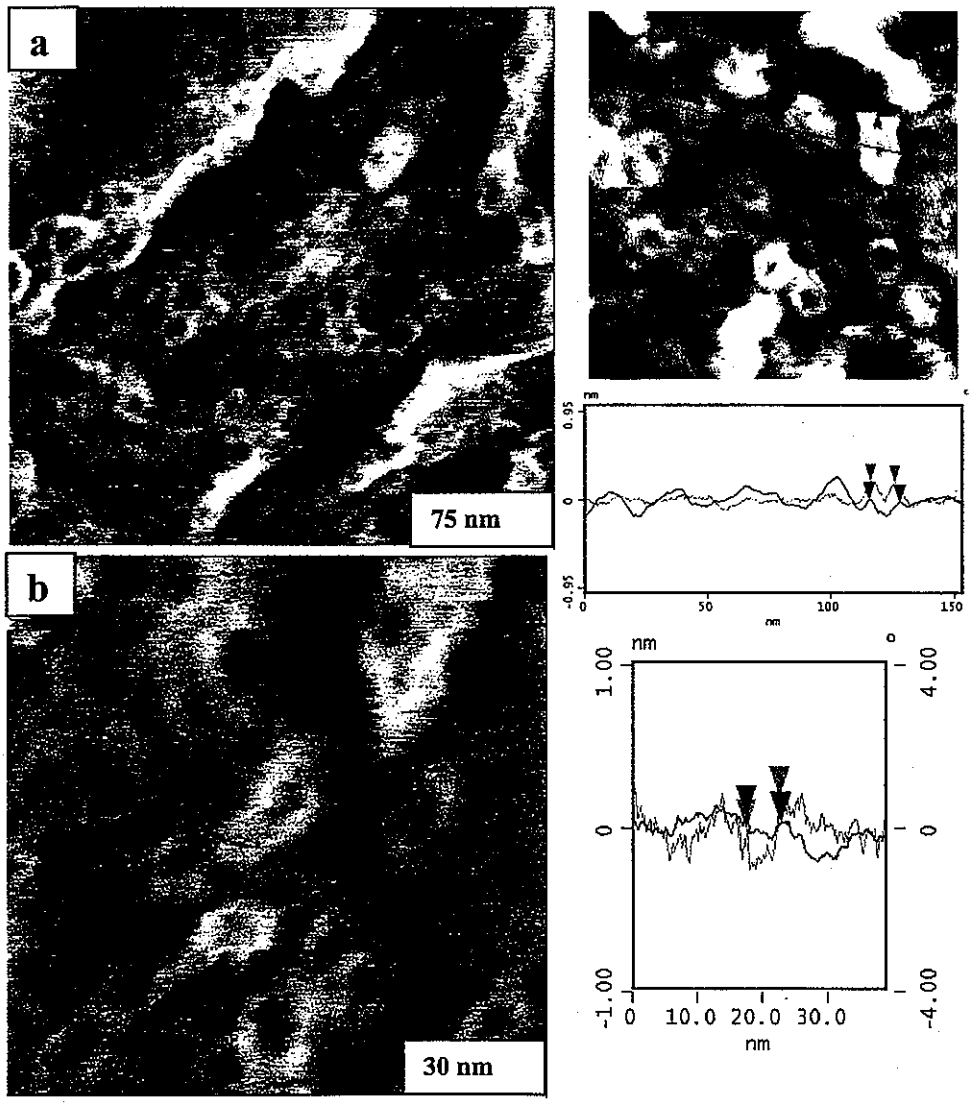

Figure 81. High-resolution phase AFM images of LB monolayer from **MT-1** at molecular area 1.21 nm^2 (a, b) and representative cross-sections of a ring structure; green line is phase and red line is topography with markers showing rim-to-rim distance (right column).

7.3.1.3 Model of Micellar Formation at Interface

Here, possible molecular packing for tree-like **MT-1** observed in the condensed state of the LB monolayer will be discussed. First, it is clear that the relatively low thickness of 1 - 1.5 nm for the monolayer along with the mixed surface presence of hydrophobic and hydrophilic fragments effectively excludes a model of a densely packed monolayer featuring molecular packing with vertical orientation of the rod-like fragments. Thus, a major element of any molecular packing should be a flat orientation of the molecules with hydrophilic branches preferably spread beneath the hydrophobic rod fragments (Figure 82).

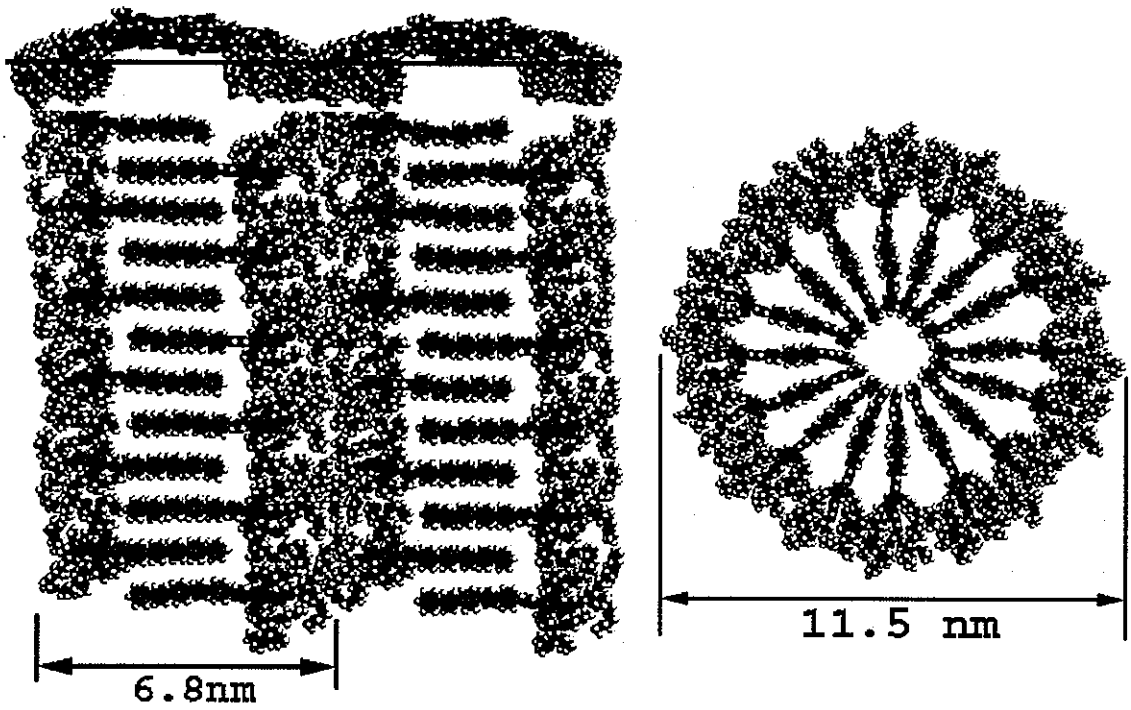

Figure 82. Molecular models of **MT-1** packing showing interdigitated layering (left), side and top view. Molecular model of a circular planar structure (right).

Second, due to the large cross-sectional mismatch between the hydrophobic rods and hydrophilic branches, spherical or cylindrical aggregates should be preferably formed in the solution as was already revealed.[221] The two-dimensional analog of these highly curved spherical aggregates are circular structures which can fill out on a planar interface (Figure 82). Steric interactions should naturally place the rod-like fragments in the interior which

will be stabilized by strong hydrophobic interactions between polyphenylene chains, while the bulkier hydrophilic branches should make up the outer edge of the ring. Finally, considering significant steric mismatch, ribbon-like surface structure can be formed from these molecules only under the condition of significant lateral compression. Under this compression, the bulkier hydrophilic branches can be displaced from the interface and submerged while rod-like fragments should interdigitate to compensate for remaining cross-sectional mismatch (Figure 82).

The models of possible molecular packing discussed above describe fairly well the two surface structures, ribbon-like and circular, observed for **MT-1** at high surface pressures. The lateral dimension of the model of the circular aggregate proposed is evaluated to be about 11 nm which is very close to AFM data on lateral dimensions (Figures 82, Table 15). The thickness of this molecular structure below 2 nm fits to experimental results on the second layer thickness as well. The planar layered structure suggested as an alternative packing model can be assigned to the thin, ribbon-like surface structures (Figure 80). The effective width of the interdigitated packing suggested in this model of about 7 nm is close to the effective width of poorly visible lamellar structures observed in a loosely packed monolayer indicating initial stages of its formation under low lateral compression. At much higher lateral compression, the ribbon-like structures of 15-35 nm packed in correlated manner are several times wider than the width of an individual bilayer (Figure 80, Table 15). This indicates the multilayered internal structure of ribbons composed of several (from 2 to 5) correlated planar layers.

Table 15. Calculated parameters vs. observed values for **MT-1** structures

Parameter	Calculated	Observed
Ring diameter	11.5 nm	10.8 ± 0.95 nm
Ribbon bilayer (width)	6.8 nm/period	15-35 nm
Ribbon bilayer (height)	1.9 nm	1.9 ± 0.2 nm

The formation of ribbon-like structures within the monolayer at lateral compressions close to collapse is consistent with expectations for conditions needed for this type of

packing. It is suggested that initial rupture of some monolayer areas on the verge of the monolayer collapse followed by the formation of the bilayer surface domains releases the lateral pressure and creates conditions for assembling of circular planar structures within the topmost layers. The topmost molecules within the bilayer domains are situated on a top of underlying mixed monolayer that is more favorable for circular packing of these asymmetric molecules by preventing direct interactions. Confinement of the bilayer domains at the interface restricted micellar formation to two dimensional circular micelles in contrast to the preferred three dimensional spherical aggregates observed in solution for similar molecules.[221,222] Similar to the spherical micelle formation in dilute solutions, the circular micelles were preferentially formed when the lateral pressure was removed. However, the location of the domains at the air-water interface confined the micelles to a two-dimensional shape versus the three-dimensional spheres formed in solutions. It is believed that the presence of 12 hydrophobic terminal groups in hydrophilic PEO branches is a critical factor in the formation of these surface structures. Their presence stabilizes the formation of organized surface structures, not allowing the PEO chains to completely submerge in the water subphase during lateral compression as usually observed for non-capped PEO chains in branched molecules.[223,224]

Although the structural reorganizations within the monolayers observed here for tree-like **MT-1** resemble those observed for other amphiphilic rod-coil and star molecules reported recently, [225,220] the branching of hydrophilic fragments makes significant difference in their surface behavior. In fact, linear rod-coil molecules exhibited transformation from rectangular packing of molecular clusters at low surface pressure to well-ordered layering at high surface pressure caused by the submergence of hydrophilic end blocks in the water subphase. This is unlike the dendritic-rod molecules studied here, which showed interdigitated layering caused by their asymmetric character already at low surface pressure and circular micellar structures in the pre-collapsed state. In their two-dimensional state within the monolayers, these tree-like molecules adapt the wedged shape which is favorable for the assembling of a variety of highly-curved organized structures already found in the bulk state for multi-branched molecules.[226] It is suggested that the confinement of the compressed monolayers imposed by the planar interface combined with lateral pressure

enforced the formation of the interdigitated layering instead of the highly-curved cylindrical or spherical micellar structures favorable for these molecules in solution. Partial submergence of the hydrophilic branches in the water subphase combined with this interdigitated layering of the rigid fragments provided an appropriate combination for dense intra-monolayer packing of these highly asymmetrical molecules at the planar interfaces. To the best of our knowledge, such circular surface structures within planar monolayers have been never observed before.

7.3.2 Formation of One-dimensional Structures from Solution

Spontaneous self-assembly of the rod-dendron molecules into one-dimensional ribbons was observed at the air-solvent interface within small droplets of highly concentrated solutions spread on hydrophilic and hydrophobic substrates (Figure 83). Octadecanol, a less volatile, nonpolar solvent, controlled the slow evaporation of the droplet in addition to the uniform dispersion of molecules within the solution. The tree-like rod-dendron molecules have been previously shown to form micelles in polar solvents and at interfaces attributed to the amphiphilic nature of the molecular structure.[217,218] The random growth directionality of ribbons created a web of fibers connecting densely packed ribbon nuclei, resulting in fibers twisting around and weaving together.

Initial stages of the slow solvent evaporation revealed the nucleation of clusters of ribbons at the receding evaporation line (Figure 84). Time lapse optical micrographs revealed the number of ribbons radiating from clusters rapidly multiplied with slower growth along the ribbons once multiple nuclei formed. Further evaporation of the solvent droplet bought about the third stage of exponential growth of the ribbon length with gradual thickening of the ribbons creating a high aspect ratio of the ribbon dimensions. The length (100-1000 microns) of the one-dimensional structures was two orders of magnitude higher than the average ribbon diameter (3.0 ± 2.0 microns) thus confirming preferential ordering of the rod-dendron molecules. The lengthening ribbons drove the cluster nuclei into the droplet thus developing the network of interpenetrating ribbons from neighboring clusters (Figure 84). Formation of ribbon clusters within the droplet was observed after two hours and ribbons formed independent of nucleation points after three hours. The spontaneous self-

assembly of the tree-like rod-dendron moledules occurred in droplets deposited on HOPG, glass, and silicon substrates suggesting the ribbon formation was independent of surface chemistry. Additionally, the shifting location of ribbon nucleation from receding evaporation line to within the droplet suggested the self-assembly behavior was controlled by the droplet concentration. The time scale of the self-assembly of the rod-dendron molecules into the interpenetrating network of ribbons was approximately two hours from nucleation of clusters to complete network formation with complete solvent evaporation after 24 hours.

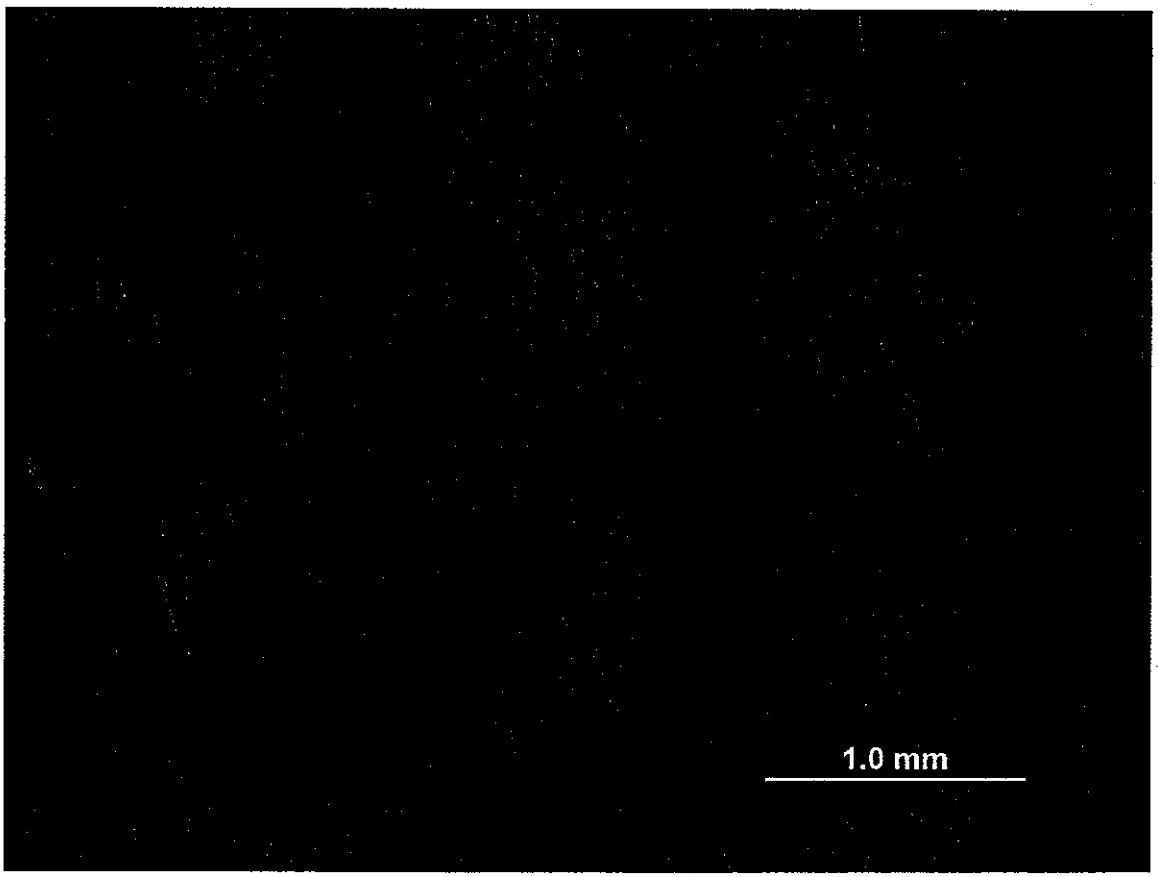

Figure 83. Fluorescent micrograph of dense web-like network of 1D fibers of rod-coil dendrons.

The one-directional growth of the nanostructures was confirmed by the calculation of the Avrami exponent using the following equation.

$$1 - V(t) = \exp(-Bt^{k}) \qquad (6)$$

V(t) was the volume fraction of polymer crystallized at time t, B was a collection of constants, and the Avrami exponent k was determined by the nucleation mode and dimensionality of the crystal growth.[227] For the self-assembled ribbons of the rod-dendron molecules k was calculated to be approximately equal to one, thus indicating the one-dimensional (1D) growth of the nanostructures. The 1D growth mechanism was further observed in the higher aspect ratio of the ribbons created by the high growth rate of the ribbon length as the fiber cross-section gradually thickened.

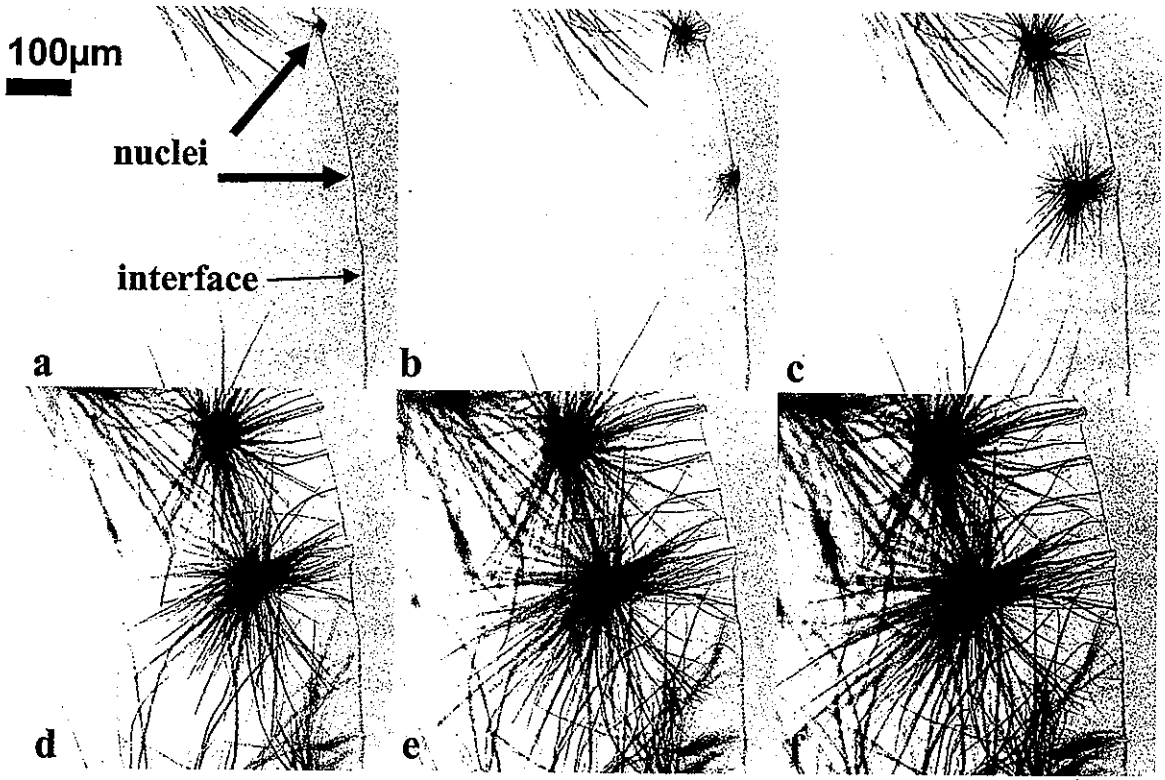

Figure 84. Time lapse optical micrographs of fiber growth at the receding evaporation line taken at a) 40, b) 50, c) 60, d) 100, e) 140, and f) 180 minutes.

Higher resolution optical micrographs demonstrated the tendency of the rod-dendron molecules to form highly crystalline, one-dimensional ribbon structures (Figure 85a). The transparency of the core coupled with the opaque edge of the one-dimensional structures suggested the rod-dendron molecules formed a cylindrical fiber or a collapsed tubular fiber. The 1D fibers exhibited no trend of preferential ordering directionality while illuminated.

with polarized light. Helices along the fibers pinned between the interface and nuclei conflicted with the cylindrical cross-section. Conversely, high resolution SEM images revealed inconsistent cross-section geometry of the larger fibers. The high network density forced the smaller fibers to intertwine and layer over larger fibers with a fine surface texture in the growth direction. Uniform fluorescent behavior along the fibers coupled with the higher intensity fluorescence at intersections of fibers suggested a solid ribbon formation with rectangular cross-section. The higher intensity fluorescence observed for overlapping fiber was attributed to constructive interference between the two fibers. Further conformation of the ribbon structure was revealed from AFM presented below.

Complex ordering of the rod-dendrons in the ribbon growth was further exposed in large scale morphology studies. Tens of large ribbons radiated from the nuclei with no preferential growth direction with additional smaller diameter ribbons further congesting the ribbon network. A dense web-like network formed as the growing ribbons from neighboring nuclei layered and entangled. The ribbons exhibited twisting, branching, and recombination in addition to the irregular helical structures discussed above (Figure 85b). Random directionality and rate of ribbon growth exhibited in the network indicate stepwise growth with ordering focused along the ribbons. Similar dense networks were observed on quartz, glass, HOPG, and silicon substrates, concluding the substrate surface chemistry did not affect the ribbon growth. Smaller diameter ribbons appeared to bundle into and splinter off larger diameter ribbons with the uneven surface structure suggesting uneven ribbon growth.

Helices formed along ribbons pinned between the nuclei and the interface lacked preferential directionality in addition to exhibiting the indiscriminate periodicity (Figure 85b). Compression along the length of the ribbons constrained between the nuclei and the interface caused the left- and right-handed helices, however the rod-dendron molecules lacked preferential asymmetric ordering as demonstrated by the bidirectionality of the helical defects. The confinement of the helical defects to mechanically pinned fibers confirmed the defects originated from the torsion forces created from the fibers interaction with the interface or another fiber. Similar helical defects were observed within the dense network of ribbons suggesting similar compression along the ribbons occurred as two ribbons converged. The majority of the defects occurred near the initial air-liquid interface and dense

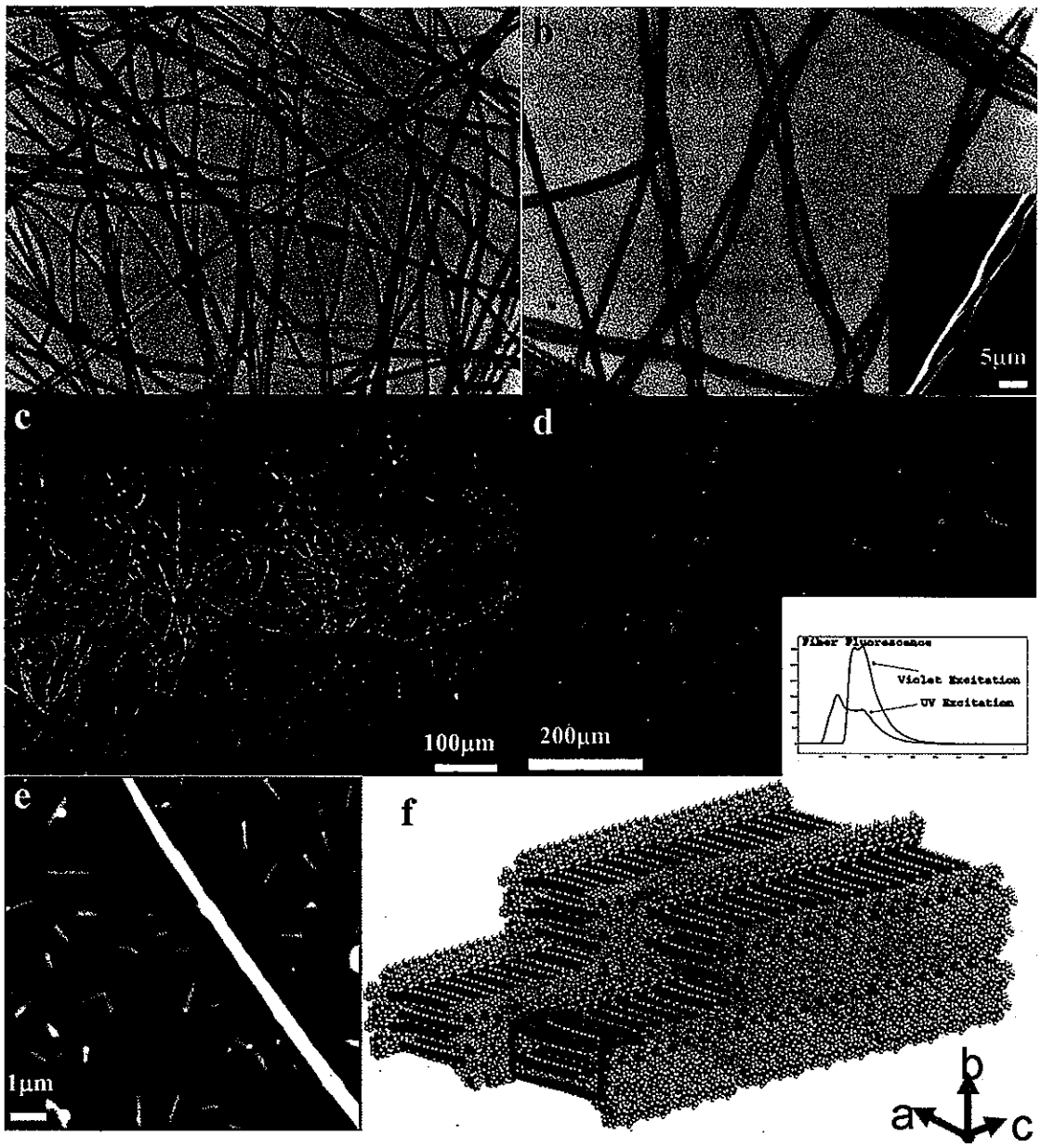

Figure 85. a) Optical micrograph of ribbon network; b) Helical defects along 1D structures, inset High resolution SEM image of helical defects; c) SEM image exhibiting the layering and entangling of fiber in the ribbon clusters as well as in the dense network; d) Topography image of large ribbon surrounded by nanofiber building blocks, z-range 10nm; e) Fluorescent micrograph of ribbon network, inset fluorescence spectra; f) molecular model of 1D growth of ribbon structure

regions of fiber nuclei formation. Similar twisting of crystallizing polymer fibrils in long chain polymers generating helical structures within spherulites.[228]

Insight into the ordering of the individual rod-dendrons within the one-dimensional ribbon structures was revealed during fluorescent optical microscopy (Figure 85d). The ribbons exhibited three fluorescence peaks dependent on exciting radiation. Fluorescence bands at 437 and 470 nm were observed for the ribbon structures illuminated with a 365 nm ultraviolet wavelength (Figure 85d inset). Illuminated with 405 nm wavelength, the ribbons were observed to fluoresce at 470 and 489 nm (Figure 85d inset). The multiple fluorescence peaks yielded from two dissimilar π-π stacking conformations suggests a more complicated crystalline structure of the self-assembled ribbons.[229] The tree-like rod-dendrons formed a herringbone structure in bulk, thus forming two π-π stacking conformations similar to the structure for the 1D ribbon formation presented below.[218] The red-shift of the peaks and reduced intensity observed for the shorter wavelength suggests quenching of the fluorescent behavior due to the close packed ordering of the rigid phenylene rods. The tree-like rod-coil molecules lacked anisotropic ordering confirmed by little response to polarized light illumination thereby allowing the magnified fluorescent response observed for overlapping ribbons. The higher intensity observed at intersections of fiber in fluorescent images was attributed to constructive interference.

Further confirmation of the close packed crystalline structure of the ribbons was demonstrated by comparison of X-ray diffraction data for the ribbon structures and the bulk material (Figure 86). The calculated unit cell of a= 2.4 nm, b= 1.9 nm, and c= 4.8 nm for the crystal structure of the ribbons was comparable to the bulk supercell structure reported previously.[218] The tree-like molecules formed a supercell structure with the rod cores oriented horizontally along the *a* direction. Similarly, the one-dimensional self-assembled structure had high degree crystallinity, comparable to the bulk material suggesting an analogous herringbone alignment of the rod-dendron molecules. The herringbone alignment of the MT molecules allows for π-π interactions between parallel rods as well as between rods that are angled.

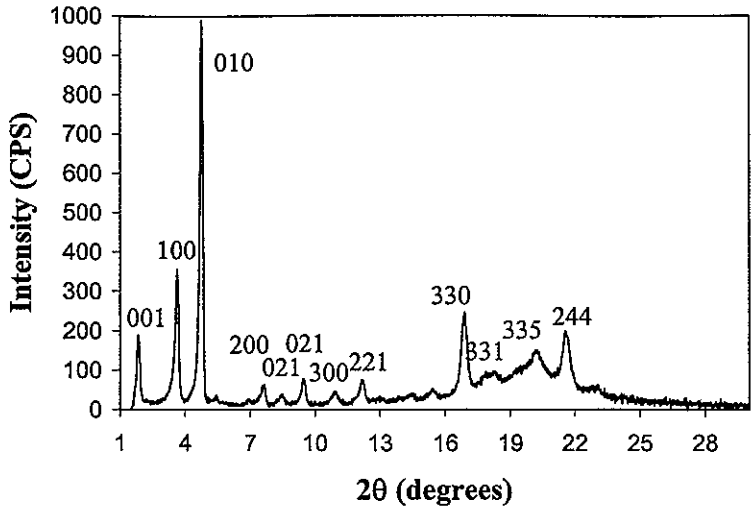

Figure 86. XRD of one-dimensional ribbon structures of tree-like rod-coil molecules.

Closer examination of the ribbon formation in smaller scale morphology studies suggests stepwise growth of the ordered one-dimensional structures with a critical size for ribbon formation (Figure 85e). The tree-like rod-coil molecules assembled into smaller one-dimensional nanofibers, creating nanoscale building block for larger 1D structure formation (Figure 85e). Dissimilar to the larger ribbon structures described earlier, the nanofibers had a low aspect ratio with the average length (695 $\pm$ 150 nm) three times larger than the average width (228 $\pm$ 27). The nanofibers were composed of only a few molecular layers with the average height 3.1 $\pm$ 0.4 nm near the dimensions of the unit cell. The varying step-like height cross-section of the nanofibers suggested a layered ordering of the tree-like rod-coil molecules (Figure 85f). The absence of intermediate scale fibers further suggests a threshold for ribbon formation with smaller scale fibers aggregating to diffusion sites along the large scale ribbons as the solvent evaporates.

Initial nucleation at the receding evaporation line indicated localized concentration controlled the spontaneous self-assembly of the rod-dendron molecules. Slow evaporation of the droplet created a gradient of concentration across the diameter as the localized concentration increased more rapidly at the edge than the center of the droplet. The concentration controlled aggregation and ordering was limited to the edge region until the concentration gradient reduced. As the gradient equalized across the droplet diameter cluster nucleation was observed within the center of the droplet. The slow evaporation rate allowed

the overall droplet concentration to rise as the escape rate of solvent molecules exceeded the escape rate of the solute. Additionally, as the concentration decreased further ribbon growth occurred independent of nucleation point suggesting high concentration negated the defect sites necessary at lower concentrations for spontaneous self-assembly. The growth of individual ribbons within the droplet as the concentration rose confirmed the favorable ordering of the tree-like rod-dendron molecules within one-dimensional structures.

Slow evaporation allowed preferentially ordering of MT molecules within crystal structures similar to the bulk structure (Figure 85f). The ribbons formed at high concentration due to the attractive forces between the phenylene cores. The asymmetric molecular architecture facilitated the layered herringbone structure with the hydrophilic branches of opposite facing molecules forming an amorphous shell around the crystalline cores. The one-dimensional growth was in part caused by the layered ordering of the rigid phenylene cores. The desirable crystal growth direction was perpendicular to the core axis due to the strong van der Wahl's forces between phenylene rods.

Stepwise growth of the 1D structures was concluded from the observation of fiber structures at two molecular scales. The tree-like rod-coil molecules formed nanofiber blocks initially with the smaller blocks assembling into the larger ribbon structures. The pointed deficiency of intermediate blocks or fiber indicated a threshold for ribbon formation. The stripe texture along the larger ribbons further concluded the stepwise growth from nanofiber building blocks.

One-dimensional ordering of rod-coil molecules was demonstrated to be driven by hydrogen bonding between the coil fragments and π-π stacking of the rod fragments, forming ribbon structures.[108] A red-shifted, quenched fluorescence spectrum observed for self-assembled ribbon structure by Stupp et al revealed the dense ordering of the rod segments.[108f] Photoluminescence of the 1D structure was shown to greatly heighten the electronic conductivity of the materials created by the π orbital overlap in ribbon structures. The sparse network ribbon structures formed from cast solution films lacked directionality, but applying an alternating current electric field during solution casting forced the 1D nanostructures to align in the electric field direction.[108f] A similar quenching of the fluorescence spectrum for the 1D structures was observed, thus concluding the π-π stacking of the rod cores drive the

ribbon formation. The two peaks confirmed the herringbone packing suggested by the X-ray scattering.

Novel tree-like rod-coil molecules formed 1D fluorescent ribbon structures from nanofiber building blocks on hydrophobic and hydrophilic surfaces. The ribbon growth was controlled by the concentration gradient, limiting growth to nuclei at the receding evaporation line initially and gradually moving across the droplet diameter as the gradient was reduced. The radial orientation of the fibers from the nuclei during growth forced the ribbons to layer over and entangle with ribbons from adjacent clusters, creating helical defects. The two fluorescent peaks were attributed to the herringbone structure of the rigid cores while the highly branched tails effectively quenched the fluorescence behavior.

7.4 Discussion and Conclusions of Rod-Coil Molecules

Comparison of the ordering behavior of the three rod-coil molecular series revealed role of the core nature versus the shell nature and tail type. All molecules possessed similar rigid rod cores with flexible, hydrophilic tails attached on one or two ends. The length and degree of branching of the hydrophilic tails was varied in addition to the symmetry of attachment.

Comparison of the two symmetrical rod-coil series suggests the stability of the monolayer increases with the longer hydrophilic tails and the delicate balance is disrupted when the molecular fragment ratio favors one block too much. The two lowest generations of the linear rod-coil molecules (**CRC-3** and **CRC-6**) had an incomplete bilayer structure with defects. The first generation of the branched rod-coil molecules, **RDM-1** had 12 monomeric units per tails, yet the monolayer formation was incomplete. The monolayer deposited at the highest surface pressure forms a continuous domain structure with small defects. Branching the flexible coil tails creates further disorder shown in the formation of circular domains with no ordering between the domains shown. **RDM-2** and **RDM-3** compounds formed domains of varying sizes on top of the disordered monolayers. Further branching of the coils seen in the **RDM-4** compound reduces the flexibility of the coils and hinders the monolayer formation. Although the degree of branching is increased, the ratio between the molecular fragments is held constant therefore the balance in the amphiphilic

nature favors the rod blocks for all four generations. The increase in the number of focal groups changes the morphology of the monomolecular layers formed at the air-water interface but the formation of a stable monolayer is incomplete.

The **CRC-N** compounds clearly indicate the importance of the balancing of molecular fragments play in the ability of the molecules to form ordered layers at the air-water interface. The lower molecular weight compounds prefer the formation of disordered multilayer structures. The hydrophobic cores overpower the hydrophilic tails attraction to the water subphase and push out of the air-water interface. The molecular fraction of the coil blocks is increased three times between the second and third generations. This increase makes the molecular block ratio to favor the coil blocks versus the rod blocks as was seen for the lower generations. The increase in molecular weight of the hydrophilic tails balances the molecular fragments better in the **CRC-17** compounds and allows for the cores to form preferred ordered structures. The cores aggregate toward one another, pushing the hydrophilic tails into the water subphase. By decreasing the area per molecular the molecular block ratio becomes more favorable toward the rod blocks as more of the coil blocks are forced out of the surface plane. In turn the coil blocks support the rod blocks above the water surface. The increase in coil blocks from the second to fourth generations is nearly four-fold, however the rod blocks role is severely reduced and the balance is disrupted.

The asymmetric **MT-1** formed a rich array of highly ordered structures in solutions and at interfaces. At low surface pressure the tree-like rod-coil molecules formed fingerlike lamellae with the rod cores oriented head to toe. The formation of a bilayer structure at higher surface pressures resulted in the asymmetric molecules forming ring-like micellar structures. Similar spherical micelles were observed in solution, facilitated by the asymmetric molecular architecture and the amphiphilic nature. The molecular design and composition of the **MT-1** molecules aided the formation of one-dimensional neuron-like fibers at the air-solvent-substrate interface. The strong π-π^* interactions between the rigid rod cores drove the formation of nanofibers and the stepwise formation of the larger molecular fibers.

Comparison of the generations of the symmetric series showed all compounds with six or less monomeric units in the coils formed bilayer structures. The π~A isotherms of those compounds indicated the bilayer structure with the intermediate cross-sectional area between the edge-on and face-on orientation of rigid core. Increasing the length coil block achieves a balance in the amphiphilic behavior of the linear rod-coil molecules. However overcompensation by lengthening of the coil blocks also disrupts the balance in the molecular fragments that led to the phase transition. While **CRC-17** displayed full range of phase transitions indicating a shift in the volume fraction of the coil block, **CRC-22** lacks the clear phase transitions. The hydroxyl terminated asymmetric rod-coil molecule formed disordered monolayers at the air-water interface while the methyl terminated **MT-1** formed ordered structures in solutions and at interfaces. The tail nature controlled the amphiphilic balances and drove the formation of highly ordered structures at interfaces. Shorter linear and highly branched tails lacked the ability to anchor the hydrophobic rod core at the interface while the longest linear hydrophilic coils insulated the cores, prohibiting the preferential ordering.

CHAPTER 8. GENERAL CONCLUSIONS

The effect of molecular design of branched macromolecules at ordered interfaces was examined. The core architecture and chemistry was revealed to effect the ordering of chemically disparate molecular fragments at interfaces. The flexibility and chemistry of the branched core determined the preferential ordering of molecular fragments was found to be induced by favorable interactions with the substrate. The effect of volume fraction ratio of chemically competing fragments within the molecular shell was ascertained to be dependent on the rigidity and relative size of the molecular core. Similarly, the influence of the generation number on the ordering behavior was shown to be controlled by the core nature. The substrate/subphase chemistry was determined to induce phase separation and favorable packing structures for branched macromolecules. Binary molecules demonstrated the ability to organize in supramolecular one-dimensional structures under favorable conditions at air-liquid and liquid-solid interfaces.

8.1 Overview of Results

The controlling design aspects for branched macromolecules at interfaces were studied. The balance of the molecular architecture and chemistry dictated the ordering behavior of branched macromolecules at interfaces. Volume fraction and amphiphilic balance of competing fragments had greater influence on the molecular organization than the shape or rigidity of the core. Favorable interactions with the surrounding environment facilitated molecular reorganization and suppressed preferential ordering of fragments.

8.1.1 Photochromic monodendrons

The cross-sectional mismatch between the polar head and the varying number of alkyl tails compelled the molecules to adopt "kinked" structure, allowing for the densest packing structure at the air-water interface. The larger than ideal molecular areas for the single tail molecules (**AD12-1**, **AA-1**, and **AE-1**) forced the alkyl tails to assume large tilt angles and imperfect crystal lattices in order to form densely packed molecular structures. The polar

groups of the highest generations tilted away from the surface normal to fill the large cross-sectional area of the multiple alkyl tails.

8.1.2 Liquid Crystalline Terminated Carbosilane Monodendrons

Favorable interactions between the substrate chemistry and the LC terminal groups forced the flexible carbosilane cores of third and fifth generation dendrimers to adopt a squashed, elliptical conformation in thin surface films. The layered ordering of the BPB groups forces a bowtie conformation of the dendrimers, thus causing a staggered packing structure within short range ordered lamellae. The third generation codendrimer formed a similar ordering as the fifth generation dendrimer with a complete BPB shell, suggesting the strong attraction of the BPB groups to the hydrophilic silicon surface overwhelmed the effect of the additional terminal groups and the less crowded shell. Similar molecular reorganization was observed for CB terminated molecules on mica substrates. Functionalizing the substrate with a hydrophobic SAM disrupted the preferential layered ordering of the LC terminal groups and the preferential radial ordering of the core dominant the molecular ordering.

8.1.3 Star Polymers

The volume fraction of the molecular fragments was concluded to largely influence the ordering behavior of star polymers at interfaces. The larger asymmetric 12-arm star polymer formed circular micelles spontaneously at the air-water interface partly due to the spatial segregated of the polymeric arms. The PAA arms submerged in the water subphase, supporting the rigid core and the glass PS arms, but the hydrophilic arms dehydrated upon deposit, thus collapsing and the monolayer thickness was attributed to the glassy PS block. The limiting cross-sectional area was determined to be controlled by the glassy PS block for the large asymmetric star and the smaller symmetric star polymer. The smaller, symmetric 12-arm star polymer lacked the organized two dimensional micelle formation suggesting the volume fraction controlled the ordering behavior of the binary molecules. The branching molecular architecture of the block star copolymers suppressed the morphological relationship with the molecular composition known for PEO-PS linear copolymers. Low

PEO (19 wt%) weight fraction star polymers formed cylindrical lamellae at the air-water interface. The moderate PEO blocks (39 wt%) disrupted the lamellae into circular micellar structures. The block star copolymer with the highest PEO content (88 wt%) formed dendritic structures in the dip direction at the air-solid interface.

8.1.4 Branched Gold Nanoparticles and Polymer Brushes Molecules

The functionalized gold nanoparticle with y-shaped polymer brushes formed ordered monolayers at air-water and air-solid interfaces. Molecular area calculated from AFM images and π~A isotherm confirmed the long polymeric arms of the polymer brush corona collapsed into a phase segregated polymer coating. The inclusion of the gold nanoparticle within the binary molecular resulted in the ability to observed Raman spectra of the ultrathin monolayer due to surface enhanced effects.

8.1.5 Rod-Coil Molecules

Molecular symmetry and volume fraction contributed to the formation of ordered structures for the three rod-coil molecular series. The ordering behavior of the linear rod-coil molecules depended on the volume fraction ratio of the coil blocks to the rod core. The third generation (**CRC-17**) exhibited remarkable reorganization of hydrophilic chains at the air-water interface demonstrated by the variety of ordered structures observed as the molecular area was reduced. The lower generations of the linear rod-coil molecules (**CRC-3** and **CRC-6**) in addition to the dumbbell shaped rod-coil molecules (**RDM-N**) lacked the amphiphilic balance to form ordered monolayers at the air-water interface. The tree-shaped rod-coil dendrons formed finger-like lamellae in low surface pressure monolayers at the air-water interface. The formation of a bilayer revealed the molecules preferentially form circular micelles in unconstrained monolayers. The rod-coil dendrons formed one dimensional nanofibers in highly concentrated solutions under favorable solvent conditions. The stepwise growth of the nanofibers resulted in long ribbon like structures with unique fluorescent behavior.

8.2 Role of Amphilphilic Balance on Molecular Ordering

Comparison of the ordering behavior and structure organization of the multiple molecular series provided several key observations of molecular design of branched macromolecules. Further understanding of the effect of the molecular architecture and chemistry on packing structures was discerned from comparison of the overall conclusions.

8.2.1 Influence of Shell Structure

The flexibility, functionality and shape of the terminal groups greatly affected the ordering behavior of the branched and binary molecules at interfaces. Additionally, the orientation and position in the molecular architecture dictated the degree of influence of the shell on the molecular packing structure. The number of terminal groups and volume fraction of the shell was determined to affect the degree of influence the shell nature exerted on the ordering of the surface film.

The influence of the shell structure on the molecular ordering and monolayer organization was demonstrated in several molecular series. The number and symmetry of attachment of the end groups was varied to discern the effect of the shell structure. The shell structure differed from a single end group attached symmetrically or asymmetrically to multiple end groups attached asymmetrically or radially attached.

The attachment of multiple functional terminal groups with well known ordering behaviors to a single molecular core resulted in competing ordering trends. The surrounding environment, particularly the subphase or substrate chemistry, contributed to the molecular organization at interfaces. The attractive forces between the polar LC terminal groups and the hydrophilic silicon substrate compelled the flexible carbosilane cores of G5-BPB to form a compressed and elliptical conformation. The molecular reorganization caused a staggered packing structure within the thin surface films. The incomplete shell of mesogenic terminal groups for the third generation co-dendrimer exerted similar control over the molecular organization suggesting the LC group/substrate interaction was stronger than the preferential radial conformation of the molecular core. The flexible nature of the carbosilane core contributed to the molecular reorganization.[61a] Another example of competing ordering trends of the dendritic core and the terminal groups was observed for the higher generations

of the photochromic monodendrons. The four and eight tail molecules for both series (**AA-4**, **AA-8**, **AD12-4**, and **AD12-8**) formed limited short range ordering at the air-water and air-solid interfaces despite the long range ordering observed for the single tail molecules attached to same polar groups. The attachment of multiple alkyl tails to a single branching unit (phenyl ring) limited the ability of the alkyl tails to reorganize at interfaces. The branching unit determined the spacing between adjacent alkyl tails and the tilt behavior of the alkyl tails. The alkyl tails of the lowest generations adopted large tilt angles and preferential tilt directions to form densely packed structures despite the large cross-sectional mismatch created by the bulky focal groups.

Comparison of the linear rod-coil molecules and star polymers established the role of the volume fraction of competing fragments on the molecular organization. Small changes in the volume fraction resulted in completely dissimilar ordering behavior. The larger asymmetric 12-arm star polymer spontaneously formed two dimensional micelles at the air-water interface. The smaller symmetric 12-arm star polymer lacked the micellar formation, forming disorganized monolayers. The 15% reduction in the PS chain length results in a 40% reduction in the volume fraction of the glassy block, causing the balance to shift toward the PAA block. The disrupted balance resulted in disordered monolayer formation. Similar results were seen for the linear rod-coil molecules. The intermediate length linear rod-coil molecules formed various preferential ordering at the air-water interface while the shorter tail molecules lacked the amphiphilic balance to form stable monolayers and the longer tails of the **CRC-22** insulated the cores thereby prohibiting the preferential ordering of the rod cores. The block star copolymers exhibited a transition of morphological structure from cylindrical lamellae to circular micelles to dendritic structures as the molecular composition varied from larger PS block to dominating PEO block. The volume fraction of molecular fragments dictated the ability of branched molecules formed with rigid cores to formed ordered structures.

8.2.2 Effect of Core Nature

The architecture and nature of the molecular core affect the packing structure at interfaces by controlling the orientation of the end-groups and limiting the ability of the

attached tails to reorganize. In contrast, strong attractive forces between molecular cores enable the formation of highly oriented structures with ordering over hundreds of unit cells. The core nature controls the molecular ordering when the molecular composition is balanced for the molecular architecture.

The monodendron core of the **AA-N** and **AD12-N** allowed preferential perpendicular orientation of alkyl tails for higher generation but limited long range ordering due to the adjacent attachment of the alkyl tails. The hydrophilic head group anchored the wedge-shaped molecule at the air-water interface as the repulsive force between the alkyl tails and the water subphase forced the molecule to orient along the surface normal. The lower generations demonstrated a greater ability to reorganize at the air-water interface, attributed to the lack of steric restriction exhibited on the higher generations. The alkyl tails of the higher generations were constrained by the adjacent attachment on the phenyl ring. Therefore the attachment of multiple tails per a single wedge shaped core impeded the molecular reorganization required to form long range ordering.

The attachment of multiple polymeric arms to a central core for the block star copolymer suppressed the morphological relationship with molecular composition as observed for linear copolymers. The chain length was reduced as the molecular block volume fraction divided by reducing the chain mobility. The shorter polymeric arms combined with the limited ability to reorganize due to multiple arms attached to a single defined central core and contributed to the impediment of the molecular ordering within the monolayer. Comparison of the multi-arm star polymers with linear diblock copolymers concluded the branched structure significantly suppressed the cylindrical lamellae to spherical micelle transition in LB monolayers. Thus, the morphology trend in monolayers was controlled by the branching architecture as well as the chemical composition.

Conversely, strong π-π attraction between the rigid rod cores for both linear and tree-like rod-coil molecules directed the formation of highly ordered structures. The linear rod-coil molecules formed a rich array of ordered structures, largely driven by the attraction between the symmetrical cores. The ordering behavior of the moderate length rod-coil molecules was highly repeatable with the lamellae continuous over hundreds of nanometers without defect.

8.2.3 Impact of Generation Number

The generation number of dendritic molecules affects the size and branching of the core as well as the number of terminal groups occupying the shell. Therefore, the generation number impacts the molecular ordering by influencing the flexibility of core, the overall molecular dimensions, and the density of the shell. Although the shell nature and the core nature to some extent encompass them, these factors have a more direct relationship to the generational effect of dendritic polymers. The influence of the generational effect was limited to the photochromic monodendrons, the carbosilane dendrimers and the dumb-belled shaped rod-coil molecules.

Similar ordering behavior for third and fifth generation carbosilane dendrimers was observed for surface films deposited on hydrophilic substrates. The flexible dendritic core was capable of molecular reorganization under favorable conditions for the layered ordering of the mesogenic terminal groups. Little variance in the molecular dimensions of the nanometer scale features implied the third and fifth generation cores occupied approximately the same space. Conversely, only the third generation dendrimer formed ring structures on hydrophobic substrates, suggesting the generational effect was conditional. A fourfold difference in the number of terminal groups resulted in a dramatic rise in shell density from the third to fifth generation; however, the flexible carbosilane core allowed molecular reorganization, thereby limiting the crowding produced by the generational growth. This comparison demonstrated the flexible core structure reduced the impact of the generation number on the molecular ordering.

A generational effect observed on the ordering behavior for the photochromic monodendrons was attributed the rigidity of the branched structure. The rigidity of the branching structure limited the spacing and rotation of the alkyl tails. The alkyl tails attached to higher generation cores were incapable of complete reorganization thus limiting the molecular ordering within monolayers. Although cross-sectional mismatch favored the polar group for lower generations, the one and two molecules exhibited higher ordering. The mobility of the alkyl tails was essential for long range ordering, thereby suggesting the cross-

sectional area balance should favor the polar head, allowing space for molecular reorganization.

Lastly, the degree of branching for the hydrophilic coil tails of the dumb-belled shaped rod-coil molecules minimally affected the molecular ordering at the air-water and air-solid interfaces. The molecules formed inhomogeneous surface films at the air-water and air-solid interface for all generations. The lack of ordering suggested an inappropriate amphiphilic balance which no generation exhibited a branching structure capable of balancing the effect of the symmetric attachment to the rigid rod core.

8.2.4 Influence of Interfacial Interactions

Favorable interactions with the surrounding environment disturbed the preferential ordering of molecular fragments resulting in the formation of novel molecular structures. A characteristic of Langmuir and LB films is the preferential orientation of amphiphilic molecules at the air-water interface and the ability to maintain the ordering upon deposition to a solid substrate. Strong interactions between molecules and substrate drive the formation of ordered structures in grafted and cast films. Conversely, less active forces between the molecules and environment would allow the appearance of novel structures due to the favorable interactions between the molecular fragments.

The molecular conformation of LC terminated carbosilane dendrimers was controlled by the underlying substrate chemistry. Similar lamellae ordering was observed for BPB terminated fifth generation dendrimers on hydrophobic silicon surfaces as detected for CB terminated molecules on Mica. Favorable surface chemistry induced layered ordering of mesogenic groups, forcing the flexible core to adopt a compressed, elliptical conformation. Change in the surface chemistry disrupted the preferential ordering revealing molecular reorganization controlled by the favorable surface interactions. In contrast, the third generation molecule formed preferential radial conformations on hydrophobic SAM functionalized substrates, concluding the molecular conformation was conditionally controlled.

Phase separation of competing molecular fragments at the air-water interface drove the reorganization of amphiphilic molecules in numerous ordered structures. The polymeric

arms of the 12-arm star polymer segregated at the air-water interface causing the spontaneous formation of circular domains. The block star copolymers formed a rich variety of molecular structures at the air-water interface due to the phase separation of the PEO and PS arms. Similar phase separation of the polymer arms of the y-shaped brushes of the gold nanoparticle binary molecule created a ring-shaped texture within monolayers and insulated the nanoparticle cores from neighboring molecules.

Finally, the tree-like rod coil molecules formed one-dimensional fiber structures upon evaporation from a nonpolar, nonvolatile solvent. The absence of selective solvent interactions with either the flexible coils or rigid rod cores allowed the alternating stacking formation within one-dimensional structures. The asymmetric rod-coil dendrons formed spherical micelles in solutions and at the air-water interface to reduce the unfavorable interactions of the hydrophobic core with the polar solvent. Slow evaporation from a solvent with no preferential interaction with the coils or rod segments allowed the molecules to form a one dimensional structure.

8.2.5 Effect of Tail Type

Long tail segments can be attached to molecular cores of competing chemical composition to create an appropriate amphiphilic balance. A small, hydrophilic polar group balances multiple hydrophobic alkyl tails connected, thereby allowing the tails to orient in a preferential packing structure at interfaces. Long, flexible hydrophilic tails attached to a rigid, hydrophobic core anchor the amphiphilic molecule to the air-water interface.

Short alkyl tails balance wedge shaped monodendrons at the air-water interface and drive molecular reorganization within the monolayers. van der Wahl forces between adjacent alkyl tails dictate the formation of preferential close packed structures. It has been demonstrated the lower generation monodendron cores exerted less forces on the alkyl tails thereby allowing the preferential structures to form over greater lengths. Additionally, the alkyl tails demonstrate the preferred molecular ordering in the large tilt angles observed for molecules with large cross-sectional mismatches.

Analysis of the ordering behavior of the rod-coil molecular series concluded the architecture and chemistry of the functional terminal groups more largely controlled the

molecular organization at interfaces. The three molecular series were composed of a short rigid phenylene core with the symmetry, branching, length, and end group functionality of the attached hydrophilic tails varied. The rod-coil molecules with short linear or branched hydrophilic tails attached symmetrically to the rigid core formed disordered monolayers with collapse observed at low surface pressures. Shorter linear or branched hydrophilic tails lacked the chain mobility to anchor the molecules at the air-water interface. However, the linear rod-coil molecule with the longest hydrophilic, flexible tails formed uniform monolayers but lacked the highly ordered structure observed for the linear rod-coil with moderate length chains. The amphiphilic balance of the rigid rod core and the flexible coils demonstrated not only the capability to form highly ordered structures but presented novel molecular reorganization stimulated by the changing volume fraction of blocks within the monolayer. Conversely, the tree-shaped molecule with three tetra-branched flexible hydrophilic tails formed highly ordered structures at the air-water interface and in highly concentrated solution under favorable solvent conditions. Replacing the functional terminal groups for the tree-shaped molecules disrupted the molecular organization within monolayers at interfaces. The formation of highly ordered molecular structures required the balancing of molecular composition and tail architecture. Minute changes in molecular composition and architecture greatly affected the ordering behaviors of rod-coil molecules, thereby concluding the overall balance of the molecular fragments and not the core geometry predicts the possibility for molecular organization at interfaces.

8.3 Final Conclusions

The analysis of the molecular series presented above presented several broad conclusions on the ordering behavior of molecular fragments attached to fragments with competing trends. Shifts in the volume fraction, branching, and attachment of the tails facilitates or prohibits preferential ordering driven by the core nature. Changes in the molecular area at the air-water interface affect the composition of molecular fragments at the interface, thereby causing reorganization within the monolayer.

The studies presented above demonstrated a trend in the molecular organization within monolayers was directed by rigid or glassy hydrophobic fragments. The molecules

with mobile rigid fragments formed ordered structures over tens and hundreds molecular units in length, and in several examples the molecules formed highly oriented structures. The hydrophilic or flexible fragment or block was concluded to overwhelm and disrupt the ordering behavior of the rigid fragment in several molecular series and for specific molecular examples. Highly branched structures limited the ability of the rigid fragments to reorganize in preferred ordered structures by reducing the flexibility of the molecular structure and the crowding of terminal groups at the periphery. The mobility of the dominant molecular fragments significantly affected the reorganization within monolayers at the air-water and air-solid interface. Finally, molecular interactions with the subphase strongly affected the ordering at interfaces, causing phase separation, inducing layered ordering of terminal groups, and suppressing the preferential ordering behavior of fragments due to favorable or nonfavorable interactions. The ability to design ordered interfaces for biomedical applications requires controlling the molecular architecture and chemical composition of branched macromolecules. This study demonstrated several important aspects in molecular design for nanobiotechnology applications.

CHAPTER 9. REFERENCES CITED

[1] Lee, S.C. "Dendrimers in Nanobiological Devices" in *Dendrimers and Other Dendritic Structures* (Eds. Frechet, J.M.J.; Tomalia, D.A.) Wiley: New York, **2001**.

[2] Ruhe, J. in Advincula, R.C.; Brittain, W.J.; Caster, K.C.; Ruhe, J. (Eds.) *Polymer Brushes* Wiley-VCH: Weinheim, **2004**.

[3] Kitching, K.J.; Pan, V.; Ratner, B.D. *Plasma Polymer Films* **2004**, 325.

[4] (a) Murthy, N.; Xu, M.; Schuck, S.; Kunisawa, J.; Shastri, M.; Frechet, J.M.J. *PNAS*, **2003**, *100*, 4997; (b) Ihre, H.R.; Padilla De Jesus, O.L.; Szoka, F.C.Jr.; Frechet, J.M.J. *Bioconjugate Chem.* **2002**, *13*, 443

[5] Weber, N.; Bolikal, D.; Bourke, S.L.; Kohn, J. *J. Biomed. Mater. Res.* **2004**, *68A*, 496

[6] Gray, J.J. *Curr. Opin. Struct. Bio.* **2004**, *14*, 110.

[7] Vazquez, E.; Dewitt. D.M.; Hammond, P.T.; Lynn, D.M. *J. Am. Chem. Soc.* **2003**, *125*, 11452.

[8] Seiler, M. *Chem. Eng. Technol. Biotechnol.* **2001**, *75*, 237.

[9] Murthy, N.; Xu, M.; Schuck, S.; Kunisawa, J.; Shastri, M.; Frechet, J.M.J. *PNAS* **2003**, *100*, 4997.

[10] Ihre, H.R.; Padilla, De Jesus, O.L.; Szoka, F.C.Jr.; Frechet, J.M.J. *Bioconjugate Chem.* **2002**, *13*, 443.

[11] Zhang, S.; Rio, Y.; Cardinali, F.; Bourgogne, C.; Gallani, J.-L.; Nierengarten, J.-F.; *J. Org. Chem.* **2003**, *68*; 9787

[12] Advincula, R.C.; Brittain, W.J.; Caster, K.C.; Ruhe, J. (Eds.) *Polymer Brushes* Wiley-VCH: Weinheim, **2004**.

[13] Muller, R.S. in *Micro/Nanotribology and Its Applications* (Ed. B. Bhushan) Kluwer: Academic Press: Dordrecht, **1997**

[14] Tsukruk, V.V. in *Nanotribology* (Eds. S.M. Hu, C. Z. Ying) Kluwer Academic Press: Boston, **2002**

[15] Israel, R.; Leermakers, F.A.M.; Fleer, G.J.; Zhulina, E.B. *Macromolecules* **1994**, *27*, 3249.

[16] Takei, Y.G.; Aoki, T.; Sanui, K.; Ogata, N.; Sakurai, Y.; Okanao, T. *Macromolecules* **1994**, *27*, 6163.

[17] (a) Auroy, P.; Auvary, L.; Leger, L. *Phys. Rev. Lett.* **1991**, *66*, 719; (b) Raviv, U.; Tadmor, R.; Klein, J. *J. Phys. Chem. B* **2001**, *105*, 8125; (c) Grest, G.S.; Murat, M. *Macromolecules* **1993**, *26*, 3108.

[18] Niemeyer, C. M. *Angew. Chem. Int. Ed.* **2001**, *40*, 4128.

[19] Tully, D.C.; Frechet, J.M.J. *Chem. Commun.*, **2001**, 1229.

[20] Percec, V.; Cho, W.-D.; Ungar, G.; Yeardley, D.J.P. *J. Am. Chem. Soc.* **2001**, *123*, 1302.

[21] Percec, V.; Cho, W.-D.; Mosier, P.E.; Ungar, G.; Yeardley, D.J.P. *J. Am. Chem. Soc.* **1998**, *120*, 11061.

[22] Gillies, E.R.; Frechet, J.M.J. *Chem. Commun.* **2003**, 1640.

[23] Aldrich "Products for Materials Science" 2004-2005 Catalog.

[24] Hawker, C.J.; Lee, R.; Frechet, J.M.J. *J. Am. Chem. Soc.* **1991**, *113*, 4583.

[25] Voit, B. *J. Polym. Sci. A: Polym. Chem.* **2000**, *38*, 2505.

[26] Hadjichristidis, N.; Pitsikalis, M.; Pispas, S.; Iatrou, H. *Chem. Rev.* **2001**, *101*, 3747.

[27] Buhleier, E.; Wehner, W.; Vogtle, F. *Synthesis* **1978**, 155.

[28] Newkome, G.R.; Moorefield, C.N.; Vogtle, F. (Ed.) *Dendritic Molecules* VCH:Weinheim, **1996**.
[29] Frechet, J.M.J.; Tomalia, D.A. *Dendrimers and other dendritic polymers*, Wiley & Sons, Inc.: New York, NY, **2001**.
[30] Abetz, V. in Ciferri, A. (Ed.) *Supramolecular Polymers, Second Edition* CRC Press: Boca Raton, **2005**.
[31] Arys, X.; Jonas, A.M.; Laschewsky, A.; Legras, R.; Mallwitz, F. in Ciferri, A. (Ed.) *Supramolecular Polymers, Second Edition* CRC Press: Boca Raton, **2005**.
[32] Ulman, A. *An Introduction to Ultrathin Organic Films*; Academic Presses: San Diego, CA, **1991**.
[33] Dykes, Graham M. *J. Chem Technol Biotechnol*, **2001**, 76, 903.
[34] Inoue, K., *Prog. Polym. Sci.*, **2000**, *25*, 453.
[35] (a) Julthongpiput, D.; Lin, Y-H.; Teng, J.; Zubarev, E. R.; Tsukruk, V. V. *J. Am. Chem. Soc.* **2003**, *125*, 15912; (b) Luzinov, I.; Minko, S.; Tsukruk, V. V. *Prog. Polym. Sci,*. **2004**, *29*, 635; (c) Tsukruk, V. V. *Prog. Polym. Sci.*, **1997**, *22*, 247.
[36] (a) Ikeda, T. *J. Mater. Chem.* **2003**, *13*, 2037; (b) Nishihara, H. *Bull. Chem. Soc. Jpn* **2004**, *77*, 407; (c) Shibaev, V.; Borbovsky, A.; Boiko, N. *Prog. Polym. Sci.*, **2003**, *28*, 729; (d) Seki, T. in *Handbook of Photochemistry and Photobiology*, Ed. Nalwa, H. S., **2003** American Scientific Publishers, California, p. 435.
[37] (a) Rochon, P.; Batalla, E.; Natanson, A. *Appl. Phys. Lett.* **1995**, *66*, 136; (b) Kim, D.Y.; Tripathy, S.K.; Li, L.; Kumar, J. *Appl. Phys. Lett.* **1995**, *66*, 1166.
[38] Kawata, S.; Kawata Y. *J. Opt. Soc. Am. B* **2001**, *18*, 1777.
[39] (a) Meng, X.; Natansohn, A.; Barrett, C.; Rochon, P. *Macromolecules* **1996**, *29*, 946; (b) Ho, M.; Natansohn, A.; Barrett, C.; Rochon, P. *Can. J. Chem.* **1995**, *73*, 1773; (c) Natansohn, A.; Rochon, P.; Ho, M.; Barrett, C. *Macromolecules* **1995**, *28*, 4179.
[40] Ichimura, K. *Chem. Rev.* **2000**, *100*, 1847.
[41] Yamaoka, T.; Makita, Y.; Sasatani, H.; Kim, S.-I.; Kimura, Y. *J. Contr. Releas,* **2000**, *66*, 187.
[42] (a) Seki, T.; Kojima, J.; Ichimura, K. *Macromolecules* **2000** *33*, 2709; (b) Seki, T.; Sekizawa, H.; Fukuda, R.; Tamaki, T.; Yokoi, M.; Ichimura, K. *Polymer J.* **1996** *28*, 613; (c) Seki, T.; Sekizawa, H.; Fukuda, R.; Morino, S.; Ichimura, K. *J. Phys. Chem.* **1998** *102*, 5313; (d) Seki, T.; Fukuda, R.; Tamaki, T.; Ichimura, K. *Thin Solid Films* **1994**, *243*, 675; (e) Seki, T.; Sakuragi, M.; Kawanishi, Y.; Suzuki, Y.; Tamaki, T. *Langmuir* **1993**, *9*, 211.
[43] Siewierski, L.M.; Brittain, W.J.; Petrash, S.; Foster, M.D. *Langmuir* **1996**, *12*, 5838.
[44] Kumar, G. S.; Neckers, D. C. *Chem. Rev.*, **1989**, *89*, 1915.
[45] Irie, M.; Ikeda, T. in *Functional Monomers and Polymers (2nd Edition)*, Takemoto, K.; Ottenbite, R.; Kamachi, M. (Eds.) Dekker: New York, **1997**.
[46] Hashemzadeh, M.; McGrath, D.V. Am. Chem. Soc., Div. Polym. Chem., Prep., **1998**, 39, 338.
[47] Villavicencio, O.F.; McGrath, D.V in preparation
[48] (a) Larson, K.; Vaknin, D.; Villavicencrio, O.; McGrath, D.V.; Tsukruk, V.V. *J. Phys. Chem.* **2002**, *106*, 7246; (b)Genson, K. L.; Vaknin, D.; Villacencio, O.; McGrath, D. V.; Tsukruk, V. V. *J. Phys. Chem. B* , **2002**, *106*, 11277.

[49] Peleshanko, S.; Sidorenko, A.; Larson, K.; Villavicencio, O.; Ornatska, M.; McGrath, D.V.; Tsukruk, V.V. *Thin Solid Films* **2002**, *406*, 233.
[50] Sidorenko, A.; Houphoouet-Boigny, C.; Villavicencio, O.; McGrath, D.V.; Tsukruk, V.V. *Langmuir*, **2000**, *16*, 10569.
[51] Mathias, L.J.; Carothers, T.W. *Advances in Dendritic Macromolecules, Vol 2* **1995** JAI Press, p 101.
[52] Frey, H.; Lach, C.; Lorenz, K. *Adv. Mater.* **1998**, *10*, 279.
[53] Schlenk, C.; Frey, H. *Monatshefte fur Chemie* **1999**, *130*, 3.
[54] (a) Tsukruk, V.V. *Adv. Mater.* **1998**, *10*, 253; (b) Tsukruk, V. V. *Progr. Polym. Sci.* **1997**, *22*, 247.
[55] Shibaev, V.; Bobrovsky, A.; Boiko, N. *Prog. Polym. Sci.* **2003**, *28*, 729
[56] Lehmann, M.; Fischbach, I.; Spiess, H.W.; Meier, H. *J. Am. Chem. Soc.* **2004**, *126*, 772.
[57] Bosman, A. W.; Janssen, H. M.; Meijer, E. W. *Chem. Rev.* **1999**, *99*, 1665.
[58] Bobrovsky, A. Yu.; Pakhomov, A.A.; Zhu, X.-M.; Boiko, N.I.; Shibaev, V.P.; Stumpe, J. *J. Phys. Chem. B* **2002**, *1006*, 540.
[59] Pastor, L.; Barbera, J.; McKenna, M.; Marcos, M.; Martin-Rapun, R.; Serrano, J.L.; Luckhurst, G.R.; Mainal, A. *Macromolecules* **2004**, *37*, 9386.
[60] Marcos, M.; Omenat, A.; Serrano, J.L. *C. R. Chemie* **2003**, *6*, 947.
[61] (a) Ponomarenko, S.A.; Boiko, N.I.; Shibaev, V.P.; Richardson, R.M.; Whitehouse, I.J.; Rebrov, E.A.; Muzafarov, A.M. *Macromolecules* **2000**, *33*, 5549; (b) Agina, E.V.; Ponomarenko, S.A.; Boiko, N.I.; Rebrov, E.A.; Muzafarov, A.M.; Shibaev, V.P. *Polymer Science A* **2001**, *43*, 1000.
[62] Ponomarenko, S.A.; Boiko, N.I.; Shibaev, V.P.; Magonov, S.N. *Langmuir*, **2000**, *16*, 5487.
[63] Ponomarenko, S.A.; Boiko, N.I.; Shibaev, V.P.; Richardson, R.M.; Whitehouse, I.J.; Rebrov, E.A.; Muzafarov, A.M. *Macromolecules* **2000**, *33*, 5549.
[64] Agina, E.V.; Ponomarenko, S.A.; Boiko, N.I.; Rebrov, E.A.; Muzafarov, A.M.; Shibaev, V.P. *Polymer Science A* **2001**, *43*, 1000.
[65] Boiko, N.; Zhu, X.; Bobrovsky, A.; Shibaev, V. P. *Chem. Mater.*, **2001**, *13*, 1447.
[66] (a) Hadjichristidis, N.; Pitsikalis, M.; Pispas, S.; Iatrou, H. *Chem. Rev.* **2001**, *101*, 3747; (b) Hong, K.; Uhrig, D.; Mays, J. W. *Curr. Opin. Solid State Mater. Sci.* **1999**, *4*, 531; (c) Coessens, V.; Pintauer, T.; Matyjaszewski, K. *Prog. Polym. Sci.* **2001**, *26*, 337; (d) Hawker, C. J.; Bosman, A. W.; Harth, E. *Chem. Rev.* **2001**, *101*, 3661;
[67] (a) Jacob, S.; Majoros, I.; Kennedy, J. P. *Macromolecules* **1996**, *29*, 8631; (b) Heise, A.; Hedrick, J. L.; Frank, C. W.; Miller, R. D. *J. Am. Chem. Soc.* **1999**, *121*, 8647; (c) Heise, A.; Trollsas, M.; Magbitang, T.; Hedrick, J. L.; Frank, C. W.; Miller, R. D. *Macromolecules* **2001**, *34*, 2798; (d) Ohno, K.; Wong, B.; Haddleton, D. M. *J. Polym. Sci., Polym. Chem.* **2001**, *39*, 2206; (e) Angot, S.; Murthy, K. S.; Taton, D.; Gnanou, Y. *Macromolecules* **1998**, *31*, 7218; (f) Ueda, J.; Kamigaito, M.; Sawamoto, M. *Macromolecules* **1998**, *31*, 6762; (g) Klok, H. A.; Hernandez, J. R.; Becker, S.; Mullen, K. *J. Polym. Sci., Polym. Chem.* **2001**, *39*, 1572; (h) Hirao, A.; Hayashi, M.; Tokuda, Y.; Haraguchi, N.; Higashihara, T.; Ryu, S. W. *Polym. J.* **2002**, *34*, 633; (i) Francis, R.; Skolnik, A. M.; Carino, S. R.; Logan, J. L.; Underhill, R. S.; Angot, S.; Taton, D.; Gnanou, Y.; Duran, R. S. *Macromolecules*, **2002**, *35*, 6483; (j) Hou, S.; Chaikof, E.L.; Taton, D.; Gnanou, Y. *Macromolecules*, **2003**, *36*, 3874; (k) Francis,

R.; Taton, D.; Logan, J.L.; Masse, P.; Gnanou, Y.; Duran, R.S. *Macromolecules*, **2003**, *36*, 8253.

[68] (a) Voulgaris, D.; Tsitsilianis, C.; Esselink, F. J.; Hadziioannou, G. *Polymer* **1998**, *39*, 6429; (b) Voulgaris, D.; Tsitsilianis, C.; Grayer, V.; Esselink, F. J.; Hadziioannou, G. *Polymer* **1999**, *40*, 5879; (c) Tsitsilianis, C.; Voulgaris, D.; Stepanek, M.; Podhajecka, K.; Prochazka, K.; Tuzar, Z.; Brown, W. *Langmuir* **2000**, *16*, 6868; (d) Voulgaris, D.; Tsitsilianis, C. *Macromol. Chem. Phys.* **2001**, *202*, 3284.

[69] Teng, J.; Zubarev, E. R. *J. Am. Chem. Soc.*, **2003**, *125*, 11840.

[70] Jin, R. H. *Macromol. Chem. Phys.* **2003**, *204*, 403.

[71] (a) Granick, S. *Macromolecules* **1985**, *18*, 1597; (b) Kawaguchi, M.; Sauer, B. B.; Yu, H. *Macromolecules* **1989**, *22*, 1735; (c) Brinkhuis, R. H. G.; Schoutern, M. J. *Macromolecules* **1991**, *24*, 1487.

[72] (a) Zhu, J.; Eisenberg, A.; Lennox, R. B. *J. Am. Chem. Soc.* **1991**, *113*, 5583; (b) Zhu, J.; Lennox, R. B.; Eisenberg, A. *Langmuir* **1991**, *7*, 11579; (c) Zhu, J.; Eisenberg, A.; Lennox, R. B. *Makromol. Chem.* **1992**, *53*, 211; (d) Zhu, J.; Lennox, R. B.; Eisenberg, A. *J. Phys. Chem.* **1992**, *96*, 4727; (e) Zhu, J.; Eisenberg, A.; Lennox, R. B. *Macromolecules* **1992**, *25*, 6547; (f) Zhu, J.; Eisenberg, A.; Lennox, R. B. *Macromolecules* **1992**, *25*, 6556.

[73] (a) Gonçalves da Silva, A. M.; M.Filipe, E. J.; d'Oliveira, J. M. R.; Martinho, J. M. G. *Langmuir* **1996**, *12*, 6547; (b) Gonçalves da Silva, A. M.; Simoes Gamboa, A. L.; Martinho, J. M. G. *Langmuir* **1998**, *14*, 5327.

[74] Cox, J. K.; Yu, K.; Constantue, B.; Eisenberg, A.; Lennox, R. B. *Langmuir* **1999**, *15*, 7714.

[75] Li, S.; Hanley, S.; Khau, I.; Varshney, S. K.; Eisenberg, A.; Lennox, R. B. *Langmuir* **1993**, *9*, 2243.

[76] Zhang, W.; Shi, L.; An, Y.; Shen, X.; Guo, Y.; Gao, L.; Liu, Z.; He, B. *Langmuir* **2003**, *19*, 6026.

[77] (a) Zhang, L.; Eisenberg, A. *Science* **1995**, *268*, 1728. (b) Li, S.; Clarke, C.J.; Lennox, R.B.; Eisenberg, A. *Colloids Surf A* **1998**, *133*, 191. (c) Terreau, O.; Luo, L.; Eisenberg, A. *Langmuir* **2003**, *19*, 5601. (d) Li, S.; Clarke, C.J.; Eisenberg, A.; Lennox, R.B. *Thin Solid Films* **1999**, *354*, 136. (e) Schnitter, M; Engelking, J.; Heise, A.; Miller, R.B.; Menzel, H. *Macromol. Chem. Phys.* **2000**, *201*, 1504. .

[78] Herman, D.S. Kinning, D.J.; Thomas, E.L.; Fetters, L.J. *Macromolecules* **1987**, *20*, 2940;

[79] Francis, R.; Taton, D.; Logan, J.L.; Masse, P.; Gnanou, Y.; Duran, R.S. *Macromolecules* **2003**, *36*, 8253

[80] Peleshanko, S.; Gunawidjaja, R.; Jeong, J.; Shevchenko, V. V.; Tsukruk, V. V. *Langmuir* **2004**, *20*, 9423.

[81] Hammond PT. Adv. Mater. 2004, 16(15), 1271-1293.

[82] Goodson T, Varnavski O, Wang Y. Int. Rev. Phys. Chem. 2004, 23, 109

[83] Eychmuller A. J. Phys. Chem. B 2000, 104, 6514.

[84] Antonieeti M, Goltner C. Angew Chem. Int. Ed. Engl. 1997, 36, 910.

[85] Antonietti M, Grohn F, Hartmann J, Bronstein L. Angew Chem. Int. Ed. Engl. 1997, 36, 2080.

[86] Balogh L, Tomalia DA. J. Am. Chem. Soc. 1998, 120, 7355-7356.

[87] Esumi K, Suzuki A, Yamahira A, Torigoe K. Langmuir 2000, 16, 2604-2608.

[88] Grohn F, Gu H, Grull H, Mededith JC, Nisato G, Bauer BJ, Karim A, Amis EJ. Macromolecules 2002, 35,4852-4854.
[89] Grohn F, Bauer BJ, Akpalu YA, Jackson CL, Amis EJ. Macromolecules 2000, 33, 60-42-6050.
[90] Zhao M, Sun L, Crooks RM. J. Am. Chem. Soc. 1998, 120, 4877-4878.
[91] Zhao M, Crooks RM. Adv. Mater. 1999, 11(3), 217-220.
[92] Zhao M, Crooks RM. Angew. Chem. Int. Ed. 1999, 38(3), 364-366.
[93] Shan J., Nuopponen M., Jiang H., Viitala T, Kauppinen E, Kontturi K, Tenhu H. Macromolecules 2005, 37, ??
[94] Swami A, Kumar A, Selvakannan PR, Mandal S, Sastry M. J. Coll. Inter. Surf. 2003, 260, 367-373.
[95] Fendler JH, Meldum F. Adv. Mater. 1995, 7, 607.
[96] Brown JJ, Porter JA, Daghlian CP, Gibson UJ. Langmuir 2001, 17, 7966-7969.
[97] Liu J, Alvarez J, Ong W, Roman E; Kaifer AE. J. Am. Chem. Soc. 2001, 123, 11148-11154.
[98] Kang Y., Taton T.A. Angew. Chem. Int. Ed. 2005, 44, 409-412.
[99] Khomutov GB, Kislov VV, Gainutdinov RV, Gubin SP, Obydenov Ayu, Pavlov SA, Sergeev-Cherenkov AN, Soldatov SA, Tolstikhina AL, Trifonov AS. Surf. Sci. 2003, 532-535, 287-293.
[100] Zubilov AA, Gubin SP, Korotkov AK, Nikolaev AG, Soldatov ES, Khanin VV, Khomutov GB, Yakovenko SA. Tech. Phys. Lett. 1994, 20, 195.
[101] Khomutov GB, Soldatov ES, Gubin SP, Yakovenko SA, Trifonov AS, Obydenov AYu, Khanin VV. Thin Solid Films, 1998, 327-329, 550.
[102] Jiang C, Lio WY, Tsukruk VV. Phys. Rev. Lett. 2005, 95(11), 115503/1-115503/4.
[103] Jiang C, Markutsya S, Shulha H, Tsukruk VV. Adv. Mater. Int. Ed. 2005, 17(13), 1669-1673.
[104] Hu X, Cheng W, Wang T, Wang Y, Wang E, Dong S. J. Phys. Chem. B 2005, 109(41), 19385-19389.
[105] Pergolese B, Bonifacio A, Bigotto A. Phys. Chem. Chem. Phys. 2005, 7(20), 3610-3613.
[106] Orendorff CJ, Gole A, Sau TK, Murphy CJ. Anal. Chem. 2005, 77(10), 3261-3266.
[107] Zubarev, E.R. in preparation.
[108] (a) S.I. Stupp, V. LeBonheur, K. Walker, L.S. Li, K.E. Huggins, M. Keser, A. Amstutz, *Science* **1997**, *276*, 384; (b) E.R. Zubarev, M.U. Pralle, E.D. Sone, S.I. Stupp, *J. Am. Chem. Soc.* **2001**, *123*, 4105; (c) E.D. Sone, E.R. Zubarev, S.I. Stupp, *Angew. Chem. Int. Ed.* **2002**, *41*, 1706; (d) J.D. Hartgerink, E. Beniash, S.I. Stupp, *Science* **2001**, *294*, 1684; (e) B.W. Messmore, J.F. Hulvat, E.D. Sone, S.I. Stupp, *J. Am. Chem. Soc.* **2004**, *126*, 14452.
[109] (a) V. Percec, M. Glodde, T.K. Bera, Y. Miura, I. Shiyanovskaya, K.D. Singer, V.S.K. Balagurusamy, P.A. Heiney, I. Schnells, A. Rapp, H.-W. Spiess, S.D. Hudson, H. Duan, *Nature* **2002**, *419*, 384; (b) X. Zeng, G. Ungar, Y. Liu, V. Percec, A.E. Dulcey, J.K. Hobbs, *Nature* **2004**, *428*, 157; (c) V. Percec, A.E. Dulcey, V.S.K. Balagurusamy, Y. Miura, J. Smidrkal, M. Peterca, S. Nummelin, U. Edlund, S.D. Hudson, P.A. Heiney, H. Duan, S.N. Maganov, S.A. Vinogradov, *Nature* **2004**, *430*, 764; (d) G. Ungar, Y. Liu, X. Zeng, V. Percec, W.-D. Cho, *Science* **2003**, *299*, 1208.

[110] (a) P. Gopalan, X. Li, M. Li, C.K. Ober, C.P. Gonzales, C.J. Hawker, *J. Polym. Sci.* **2003**, *41*, 3640; (b) M. Lee, B-K. Cho, W-C. Zin, *Chem. Rev.* **2001**, *101*, 3869.

[111] (a) S. Loi, H-J. Butt, C. Hampel, R. Bauer, U-W. Wiesler, K. Mullen, *Langmuir* **2002**, *18*, 2398; (b) S. Loi, U-W. Wiesler, H-J. Butt, K. Mullen, *Macromolecules* **2001**, *34*, 3661; (c) W-D. Jang, T. Aida, *Macromolecules* **2004**, *37*, 7325.

[112] (a) S. Loi, U-M. Wiesler, H-J. Butt, K. Mullen *Chem. Commun.* **2000**, 1169; (b) D. Liu, S. De Feyter, P.C.M. Grim, T. Vosch, D. Grebel-Koehler, U-M. Wiesler, A.J. Berresheim, K. Mullen, F.C. De Schryver, *Langmuir* **2002**, *18*, 8223; (c) D. Liu, H. Zhang, P.C.M. Grim, S. De Feyter, U-M. Wiesler, A.J. Berresheim, K. Mullen, F.C. De Schryver, *Langmuir* **2002**, *18*, 2385; (d) D. Liu, S. De Feyter, M. Cotlet, U-W. Wiesler, T. Weil, A. Herrmann, K. Mullen, F.C. De Schryver, *Macromolecules* **2003**, *36*, 8489.

[113] D. Liu, S. De Feyter, M. Cotlet, A. Stefan, U-W. Wiesler, A. Herrmann, D. Grebel-Koehler, J. Qu, K. Mullen, F.C. De Schryver, *Macromolecules* **2003**, *36*, 5918.

[114] (a) J. Wu, A. Fechtenkotter, J. Gauss, M.D. Watson, M. Kastler, C. Fechtenkotter, M. Wagner, K. Mullen, *J. Am. Chem. Soc.* **2004**, *126*, 11311; (b) P. Samon, X. Yin, N. Tchebotareva, Z. Wang, T. Pakula, F. Jackel, M.D. Watson, A. Venturini, K. Mullen, J.P. Rabe, *J. Am. Chem. Soc.* **2004**, *126*, 3567; (c) J. Wu, M.D. Watson, N. Tchebotareva, Z. Wang, K. Mullen, *J. Org. Chem.* **2004**, *69*, 8194; (d) J. Piris, M.G. Debije, N. Stutzmann, B.W. Laursen, W. Pisula, M.D. Watson, T. Bjornholm, K. Mullen, J.M. Warman, *Adv. Funct. Mater.* **2004**, *14*, 1053; (e) H. John, R. Bauer, P. Espindola, P. Sonar, J. Heinze, K. Mullen, *Angew. Chem. Int. Ed.* **2005**, *44*, 2447.

[115] (a) M. Ornatska, S. Peleshanko, B. Rybak, J. Holzmueller, V.V. Tsukruk, *Adv. Mater.* **2004**, *16*, 2206; (b) M. Ornatska, K. Bergman, B. Rybak, S. Peleshanko, V.V. Tsukruk, *Angew. Chem.* **2004**, *43*, 5246; (c) M. Ornatska, S. Peleshanko, K.L. Genson, B. Rybak, K. Bergman, V.V. Tsukruk, *J. Am. Chem. Soc.* **2004**, *126*, 9675.

[116] Lee, M.; Cho, B.K.; Jang, Y.G.; Zin, W.C. *J. Am. Chem. Soc.*, **2000**, 122, 7449.

[117] Lee, M.; Kim, J.-W.; Hwang, I.-W.; Kim, Y.-R.; Oh, N.-K.; Zin, W.-C. *Adv. Mater.*, **2001**, *13*, 1363.

[118] Lee, M.; Jeong, Y.-S.; Cho, B.-K.; Oh, N.-K.; Zin, W.-C. *Chem. Eur. J.*, **2002**, *8*, 876.

[119] Yoo, Y-S.; Choi, J-H.; Song, J-H.; Oh, N-K.; Zin, W-C.; Park, S.; Chang, T.; Lee, M. *J. Am. Chem. Soc.* **2004**, *126*, 6294.

[120] Holzmueller, J.; Genson, K.L.; Park, Y.; Yoo, Y.-S.; Park, M.-H.; Lee, M.; Tsukruk, V.V. *Langmuir* **2005**, *21*, 6392.

[121] Ruhe, J. in *Polymer Brushes* Advincula, R.C.; Brittain, W.J.; Caster, K.C.; Ruhe, J. (Eds.) Wiley-VCH; Weinheim, **2004**.

[122] Tsukruk, V.V.; Bliznyuk, V.N., *Langmuir*, **1998**, 14, 446.

[123] Tsukruk, V.V.; Bliznyuk, V.N.; Hazel, J.; Visser, D.; Everson, M.P. *Langmuir* **1996**, *12*, 4840.

[124] Tsukruk, V.V.; Bliznyuk, V.N. *Langmuir* **1998**, *14*, 446.

[125] Langmuir, I. *J. Am. Chem. Soc.*, **1917**, *39*, 1848.

[126] Blodgett, K. A. *J. Am. Chem. Soc.*, **1935**, *57*, **1007.**

[127] Blodgett, K. A. *Phys. Rev.*, **1937**, *51*, 964,

[128] Tsukruk, V.V.; Bliznyuk, V.N.; Hazel, J.; Visser, D.; Everson, M.P., *Langmuir*, **1996**, 12, 4840.
[129] Tsukruk, V.V.; Bliznyuk, V.N. *Langmuir* **1998**, *14*, 446.
[130] Gregory, B.W.; Vaknin, D.; Gray, J.D.; Ocko, B.M.; Stroeve, P.; Cotton, T. M.; Struve, W.S. *J.Phys. Chem. B* **1997**, 101, 2006.
[131] Kaganer, V. M.; Mohwald, H.; Dutta, P. *Rev. Mod. Phys.*, **1999**, *71*, 779.
[132] Kaganer, V. M.; Loginov, E. B. *Phys. Rev. B*, **1995**, *51*, 2237.
[133] Kaganer, V. M.; Osipov, M. A.; Peterson, I. R. *J. Chem. Phys.*, **1993**, 98, 3512.
[134] Hosemann, R.; Bagchi, S. N. *Direct Analysis of Diffraction by Matter*; Interscience: New York, **1962**
[135] Bohm, C.; Leveiller, F.; Jacquemain, D.; Mohwald, H.; Kjaer, K.; Als-Nielsen, J.; Weissbuch, I.; Leiserowitz, L. *Langmuir* **1994**, *10*, 830.
[136] Weissbuch, I.; Leveiller, F.; Jacquemain, D.; Kjaer, K.; Als-Nielsen, J.; Leiserowitz. L. *J. Phys. Chem.* **1993**, *97*, 12858.
[137] Vaknin, D.; Kelley, M.S. *Biophys. J.* **2000**, *79*, 2616.
[138] Vankin, D. in: *Methods of Materials Research*, Eds. E. N. Kaufmann, R. Abbaschian, P. A. Barnes, A. B. Bocarsly, C. L. Chien, B. L. Doyle, B. Fultz, L. Leibowitz, T. Mason, J. M. Sanchez, John Wiley & Sons: New York, **2001**, 10d.2.1
[139] Klug, H. P.; Alexander, L. E. *X-ray Diffraction Procedures for Polycrystalline and Amorphous Materials*, Wiley: New York, **1954**.
[140] Foster, B. in *Comprehensive Desk Reference of Polymer Characterization and Analysis* Brady, R.F Jr. (Ed.) Oxford University Press: New York, **2003**.
[141] Tsukruk, V. V.; Wahl, K. J. (Eds.) *Microstructure and Microtribology of Polymer Surfaces*, Oxford University Press:Washington, DC, **2000**.
[142] Tsukruk, V.V., *Rubber Chem. Techn.*, **1997**, 70, 430.
[143] Tsukruk, V.V.; Reneker, D.H., *Polymer*, **1995**, 36, 1791.
[144] Hazel, J. L.; Tsukruk, V. V. *Polym. Prepr.* **1996**, 37(2), 567.
[145] Jiang, C.; Ko, H.; Tsukruk, V.V. *Advanced Materials* (Weinheim, Germany) **2005**, *17*, 2127.
[146] Helfer, C.A.; Mendicuti, F.; Mattice, W.L. in *Comprehensive Desk Reference of Polymer Characterization and Analysis* Brady, R.F Jr. (Ed.) Oxford University Press: New York, **2003**.
[147] Tompkins, H. G.; McGahan, W. A. *Spectroscopic Ellipsometry and Reflectometry*, John Wiley & Sons, Inc.: New York, **1999**.
[148] Owen, M.J. in *Comprehensive Desk Reference of Polymer Characterization and Analysis* Brady, R.F Jr. (Ed.) Oxford University Press: New York, **2003**.
[149] Cerius^2 3.9, San Diego: Molecular Simulations Inc., **1997**.
[150] Maple, J. R.; Dinur, U.; Hagler, A. T. *Proc. Natl. Acad. Sci. US*, **1988**, *85*, 5350.
[151] Haile, J.M. *Molecular Dynamics Simulation: Elementary Methods* John Wiley & Sons, Inc.: New York **1992**
[152] (a) Julthongpiput, D.; Lin, Y-H.; Teng, J.; Zubarev, E. R.; Tsukruk, V. V. *J. Am. Chem. Soc.* **2003**, *125*, 15912; (b) Luzinov, I.; Minko, S.; Tsukruk, V. V. *Prog. Polym. Sci,*. **2004**, *29*, 635; (c) Tsukruk, V. V. *Prog. Polym. Sci.*, **1997**, *22*, 247.

[153] (a) Yesodha, S.K.; Sadashiva Pillai, S.K.; Tsutsumi, N. *Prog. Polym. Sci.* **2004**, *29*, 45; (b) Tsukruk, V. V.; Bliznyuk, V. N. *Prog. Polym. Sci.*, **1997**, *22*, 1089.
[154] Steitz, R.; Peng, J. B.; Peterson, I. R.; Gentle, I.R.; Kenn, R. M.; Goldmann, M.; Barnes, G.T. *Langmuir*, **1998**, 14, 7245.
[155] Peterson, I. R.; Brezesinski, G.; Struth, B.; Scalas, E. *J. Phys. Chem. B*, **1998**, *102*, 9437.
[156] Gunier, A. *X-Ray Diffraction In Crystals, Imperfect Crystals, and Amorphous Bodies*; Dover: New York, 1994.
[157] Tsukruk, V. V.; Shilov,V. *Structure of Polymeric Liquid Crystals* Kiev, Naukova Dumka, 1990.
[158] Kaganer, V. M.; Peterson, I.R.; Kenn, R. M.; Shih, M. C; Durbin, M.; Dutta, P. *J. Chem. Phys.*, **1995**, 102(23), 9412.
[159] Peterson, I.R.; Russell, G.J.; Earls, J. D.; Girling, I. R. *Thin Solid Films*, **1988**, 161, 325.
[160] Pao, W. J.; Stetzer, M., Heiney, P.; Cho, W. D.; Percec, V. *J. Phys. Chem. B*, **2001**, 105, 2170.
[161] Peterson, I. R. *J. Phys. D: Appl. Phys.* **1990**, *23*, 379
[162] Kaganer, V. M.; Möhwald, H.; Dutta, P. *Rev. Mod. Phys.* **1999**, *71*, 779.
[163] Weidemann, G.; Brezesinki, G.; Vollhardt, D.; Mohwald, H. *Langmuir* **1998**, *14*, 6458.
[164] Seki, T.; Takashi, F.; Kunihiro, I. *Bull. Chem. Soc. Jpn.* **1998**, *71*, 2807.
[165] Hoebbel, D.; Nacken, M.; Schmidt, H. *J. Sol-Gel Sci. Techn.* **1998**, *12*, 169.
[166] Peterson, I. R.; Brezesinski, G.; Struth, B.; Scalas, E. *J. Phys. Chem. B* **1998**, *102*, 9437.
[167] Dutta, P. *Colloids and Surfaces A* **2000**, *171*, 59.
[168] Peterson, I. R.; Brezesinski, G.; Struth, B.; Scalas, E. *J. Phys. Chem. B* **1998**, *102*, 9437.
[169] Durbin, M. K.; Malik, A.; Richter, A. G.; Yu, C. J.; Eisenhower, R.; Dutta, P. *Langmuir* **1998**, *14*, 899.
[170] Harada, J.; Ogawa, K.; Tomoda, S. *Acta Cryst.* **1997**, *B53*, 662.
[171] Genson, K.L.; Holzmueller, J.; Villavicencio, O.; McGrath, D.; Tsukruk, V.V. *Thin Solid Films* **2005**, *493*, 237.
[172] Kumar, G. S.; Neckers, D. C. *Chem. Rev.*, **1989**, *89*, 1915.
[173] Jiang, C.; Markutsya, S.; Tsukruk, V.V. *Adv. Mater.* **2004**, *16*, 157.
[174] Cho, J.; Char, K.; Hong, J.-D.; Lee, K.-B.; *Adv. Mater.* **2001**, *13*, 1076.
[175] Chiarelli, P.A.; Jonal, M.S.; Carron, J.L.; Roberts, J.B.; Robinson, J.M.; Wang, H.-L. *Langmuir* **2002**, *18*, 168.
[176] Tsukruk, V.V.; Luzinov, I.; Larson, K.; Li, S.; McGrath, D.V. *J. Mater. Sci. Let.* **2001**, *20*, 873.
[177] Zhu, Y. M.; Jia, X. B.; Xiao, D.; Lu, Z. H.; Wei, Y.; Wu, Z. H.; Hu, Z. L.; Xie, M. G. *Phys. Lett.*, **1994**, *188*, 287.
[178] Zhu, Y. M.; Wei, Y. *J. Chem. Phys.*, **1994**, *101*, 10023.
[179] Zhu, Y. M.; Lu, Z. H.; Wei, Y. *Phys. Rev. E*, **1995**, *51*, 418.
[180] Bobrovsky, A.Yu.; Pakhomov, A.A.; Shu, X.-M.; Boiko, N.I.; Shibaev, V.P.; Stumpe, J. *J. Phys. Chem. B* **2002**, *106*, 540.
[181] Weener, J.-W.; Meijer, E.W. *Adv. Mater.* **2000**, *12*, 741.
[182] Bobrovosky, A.; Ponomarenko, S.; Boiko, N.; Shibaev, V.; Rebrov, E.; Muzafarov, A.; Stumpe, J. *Macromol. Chem. Phys.* **2002**, *203*, 1539

[183] Tsuda, K.; Dol, G.C.; Gensch, T.; Hofkens, J.; Latterini, L.; Weener, J.W.; Meijer, E.W.; De Schryver, F.C. *J. Am. Chem. Soc.* **2000**, *122*, 3445.
[184] Richardson, R.M.; Ponomarenko, S.A.; Boiko, N.I.; Shibaev, V.P. *Liq. Cryst.* **1999**, *26*, 101.
[185] Ponomarenko, S.A.; Boiko, N.I.; Shibaev, V.P.; Richardson, R.M.; Whitehouse, I.J.; Rebrov, E.A.; Muzafarov, A.M. *Macromolecules* **2000**, *33*, 5549.
[186] Agina, E.V.; Ponomarenko, S.A.; Boiko, N.I.; Rebrov, E.A.; Muzafarov, A.M.; Shibaev, V.P. *Polymer Science A* **2001**, *43*, 1000.
[187] Tsukruk, V. V., Shilov, V. V. *Structure of Polymeric Liquid Crystals*, Naukova Dumka, Kiev, **1990**.
[188] Ponomarenko, S.A.; Boiko, N.I.; Shibaev, V.P.; Magonov, S.N. *Langmuir*, **2000**, *16*, 5487.
[189] Shibaev, V.; Bobrovsky, A.; Boiko, N. *Prog. Polym. Sci.* **2003**, *28*, 729
[190] Gregory, B.W.; Vaknin, D; Gray, J.D.; Ocko, B.M.; Stroeve, P.; Cotton, T.M.; Struve, W.S. *J. Phys. Chem.* **1997**, *101*, 2006.
[191] Spratte, K.; Riegler, H. *Makromol. Chem. Macromol. Symp.* **1991**, *46*, 113.
[192] Roberts, G. (ed.) *Langmuir-Blodgett films* **1990**, Plenum Press: New York.
[193] Petty, M. *Langmuir-Blodgett films: an introduction* **1996**, Cambridge University Press: Cambridge, New York.
[194] Zhang, L.; Eisenberg, A. *Science* **1995**, *268*, 1728.
[195] Li, S.; Clarke, C.J.; Lennox, R.B.; Eisenberg, A. *Colloids Surf A* **1998**, *133*, 191.
[196] Terreau, O.; Luo, L.; Eisenberg, A. *Langmuir* **2003**, *19*, 5601.
[197] Li, S.; Clarke, C.J.; Eisenberg, A.; Lennox, R.B. *Thin Solid Films* **1999**, *354*, 136.
[198] Schnitter, M; Engelking, J.; Heise, A.; Miller, R.B.; Menzel, H. *Macromol. Chem. Phys.* **2000**, *201*, 1504.
[199] Karim, A.; Tsukruk, V.V.; Douglas, J.F.; Satija, S.K.; Fetters, L.J.; Reneker, D.H.; Foster, M.D. *J. Phys., II* **1995**, *5*, 1441.
[200] (a) Zhu, J.; Eisenberg, A.; Lennox, R. B. *J. Am. Chem. Soc.* **1991**, *113*, 5583; (b) Zhu, J.; Lennox, R. B.; Eisenberg, A. *Langmuir* **1991**, *7*, 11579; (c) Zhu, J.; Eisenberg, A.; Lennox, R. B. *Makromol. Chem.* **1992**, *53*, 211; (d) Zhu, J.; Lennox, R. B.; Eisenberg, A. *J. Phys. Chem.* **1992**, *96*, 4727; (e) Zhu, J.; Eisenberg, A.; Lennox, R. B. *Macromolecules* **1992**, *25*, 6547; (f) Zhu, J.; Eisenberg, A.; Lennox, R. B. *Macromolecules* **1992**, *25*, 6556.
[201] Luzinov, I.; Julthongpiput, D.; Tsukruk, V. V. *Macromolecules*, **2000**, *33*, 7629.
[202] Tsukruk, V.V.; Genson, K.; Peleshanko, S.; Markutsya, S.; Lee, M.; Yoo, Y.-S. *Langmuir* **2003**, *19*, 495.
[203] Cox, J. K.; Yu, K.; Constantine, B.; Eisenberg, A.; Lennox, R. B. *Langmuir* **1999**, *15*, 7714.
[204] Peleshanko, S.; Jeong, J.; Gunawidjaja, R.; Tsukruk, V. V. *Macromolecules*, **2004**, *37*, 6511.
[205] Logan, J. L., Masse, P.; Dorvel, B.; Skolnik, A.M.; Sheiko, S.S.; Francis, R.; Taton, D.; Gnanou, Y.; Duran, R.S.*Langmuir* **2005**, *21*, 3424
[206] Raman reference
[207] Williams, D.R.; Fredrickson, G.H. *Macromolecules* **1992**, *25*, 3561.
[208] Li, W.; Gersappe, D. *Macromolecules* **2001**, *34*, 6783.
[209] Molau, G. E. in *Block Copolymers*, S. L. Aggarwal, Ed. Pelnum, New York, **1970**.

[210] Dawkins, J. V. in: *Block Copolymers,* D. C. Allport and W. H. James, Eds., John Wiley & Sons, New York ,**1973.**
[211] Xu, Z.; Holland, N. B.; Marchant, R. E *Langmuir*, **2001**, *17*, 377.
[212] Kampf, J. P.; Frank, C. W.; Malmstrom, E. E.; Hawker, C. J. *Langmuir*, **1999**, *15*, 227.
[213] Karim, A.; Tsukruk, V. V.; Douglas, J. F.; Satija, S. K.; Fetters, L. J.; Reneker, D. H.; Foster, M. D. *J. Phys., II,* **1995**, *5*, 1441.
[214] Luzinov, I.; Julthongpiput, D.; Malz, H.; Pionteck, J.; Tsukruk, V. V. *Macromolecules* **2000**, *33*, 1043.
[215] Halperin, A.; Tirrell, M.; Lodge, T. P. *Adv. Polym. Sci.* **1992**, *100*, 33.
[216] (a) H.-A. Klok, S. Lecommandoux, *Adv. Mater.* **2001**, *13*, 1217; (b) P. Gopalan, X. Li, M. Li, C.K. Ober, C.P. Gonzales, C.J. Hawker, *J. Polym. Sci.* **2003**, *41*, 3640; (c) M. Lee, B-K. Cho, W-C. Zin, *Chem. Rev.* **2001**, *101*, 3869; (d) A.P.H.J. Schenning, C. Elissen-Roman, J. Weener, M.W.P.L. Baars, S.J. van der Gaast, E.W. Meijer, *J. Am. Chem. Soc.* **1998**, *120*, 8199.
[217] Holzmueller, J.; Genson, K.L.; Park, Y.; Yoo, Y.-S.; Park, M.-H.; Lee, M.; Tsukruk, V.V. *Langmuir* **2005**, *21*, 6392.
[218] Y-S. Yoo, J-H. Choi, J-H. Song, N-K. Oh, W-C. Zin, S. Park, T. Chang, M. Lee, *J. Am. Chem. Soc.* **2004**, *126*, 6294.
[219] Mahltig, B.; Jérôme, R.; Stamm, M. *Phys. Chem. Chem. Phys* **2001**, *3*, 4371.
[220] Genson, K.L.; Huffman, J.; Teng, J.; Zubarev, E.R.; Vaknin, D.; Tsukruk, V.V. *Langmuir,* **2004**, *20,* 9044.
[221] Lee, M.; Jang, C.-J.; Ryu, J.-H. *J. Am. Chem. Soc.* **2004**, *126*, 8082.
[222] Yoo, Y.-S.; Choi, J.-H.; Song, J.-H.; Oh, N.-K.; Zin, W.-C.; Park, S.; Chang, T.; Lee, M. *J. Am. Chem. Soc.* **2004**, *126*, 6294.
[223] Cox, J. K.; Yu, K.; Eisenberg, A.; Lennox, R. B. *Phys. Chem. Chem. Phys*. **1999**, *1*, 4417.
[224] Richards, R. W.; Rochford; B. R., Webster, J. R. P. *Polymer* **1997**, *38* 1169.
[225] Tsukruk, V.; Genson, K.; Peleshanko, S.; Markutsya, S.; Lee, M.; Yoo, Y.-S. *Langmuir* **2003**, *19*, 495.
[226] (a) Percec, V.; Glodde, M.; Johansson, G.; Balagurusamy, V. S. K.; Heiney, P. A. *Angewandte Chemie, Int. Ed.* **2003**, *42*, 4338. (b) Jung, H. T.; Kim, S. O.; Ko, Y. K.; Yoon, D. K.; Hudson, S. D.; Percec, V.; Holerca, M. N.; Cho, W.-D.; Mosier, P. E. *Macromolecules* **2002**, *35*, 3717. (c) Pao, W.-J.; Stetzer, M. R.; Heiney, P. A.; Cho, W.-D.; Percec, V. *J. Phys. Chem. B* **2001**, *105*, 2170. (d) Percec, V.; Cho, W.-D.; Ungar, G. *J. Am. Chem. Soc.* **2000**, *122*, 10273. (d) Yeardley, D. J. P.; Ungar, G.; Percec, V.; Holerca, M. N.; Johansson, G. *J. Am. Chem. Soc.* **2000**, *122*, 1684. (e) Hudson, S. D.; Jung, H.-T.; Percec, V.; Cho, W.-D.; Johansson, G.; Ungar, G.; Balagurusamy, V. S. K. *Science*, **1997**, *278*, 449. (f) Percec, V.; Ahn, C.-H.; Ungar, G.; Yeardley, D. J. P.; Moller, M.; Sheiko, S. S. *Nature*, **1998**, *391*, 161.
[227] (a) M.V. Kozlovsky, *Cryst. Res. Technol.* **2001**, *36*, 1083; (b) M.J. Avrami, *Chem. Phys.* **1940**, *8*, 212.
[228] (a) F.P. Price, *J. Poly. Sci.* **1961**, *54*, S40; (b) F.P. Price, R.W. Kilb, *J. Poly. Sci.* **1962**, *57*, 395.

[229] C.A. Helfer, F. Mendicuti, W.L. Mattice, in *Comprehensive Desk Reference of Polymer Characterization and Analysis* (Ed. R.F. Brady, Jr.) Oxford University Press, New York, **2003**.

BIOGRAPHICAL SKETCH

[redacted] She attended Western Michigan University between August, 1997 and April, 2000. In August, 2000 she transferred into the MS/BS concurrent program in the Materials Science and Engineering Department at Iowa State University. She received concurrently the Bachelor of Science in Materials Engineering and Master of Science in Materials Science and Engineering in May, 2003. She had interned with the Naval Research Laboratory in Washington, DC in the summer of 1998 and interned at IBM's Almaden Research Center outside San Jose, CA in the summer of 1999. Summer 2003, Genson took part in the National Science Foundation East Asia Summer Institute and worked at Fukuoka University, Kyusu, Japan. She worked as an undergraduate Research Assistant at Western Michigan University, served as a Graduate Research Assistant at Iowa State University, and taught the laboratory section of the undergraduate and graduate course Polymer Characterization. Her work resulted in 15 refereed papers (7 first author), 14 proceedings and abstract, 2 publicity articles in APS Annual Reviews, and 7 presentations at professional society national meetings. In addition Genson mentored high school girls attending the ISU Women in Science Summer program in 2002 and 2004, and was the graduate student representative for the MSE department faculty meetings for the 2003-2004 academic year. Dr. Genson was selected in 2005 to be a National Research Council postdoctoral research associate at the National Institute of Standards and Technology in Gaithersburg, Maryland.

PROFESSIONAL PUBLICATIONS

Refereed Publications

1. Gunawidjaja, Ray; Genson, Kirsten L.; Peleshanko, Sergiy; Tsitsilianis, Constaninos; Tsukruk, Vladimir V. "Uniform and Dendritic Surface Morphologies of Langmuir-Blodgett Monolayers of PEO_n-PS_n Star Block Copolymers with Large Number of Arms," *Macromolecules* **2006**, submitted.
2. Genson, Kirsten L.; Holzmueller, Jason; Ornatska, Maryna; Lee, Myongsoo; Yoo, Yong-Sik; Par, Myoung-Hwan; Tsukruk, Vladimir V. "Assembling of dense fluorescent supramolecular webs via self-propelling of rod-dendron molecules into star-shaped aggregates," *Nano Letters* **2006**, submitted.
3. Rybak, Beth; Bergman, Kathryn; Ornatska, Maryna; Genson, Kirsten L.; Tsukruk, Vladimir V. "The formation of silver nanoparticles at the air-water interface mediated by functionalized hyperbranched molecules," *Langmuir*, **2005**, accepted.
4. Genson, Kirsten L.; Holzmueller, Jason; Vaknin, David; Villacencio, Ovette; McGrath, Dominic V.; Tsukruk, Vladimir, V., "Ordering Behavior of Langmuir Monolayers of Photochromic Amphiphilic Monodendrons." *Journal of Physical Chemistry B* **2005**, *109*, 20393.
5. Genson, Kirsten L.; Holzmueller, Jason; Leshchiner, Ignaty; Agina, Elena; Boiko, Natalia; Shibaev, Valery; Tsukruk, Vladimir V., "Surface Nanostructures within Monolayers of Carbosilane Dendrimers with Mesogenic Terminal Groups." *Macromolecules*, **2005**, *38*, 8028.
6. Genson, Kirsten L.; Holzmueller, Jason; Vaknin, David; Villacencio, Ovette; McGrath, Dominic V.; Tsukruk, Vladimir, V., "Langmuir Monolayers from Functionalized Amphiphiles with Epoxy Terminal Groups." *Thin Solid Films* **2005**, *493*, 237.
7. Holzmueller, Jason; Genson, Kirsten L.; Park, Yushin; Lee, Myongsoo; Tsukruk, Vladimir V., "Non-Symmetrical Dendron-Rod Amphiphiles, from Layered Stems to Circular Micelles." *Langmuir* **2005**, *21*, 6392.

8. Genson, Kirsten L.; Huffman, Joshua; Teng, Jing; Zubarev, Eugene, R.; Vaknin, David; Tsukruk, Vladimir V., "Interfacial Micellar Structures from Novel Amphiphilic Star Polymers." *Langmuir* **2004**, *20*, 9044.
9. Peleshanko, S.; Jeong, J.; Shevchenko, V.V; Genson, K. L.; Pikus, Y.; Ornatska, M.; Petrash, S.; Tsukruk, V. V., "Synthesis and properties of asymmetric heteroarm PEO_n-b-PS_m star polymers with end functionalities." *Macromolecules* **2004**, *37*, 7497.
10. Ornatska, Maryna; Peleshanko, Sergiy; Genson, Kirsten L.; Rybak, Beth; Bergman, Kathy N.; Tsukruk, Vladimir V., "Assemblying of amphiphilic highly branched molecules in supramolecular nanofibers." *Journal of American Chemical Society* **2004**, *126*, 9675.
11. Zhai, X.; Peleshanko, S.; Klimenko, N. S.; Genson, K. L.; Vortman, M. Ya.; Shevchenko, V. V.; Vaknin, D.; Tsukruk V. V., "Amphiphilic hyperbranched polyesters with alkyl-terminated branches." *Macromolecules* **2003**, *36*, 3101
12. Tsukruk, Vladimir V.; Genson, Kirsten; Peleshanko, Sergiy; Markutsya, Sergiy; Greco, Aaron; Lee, Myongsoo; Yoo, Yong-Sik, "Molecular reorganizations of rod-coil molecules on a solid surface." *Langmuir* **2003**, *19*, 495
13. Genson, Kirsten L.; Vaknin, David; Villacencio, Ovette; McGrath, Dominic V.; Tsukruk, Vladimir V., "Microstructure of amphiphilic monodendrons at the air-water interface." *Journal of Physical Chemistry B* **2002**, *106*, 11277
14. Lee, M.; Kim, J.-W.; Peleshanko, S.; Larson, K.; Yoo, Y.; Vaknin, D.; Markutsya, S.; Tsukruk, V. V., "Amphiphilic hairy disks with branched hydrophilic tails and a hexa-peri-hexabenzocoronene core." *Journal of the American Chemical Society* **2002**, *124*, 9121
15. Larson, K.; Vaknin, D.; Villavicencio, O.; McGrath, D.; Tsukruk, V. V. "Molecular packing of amphiphiles with crown polar heads at the air-water interface." *Journal of Physical Chemistry B* **2002**, *106*, 7246
16. Peleshanko, S.; Sidorenko, A.; Larson, K.; Villavicencio, O.; Ornatska, M.; McGrath, D. V.; Tsukruk, V. V., "Langmuir-Blodgette monolayers from lower generation amphiphilic monodendrons." *Thin Solid Films* **2002**, *406*, 233

17. Tsukruk, V. V.; Luzinov, I.; Larson, K.; Li, S.; McGrath, D. V., "Intralayer reorganization of photochromic molecular films." *Journal of Materials Science Letters* **2001**, *20*, 873

Proceedings and Abstracts

1. Genson, Kirsten L.; Huffman, Joshua; Teng, Jing; Zubarev, Eugene R.; Vaknin, David; Tsukruk, Vladimir V., "Interfacial behavior of 12-arm star polymers with alternating arms." *Polymeric Materials: Science and Engineering* **2004**, *91*, 1002.
2. Genson, Kirsten L.; Holzmueller, Jason; Villavincencio, Ovette F.; McGrath, Dominic V.; Vaknin, David; Tsukruk, Vladimir V. "Stability of photochromic monodendrons at the interfaces." *Polymeric Materials: Science and Engineering* **2004**, *91*, 930.
3. Omatska, Maryna; Peleshanko, Sergiy; Genson, Kirsten L.; Rybak, Beth; Bergman, Kathryn N.; Tsukruk, Vladimir V., "Directed Self Assembly of Aliphatic Hyperbranched Polyesters." *Polymeric Materials: Science and Engineering* **2004**, *91*, 196.
4. Genson, Kirsten L.; Huffman, Joshua; Teng, Jing; Zubarev, Eugene R.; Vaknin, David; Tsukruk, Vladimir V., "Interfacial behavior of 12-arm star polymers with alternating arms." *Abstracts of Papers, 228th ACS National Meeting, Philadelphia, PA, United States, August 22-26, 2004*, **2004**, PMSE-545.
5. Genson, Kirsten L.; Holzmueller, Jason; Villavicencio, Ovette F.; McGrath, Dominic V.; Vaknin, David; Tsukruk, Vladimir V. "Stability of photochromic monodendrons at interfaces." *Abstracts of Papers, 228th ACS National Meeting, Philadelphia, PA, United States, August 22-26, 2004*, **2004**, PMSE-505.
6. Ornatska, Maryna; Peleshanko, Sergiy; Genson, Kirsten L.; Rybak, Beth; Bergman, Kathryn N.; Tsukruk, Vladimir V. "Directed self assembly of aliphatic hyperbranched polyesters." *Abstracts of Papers, 228th ACS National Meeting, Philadelphia, PA, United States, August 22-26, 2004*, **2004**, PMSE-112.
7. Genson, Kirsten L.; Teng, Jing; Zubarev, Eugene R.; Vaknin, David; Tsukruk, Vladimir V. "Amphiphilic star polymer at air-water and air-solid interfaces." *Polymeric Materials Science and Engineering* **2003**, *89*, 257.

8. Genson, Kirsten L.; Teng, Jing; Zubarev, Eugene R.; Vaknin, David; Tsukruk, Vladimir V., "Amphiphilic star polymer at air-water and air-solid interfaces." *Abstracts of Papers, 226th ACS National Meeting, New York, NY, United States, September 7-11, 2003*, **2003**, PMSE-170.
9. Lee, Myongsoo; Kim, Jung-Woo; Yoo, Yong-Sik; Peleshanko, Sergiy; Larson, Kirsten; Vaknin, David; Markutsya, Sergei; Tsukruk, Vladimir, "Organization of Amphiphilic Molecular Disks with Branched Hydrophilic Tails and Hexa-peri-hexabenzocoronene Core" *Bulletin of the American Physical Society, March 2002 Meeting 47*, **2002**, M33 28.
10. Larson, K.; Vaknin, D.; Villavicencio, O.; McGrath, D.; Tsukruk, V.V., "Molecular Packing of Amphiphiles with Crown Polar Heads at the Air-Water Interface" *Bulletin of the American Physical Society, March 2002 Meeting 47*, **2002**, U31 11.
11. Larson, K.; Vaknin, D.; Villavicencio, O.; McGrath, D.; Stephenson, N.; Tsukruk, V. V., "Synchrotron studies of amphiphiles with crown polar heads at air-water interface." *Polymeric Materials Science and Engineering* **2001**, *85*, 229.
12. Larson, Kirsten; Vaknin, David; Villavicienco, O.; McGrath, Dominic V.; Stephenson, Nicole; Tsukruk, Vladimir V., "Synchrotron studies of amphiphiles with crown polar heads at air-water interface." *Abstracts of Papers, 222nd ACS National Meeting, Chicago, IL, United States, August 26-30, 2001*, **2001**.